MODELLING AND EXPERIMENTAL STUDY OF MILLIMETRE WAVE REFRACTIVE SYSTEMS

A thesis submitted to The University of Manchester for the degree of
Doctor of Philosophy
in the Faculty of Engineering and Physical Sciences

2013

Fahri Ozturk
School of Physics and Astronomy

Contents

Word Count: 58.510

List of Tables

List of Figures

Abstract

MODELLING AND EXPERIMENTAL STUDY OF
MILLIMETRE WAVE REFRACTIVE SYSTEMS
Fahri Ozturk
A thesis submitted to the University of Manchester
for the degree of Doctor of Philosophy, 2013

Astronomical instruments dedicated to the study of Cosmic Microwave Background polarization are in need of optics with very low systematic effects such as beam shape and cross-polarization in an optical configuration. With the demand for millimetre wave larger focal planes comprising thousands of pixels, these systematic effects have to be minimal across the whole focal surface. In order to reach the instrument requirements such as resolution, cross-polarization and beam ellipticity, new optical configurations with well-understood components have to be studied. Refractive configurations are of great importance amongst the potential candidates. The aim is to bring the required technology to the same level of maturity that has been achieved with well-understood existing ones. This thesis is focused on the study of such optical components for the W-band spectral domain. Using optical modelling with various software packages, combined with the manufacture and accurate experimental characterisation of some prototype components, a better understanding of their performance has been reached. To do so, several test set-ups have been developed. Thanks to these new results, full Radio-Frequency refractive systems can be more reliably conceived.

Declaration

No portion of the work referred to in this thesis has been submitted in support of an application for another degree or qualification of this or any other university or other institute of learning.

Copyright

Acknowledgements

I would firstly like to express my warm thanks to my supervisor, Dr. Bruno Maffei, who gave to me the chance to study with him. He provided me with advice, technical support and many other opportunities to complete my research at JBCA. His expertise and understanding contributed a lot to my PhD experience during the completion of this thesis.

I would like to extend my gratitude to Dr. Giampaolo Pisano. Whenever I knocked his door, he interrupted his work and answered my questions patiently. Similarly, I also wish to send special thanks to my friend, Peter Schemmel, read my thesis, helped me correct countless grammar problems and discussed my work with me even at his weekends. I also thank to Dr. Ming Wah Ng for his skilled hand in my RF lab experiments and Vic Haynes for advising me during the lens coating work.

I owe many thanks to all members of JBCA Technology Group. I made very useful scientific discussions with Ho-Ting Fung. I also thank to Imran Mohamed and Stefania Maccalli for their support and contribution to my life in Manchester. They shared the same destiny with me, and many times I did not attend to their organizations by excusing my work. I also thank to Dr. Scott Lewis for motivating me whenever we met in the school halls.

I am aware of the danger of forgetting people who contributed to my PhD thesis when listing their names. I am grateful to Prof. Peter Wilkinson for helping me by advising during my first year report. I am thankful to technical staff of the Schuster Workshop for their advise on manufacturing many components used for my research.

Many thanks to my family for supporting me in my educational pursuits. They always sent their prayers from a couple of thousand miles away to keep me motivated.

I thank a lot for her inestimable friendship to Nil Mansuroglu, who has always been around when I needed a support throughout my life in the UK. I also thank to Ms Claire Vane who supported and guided me during my stay in Cambridge.

I would like to acknowledge the support of Ministry of National Education of

Turkey. They supported my PhD research with a PhD scholarship during my education in the UK.

Finally, my last and very special gratitude goes to my wife, Sevcan Ozturk, who is making my life. I cannot thank her enough for all she has given me. Without her constant love and support throughout my life in the UK, I would have not made this possible. It is not only about her wonderful cooks.

Abbreviations & Acronyms

RF: Radio Frequency
EM: Electromagnetism
PSB: Polarization Sensitive Bolometer
TES: Transition Edge Sensor
HEMT: High Electron Mobility Transistor
LFI: Low Frequency Instrument
HFI: High Frequency Instrument
r(T/S): Tensor to Scalar ratio
CTR: Compact Test Range
CATR: Compact Antenna Test Range
GO: Geometrical Optics
GTD: Geometrical Theory of Diffraction
PO: Physical Optics
PTD: Physical Theory of Diffraction
MOM: Method Of Moments
MLFMM: Multi Fast Multipole Methods
RL-GO: Ray Launching Geometrical Optics
FEM:Finite Element Method
FDTD: Finite Difference Time Domain
FWHM: Full Width Half Maximum
BW: Beam-width
SL: Side-lobe
BE: Beam ellipticity
CP: Co-Polarization
XP: Cross-Polarization
RL: Return loss
SWE: Spherical wave expansion

AP: Aperture field
RAD: Radiation pattern
ARC: Anti-Reflection Coating
TDG: Time Domain Gating
TRL: Transmission Reflection Line
TRM: Transmission Reflection Match
TRC: Rectangular to circular transition
FOV: Field Of View
FP: Focal Plane
DLFOV: Diffraction Limited Field Of View

List of Publications

Journal articles

1. **F. Ozturk**, et. al., ”Detailed modelling of MM-wave lenses for Astronomical instruments”, in preparation, 2013.

2. **F. Ozturk**, et. al., ”A wide field of view characterization of MM-wave lenses for Astronomical instruments”, in preparation, 2013.

3. G. Pisano, M. W. Ng, **F. Ozturk**, B. Maffei, V. Haynes, Dielectrically embedded flat mesh lens for MM waves applications, Applied Optics, Vol:52, No:11, 2218-2225, 2013.

Proceeding papers

1. **F. Ozturk**, B. Maffei, G. Pisano, M. W. Ng, V. Haynes, ”Systematic effects introduced by lenses at MM-wavelengths in CMB applications”, Proc. of SPIE, Vol.84520I, 2012.

2. **F. Ozturk**, B. Maffei, M. W. Ng, ”A quasi-optical free-space S-parameters measurement system for material characterization in W and Ka bands”, 33^{rd} Antenna Workshop on Challenges for Space Antenna Systems, 2011.

3. P. Schemmel, S. Maccalli, B. Maffei, **F. Ozturk**, M. W. Ng, ”A near field 3D scanner for millimetre wavelengths”, 35^{th} Antenna Workshop on Antenna and Free Space RF Measurements, 2013.

4. B. Maffei, S. Legg, M. Robinson, **F. Ozturk**, M. W. Ng, P. Schemmel, G. Pisano, ”Implementation of a quasi-optical free-space S-parameters measurement system”, 35^{th} Antenna Workshop on Antenna and Free Space RF Measurements, 2013.

5. I. Mohammed, G. Pisano, B. Maffei, N. G. Wah, **F. Ozturk**, ”A negative refractive index metamaterial plate for millimeter-wave applications”, Proc. of SPIE, Vol.845228, 2012.

6. B. Maffei, G. Pisano, M. W. Ng, V. Haynes, **F. Ozturk**, ”Millimetre wave photolithographic polarizer beam effect”, Proc. of PIERS, 2012.

Conference posters

1. **F. Ozturk**, B. Maffei, H. T. Fung, A lens antenna system study for future CMB polarization projects, UK-Germany National Astronomy Meeting (NAM), 2012.

2. H. T. Fung, **F. Ozturk**, B. Maffei, Instrumental systematic effects of quasi-optical components for astronomical instruments, UK-Germany National Astronomy Meeting (NAM), 2012.

Chapter 1

INTRODUCTION

Each portion of the electromagnetic (EM) spectrum provides unique information on the Universe. People only relied on their eyes and visible telescopes to observe the sky for a long period in history. However, the EM spectrum covers not only visible light but also many other wavelengths from Radio (long wavelengths) to Gamma-rays (short wavelengths) (Figure 1.1). Multi-wavelength observations of the Universe have revealed different properties of cosmic structures. For instance, in Figure 1.2 the Andromeda Galaxy appears drastically different when observed at different wavelengths. The millimetre (mm) wave spectrum lies between the 30 GHz ($\sim$1cm) and 300 GHz ($\sim$1mm) ranges. Observations at mm wavelengths have revealed a hidden Universe by revealing many unkown formations and structures.

Karl Jansky, the pioneer of Radio Astronomy, observed weak signals that originated from the centre of the Milky Way in 1931 [2]. Following Jansky, Grote Reber

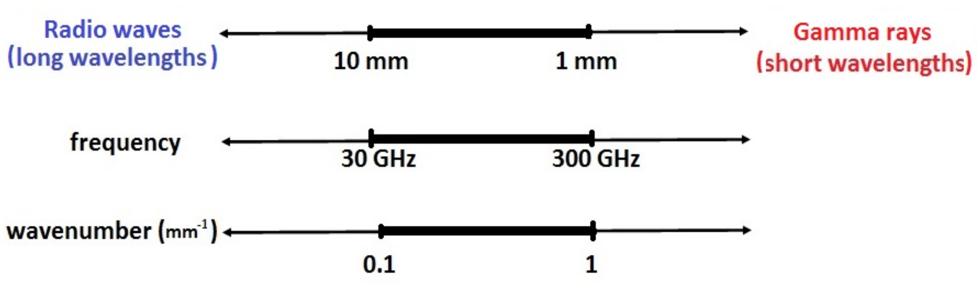

Figure 1.1: The electromagnetic spectrum. Its limits extend from radio waves to gamma rays. The Mm-wave regime lies between the microwave and infrared ranges.

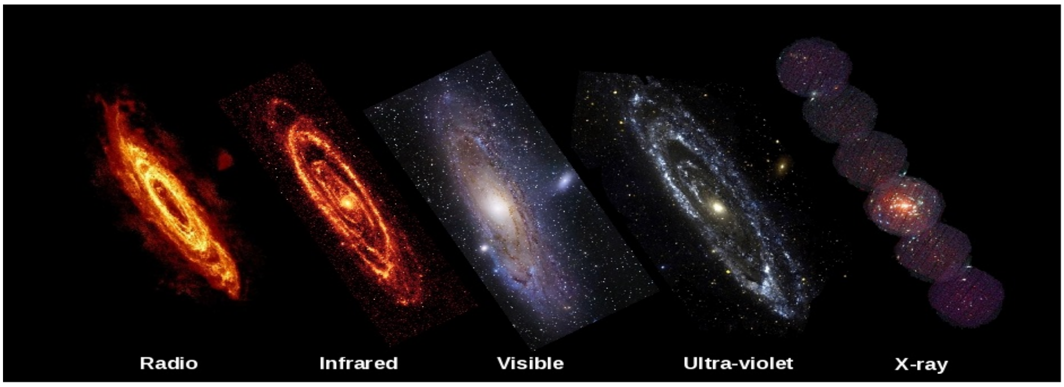

Figure 1.2: The Andromeda Galaxy seen at different wavelengths from Radio to X-rays [1].

mapped the radio sky by using the first parabolic reflector in 1937 [3]. Cosmic mm-wave radiation is weak compared to sources used in telecommunication systems. Detection of weak astronomical sources requires very sensitive receivers for the mm-wave range. The spectrum of complex molecules and cold dust in the interstellar medium are the primary subjects of mm-wave observations. Additionally, the first light of the Universe, the CMB, radiates at a temperature of ∼2.75 K, which is cool enough to be probed by MM-wave observations.

Most astronomical systems rely on an optical system to collect and focus the incoming radiation onto an instrument. These systems could be either refractive or reflective, or a hybridization of both. In the visible range, refractive technology is well understood, and optical simulations with conventional ray-based optics are very reliable. However, refractive technology is not mature enough at mm wavelengths. Mm-wave refractive instrumentation, which I will study in this thesis, can potentially be used in experiments dedicated to measurements of B mode polarization in CMB radiation (see Chapter 2). CMB instruments are in need of very well understood optics with low systematic effects in order to detect weak B-mode signals. To this end, new low-systematic telescope configurations are being studied to be coupled to very large focal planes, in order to obtain a high sensitivity. Future instrumental requirements (see Section 2.2) of B-mode observations are more stringent than those of previous missions such as Planck (see Section 1.3.1). For example, simulations of Planck mirrors were performed using a reflector based software package (GRASP). Predictions of co- (CP) and cross-polarization (XP) beam patterns were validated by real measurements down to a dynamic range of -60 to -80 dB [4]. However, refractor based systems are not at the same level of technology readiness compared to mm-wave reflector based systems. It is clear that ray optics alone is not enough to describe light propagation in the mm-wave regime. Effects of diffraction and detailed polarisation are not considered in Geometrical Optics (GO) calculations. For this reason, depending on the problem size, a further investigation of mm wave lenses should be made by using full-wave modellers, such as Method of Moments (MOM) with FEKO simulations. An optical code, which models CMB components, should also consider multiple reflections in the optical chain of the instrument. All these effects are expected to be taken into consideration only by means of a full-wave modeller. For a successful lens design, a hybridization of different numerical solution tools might also be needed. Typically, the initial design of the lens is conducted with a basic model such as GO, and then expanded to full-wave model analysis.

Validations of lens simulations should also be carried out by experimental measurements of horn-lens systems with and without ARC. In order to obtain the required confidence in models of refractive elements, RF characterizations of refractive materials need to be provided. Accurate material information obtained from these RF characterizations will help to design, manufacture and measure the refractive components to high precision. In the end, all the characterization processes mentioned above will provide a good understanding of the polarization systematic effects (e.g. XP, instrumental polarization, main beam shape) that lens systems introduce for both on-axis and off-axis pixel horn antennas.

1.1 CMB Science rationale

CMB radiation is the oldest light coming from the furthest part of the Universe. CMB radiation almost isotropically fills our universe and peaks at microwave wavelengths. CMB was first detected by A. Penzias and R. Wilson in 1965 [5]. However, they were not aware that they had found something that had already been proposed by G. Gamov, R. Alpher, and R. Herman in 1946 [6]. These three researchers stated that the early universe should have left behind radiation that should be observed at 5K throughout the sky.

At an earlier time, the Universe was extremely dense ($\sim 5x10^{93} gr/cm^3$) and hot. Since the mean free path of photons was not long, free-electrons captured photons and did not let them travel freely. At that time, the Universe resembled an ionised soup of fundamental particles (baryons, electrons, positrons, neutrinos, photons). At ~ 1 second, there were only quarks that later produced baryons. Around 380.000 years after the Big Bang, the temperature of the Universe was $\sim$3000 K. At that time, photons were able to radiate through a transparent universe without interacting with electrons. This phase is known as the surface of last scattering. Proton-electron couples formed the first atoms (neutral hydrogen) during the so-called re-combination era. Photons emitted by the last scattering surface provide a picture of the Universe taken about 13 billion years ago. Just before the last scattering, there was an equilibrium of particle annihilation and creation; therefore the physical properties of particles, such as statistical distributions of location and energy, did not change. The particle interactions of the re-combination era were close to a thermal equilibrium. This era left behind the CMB photons that we observe today. The main characteristics of these photons depend only on the temperature at a given wavelength (Planck‘s law). This kind of radiation is known as blackbody radiation. Due to the expansion of the Universe, the temperature of photons cooled from 3000 K to $\sim$2.73 K [7].

Observations have brought about several breakthroughs in constraining key cosmological parameters that provide information on the composition, age and geometry of the Universe [8]. Researchers are now looking for answers to two key questions: what triggered the Big Bang and what is the fate of the universe ? [9].

The ΛCDM (Lambda Cold Dark Matter), the standard model, predicts that the present universe is flat and homogenous on a large scale [10]. The flatness of the universe is a result of exponential expansion of the very early universe, which occurred between 10^{-36} and 10^{-32} seconds. This theory is known as Inflation [11]. Thanks to this superfast expansion, the large scale universe sustained its thermal spectrum through casual contact present before Inflation.

1.1.1 Observable characteristics of the CMB

Inflation theory addresses a phase that is not accessible with direct observations [2]. Three observable quantities of CMB radiation have become prominent. First, the temperature of the CMB, the most perfect blackbody ever in nature, was measured at $\sim$2.75 K. Two other observable quantities of the CMB are anisotropies in both temperature and polarization which inhomogeneity in the Universe grew from far smaller and unstable fluctuations. Their detection to a high degree of accuracy is of paramount importance to the field of cosmology. The anisotropies are related to density fluctuations, which are thought to be the seeds of massive structures such as galaxies and stars seen

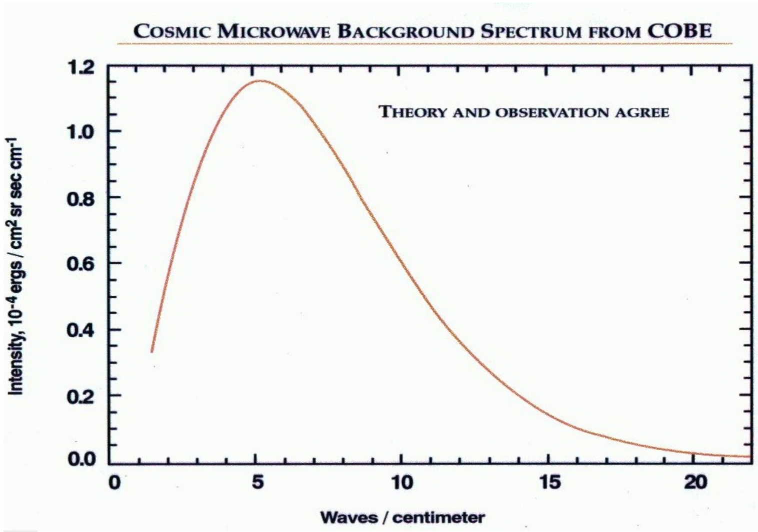

Figure 1.3: The measured CMB blackbody spectrum is in very good agreement with the model. The error bars of the experimental data are so tiny that they are not visible compared to the blackbody curve [17].

in the existing universe.

CMB temperature fluctuations can be expressed by a sum of spherical harmonics [13] as,

$$\frac{\Delta T(\theta,\phi)}{T} = \sum_{l=0}^{\infty}\sum_{m=-l}^{l} a_{lm} Y_{lm}(\theta,\phi) \tag{1.1}$$

where

$$a_{lm} = \int_0^{2\pi}\int_0^{\pi} \frac{\Delta T(\theta,\phi)}{T} Y_{lm} \sin\theta d\theta d\phi \tag{1.2}$$

θ and ϕ are the spherical angles. Y_{lm} is the Legendre multipole moments and l denotes the Legendre multipoles. θ gives the angular resolution and has a relationship of $l = \pi/\theta$ with the multipoles.

Conventionally, the CMB temperature power spectrum ($l(l+1)C_l/2\pi$) is plotted as a function of the multipole l where $C_l =<| a_{lm} |^2>$. For example, the case of $l = 0$ corresponds to the monopole and the total power is the average of temperature (T) over the whole sky. In this case, there is no anisotropy in T. Similarly, $l = 1$ is for the dipole and corresponds to an angular scale of 180°. $l = 2$ is for the quadrupole and so on. In the CMB power spectrum, the position and magnitudes of the acoustic peaks reveal the fundamental properties of the universe such as its geometry and composition. The first three peaks have already been measured precisely in many experiments and recently higher order peaks have also been measured with PLANCK (see Figure 1.9).

1.2 CMB polarization

So far, we have assumed that the early universe underwent a period, called inflation, inthe first fraction of a second. However, there is no direct evidence of inflation. If it did happen, quantum fluctuations during inflation should have generated gravitational waves that left their signature on CMB polarization. The mechanism that caused the CMB photons to be polarized was Thomson scattering of photons from free electrons. The quadrupole temperature anisotropy generates linear polarization as shown in Figure 1.4. Temperature fluctuations present three types of perturbation sources: scalar perturbations due to density fluctuations, vector perturbations due to vorticity, and tensor perturbations due to gravity waves [14]. Generated polarization patterns in the sky can be separated into two components: E-mode (curl-free component) and B-mode (gradient-free component). Scalar and tensor perturbations can generate E-modes; however B-modes can only be due to tensor perturbations as shown in Figure 1.5. B-mode polarization is a clear signature of gravitational waves generated during inflation. Accurate detection of the polarization anisotropies of the CMB could confirm the existence of these gravitational waves, and hence the confirmation of inflation theory and its energy scale could be achieved.

1.3 A review of past and present CMB surveys

Since there are a large number of experiments dedicated to observing CMB anisotropies both in temperature and polarization, it is very difficult to mention all of them in this report. This section describes the general characteristics of the pioneer CMB experiments.

The first space experiment, Relikt-1, was launched in 1983. It scanned the sky at 37 GHz with a resolution of 5.5° [16]. The second satellite, the Cosmic Background Explorer (COBE) [17] was one of the leading missions launched in 1989. It paved the way for subsequent ground-based and balloon-borne observations with greater sensitivity and higher resolution. It consisted of three instruments: the Far Infrared Absolute Spectrometer(FIRAS), the Differential Microwave radiometer (DMR) and the Diffuse Infrared Background Experiment (DIRBE). The first instrument was used to measure

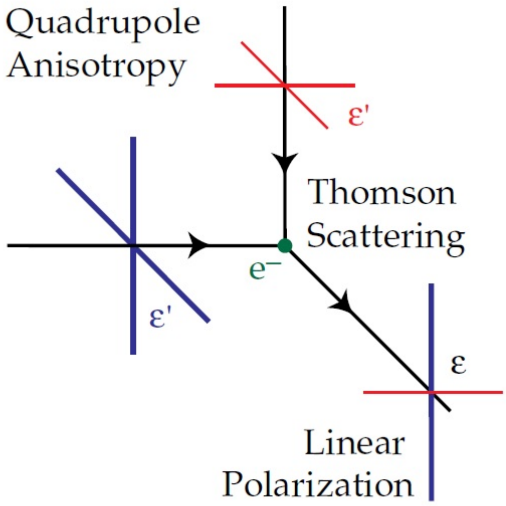

Figure 1.4: A linearly polarized photon can be generated via Thomson scattering of radiation with quadrupole anisotropy. Hot and cold radiations are denoted by the red and blue lines, respectively [14].

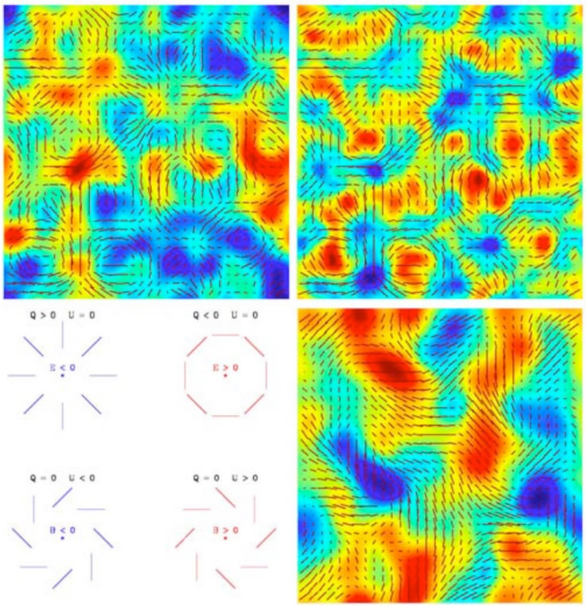

Figure 1.5: A simulation of the CMB map. The top left panel shows the temperature map in the background of polarization rods. Only the E map of the polarization field is shown in the top right panel. The bottom right panel represents the B map of the polarization field. The last figure sketches the E and B modes in terms of linear polarized Stokes parameters Q and U (see Appendix A) [15].

the blackbody behaviour of CMB radiation at wavelengths between 0.1 mm to 10 mm. The DMR mapped CMB temperature anisotropies with a level of $\Delta T/T = 10^{-5}$, by using horn antennas operating at three frequency values of 31.5, 53, and 90 GHz. DIRBE aimed at detection of cosmic infrared radiation. COBE operated at the multipole scale (l) from 2 to 30 corresponding to very large angular scale measurements. Its observations provided an almost perfect match of the CMB power spectrum with the theoretical blackbody spectrum for a temperature of 2.725$\pm$0.001 K (see Figure 1.3).

BOOMERanG (Balloon Observations Of Millimetric Extragalactic Radiation and Geophysics) [18] was a balloon-borne experiment designed to measure CMB temperature anisotropies from $l = 50$ to 600 at four frequencies of 90, 150, 240 and 410 GHz. It flew between 1998 and 2003. Its focal plane array hosted 16 bolometric detectors that were cooled to 0.3 K. In addition to this, BOOM03, the second flight of BOOMERanG made polarization measurements as well as temperature measurements in 2003. The new receiver system of BOOM03, which was modified from that of BOOMERanG, operated at 145 GHz by using polarization sensitive bolometers (PSB) and at 245 and 345 GHz with Spider-Web bolometers, including polarising grids to provide higher sensitivity [19]. Following these experiments, the Archeops balloon, which was a counterpart of Planck, measured CMB temperature anisotropies between the multipole ranges of l =10 and 700 [20]. Archeops also acted as a test bed for Planck instruments.

DASI (the Degree Angular Scale Interferometer) is a ground based telescope and was the first experiment to detect the polarization of the CMB in 2002 [21]. Its instrument comprises a 13 element interferometer operating at frequencies of 26 and 36 GHz. CMB radiation was mapped with angular resolution of 0.2° to 1.3° at multipoles of l =100 to 900. A few years later, QUAD made high precision measurements of the CMB E-mode polarization. It used a 2.6 m reflector based Cassegrain telescope optics to feed polarization sensitive bolarimeters (PSB) operating at 100 and 150 GHz [22]. Following DASI, other confirmation of the CMB polarization detections came from CAPMAP[23], CBI[24], WMAP for both the TE [25] and EE [26] power spectrums and BOOM03. Improved results have also been reported by QUAD[26], BICEP [27] and QUIET [28]. These results are summarized in Figure 1.6.

The third spacecraft, WMAP (the Wilkinson Microwave Anisotropy Probe) started to scan the whole sky in 2001 and is still observing the temperature and polarization anisotropies of the CMB. It operated at 5 different frequencies from 22 to 90 GHz by

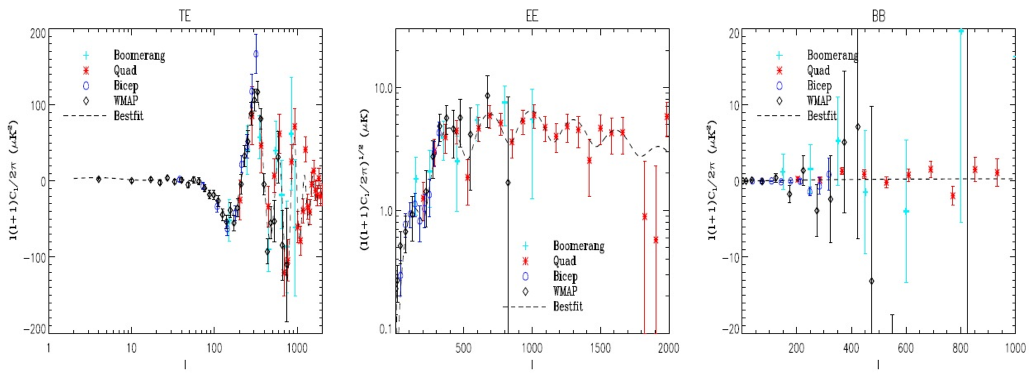

Figure 1.6: The left figure shows the results of the TE power spectrum measured with Boomerang, QUAD, BICEP and WMAP. The middle figure shows the E mode polarization measurements obtained from the same experiments above. The right figure shows the upper limit on B-mode polarization. The results were also compared with the model best fitting the WMAP TT power spectrum. The three plots have different power scales [80].

using a 1.6 m off-axis Gregorian telescope [29]. WMAP minimized sidelobe contamination, which the DMR instrument of the COBE suffered during its observations, by being located in one of the Lagrangian points in our solar system. In this location, the telescope avoids contamination from solar, terrestrial and lunar emissions. The detector system consists of differential polarization sensitive HEMT amplifiers. Compared to the instrument performance of the COBE telescope, its instrumentation presented 45 times greater sensitivity and 33 times higher angular resolution.

Additionally, the first detection of B-modes due to gravitational lensing was achieved by the SPTpol experiment [30]. The importance of this achievement for the detection of pure B-modes is that the lensing B-mode data can be subtracted from the prospective measured B-mode data in order to reduce the effective noise level required for the detection of pure B-modes.

Following these pioneer missions, the PLANCK satellite, known as the fourth space mission dedicated to CMB detection, was launched in 2009. PLANCK is worth being discussed separately in terms of many aspects, from its optical features to its scientific achievements.

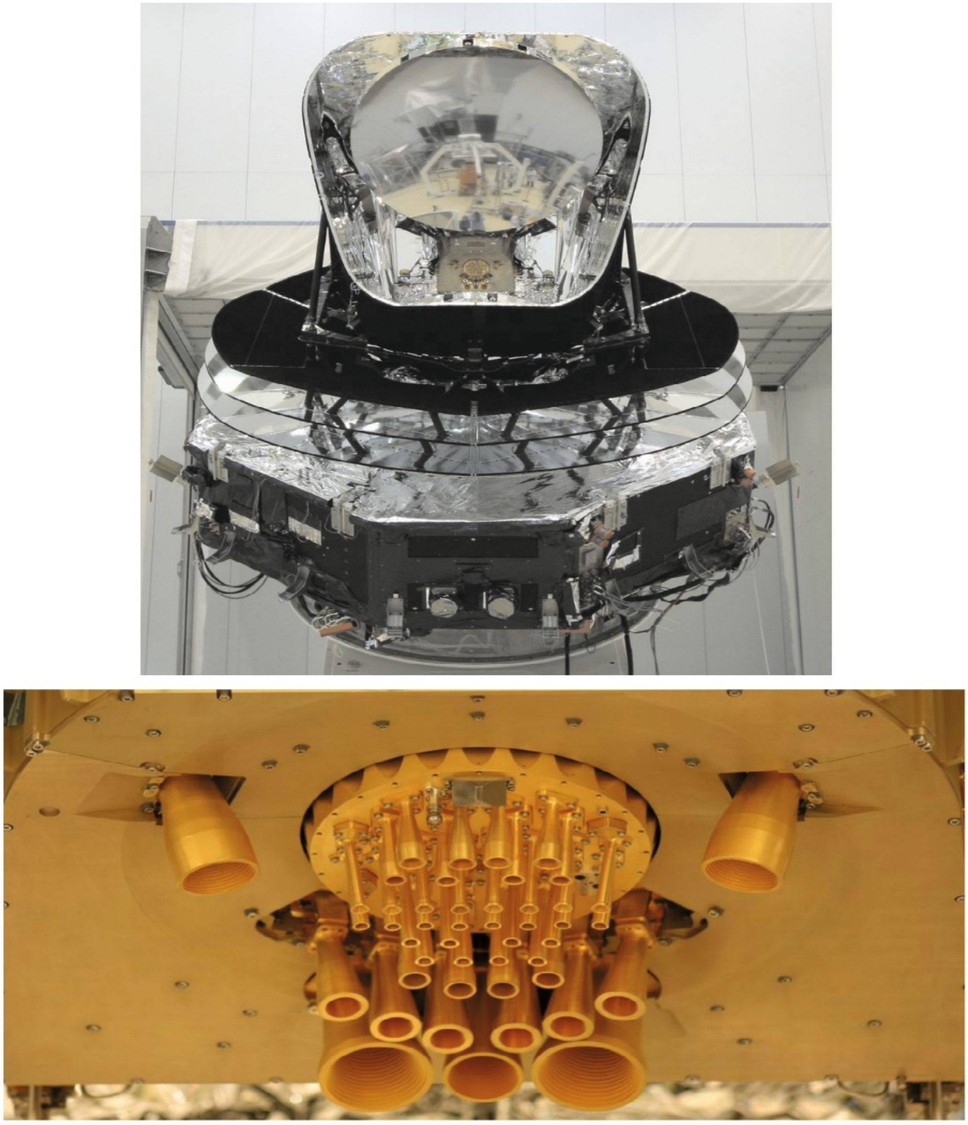

Figure 1.7: The upper photograph shows the PLANCK satellite with the focal plane unit reflected in the main mirror. The lower photograph is a magnified photo of the focal plane unit. The LFI feed horns operating at 30, 44 and 70 GHz are located around the HFI feed horns operating at 100, 143, 217, 353, 545 and 857 GHz. Credits: ESA.

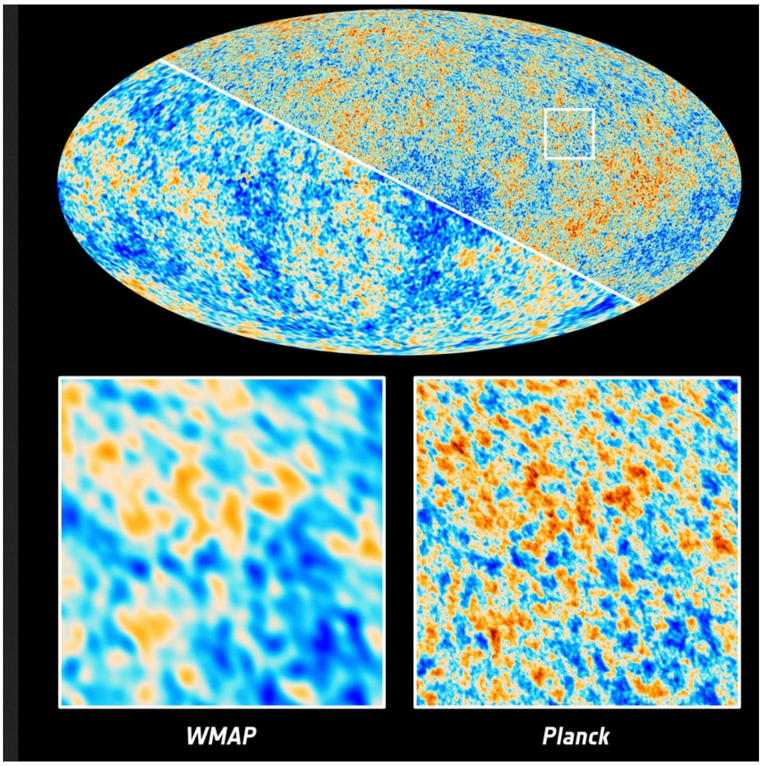

Figure 1.8: The upper half of the top figure shows the CMB temperature map measured by PLANCK while the lower half shows the map generated by WMAP. The PLANCK map is formed by the data collected for over nine frequency channels and based on a 15.5 months survey. Credits:ESA

1.3.1 PLANCK

As summarised above, a great number of CMB experiments have measured the anisotropies with increasing sensitivity and resolution. In order to probe the physics of inflation [32], we want to extract all the cosmological information from CMB temperature anisotropies [31]. To this end, PLANCK (Figure 1.7), the first European CMB satellite programme commissioned by the European Space Agency (ESA), was designed to map the full-sky temperature anisotropies in more detail. PLANCK also measures the polarization of the CMB by using the coolest detectors operating with unprecedented sensitivity [33]. The satellite also surveyed foreground sources. A cyrogenic system cooled the bolometric detectors down to 0.1 K. The focal plane accommodates two receiver systems: the Low Frequency Instrument (LFI) [34] using a receiver set based on HEMT amplifiers operating at frequencies between 30 to 70 GHz and the High Frequency Instrument (HFI) [35] using bolometric receivers operating at frequencies

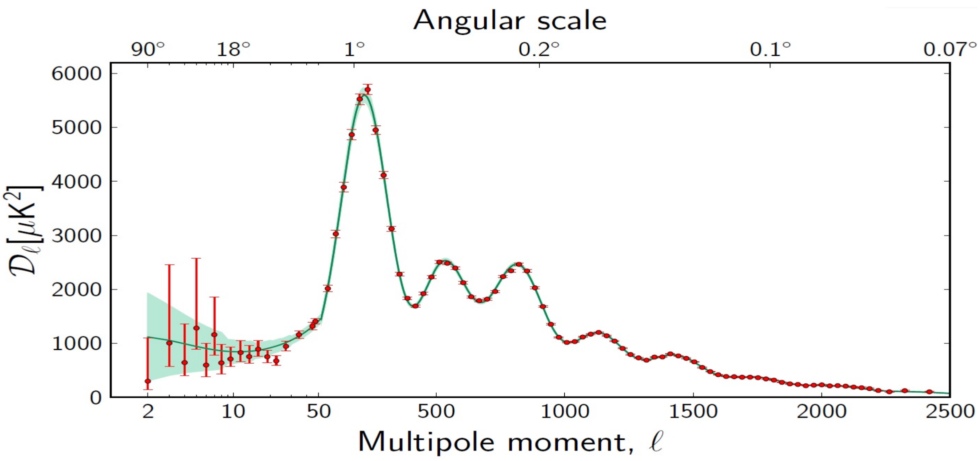

Figure 1.9: The PLANCK data compares with the best fit six-parameter of ΔCDM model for the first seven acoustic peaks of the CMB temperature power spectrum. The vertical scale denotes $l(l+1)C_l/2\pi$ (D_l) as a function of multipole number l. The error bars of the measured data include cosmic variance shown by the green shaded area [31].

between 100 to 857 GHz. The bolometers are coupled to corrugated feed horns developed for both single- and multi-modes. Multi-mode receivers operate only at the two highest frequency bands (545 GHz and 857 GHz) to increase the detection sensitivity and keep a resolution of $5^{'}$ [36]. The main reflector, which is the primary part of the off-axis Gregorian design, has a projected diameter of 1.5 m so that PLANCK scans the sky with a resolution of $5^{'}$ at the highest frequency and 0.5° at the lowest frequency. All information regarding the instrument performance of the PLANCK satellite is given in a special issue of *Astronomy* & *Astrophysics* Volume 520, 2010.

A set of scientific and technical papers have been released by the PLANCK collaboration to present the initial results from the 15.5 months of PLANCK survey. The CMB temperature map generated by WMAP and PLANCK is shown in Figure 1.8 for a comparison of resolution and sensitivity. PLANCK scanned the full sky with 3 times greater resolution than WMAP. Analysis of all PLANCK data, including many scientific results, is presented in a series of papers entitled PLANCK 2013 Results [31]. The PLANCK observations improved the accuracy in the values of cosmological parameters and placed stronger constraints than previous observations [37]. The measured results are in good agreement with the predictions of a six parameter ΔCDM model, in particular at high multipoles (Figure 1.9). The CMB temperature power spectrum shows the first seven acoustic peaks measured by PLANCK. Residual systematics limit the sensitivity of the PLANCK instruments for observations of the CMB polarization power spectrum at low multipoles ($l < 20$). The full data set of E-mode polarization results has not yet been released by the PLANCK team and is expected to be delivered in mid-2014. The PLANCK observations will also place a constraint on the observations of B-mode polarization. More importantly, the polarization map of foreground sources over the full sky will help determine the ultimate sensitivity and frequency coverage requirements of a candidate B-mode polarization mission.

1.4 Thesis outline

This thesis focuses on the modelling and experimental study of millimetre (mm) wave refractive systems, which is not only useful for the measurement of CMB B-mode polarization but also for any mm wave systems that include refractive components. In particular, I have aimed at comparing lens models with measured data, instead of optimizing a lens design that is specifically dedicated to CMB telescopes.

Chapter 2 outlines the scientific and instrumental requirements for detection of CMB B-mode polarization. This chapter also discusses the candidate CMB experiments using different optical configurations based on reflective and refractive elements in terms of optical performance. In particular, polarization systematic effects from which CMB dedicated telescopes may suffer are introduced.

In **Chapter 3**, the main theoretical tools employed to model quasi-optical devices used throughout this research, and their underlying theory are introduced. I particularly focus on full wave simulations of mm wave lens systems.

The design, construction, implementation processes and full characterization of a mirror based quasi-optical free-space S-parameter measurement system are detailed in **Chapter 4**.

In **Chapter 5**, modelling of horn-lens systems by using a variety of simulation tools that FEKO provides is discussed. Two different lens systems were used in the analysis. The chapter concludes with a discussion on the simulation feasibility of large size lenses.

Following the lens simulations, **Chapter 6** and **7** present the experimental study of horn-lens systems for both on-axis and off-axis pixel configurations, respectively. Lens systems were measured in both far-field and near field. Modelling and experimental studies of ARC lens system have also been performed. Then, the results were compared to the model data.

Finally, the main results of this research are summarized and future plans are presented in **Chapter 8**.

Chapter 2

DETECTION OF CMB B-MODES

This chapter will present the scientific goals and discuss their corresponding technical requirements, in order to detect B-mode polarization in CMB radiation. Reflector and refractor based optical designs dedicated to CMB polarization missions are also outlined. Finally, a variety of concept studies dedicated to CMB B-mode polarization missions are presented in a descriptive way.

The next challenge for CMB researchers is to measure B-mode polarization in CMB radiation. The signal level of the B-mode polarization is expected to be 10-100 times weaker than the E-mode signal [64]. According to the inflationary energy scale, detection of these faint signals demands a very sensitive detection system that operates across a very wide frequency range. The inflationary energy scale given in Equation 2.1 is proportional to tensor to scalar ratio ($T/S = r$), the amplitude of r. The ratio r also quantifies the amplitude of the B-modes. B-modes are being searched for high energy scale, for different values of r, compared to the energy scales of Grand Unified Theories ($\sim 10^{16}$ GeV) [39].

$$V^{1/4} = 1.06 \times 10^{16}(r/0.01)^{1/4} GeV \tag{2.1}$$

B-modes have not yet been detected. However, some experiments have placed upper limits on the B-mode amplitude. The two-year BICEP and QUAD data determined the upper limit of r to be r<0.72, directly from the B mode measurements [40]. Also, the best limit was r<0.33 at a 95% confidence level, which was obtained from the CMB data of the QUAD observations [41]. PLANCK can place an even tighter limit on r.

The noise limit of bolometric detector systems is at the level of photon noise. This leaves two solutions possible for improving telescope sensitivity. Next generation telescopes should either be coupled to a large focal plane (FP) unit, which accommodates many polarimetric pixel antenna systems, or use multi-mode pixel systems, which is an alternative option. Multi-mode systems are preferred in order to increase the throughput of the detector system if diffraction limited resolution is not needed [36]. In addition to these primary requirements, the optical design of CMB polarization telescopes should have very low systematics such as cross-polarization (XP) and beam ellipticity. Large field of view (FOV) telescopes should be studied with both reflector-based and refractor based optical combinations. The optical design that presents the best performance trade-off between large FOV and polarization purity should be selected. Exquisite control of systematic errors should be obtained at both the component level and instrument level.

The instrumental requirements of each mission are set by the scientific requirements of a CMB polarization mission. Depending on the optimum frequency coverage and the number of frequency channels, scanning strategy, telescope optics, detector type, polarization modulators and their associated components are all determined from these requirements. Recent CMB proposals have come up with concept studies utilizing many different optical configurations. Some of the reflector based examples are COrE, EPIC-IM and PRISM while the refractor based ones are BPOL, LSPE and EPIC-LC.

All the telescope missions, referred to in later sections, have different detector technology. For example, SPTpol and ACT pol have classic feed-horn coupled antennas while BICEP2, Keck and SPIDER use planar antenna arrays [42]. The focal plane of the POLARBEAR telescope comprises lens-let antennas [43]. Other technologies for polarization modulation are under investigation by ESA and NASA consortiums. All these components will determine the final performance of the telescope by taking into account all component interactions.

2.1 Scientific requirements

The primary objective of a candidate CMB polarization mission is to search for the B-mode polarization signal from inflationary gravitational waves. In the CMB science report published in 2005 by the Weiss Committee [15], scientific goals and recommendations were set for B-mode detection. In the light of these considerations, the report also outlines a roadmap for determining the optimal spatial scale and frequency bands in order to reach pure B-mode signals by separating polarized foreground emissions. The list below summarizes the points submitted by the committee.

- A direct test of inflation and its energy scale can be probed by the detection of CMB polarization on large angular scales ($l < 200$). To this end, the measurement of large-scale CMB polarization is recommended. Large angular scale space missions would be supported with small-medium angular scale ground and balloon based missions.

- Additionally, determination of foreground emission sources should be targeted. Observations of polarized foreground sources would help to limit r at or below 0.01, in particular at large angular scale observations of CMB polarization. This value corresponds to a sensitivity 10 times better than Planck.

- More additional information on inflation can be provided by small angular scale observations ($l \sim 2000$) of the CMB temperature and polarization anisotropies. These missions should include measurements of gravitational lensing and Sunyaev-Zel'dovich effects. Missions dedicated to observations of the small-scale fluctuations in the CMB were recommended in order to constrain the power spectrum of primordial fluctuations. As a result, cosmological parameters that help in quantifying the properties of dark matter, dark energy and neutrinos would also benefit from these observations.

A prospective space mission was predicted for 2018. Data will be collected from ground and balloon-based observations until this date. Following the scientific recommendations, the following technology roadmap was outlined:

- **Detector systems**

  Receiver systems that support a thousand or more polarization sensitive detectors are the highest development priority. The driving technology for these detector systems would be encouraged. The primary emphasis was put on the development of PSB systems [44]. In particular, transition edge sensor (TES) bolometers are currently in use with a detector array of $\sim 10^4$ receiver elements operating at frequencies between 30 GHz to 300 GHz [61]. Correspondingly, sub-Kelvin cryogenic systems for the large focal planes accommodating many receivers would be integrated into these detection systems. In addition to these recommendations, alternative receiver systems such as HEMT-based detectors were among the choices for operations less than 100 GHz.

- **Optics**

  Large focal planes are needed to accommodate thousands of pixels for higher sensitivity. Different optical configurations based on reflectors, refractors and hybridization of both would be studied to generate these large focal planes in terms of a high throughput optical system. These combinations would also be compared in terms of their performance for polarization purity. Regarding polarization modulation, the RF characterization of quasi-optical components such as transmission and reflective wave-plates would be developed.

2.2 Instrument requirements

2.2.1 B-mode project platform

CMB experiments can operate from the ground, balloons, or space [45]. Each one comes with advantages and disadvantages. First, ground based instruments have relaxed limits in detector assembly size and weight of the optical system. By being on ground observations, the integration time of an observation will only suffer from bad weather and geometrical conditions. The instrument is easy to reach for upgrades and modifications. On the other hand, ground based experiments do not have full access to the EM spectrum, specifically in the mm-wave range.

Similar to ground based missions, high-altitude atmosphere missions such as balloon-borne observations are much cheaper than space instrument options. Also, both are relatively quick to deploy. Balloon experiments have access to the mm-wave spectrum. However, flight constraints make the integration time of balloon-borne observations shorter.

From the current knowledge (see the subsequent sections), a candidate mission should provide all sky scanning for a wide frequency coverage. Only a space based mission achieves a full-sky survey with many frequency channels. However, size and weight limitations affect the selection of the instrument. The integration time becomes short due to the cryogenic system elements. The optical design and its associated detector system must take into consideration the size limit. All these aspects make space based missions expensive.

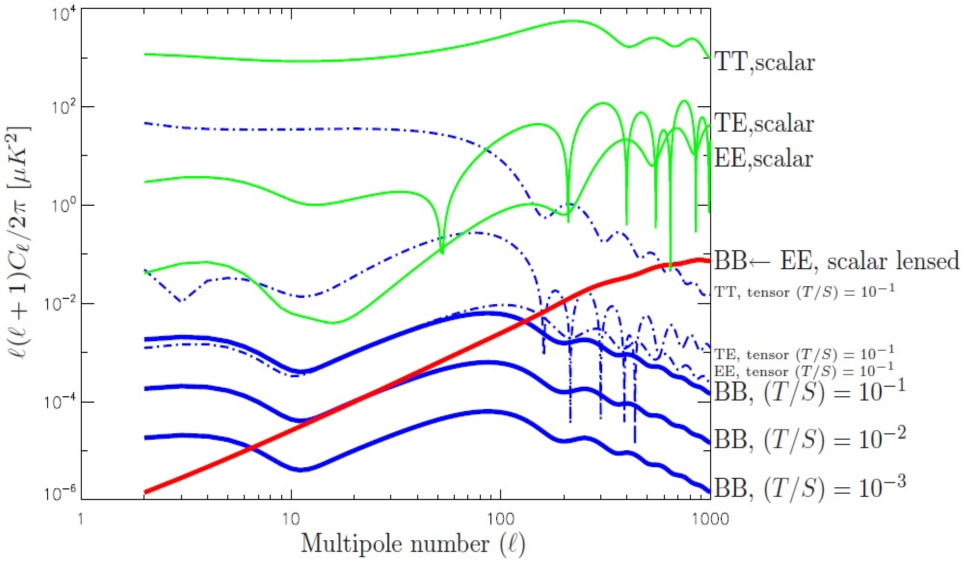

Figure 2.1: Power spectrum plotted from inflationary prediction for the CMB temperature and polarization anisotropies. The vertical scale denotes $l(l+1)C_l/2\pi$ (D_l) as a function of multipole number l. The model parameters are taken from the best-fit model from the WMAP three-year data. From top to bottom: The green lines denote the scalar power spectrums of the TT, TE and EE correlations. The red line is for the scalar BB spectrum from the gravitational lensing of the EE modes. The blue dashed lines show the tensor TT, TE and EE correlations for r=0.1 while the blue solid lines shows the tensor BB correlation spectrum for three different values at r=0.1, 0.01 and 0.001 [46].

2.2.2 Resolution

The inflationary prediction map in Figure 2.1 shows the power spectra of the CMB temperature, polarisation and their correlations. The power spectrum predicts that B-modes were generated by tensor modes. The spectrum also presents two peaks in the amplitude of B-modes around $l \sim 5$ and $l \sim 100$ during the reionisation era. This requires a telescope that observes the sky with degree scale resolution [46];

$$\theta = \frac{\pi}{l}. \tag{2.2}$$

From Equation 2.2, observations in multipole (l) scales, indicated above, is possible with one-degree scale of resolution.

In addition, there are additional multipole regions that require great care to probe. For example, cosmic shear produces a peak around $l = 1000$ while some galactic sources lie at $l > 500$. Therefore, small angular observations (0.1°) are necessary. These observations will contribute to the characterization of the gravitational lensing effect. Also, foreground effects that result from E-mode lensing should be precisely measured with high resolution observations. How much resolution a space based mission requires will be determined by the data provided from the ongoing and prospective ground and balloon based telescopes.

2.2.3 Frequency range and foreground effects

Multi-frequency observations will help to separate polarized sky components from the pure B-mode polarization signal. It is obvious that the detection of gravitational B-mode polarization is more likely in the large angular regime of the CMB power spectrum, while a mission with a high angular resolution (small angular regime) will help to remove gravitational lensing foregorund signals. On the other hand, increasing the observation resolution for lower angular scales affects the mission complexity and hence its cost. Therefore, there will be many trade-offs involved in choosing the optimum frequency range. Alternatively, missions can be handled in two groups: a low angular resolution mission and a high angular resolution mission. The EPIC mission study team have proposed two different concept studies [47], which have different optical configurations and observation strategies (see Section 2.4.1).

Two contaminants of galactic emissions and lensing B-mode will affect the decision on which observation frequency should be studied. One factor is the diffuse galactic emissions (synchrotron radiation and thermal dust). Since they should be measured accurately to allow their subtraction from the CMB signal, the best assumption on the frequency selection for a polarization mission will benefit from the foreground data sets obtained from the ongoing missions, such as Planck and suborbital telescopes. From current knowledge, this mission should provide all sky scanning for a wide frequency coverage (see Section 2.2.1). The operating frequency range of a candidate mission is dependent on the angular resolution calculated by

$$\theta \sim \frac{\lambda}{D} \tag{2.3}$$

where λ is the observation wavelength and D is the aperture diameter of the telescope. One degree-scale resolution can be provided with a telescope whose aperture diameter can be $\sim$ 25 cm. Additionally, in the case of small angular observations, large diameter operations ($\sim$ 150 cm) should probe the sky. Furthermore, from the optics point of view, large diameter missions generate a large focal plane area leading to high throughput. In conclusion, a multi-band frequency range from 30 GHz to 300 GHz is required [47].

2.2.4 Sensitivity

The ability to detect nano-Kelvin level signals of CMB B-mode polarization requires highly sensitive receiving systems. The corresponding power level of the CMB B-mode polarization to *r*, in the inflationary prediction map, sets the sensitivity requirement. As *r* decreases, the sensitivity requirement becomes more stringent. The detector choice with its suitable focal plane unit, polarization modulations, mission lifetime and the amplitude of the foreground signals are all factors that contribute to the actual sensitivity of a CMB telescope.

The sensitivity of an instrument can be improved by increasing the number of detectors. The sensitivity of a candidate instrument is shown with a common notation, $W^{-1/2}$ in terms of μK·arcmin. This value is calculated for an instrument with a given Full Width at Half Maximum (FWHM). For one degree scale observation (l<200) of B-modes, the sensitivity criteria on is set to be $W^{-1/2} < 6\mu K \cdot arcmin$ [47]. Some of the ongoing and candidate CMB experiments with their different instruments are listed in Table 2.1. Instrument sensitivity was calculated for a frequency of 150 GHz [45]. Many of them have around a thousand pixels and aim to achieve sensitive observations with $\sim$1 to 10 μK·arcmin.

MISSION	BEAM-WIDTH [arcmin]	SENSITIVITY [μK·arcmin]	r
Planck	7	30	0.05
BICEP-1	36	15	0.72
BICEP-2	36	3.5	0.01
KECK-Array	36	1.6	0.006
SPTpol	1	6	0.025
POLARBEAR-I	3.5	8	0.025
ABS	30	4.5	0.015
ACTpol	1	20,3	0.03,0.01
EBEX	8	14	0.03
SPIDER	30	8	0.02
POLAR-1	6	0.5	0.01
POLARBEAR-II	3.5	5	0.01
PIPER	15	$\sim$3	0.007
POLARBEAR-EXT	3.5	3	0.001
POLAR-Array	4	0.2	0.008
LiteBird	30	2	0.002
COrE	8	3	$\sim$0.001
CMBpol	5.6	1.5-3.5	$\sim$0.001

Table 2.1: Some of the ongoing and candidate CMB experiments are listed with their specifications. The beam-width at 150 GHz expressed in arcmin, the calculated sensitivity expressed in μK·arcmin and tensor to scalar ratio r are calculated by excluding systematics and foregrounds [45].

2.3 Systematic effects

The impact of beam systematics on an observable quantity should be suppressed below the requirements (see Table 2.2) and kept under control. Many task reports place a target of $r = 0.01$ to achieve a CMB B-mode polarization observation [15], [47]. The predicted CMB power level for this value is around 30 nK rms. It is aimed to control systematic effects up to a signal level of 3 nK, which is a tenth of the expected power level [15].

A wealth of experience in determination and mitigation of systematic effects has already been gained from the instrumentation of CMB temperature anisotropy missions. The addition of polarization sensitive detectors adds a new systematic challenge to optical system design. Generally speaking, instrumental polarization and XP have an impact on polarization sensitivity.

Systematic effects resulting from optical designs and individual components can be controlled to some extent. Polarization modulators [48] and scanning strategies will help to mitigate these systematics. If these errors are not confronted, they will result in spurious B-mode polarization signals induced from CMB temperature and E-mode polarization, which has a much higher signal level than B-mode polarization. A few publications have discussed the impact of systematic effects on the measurable parameters [49], [50], [51].

Table 2.2 gives the instrument performance goals for a CMB B-mode polarization mission. The goal is the value at which a systematic effect causes a 10% contamination for $r = 0.01$ [15].

In addition to these systematics, more parameters (return and absorption losses, chromaticity, material birefringence etc), in particular in telescopes using refracting components, should be determined for instrumentation of CMB polarization.

Also, different definitions such as differential beam parameters have been used to investigate systematic effects. These definitions were first introduced by Wayne Hu [49] and the study was extended by Daniel O'Dea [51]. A comprehensive investigation that demonstrates differential systematic effects on a polarized telescope beam was carried out by the EPIC team [47]. In this mechanism, two linearly polarized orthogonal Gaussian beam patterns were used to compare the unequal beam outputs obtained from two bolometers. Each was sensitive to one linear polarization plane. Calculations of the main beam effects were conducted for differential beam-width, differential pointing, differential ellipticity, and differential gain. These systematics, called instrumental polarization effects, occur when the two detectors measure unequal beam-width, beam

Parameters	Effect on the B mode	Performance goal
Cross-polarization	E mode polarization	<-25 dB(or $3x10^{-3}$)
Polarization angle	E mode polarization	0.2°
Instrumental polarization	dT contamination	<-40 dB (or 10^{-4})
Beam ellipticity	dT contamination	1%
Polarized sidelobe level	E mode polarization	<-60 dB (or 10^{-6})

Table 2.2: The instrumental parameters and their impacts on the B-mode signal are given with their performance goals for $r = 0.01$ [15]. The requirements were taken from the Weiss report. XP (Integrated XP) refers to dipole and quadrupole effects arisen from the feed elements and the optics of the telescope respectively while the polarization angle leads to the XP effect known as the zero-pole effect. The numbers are given in both logarithmic scale and linear. E indicates the E-mode polarization signal while dT indicates CMB temperature anisotropies.

offset, ellipticity and gain respectively. The systematic effects are related to beam errors, as shown in Figure 2.2.

1. **Cross-polarization (XP)**

   Cross-polarization (XP) refers to polarization that is orthogonal to the reference polarization. For an ideal case, a linearly polarized detector rejects the polarization signal orthogonal to the detector polarization. XP is described as the rotation of the polarization states by the instrument optics and results in a leakage of E-mode to B-mode signal. An antenna system with a low XP is able to discriminate the Stokes parameters Q and U. Many factors, from the optical design to detector coupling effects, can generate XP in the detector. Regarding optics, the curved geometry of optical elements results in field distortions that lead to mixing the polarization states. For example, the Mizugutchi-Dragon condition minimizes this effect, which can arise from the off-axis configuration of dual-reflector designs. The XP response can be corrected by either rotating the instrument or using a half wave plate, but a residual error can still remain. The requirement given in Table 2.2 defines the minimum uncertainty in the total XP beam response. The integrated XP response over the beam pattern must be lower than 3×10^{-3} of the integrated main lobe CP response [15].

2. **Instrumental polarization**

   Instrumental polarization results in a leakage of unpolarized radiation (intensity) to polarized radiation. It causes polarization contamination from temperature

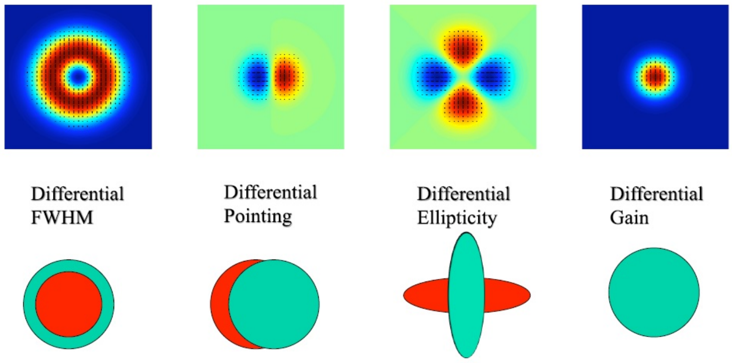

Figure 2.2: Differential beam effects from left to right: differential beam-width (FWHM), differential pointing, differential ellipticity and differential gain. The green and red shapes show the two different beam shape generated in two orthogonal bolometers. Due to the difference in the beam shapes, they present monopole, dipole, quadrupole and zero-pole effects on the main beam [47].

(T) and temperature anisotropy (ΔT) to B-mode polarization. Telescope components can be reflector, refractor or other feed elements between the sky and the detector system via the instrument. For example, oblique reflections from reflector surfaces or refractions of oblique incident light through a lens without an anti-reflection coating lead to instrument polarization systematics. Imperfections in the main optical components can also result in errors. For example, a reflector surface can have different conductivity values in two axes, so its effect on the reflected beam increases for receivers away from the centre of the focal plane (off-axis angles). In refractor systems, material birefringence due to anisotropic behaviour of the refractive index between optical axes can produce spurious polarization. Poor anti-reflection properties of lenses can also generate instrumental polarization, depending on the degree of symmetry in the telescope optics.

Real polarization due to the sky beam and fake polarization due to the instrumental effects can be partially separated by either rotating the telescope over the same sky patch or using wave plates.

Depending on the beam size, the level of instrumental systematic errors as a function of l can be predicted [50]. For the conditions of half degree angular scale with $r = 0.01$, uncertainties in the instrumental polarization signal must be less than 10^{-4} [15]. This requirement is more stringent than that for XP because the temperature anisotropies are much greater than the B-mode signal.

3. **Beam ellipticity**

   The beam responses to two linearly polarized sources, which are orthogonal to each other, should ideally be identical for a symmetric beam. In reality, there is a difference between the maximum and the minimum beam-width values,which leads to beam ellipticity. This effect causes a sensitivity that results in conversion of the temperature anisotropies into false B-mode signals. The angular scale of a CMB candidate mission will determine the requirement for beam ellipticity. For a mission with half-degree resolution, it is set to be 10^{-4} in radians [15]. If it is well defined, it can be corrected by observations performed for a variety of azimuthal angles.

4. **Polarization sidelobe**

   The rejection of sidelobe responses, which are induced from the bright sources such as the Sun and galactic objects, is also crucial. Two polarized beam patterns should present the same level of sidelobe response. Otherwise, the signal difference will appear as a polarization sidelobe contaminant. To this end, they should be accurately characterized and corrected. The requirement for polarization sidelobe is 10^{-6} in radians [15].

2.4 A general comparison of reflector and refractor based optics

From [52] and Section 2.3, an ideal optical system for a B-mode experiment should have,

1. An antenna pattern independent of field position in the focal plane. This will provide a large FOV.

2. The polarization state of the incident beam should not be altered by the optical system. This will mitigate polarization systematics.

2.4.1 Reflector based telescopes

The majority of CMB telescopes use reflector based systems. These consist only of a simple feed horn - reflector system, such as QMAP and TOCO [53], or more complex

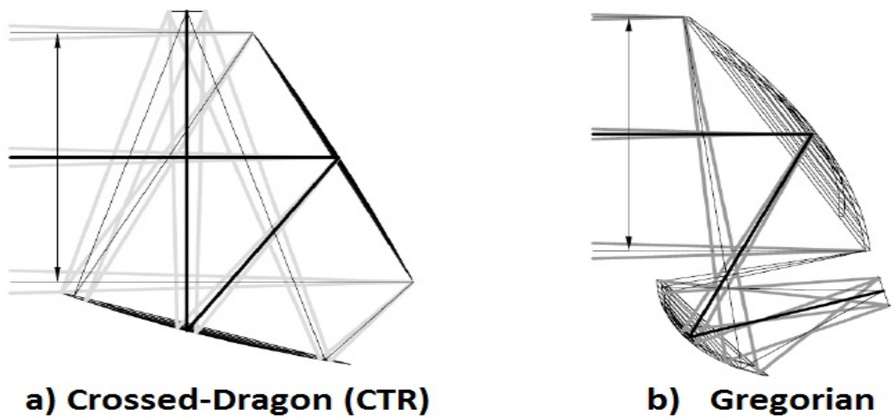

Figure 2.3: The optical configurations of Off-axis Dual Crossed Dragone and Gregorian reflectors. Both optical systems are designed according to Mitzuguchi-Dragone‘s law in order to mitigate XP [55].

combinations with three mirrors e.g. MAXIMA [54]. Reflector designs might be combinations of on-axis and off-axis configurations, with a large aperture diameter above 60 cm, achieving degree-scale resolution. The first discussion should be made on the selection between an on-axis system and off-axis mirror based system. The latter option has mostly been chosen for CMB polarisation experiments since on axis mirror systems come with some inherent problems. First, the struts of the secondary reflector generate spurious rays that cause near and far sidelobes, and aperture loss. Secondly, the first problem gets worse as the aperture size of the secondary mirror is increased in order to make a large focal plane [55]. This problem requires a trade-off between low sidelobe levels and a large FOV. There are only two CMB polarisation experiments based on an on-axis reflector design: QUAD and COMPASS. However, the secondary mirror of QUAD is maintained with a foam cone instead of using struts.

For polarisation-sensitive CMB experiments, particular attention is given to the systematics of large FOV optics and polarisation purity. In order to avoid the blockage and scattering properties of on-axis reflector configurations, off-axis dual reflector systems, which follow the Mizuguchi-Dragone condition [56] in order to reduce cross-polarisation, have been commonly used. XP effects arising from an off-axis system can be reduced to the same level as those from an on-axis system.

In multi-feed antenna systems, many of the feeds are off-centre from the telescope axis. For large focal plane areas, the beam of each pixel becomes more and more asymmetric towards the edge of the focal plane. These beam distortions should stay within the acceptable range of requirements given in Table 2.2. Otherwise, beam distortions result in serious aberrations, such as astigmatism and coma, which show up in off-axis dual reflector systems. In order to cancel coma, aplanatic Gregorian configurations, comprising a slightly more elliptical main reflector and more eccentric sub-reflector than the classical Gregorian design, have been proposed [57]. For the largest diffraction limited field of view (DLFOV), Dragone introduced two Gregorian designs: astigmatism free and astigmatism-coma free designs [58], [59]. These aplanatic configurations have been widely used for telescope designs in mm and sub-mm wave astronomy such as Planck, EBEX and Polarbear. For a CMB polarisation mission using a telescope with Gregorian optics, reimaging optics may also be required in order to create a large, flat focal plane. These kinds of telescopes have been used for Polarbear, EBEX and Boomerang. Additionally, ACT and SPT, which are the largest ground based telescopes with six and ten metres primary main reflectors in order to achieve higher resolution, used off-axis Gregorian telescopes. The SPT has an additional lens that functions as a re-imaging focuser. This optical configuration was chosen mostly for construction reasons such as use of ground shields and to minimize spillover.

A few studies have discussed and compared different dual reflector systems in terms of their cross-polarisation and spillover performances [55], [57] and [60]. The Gregorian configuration, which comprises a primary parabolic reflector and a secondary elliptical reflector as shown in Figure 2.3, has been compared to a Caseggrain configuration for the same size constraints of the main and sub-reflectors. On the one hand, the former has been found to be more compact due to its intermediate focus point, which allows it to be used as a baffling. On the other hand, the crossed-Dragone configuration, also called Compact Test Range (CTR) as shown in Figure 2.3, provides twice as large DLFOV. The CTR presents a 10 dB better XP performance than Gregorian optics for a large DLFOV [60]. CTRs were used for CMB polarisation experiments such as EPIC-IM [62], QUIET [63] and QUIJOTE [65]. In the optics of CLOVER [64], for example, a XP of -40 dB and a beam ellipticity of %1 was supposed to be achieved with the CTR design for all pixels. As far as baffling is concerned, it was found to be difficult to protect the FP unit of the CTR from scattered rays, which are directed from the ground or the sky, because the FP unit is placed close to the main beam [66]. However, this can be solved by enclosing the whole structure as with QUIJOTE [65].

In conclusion, on-axis reflector designs do not seem feasible for CMB polarization operation due to their aperture loss. Gregorian systems come with aberration problems due to the large FOV. CTRs with the highest possible FOV are more promising for CMB polarization experiments. Namely, they present low XP across a large focal plane. For instance, the EPIC team has found that CTR systems present the lowest instrumental polarization [67]. Similarly, measurements of the CTR configuration used for the QUIET telescope showed the absence of XP for on-axis pixels [63]. The main drawback of CTR designs is the large secondary mirror compared to the size of the primary mirror.

Physical properties	**Gregorian**	**Crossed-Dragone**
Secondary mirror	smaller	larger
Focal plane	not telecentric	almost telecentric
Optical properties		
DLFOV	Crossed-Dragone has 2X larger DLFOV.	
Polarization	Crossed-Dragone also shows 10 dB lower XP [66], [60]	
Beam systematics		
Differential gain	Crossed-dragone a factor of 2 lower [66]	
Differential pointing	similar performance	
Differential ellipticity	similar performance	

Table 2.3: Comparison of the most promising mirror based configurations used for the detection of CMB polarization. Cross-Dragon design (CTR) gives the best performance, in particular for the optical properties.

2.4.2 Refractor based telescopes

Lens-based telescopes have the advantage of having on-axis symmetry structure without a central obstruction. They are therefore more compact for a space mission. Mm-wave lenses have already been used as primary optics elements of some refractive based telescopes for the CMB polarization science. BICEP [68] was the first for instance. Refractive-only telescopes are generally separated into multi-receiver systems to achieve low aberration in a very wide frequency range. For this reason, they are generally small aperture systems. For example, a multi-band instrument designed for the B-Pol project will need several telescopes in order to overcome the chromaticity that the lenses will cause [46]. Each telescope is optimized for its associated frequency band. Furthermore, the balloon-borne SPIDER experiment shares the same refractive optical approach as BICEP-2 which only differs from BICEP in terms of receiver technology to increase the total number of pixels.

Also, there are other telescope missions using lenses as intermediate optical elements. These systems are called hybrid configurations, which are used as re-imaging optical elements. Hybrid telescopes may have the advantages of both high throughput and high resolution due to their large aperture. Lenses have been manufactured with a diameter of up to 38 cm for EBEX and Polarbear and 30 cm for EPIC-LC which has similar optics to BICEP leading to degree scale resolution for cosmology. Hybrid telescopes using a combination of reflective and refractive components are also used for experiments such as EBEX [69], Polarbear [70], QUAD, ACTPol [71] and SPTPol [72]. Several trade-offs will be adopted in order to limit their aberrations.

Systematic effects induced from the refractive optical configuration of BICEP were investigated by using the BICEP data [73], [74]. The benchmark parameters were calculated for $r=0.1$. It was concluded that the benchmark parameters were satisfied by the measured performance of the BICEP telescope. Two discrepancies were observed in relative gain and differential pointing, however, the relative gain mismatch was not attributed to the refractive optics. The mismatch in the differential gain might be a result of birefringence in the dielectric material (HDPE) used for the BICEP lenses [52].

The problems regarding lenses at mm-wavelengths are;

- **lack of material knowledge**

  Dielectric properties (e.g. permittivity and refractive index) should be extracted as a function of frequency and temperature. Additionally, manufacturing of low-loss cyrogenic lenses and finding their broadband AR coating materials are bound up with accurate knowledge of materials. A free space material characterization test bench, which operates at W band, was developed and presented in Chapter 4 in order to determine real and imaginary refractive indexes of dielectric materials. High density polyethylene (HDPE), Ultra high molecular weight polyethylene (UHMWPE), Teflon and Silicon are the best candidate materials to produce mm wave lenses.

- **polarization effects**

  Material birefringence will affect the polarization performance of lenses. In addition, the polarization properties of horn-lens systems are characterized for both on-axis and off-axis feeds in this thesis.

For this reason, refractive based systematics should be studied and quantified accurately by both modelling and measuring RF characteristics of lens systems for future mm-wave lenses which will be used for CMB polarization experiments.

2.5 CMB projects under consideration

In order to reach higher sensitivity requirements of the CMB polarization missions given in Section 2.2, the design of new optical systems is necessary. Current and planned observations, given in Table 2.1, use different optical systems, polarization modulation techniques and detector arrays. All of these independent missions will provide an opportunity for testing different techniques before the first B-mode satellite is launched. Here, some selected proposed missions are briefly introduced. Many of the projects such as BPOL, CoRE and PRISM have been carried out with collaboration of the University of Manchester and Joddrell Bank Central For Astrophysics (JBCA).

2.5.1 B-Polarization Satellite Mission (BPOL)

B-Pol was proposed to ESA in response to the Call for Proposals of ESA Cosmic Vision 2015-2025 in 2007 [46]. It was designed as a small size space mission and is not under consideration anymore. BPOL project aimed at detecting B modes at $\sim$0.5 angular scale. This requirement lead to a main aperture size of the B-POL telescope to be 0.6 meters. The FP unit accommodates single mode corrugated horns operating in six frequency bands at 45, 70, 100, 143, 217, and 353 GHz. In B-POL, the lens-based configuration was selected to achieve the required cold volume for the instrument. This choice gives the advantage of space in the telescope as well. One of the lens designs for B-POL and the resulting beam are presented in Figure 2.4. Figure 2.4 shows a three-lens configuration designed to reach the desired qualifications in terms of cross-polarisation, beam symmetry, and size of focal plane. The optical design promises 0.5 degree resolution at 70 GHz, 1% spillover, 1% beam ellipticity, and a -30 dB cross-polarisation.

The telescope uses many refractive elements such as lenses and half-wave plates. In order to avoid possible aberrations such as chromaticity and beam aberrations that may arise due to large operating frequency range, the telescope system is divided into eight sub-telescope/FP systems as shown in Figure 2.4.

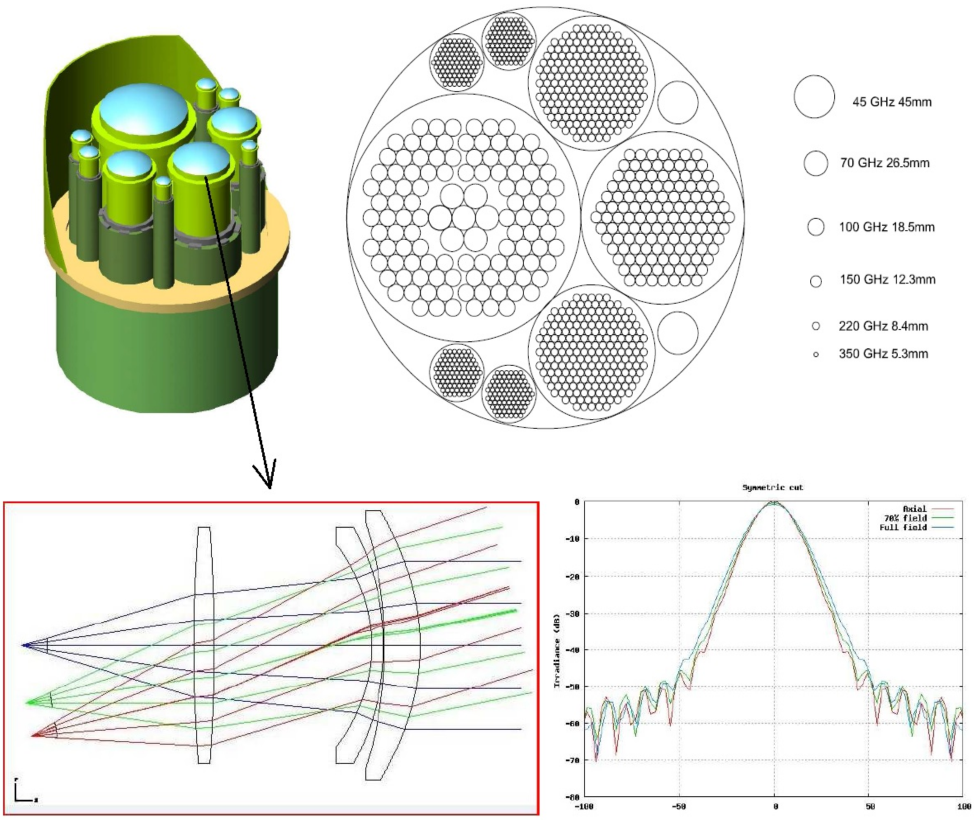

Figure 2.4: The artist‘s impression of the cyrogenic instrument is shown in upper-left figure. Upper-right figure shows the focal plane arrangement of the BPOL telescope. Lower left figure shows the one example of the lens based optical configuration and the resulting beams are given in lower right figure.

2.5.2 Cosmic Origins Explorers (COrE)

Due to a lack of confidence in lenses, the same consortium submitted a mirror based telescope to ESA within the framework of ESAs Cosmic Vision 2015-2025 in late 2010 [75]. COrE presents higher resolution in order to cover a wider science case. It aimed not only to search for B-modes with a confidence level of 3σ for r=0.001 in the full sky, but also to map the galactic magnetic fields for a better understanding of the star formation. Amongst the objectives of the COrE mission, measurements of CMB temperature anisotropies will improve the existing constraints on the cosmological parameters. COrE will scan the full sky in 15 frequency bands from 45 to 795 GHz, with a similar angular resolution to Planck. Its sensitivity is 10 times better than Planck. The scientific requirement set on the sensitivity is determined to be $5\mu K$·arcmin, which is satisfied by six frequency bands from 75 to 225 GHz. It promises better than 30 times higher sensitive measurements in many frequencies than Planck.

- **Optical considerations of the COrE**

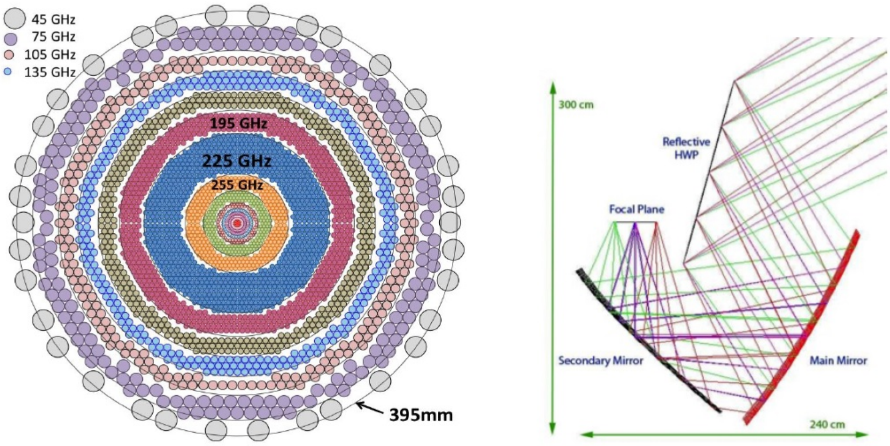

Figure 2.5: Left figure shows the focal plane unit that host 6400 feed-horn coupled antennas operated at the frequencies between 45 GHz to 795 GHz, in an order from the edges to the center. Right figure denotes the rays reflecting from the optical configurations of CORE, which comprises off-axis dual reflectors and a reflective HWP (RHWP) as the first element of the telescope [75].

The optical design of the COrE is based on a 1.2 m aperture-diameter CTR system that feeds a focal plane comprising 6400 feedhorn-coupled antennas shown in Figure 2.5. The horn antennas are supported by the orthomode transducers (OMTs) used to split the orthogonal polarisations. The focal plane, which consists of a chain of feedhorns, OMTs and bolometer detectors is cooled to 100 mK and the reflective HWP (RHWP) is kept at 30 K, while the entire telescope is cooled to $\sim$35 K. The strategy of removing the polarisation systematics relies on the RHWP. The RWHP is the first element of the optical system used to modulate the polarised sky beam. This component acts as a cold stop in front of the optics. The apparent challenge is of course to manufacture such a large diameter HWP so as not to sacrifice from the angular resolution. The predicted beams from the RHWP for the edge pixels of the 45 and 105 GHz have been found to have an ellipticity of 5% [1]. This value is quite high compared to the systematic requirement of the COrE mission on beam ellipticity with $<1\%$. Therefore, the integration of these components with the large number of detectors requires more development.

2.5.3 Polarized Radiation Imaging and Spectroscopy Mission (PRISM)

The science case of PRISM is much larger than B-mode detections. This large-class space mission aims to survey the sky for both intensity and polarization of microwave to far-infrared sources in the frequencies between 30 and 6000 GHz by using two instruments: A Polarimetric IMager (PIM) and an Absolute Spectro-Photometer (ASP) [76]. The polarimetric instrument of PRISM promises to detect B-modes for $r = 5x10^{-3}$. Its optical system uses a dual off-axis reflector with a primary aperture of 3.5 m that feeds a focal plane hosting 7600 detectors operating in 32 frequency channels. The polarization modulation relies on scanning strategies. The ASP focuses on measuring absolute microwave spectrum with even higher sensitivity than FIRAS, an instrument on COBE which measured the CMB blackbody spectrum.

2.5.4 Experimental Probe of Inflationary Cosmology - Intermediate Mission (EPIC-IM)

The EPIC team introduced three different satellite missions in three classes [47]. In the first report, the concept studies of EPIC-LC (low cost), which is a small class lens based telescope, and EPIC-CS (comprehensive science), which is a large class mirror based telescope, were presented. In the second report presented in 2009, a space based telescope EPIC-IM (intermediate mission) was released in order to study B-modes, E-modes, gravitational lensing, neutrino mass, dark energy, and galactic astronomy.

EPIC-IM promises a slightly higher sensitivity than EPIC-CS (Comprehensive Science) and 30 times higher sensitivity than Planck. The telescope operates in eight frequency bands between 30 GHz to 850 GHz. The EPIC-IM is expected to measure gravitational B-mode signals at r=0.01 after the foreground emissions are removed. Unlike EPIC-LC, the upper limit of the multipoles, as the primary objective of the EPIC-IM, is pushed from 100 to 200 thanks to the optical design of EPIC-IM. This is because the galactic emissions require less subtraction from the power spectrum at higher multipoles. The satellite is expected to operate at 4K for 4-years. As a secondary objective, EPIC-IM aims to extract all possible information from E-mode polarisation by operating at $10^{'}$ resolution (around l=1000). The other purpose of this project is to improve constraints on neutrino mass by measuring the shear signal with a resolution of $6^{'}$. Its last objective is to map Galactic magnetic fields by measuring the polarisation of Galactic dust at 500 GHz and 850 GHz. In order to achieve these mission goals, an off-axis CTR, with an aperture stop of 1.4 m was chosen as the optical configuration

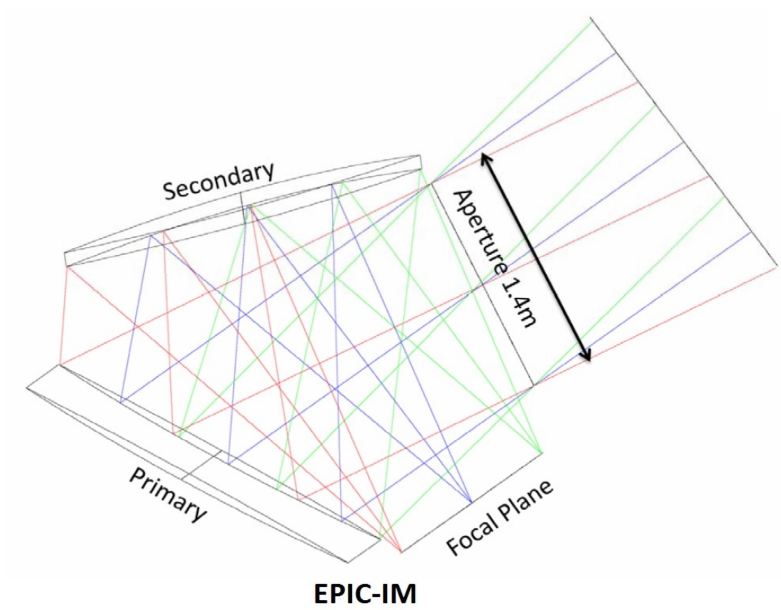

Figure 2.6: Optical ray tracing of the EPIC-IM telescope by using a CTR optics design [47].

of the EPIC-IM as shown in Figure 2.6. Since very low cross-polarisation can be achieved with the CTR configuration, the polarisation performance of the telescope strongly depends on the radiation coupling capability of the focal plane. The main optical components of the telescope comprise a cold aperture stop (located in front of primary mirror), two reflectors and bandpass filter. The FP unit is cooled down to 100 mK. The absorber rings around the reflectors help to mitigate the far-sidelobe effects originated from the edge diffraction of the mirrors.

- **Optical considerations of EPIC-IM**

The FP unit accommodates 11,000 detectors making a large gain in sensitivity. The focal plane is a telecentric design, which is not supported by any re-imaging component.

The team investigated the telescope performance in terms of systematic effects. Except for the requirement of the differential gain, the rest of the systematic have been met. This mismatch in the gain is explained by the finite conductivity of the reflector material causing one of the orthogonal polarisation beams to be absorbed more or less than the other.

Some rays are clipped by the secondary reflector due to its position relative to the primary reflector. These scattered rays lead to far side-lobes that let spurious sky signals interfere the optical system. Depending on their relative magnitudes to the B-mode signal, they might disturb the system considerably without an efficient baffling. The side-lobe level of the telescope for a Gaussian feed illumination of -25 dB at 150 GHz is calculated at around 0.1 nK rms polarised signals over the sky. It compares well below the goal of 1nK. The optical concept of the EPIC-IM does not include a polarisation modulator used to control polarization systematics. Instead, the EPIC-IM shares the same scan modulated PSB technology that Planck used. The subsystems of the EPIC-IM which forms the cyrogenic scheme covering 4K and sub-K cooling systems and the termal filters are directly inherited from Planck. A considerable effort is put on the technology developments of the large format focal plane arrays. Two options for the detector choice are transition edge sensors (TES) and microwave kinetic induction detectors (MKIDs).

2.5.5 Experimental Probe of Inflationary Cosmology - Low Cost Mission (EPIC-LC)

One of three telescope implementations prepared by the EPIC team is a lens based space telescope called EPIC-LC [47]. The main purpose of the EPIC-LC (shown in Figure 2.7) is to detect the B-mode polarisation signal from inflationary gravitational waves. In the inflationary energy scale at r=0.01 between the multipoles of l=5 and l=100, the full-sky in the angular resolution of one degree scale will be mapped for B-mode polarization.

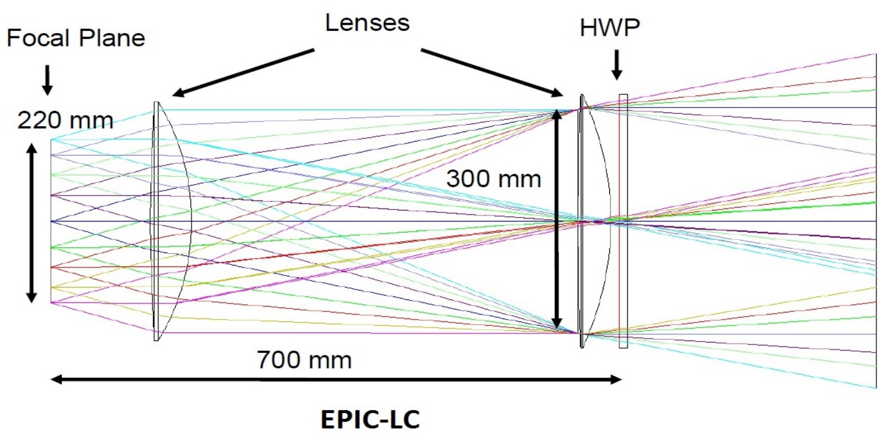

Figure 2.7: Optical design of one of the refractive telescopes used in the EPIC-LC [47].

It has multiple apertures comprising six lenses with a diameter of 30 cm that feed either antenna coupled NTD or TES detectors. Amongst the other refractor-only telescopes, this is the example giving the highest throughput with 40 cm^2sr over a large field of view of 20°. The refractive optics of EPIC-LC is mostly inherited from BICEP. The various specifications of the two telescopes are compared in Table 7.1.

	EPIC-LC	**BICEP[2]**
Aperture diameter	30 cm	25 cm
Resolution/ Frequency	$0.57°/135GHz$	$0.6°/150GHz$
Throughput	40 cm^2sr	34 cm^2sr
FOV	15.3°	17°

Table 2.4: Strehl ratio is better than 99% for FOV of 15.3°. DLFOV is 20° for EPIC-LC.

The main beam systematic errors introduced by the optics are removed carefully by means of HWPs. HWPs, located in front of each telescope of the EPIC-LC, were optimized for different frequency channels. A continuously rotating cryogenically cooled HWP has been successfully implemented and demonstrated for the MAXIPOL telescope, a balloon borne CMB polarimeter [77].

The two focal plane options for EPIC-LC are antenna-coupled Neutron-Transmutation-Doped (NTD) bolometers (baseline instrument) and transition-edge superconducting (TES) bolometers (upscope instrument). While the former consists of 830 NTD bolometers, the latter has 2366 TES bolometers.

2.5.6 The Large-Scale Polarization Explorer (LSPE)

LSPE is a fully funded balloon-borne experiment that aims to detect B-modes in CMB polarization at angular scales of $\sim 1.5°$. This is a different concept to the others mentioned. It has multi-mode receivers, so the detectors do not need the same number of receivers. Use of multi-moded pixels boosts the sensitivity by a factor >4 with respect to the diffraction-limited case [78].

The first objective of this radiation survey is to limit r to 0.03 with 99.7% confidence. Additionally, the mission aims to make a polarization map that covers 25% of the sky for foreground sources in our Galaxy such as synchrotron emission and interstellar emission. LSPE will consist of two separate instruments, the STRatospheric Italian Polarimeter (STRIP) and the Short Wavelength Instrument for the Polarization

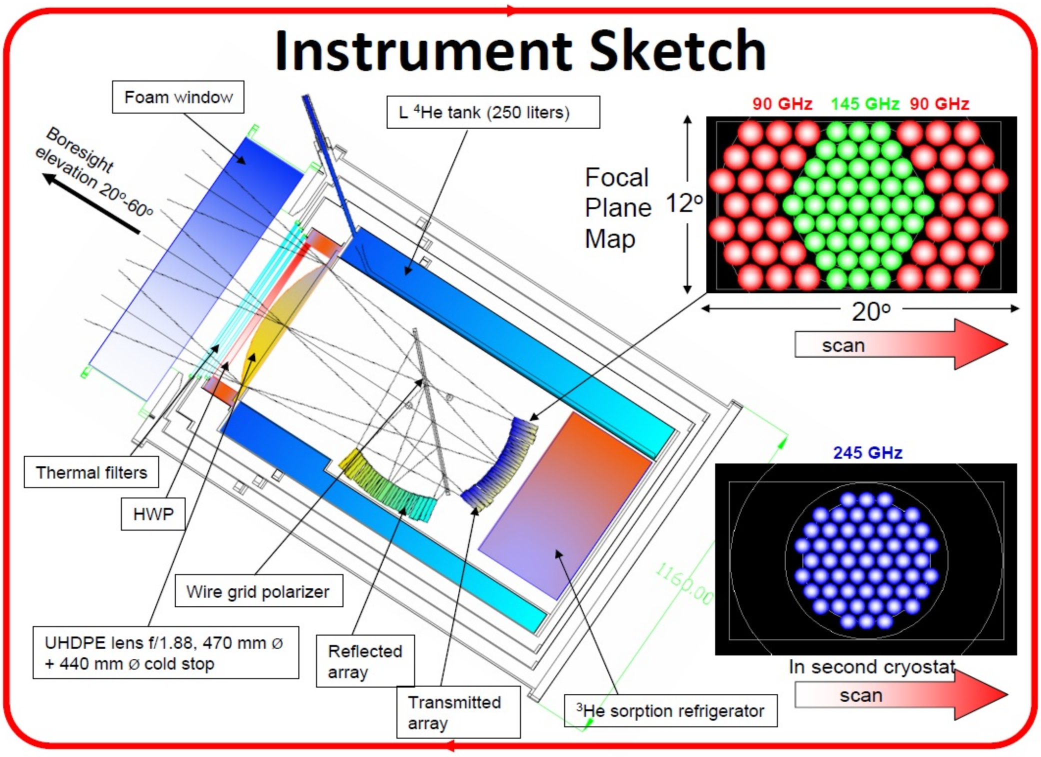

Figure 2.8: The sketch of the SWIPE instrument. The entire instrument is inside a liquid cyrostat system. Focal plane comprises two arrays : reflecting and transmitting arrays. Upper and lower right figures show the detector arrangements operating at different frequencies on the focal plane arrays [79].

Explorer (SWIPE). SWIPE will use multi-mode bolometric polarization system supported by Half Wave Plates (HWP) in the frequency bands of 95, 145 and 245 GHz. The optical configuration of SWIPE instrument is based on a refractor HDPE lens system, which is fully packed inside a liquid cyrostat system [79]. A clear aperture of 60 cm primary optics (lens has an aperture of 45 cm) feeds two focal planes with a FOV of $\pm 10^{\circ}$ thanks to a beam-splitting wire grid as shown in Figure 2.8. In STRIP instrument, cyrogenic HEMT amplifiers will operate at 43 GHz and 90 GHz.

2.6 Conclusion

Due to the expected low signal from B-modes, the scientific goals for B-mode detection constitute a major instrumental challenge. From sensitivity requirements, it is obvious that the next generation missions dedicated to the detection of the CMB B-modes need thousands of pixel arrays or multi-mode pixels. Additionally, these antenna arrays will operate in several spectral bands in order to obtain pure B-mode signals by subtracting foreground emissions. Such a large number of detectors needs to be accommodated on large focal planes. The question is what kind of optical system will be used to feed a detector array of a large focal plane? Large focal planes include many off-axis pixels that cause higher XP and beam distortions.

With the heritage of many previous experiments, e.g. PLANCK, WMAP, QUIET, CLOVER, BICEP, EBEX), a lot of experience has been gained in terms of different optical systems, polarization modulation and other individual components. The minimization and control of systematic effects are the highest priorities. Therefore, exquisite control of polarization systematics is required. Ongoing and future CMB experiments are listed in Table 2.1 in order to detail their instrumental specifications. High throughput optical systems should demonstrate their performance for low polarization systematics. Also, a similar investigation should be conducted at the component level. For example, a variety of modulators such as wave plates and variable modulators should be studied for low systematics.

CTR reflector designs are ready to present a large FOV with large number of detectors. The technology readiness level of reflector based antennas is already at flight level. However, they can produce higher XP for off-axis pixels located at the edge of large focal planes due to their off-axis configurations and hence present restricted FOV optics. Lenses have the great advantage of being on-axis. However, they are not problem free. The main problem of lens systems is lack of material information. For this reason, a free space material characterization test bench, which operates at W band, was developed and is presented in Chapter 4. Accurate material information enables simulations and measurements of lens systems to high precision. Additionally, the characterization of lens systems for both on-axis and off-axis pixels (Chapters 5, 6 and 7) are of paramount importance.

Chapter 3

DESIGN METHODS AND THEORETICAL CONCEPTS

3.1 Introduction to design tools

I used a variety of quasi-optical devices such as feed-horns, mirrors and dielectric lenses during my PhD research. This chapter covers the main theoretical tools, and their underlying theory, employed to model these quasi-optical devices. In particular, special attention was paid to the software packages used for modelling the horn-lens systems.

The experimental data contributed a great deal to the understanding of EM problems. However, measurement facilities are often too expensive to build with respect to available funds and staff in order to obtain such experimental data. Developing codes, therefore, is a necessity so that EM application of the real world can be simulated. Also, software tools are essential for optimization of optical designs. Solutions to EM problems which have large numbers of unknowns became possible by means of powerful computers with many processors. Moreover, computational electromagnetism (CEM) looks for explicit solutions to Maxwell equations which define EM problems and their interaction with a medium. The physical problems often require to be quantified by computing field components. This is possible by means of open solutions to the Maxwell equations. This is known as numerical solutions to the Maxwell equations. The numerical solutions can be either fully obtained or partly approximated depending on the electrical dimensions of EM problem. Among the full-wave solvers, the Method of Moment (MOM), the Finite Element Analysis (FEM) and the Finite Difference Time Domain (FTDT) are commonly used by CEM experts [81], [82]. These models are discussed in detail in Section 3.3.

On the other hand, there are many available approximate methods which are also known as high-frequency models in the CEM literature. However, the ”high frequency” definition is controversial because the computation intensity scales with the size of the EM problem in terms of the operating wavelength but does not scale directly with the frequency. In particular, solutions to large-scale EM problems have been successfully obtained by applying geometrical optics (GO) and physical optics (PO) methods. These models are discussed in Sections 3.2 and 3.4.

At this point, one question that needs to be asked is: do we really need a full wave modeller to solve electrically large EM problems considering the availability of efficient high-frequency models? The answer depends on how much accuracy the problem requires. The results predicted by full-wave modellers (e.g. MOM and FEM) and approximate modellers (e.g. PO and GO) are not always consistent. Since such methods give unsatisfactory results due to the approximations made, full wave modellers need to be employed to obtain accurate prediction of the field and the phase. The beam difference between results of two model approaches can be $\sim$ 10 dB in logarithmic scales. Such a discrepancy is often not acceptable for many applications, in particular in the simulation analysis of CMB polarization dedicated instruments.

There is no unified software package that can model all design elements within an optical system. The following sections will describe the feasible optical approaches for the simulations of the mm wave components. The capabilities and limitations of each model must be well understood. The selection of an efficient simulation tool for a component design is directly dependent upon the size of the component to be modelled in terms of the operating wavelength. Also, a trade-off should be obtained between the accuracy required and the optical model employed.

3.2 Physical optics (PO)

Full-wave numerical solutions to the Maxwell equations often demand very high computational resources. For this reason, the approximate model, PO is a strong candidate for handling scattering problems, in particular, for reflector based antenna systems. The algorithm is based on the field calculation from currents on a reflector surface. The software package that we use to employ the PO model is GRASP (General Reflector and Antenna Farm Analysis Software) [83]. The aim of the PO simulations with GRASP is to accurately predict CP- and XP beam patterns of reflective telescope systems. Depending on the accuracy level that can be set by the user in the GRASP, it can become computationally intensive for large reflector models.

A scattering problem can be defined with three field elements: total field, incident and scattering fields. The ultimate purpose is to calculate the total radiated field components. This can be achieved in three steps. Firstly, the induced surface currents from the incident source field on the reflector are calculated. Secondly, the scattering field due to these current elements is computed anywhere in problem space. The last step is to sum the scattering and incident fields to determine the total field.

The magnetic and the electric field integral equations which will be derived for the MOM method given in Equations 3.15 and 3.16, can be approximated for the PO model as shown in Figure 3.1. The workflow chain shows the calculation algorithm of the PO model. When the fields are being calculated, the challenging step is to compute the induced currents on the reflector. In PO, the reflector surface is assumed to be a perfect conductor and an infinitely large flat plane. The induced electric and magnetic currents flowing on the problem surface due to an incident magnetic field (H_1) and an incident electric field (E_1) are given by [84];

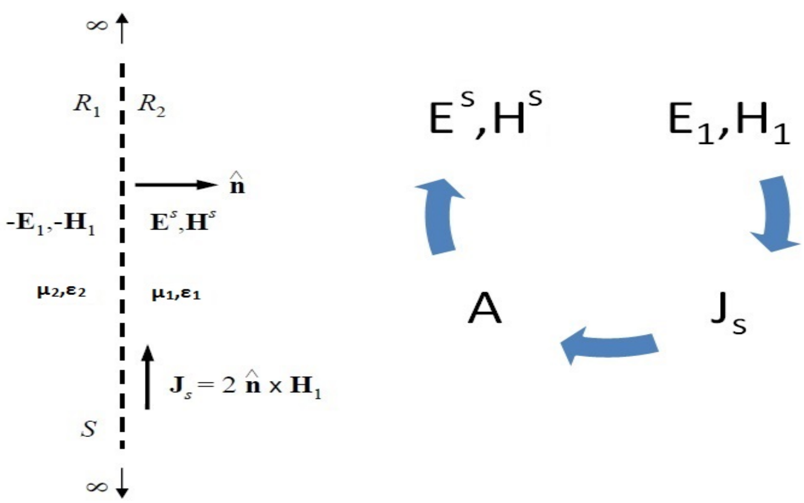

Figure 3.1: Left: The reflector is assumed to be an infinitely large and flat conductor in the PO approximation. The scattered magnetic field is equal to the incident magnetic field under this approximation. Right: The circle workflow chart shows the calculation algorithm of the scattering fields from the incident fields [84].

$$
\begin{aligned}
J_e &= 2\hat{n} \times H_1 \\
J_m &= 2\hat{n} \times E_1
\end{aligned} \tag{3.1}
$$

where the n is the normal vector to the surface of the illuminated side and J_s denote J_e and J_m. This is a good approximation for sufficiently large reflectors. By assuming that the indirectly illuminated surfaces of the problem body has a zero field, the scattering field elements can be calculated anywhere in problem space by using the relations as follows;

$$
E^s = -jw\left[A_e + \frac{1}{k^2}\nabla(\nabla \cdot A_e)\right] - \frac{1}{\varepsilon}\nabla \times A_m \tag{3.2}
$$

$$
H^s = \frac{1}{\mu_0}\nabla \times A_e - jw\left[A_m + \frac{1}{k^2}\nabla(\nabla \cdot A_m)\right] \tag{3.3}
$$

$$
A_e = \frac{\mu_0}{4\pi}\int\int_s J_e(r)\frac{e^{-jkR}}{R}dS \tag{3.4}
$$

$$
A_m = \frac{\varepsilon_0}{4\pi}\int\int_s J_m(r)\frac{e^{-jkR}}{R}dS \tag{3.5}
$$

where A is the electric vector potential, ε_0 and μ_0 are the electric permittivity and the magnetic permeability of free space. The R denotes the distance between the source and observation points.

3.2.1 The CATR modelling with GRASP

GRASP provides a variety of reflector and feed options. This package can model the electromagnetic interaction of the antenna components by using a variety methods such as PO, the Physical Theory of Diffraction (PTD), GO and Geometrical Theory of Diffraction (GTD). For example, the modelling of the CATR system discussed in detail in Section 4.2.1 was completed with GRASP.

Of all available modelling tools in GRASP, the PO/PTD analysis was chosen because it is recommended when the sub-reflector is illuminated by a high tapered beam ($\leq -12dB$). This is due to the diffraction effects that dominate the quiet zone where quasi-optical devices under test are located and hence they should be taken into consideration. On the other hand, the GO/GTD solution is preferable for time considered models if the sub-reflector is within the far-field region of the feed source.

For the PO model of the CATR system, the following checklist should be satisfied by the CATR system.

- Is the reflector (sub-reflector in the CATR case) within or close to the near field of the feed ?

  Yes, it is close. The far-field of the feed horn input that we used in the model is around 20 cm. The distance between the phase center of the feed and the center of the sub-reflector is around 25 cm.

- Is an accurate prediction of cross-polarization a requirement for the CATR system ?

  Yes, the CATR system should present a low-cross polarization and its value should be determined with a high accuracy.

- Is the field calculation needed at or close to the near field ?

  Yes, the near field characteristics of the CATR system such as amplitude and phase should be determined very accurately.

In GRASP, the PO model is combined by the PTD method in order to take into considerations the reflector edge currents. This leads to high accurate field predictions. In the method of GRASPs standard field calculation, the PO currents are first induced on the sub-reflector and then the field integrated by these surface currents on the sub-reflector are reflected to the main-reflector surface with the contribution of the PTD edge effects of the reflectors. Finally, the scattered E and H fields are calculated by the PO currents on the main reflector in either far or near field. However, in our case, the simulation runs a fully PO analysis. This is because the PTD examination cannot be applied to the edges of the reflectors which are treated by the serration application. For the CATR model, the field accuracy is set to be 80 dB below the maximum field level.

As far as the feed model is concerned, there are several options available in GRASP. The basic feed one is a Gaussian beam approximation. Additionally, simple aperture feeds can also be described to illuminate a reflector surface. However, the parameters of the simple aperture field that define the feed radiation beam pattern are limited and the model is successful only for handling rotationally symmetric smooth wall feed horns. Moreover, data feed source can be generated by the Spherical Wave Expansions (SWE) of either modelled or measured far-field data. SWE source input can be used with different software tools in an agreement such as FEKO. However, they are all approximations that sometimes poorly match with the real feed horn performance. To this end, a tabulated source data comprising the measured far-field radiation pattern of a real feed horn can also be preferred.

- **Evaluating the field equations in GRASP**

The numerical integration of the equations given above provides the electric and magnetic field computations. The reflector rim is used to determine the integration area where the currents will be computed. The simulation accuracy is dependent upon the sampling of the integration area on the reflector. This can be set by the user to increase the accuracy of the PO simulation. The integration grid is distributed over the surface area of the reflector by being specified with the variables $po1$ and $po2$. The number of integration points is equal to $po1 \times po2$. The sampling operation is first made for a given reflector geometry by default with the values $po1 = po2 = 10$ and the field is calculated. Then, po1 is doubled and the field is recalculated. In each iteration, po1 keeps on being doubled until the field converges. For example, the field accuracy of -80 dB should be understood that there can be an amplitude ripple of ± 1 dB at the -60 dB level [84].

- **Far-field calculation**

In GRASP, the far-field does not have a radial component and is defined by only two transversal components which are orthogonal to the direction of the far-field propagation. Polarization components of far field are defined according to the Ludwig‘s 3rd definition [85]. The CP and XP components are given as;

$$E_{co} = E_\theta \cos\phi \hat{\theta} - E_\phi \sin\phi \hat{\phi} \tag{3.6}$$

$$E_{xp} = E_\theta \sin\phi \hat{\theta} + E_\phi \cos\phi \hat{\phi} \tag{3.7}$$

where $\hat{\theta}$ and $\hat{\phi}$ are given by unit vectors defined in spherical coordinate system as follows. These vectors are shown in Figure 3.2.

$$\hat{\theta} = \hat{x}\cos\theta\cos\phi + \hat{y}\cos\theta\sin\phi - \hat{z}\sin\theta \tag{3.8}$$

$$\hat{\phi} = -\hat{x}\sin\phi + \hat{y}\cos\phi \tag{3.9}$$

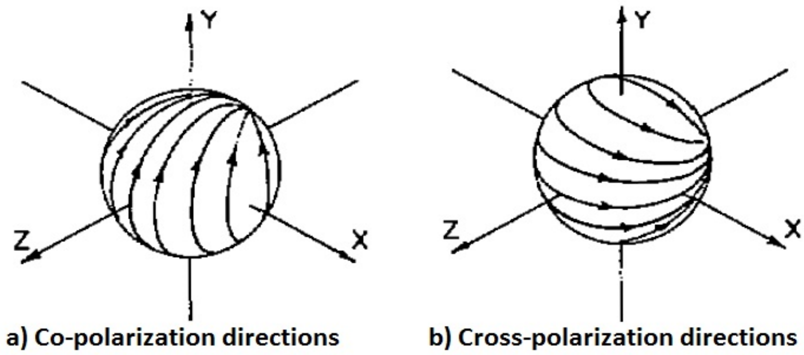

Figure 3.2: Co-polarization (a) and cross-polarization (b) field directions according to Ludwig 3rd definition. Field vectors are defined in spherical unit vectors [85].

- **Near field calculation**

The CATR system was developed with the purpose of generating a plane wave in the near field where the quiet zone is constructed. Near field characteristics of the quiet zone must be calculated as points on a defined plane cut. A linearly polarized electric field in the near field has three components in the planar cut;

$$E = E_\phi \hat{\phi} + E_\rho \hat{\rho} + E_z \hat{z} \tag{3.10}$$

where $\hat{\theta}$ and $\hat{\phi}$ are given by unit vectors defined in cylindrical coordinate system as follows.

$$\hat{\rho} = \hat{x}\cos\phi + \hat{y}\sin\phi \tag{3.11}$$

$$\hat{\phi} = -\hat{x}\sin\phi + \hat{y}\cos\phi \tag{3.12}$$

In the cylindrical symmetry and linear polarization definition, the E_ϕ and E_z show the co- and cross-polarization near fields respectively. E_ρ is the field component along the surface normal as shown in Figure 3.3.

In the definition of the planar cut, the field points are defined relative to the global coordinate system of the CATR. In order to calculate the field components, the coordinate system of the planar cut is translated at $z = z_d$.

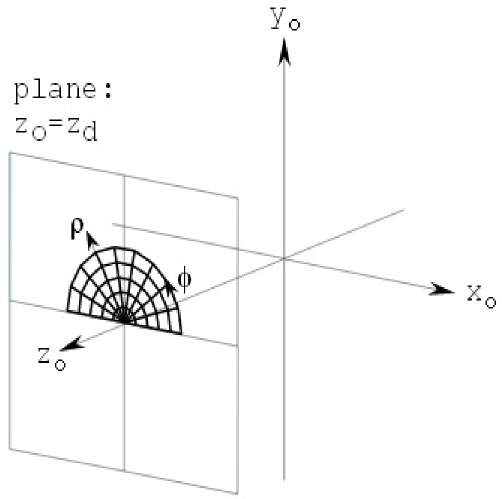

Figure 3.3: Planar output grids are described, for example, in the plane of $z_0 = z_d = 26$ cm for the CATR design [84].

3.3 Full-wave modellers

The main motivation of the study presented in this section is to investigate the feasibility of modelling the horn lens systems with various model tools. To begin with, the full-wave modellers are discussed in order to investigate their weaknesses and strengths.

There are three widely used full-wave methods to accurately model the RF systems: finite difference time domain (FDTD), finite element method (FEM), and the Method of Moments (MOM) [82]. The commercial versions of these optical codes are provided by CST microwave studio [86], HFSS [87] and FEKO [88] respectively. The information on the MOM and FEM codes provided below are based on my personal experience gained from the practical analysis of the commercial software packages that we possess in our technology group at JBCA. First, the FTDT model solves the EM problems by using the method of finite differences in the time domain. This code is suitable for the in-homogenous and nonlinear medium problems. The scattering body is discretized with tetrahedral mesh elements to handle the problem. For the wide-band microwave applications, time domain codes have an advantage, as it runs the simulation only once to calculate a wide frequency band response of an antenna system. This is different to frequency domain methods, as re-running the simulation is required for a frequency sweep.

Perfectly conducting devices such as reflectors and feed-horn antennas cannot be effectively solved with the FDTD. Similar to the FDTD, the second method, FEM, is generally preferred for the simulations of the in-homogenous and complex structures. Solution region can be discretized by a range of 2D and 3D mesh elements so that it can model complicated geometries by using different material properties for each tetrahedral mesh element without costing extra to process code. In the regions where the fields should be tackled carefully, the adaptive mesh arranges the mesh sizes by default in the FEM of the HFSS. There is a very large area of EM applications that can be handled with the FEM, from waveguide components including corrugated feed-horn antennas to dielectric material based components. However, expert users are often required in order to get the problem ready for a FEM simulation, as beginners may produce wrong results. Also, for radiation and scattering problems, extra attention is paid to deal with the model (radiation condition) boundaries. The MOM will be studied in detail in subsequent sections. As far as the runtime is concerned, all three full-wave methods scale from the fifth to sixth power of frequency and also come with their own limitations [82]. A general comparison based on the information provided above between three models is given in Table 3.1. The MOM model has an advantage of modelling dielectric structures such as dielectric lens and dewar windows by using the Surface Equivalent Principle (SEP) discussed in Section 3.3.3.

3.3.1 Simulations of refractive systems

Some progress needs to be made for developing high accurate modelling tools for refractive components in the MM wavelength range. This is true both for modelling a single lens as a primary optics element of a CMB telescope and a cascaded refractive design elements such as a window and a HWP located in front of the main lens aperture fed by a horn antenna. Dielectric lenses have been modelled by either ray-based optics or Gaussian beam optics in the MM wave [89].

The integral equations used in the MOM formulation are derived by starting from the derivation of Maxwell equations in Appendix A. In this section, the surface equivalence principle, which is the basis of the MOM in order to handle dielectric scattering problems, is explained with its mathematical formulation. Additionally, the algorithm for the accelerative model of the MOM, the Multilevel Fast Multipole Method (MLFMM), and the hybridization of the GO with the full wave modeller of MOM are introduced. Finally, the use of the PO for modelling the dielectric lenses is discussed.

	FTDT	FEM	MOM
Dielectric structure	?	$\surd$	$\surd\surd\surd$
In-homogenous structure	$\surd$	$\surd\surd$	?
Wide band performance	$\surd\surd\surd$	$\surd$	$\surd$
PEC model	$\surd$	$\surd\surd$	$\surd\surd\surd$
Mesh element	3D	2D,3D	2D, 3D
Runtime	$(d)^6$	$(d)^{5.5}$	$(d)^6$

Table 3.1: A very general comparison between the performances of the different full wave modellers (Ref-Computational EM for RF and Microwave engineering). 3 $\surd$, 2 $\surd$ and 1$\surd$ denote the best, good and acceptable model for a given EM model. Dielectric structures can be effectively modelled with the MOM while the other two models become computationally intensive due to 3D mesh elements. Electromagnetic behaviour of in-homogenous structures can be simulated with the FEM and FTDT models, in particular in dispersive structures. The time domain FTDT model is good at analysing wide-band applications. Conversely, the Perfect Electric Conductors (PEC) can be effectively modelled with the MOM and FEM models. the FTDT, FEM and MOM models mainly use 3D hexagonal, 3D tetrahedral and 2D triangular meshes respectively. While FEM is not friendly for beginners so experts are often required. The main advantage of the MOM is its hybridization with FEM, GO and PO models. In the FEM model, radiation boundaries should be defined carefully by the user. However, the MOM model sets boundaries by default. The runtime performances of three models are quite close. The electromagnetic size of the components to be modelled, d, scales with runtime dramatically [82].

3.3.2 Method of moments (MOM)

For the reasons given in Section 3.3, a full wave solution method, Method of Moments (MOM) has been chosen to model dielectric lenses.

The method of moments was first introduced by Harrington in 1968 [90]. He formulated the MOM to handle EM scattering and radiation problems. With advances in the computational electromagnetic (CEM), the use of the MOM has grown in popularity. The electromagnetic equations to be solved with MOM in the integral form require fewer number of unknowns than those in the differential form [81]. Additionally, MOM solves Maxwell‘s integral equations in the frequency domain. The fundamental idea is to discretize the problem area and calculate the surface current elements (i.e the electric and the magnetic currents) induced on generated patch elements. This process is also known as two-dimension (2D) meshing operation in the CEM. Also, the volume equivalence principle (VEP) of MOM code allows the EM problems to be solved by using three dimensional mesh elements. As the number of defined mesh elements increases, the method is expected to give higher accuracy results.

The MOM theory is based on the reduction of the EM integral equations in a form of a linear matrix system. The relations between triangular mesh elements and physical quantities such as amplitude and phase of the unknown variables are formed by basis functions. The method solves a dense matrix system to obtain the parameters of interest in an EM problem. For this reason, the MOM solutions scale rapidly with increasing problem size, thus increasing the computational time. The solution time scales with N^3 when a direct MOM solver is employed, where N is the number of the basis functions in the matrix system. The runtime increases by 64 times when the frequency doubles as a result of the scaling of f^6 in the MOM performance with frequency (f). The matrix dimension varies from a hundred to several thousands for an antenna with size of a few λ and an antenna with size of a few tens of λ respectively.

In Appendix A, the Maxwell equations were derived in the integral form to be used for the MOM equations. These field quantities are given as

$$E(r) = -jw\mu \int\int\int [J(r^{'}) + \frac{1}{k^2}\nabla^{'}\nabla^{'} \cdot J(r^{'})] \frac{e^{-jk|r-r^{'}|}}{4\pi \mid r - r^{'} \mid} dr^{'} \tag{3.13}$$

$$H(r) = -jw\varepsilon \int\int\int [M(r^{'}) + \frac{1}{k^2}\nabla^{'}\nabla^{'} \cdot M(r^{'})] \frac{e^{-jk|r-r^{'}|}}{4\pi \mid r - r^{'} \mid} dr^{'}. \tag{3.14}$$

3.3.3 The Surface Equivalence Principle (SEP)

The MOM is based on the Surface Equivalence Principle (SEP). In the SEP approach, the scattered fields are represented by the radiation of the equivalent currents (e.g. electric (J) and magnetic (M) currents which are flowing on a closed surface of the dielectric body). This representation was first produced by Schelkunoff who reformulated the idea of the Huygen‘s principle [91].

Once the equivalent currents are calculated by using the known incidence fields, the scattered fields can then be predicted by means of the boundary conditions defined on the interface between different mediums. For example, a lens has two surfaces as shown in Figure 3.4: the front surface facing the feed source and the back surface facing the sky. The equivalent current elements are denoted by J_1 and M_1 on the front surface and J_2 and M_2 on the back surface. The scattered fields are calculated by integrating the current elements defined on both surfaces [92].

- **Boundary conditions**

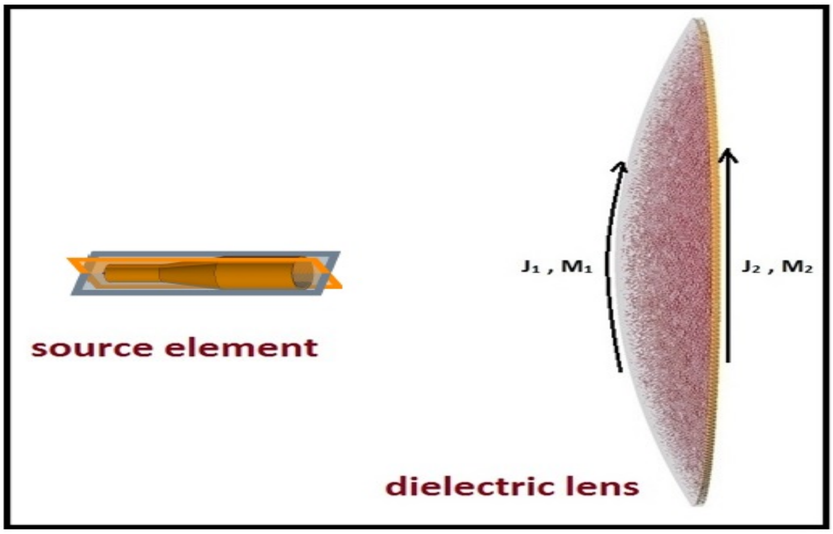

Figure 3.4: A dielectric lens antenna is illuminated by a source element. The equivalent surface currents induced on the front and back surfaces of the dielectric lens are shown.

A discontinuity between two surfaces occurs when they have different surface charge or surface current. In this boundary, the field quantities interact with these surface properties. The boundary conditions determine how these discontinuities affect the field parameters. The boundary conditions at an interface between two different dielectric regions are written in terms of electric and magnetic charges or currents.

In the field equations A.33 and A.34, the unknown electric current J and magnetic current M can be expressed by using the boundary conditions. Now, these boundary conditions are derived by the surface equivalence principle. The representation of the original problem to be solved is given in Figure 3.5. A dielectric body with the medium properties of permittivity ε_2 and permeability μ_2 and its environment with ε_1 and μ_1 are shown. Both medium are assumed to be homogenous.

From the two equivalence principles described in Figures 3.5, the electric and magnetic surface current densities are expressed by two very useful equations derived from the boundary conditions.

The external equivalence problem gives the relation;

$$
\begin{aligned}
J_s &= \hat{n} \times H_1(S^+) \\
M_s &= -\hat{n} \times E_1(S^+)
\end{aligned}
$$

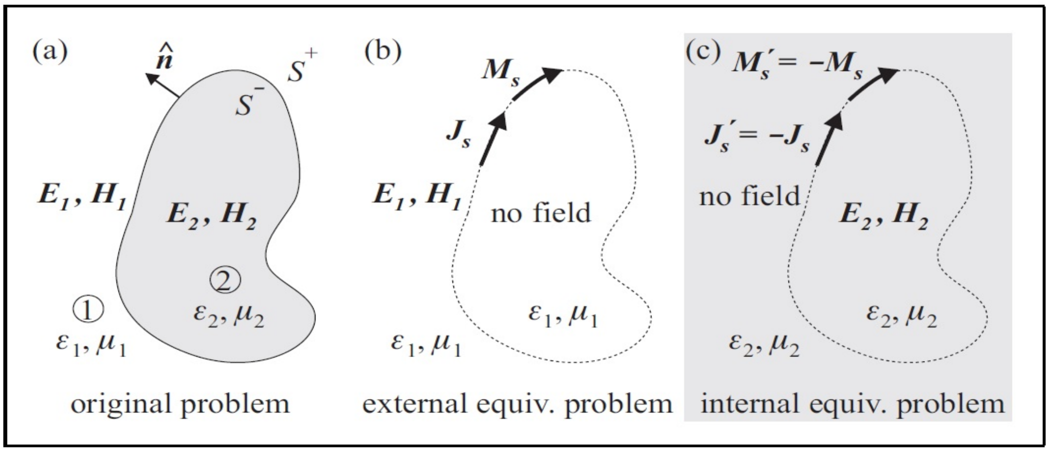

Figure 3.5: The original problem (a) is investigated with the SEP for the cases of the external (b) and internal (c) equivalent problems [91].

The internal equivalence problem gives the relation;

$$
\begin{aligned}
J_s &= \hat{n} \times H_2(S^-) \\
M_s &= -\hat{n} \times E_2(S^-)
\end{aligned}
$$

Using the equality of the surface currents given above at the boundary for the internal and external equivalence regions, the relations can be written;

$$
\begin{aligned}
J_s &= \hat{n} \times H_1(S^+) = \hat{n} \times H_2(S^-) \\
M_s &= -\hat{n} \times E_1(S^+) = -\hat{n} \times E_2(S^-).
\end{aligned}
$$

The scattered field quantities are related to the incident field quantities by means of these boundary conditions. In the dielectric interface, the tangential components of the electric field only are continuous.

Now, we have everything needed to derive the Electric Field Integral Equation (EFIE) and the Magnetic Field Integral Equation (MFIE) (also known Surface Integral Equations (SIEs)) in terms of the known incident electric field $E_1(r)$ by means of the equality of the boundary conditions.

$$
-\hat{n} \times E_1(r) = -\hat{n} \times \left(-jw\mu \int\int\int [J(r') + \frac{1}{k^2} \nabla' \nabla' \cdot J(r')] \frac{e^{-jk|r-r'|}}{4\pi \mid r - r' \mid} dr' \right) \quad (3.15)
$$

Similarly, the MFIE can be written in the same format

$$\hat{n} \times H_1(r) = \hat{n} \times \left(-jw\varepsilon \int\int\int [M(r') + \frac{1}{k^2}\nabla'\nabla' \cdot M(r')] \frac{e^{-jk|r-r'|}}{4\pi \mid r-r' \mid} dr' \right). \quad (3.16)$$

3.3.4 The MOM formulation

The set of MOM integral equations has been completed by these last formulations 3.15 and 3.16. These integrals cannot be solved with analytical approaches. A computational numerical method, the MOM formulation, is used to solve SIEs. In this method, the equivalent surface current densities are expanded in terms of basis functions with their expansion coefficients given as follows. These functions are used to convert the integral equations to a linear set of matrices. The equivalence electric and magnetic current densities can be written as follows.

$$\begin{aligned} J_s &= \sum_{n=1}^{N} C_n(J_s) f_n(J_s) \\ M_s &= \sum_{n=1}^{N} C_n(M_s) f_n(M_s) \end{aligned} \quad (3.17)$$

C is the unknown expansion coefficient and f is the basis function. The idea is to expand the unknown quantity using a set of known functions with unknown coefficients. The surface currents are defined on a triangle which is the base of the triangular mesh element. Among many models [82], the Rao-Wilton-Glisson (RWG) triangular basis function can be successfully applied. Two adjacent triangular mesh elements are defined by their associated basis functions as shown in Figure 3.6.

T1 and T2 are two adjacent triangular elements that share a common edge of n. On each triangle, the vectors of P1 and P2 are defined by being pointed from the vertex of v1 and to the vertex of v2 respectively. The basis functions on both triangle are defined as;

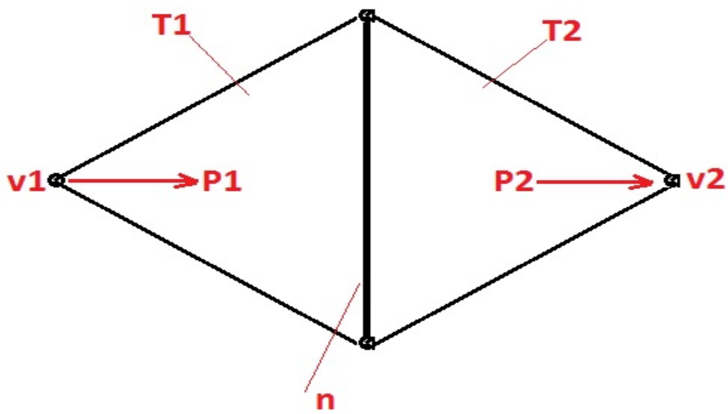

Figure 3.6: Two adjacent triangular mesh elements showing the basis function components with the RWG approach.

$$
\begin{aligned}
f_n(r) &= \frac{L_n}{2A1_n} P1_n(r), \qquad r \quad in \quad T1 \\
f_n(r) &= \frac{L_n}{2A2_n} P2_n(r), \qquad r \quad in \quad T2 \\
f_n(r) &= 0, \qquad otherwise
\end{aligned}
$$

where L_n is the length of the common edge and A_n is the area of the triangular patch. The basis function of f_n can only be defined between two adjacent triangular patches of T1 and T2 sharing a common edge.

Let us suppose that we have an unknown function *f*, electric and magnetic currents in our case, and a known excitation source e such as incident field. The linear equation system is defined as;

$$L(f) = e \tag{3.18}$$

where L is a linear operator. Similar to the equations 3.17 , the function f is a sum of N weighted basis functions. When Equation 3.18 is substituted into Equation 3.17 obtained for the currents.

$$e = \sum_{n=1}^{N} C_n L(f_n) \tag{3.19}$$

An inner product between the basis functions f_n and their corresponding testing (weighting) functions f_w should be derived.

$$< f_w, f_n >= \int_{f_w} f_w(r) \cdot \int_{f_n} f_n(r^{'}) dr^{'} dr \tag{3.20}$$

Depending on the nature of the problem, the basis functions can have surface or volume integrals. For the surface current problems where the triangular patches are defined as the basis function elements, the surface integrals are employed. When the operator function is applied to the basis function, the current function becomes;

$$< f_w, e >= \sum_{n=1}^{N} C_n < f_w, L(f_n) > . \tag{3.21}$$

This equation leads to a $N \times N$ matrix equation $Zc = x$ with the following matrix elements;

$$\begin{aligned} x_w &=< f_w, e > \\ Z_{wn} &=< f_w, L(f_n) > . \end{aligned}$$

Many approaches are used to determine the testing functions. In particular, the Galerkin method is most commonly used, because the testing functions utilize the basis functions as the weighting functions. In the MOM formalism, the Green‘s function relates each basis function to the others defined on the patch elements. One disadvantage of the MOM model is the enormous number of interactions between all triangular mesh elements. Hence, the resulting matrix is denser than with other full wave modellers. The number of basis functions is a vital parameter to represent the problem sufficiently. The number should be large enough to determine the amplitude and phase solutions accurately. A mesh operation, adapting the number of basis functions for the edge or port locations where the amplitude may vary considerably is required. In the surface problems employing the MOM formalism, the number of basis functions increases exponentially. This dramatic increase results in a large matrix system to be solved computationally and requires large memory to store them. Many methods and approximations have been developed to deal with solution of large scale matrix equations. The Gaussian elimination (GE) and Lower-Upper factorization (LU decomposition) methods are widely employed by a direct MOM solver. Depending on the properties of the EM problem, the algorithm is either set by default or selected by the user. The mathematical discussions of these approaches are detailed in Chapter 3 of [82].

3.3.5 Iterative solvers

Iterative solution methods speed up the computational process by making an initial guess for the current elements. They do not modify the matrix system formed initially. With each iteration, the solution convergence is checked and the residual vectors defined initially are calculated. The iterations continue until the convergency criteria is met. After many iterations that do not result in convergent field calculations, simulation will terminate even if the normalised residue is smaller than the defined value. The incident field elements used to make the initial guess of the current elements can be either approximated or fully solved. Current elements are calculated by using the algorithm with the iterative equations 3.22 given [93] as

$$
\begin{aligned}
J_{s,k} &= J_{s,k-1} + \frac{1}{Z}\left[E_i + E_{s,k-1} - E_{0,k-1}\right] \\
M_{s,k} &= M_{s,k-1} + \frac{1}{Y}\left[H_i + H_{s,k-1} - H_{0,k-1}\right]
\end{aligned}
$$

where the equivalent surface currents are $J_{s,k}$ and $M_{s,k}$ of the k^{th} iteration. Y and Z given as follows are defined as the wave impedances describing the interaction between the vacuum and dielectric material.

$$
\begin{aligned}
Y &= \frac{1}{2}\left[\frac{1}{n_0} + \frac{1}{n_m}\right] \\
Z &= \frac{1}{2}\left[n_0 + n_m\right]
\end{aligned}
$$

3.3.6 The multi-fast method of moments (MLFMM)

The increasing frequency and problem size has led to asymptotic growth in the requirements of computational resources. This forced code users to search for an accelerative method to model electrically large scattering problems. New approaches [94] have been used to modify the full wave model codes such as the multilevel fast multipole

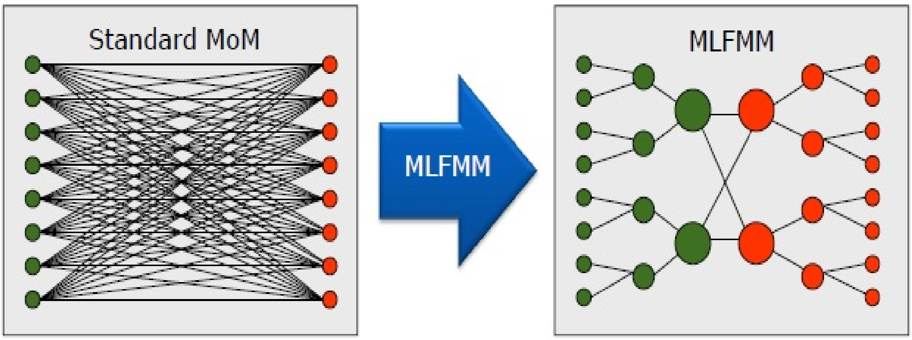

Figure 3.7: The solution algorithm difference between the MOM and the MLFMM [99]. Each connection shows the interactions between the basis functions. MLFMM accelerates the matrix-vector product by reducing the complexity of the matrix interactions defined in MOM [88].

method (MLFMM). MLFMM is an iterative solver tool used to obtain full-wave solutions to EM problems, that are different to approximate methods such as PO. For electrically large structures such as big dish antennas and large dielectric lenses ($\geq 20\lambda$), the MOM can be replaced with the MLFMM. The same problem as that treated with the MOM can be handled without changing the mesh size. Such problem may be either metallic or dielectric bodies. A huge saving in the computational resources devoted to the MLFMM simulations could be achieved without sacrificing the solution accuracy. Greengard and Rokhlin were the first to apply the MLFMM method to the EM problems [95]. The runtime is reduced from N^3 to $N[\log(N)]^2$ when the MLFMM is employed where the N is the number of basis functions [82].

Structural modifications are applied to the calculation algorithm of the discretized MOM basis functions. The MLFMM makes groups of basis functions defining the interactions between all triangle meshes. These groups are then used to calculate the interaction between groups of the MOM basis functions instead of calculating the interactions between individual basis functions as the MOM does. This is illustrated in Figure 3.7. In the FEKO software package that I used to model a wide variety of quasi-optical devices, the MLFMM firstly creates a large cube covering all problem space. This cube is then divided into 8 small cubes. This is iteratively repeated until the minimum side length of the cube reaches at a certain level where the minimum scale is a quarter λ. Only occupied cubes are taken into consideration by applying three steps: Aggregation, Translation and Disaggregation.

MLFMM may have a problem with convergence when this method is employed with complex structures as I experienced in the simulations of the corrugated feedhorn antenna. The other drawback of the MLFMM is the high material loss. As the material becomes lossier, MLFMM requires more memory and longer run-time. For this reason, the modelling of highly lossy dielectrics is recommended to be done with the volume mesh models such as the MOM with the Volume Equivalence Principle (VEP) and the FEM. The residual error should remain below 0.005 so the iterations are conducted until this criteria is met. The default value for the residual error of the maximum 500 iterations is set as 0.003 in all MLFMM simulations employed in this thesis. Also, this model may fail if there is a large space between the separated bodies defined in the problem. As a user, one expects to obtain robust results from the algorithm that we employ to model the optical design. The MLFMM, as the main code extension of FEKO, has met this expectation by presenting well agreed results to those of the full wave approach, the MOM. The selection of suitable iterative solvers and pre-conditioners has allowed us to deal with challenging EM problems.

3.4 Ray Launching Geometrical Optics (RLGO) in FEKO

The fundamentals of the basic ray-based model, Geometrical Optics, is introduced in Section 5.1. In addition to ZEMAX that I have only used for the initial design of dielectric lenses, there are other alternative software packages which are based on GO (e.g. ASAP and Code V). These models present quite accurate results and simulations take just minutes. Additionally, FEKO implemented the hybridization of a ray-based model, GO, with MOM. In this model, ray-launching procedure is used. The GO rays emanate from the MOM defined region, traced in free-space and interact with dielectric structures. On the dielectric boundary, Huygens sources due to the launched GO rays are generated. Finally, the equivalent Huygens sources radiate in free-space. The process is illustrated in Figure 3.8.

GO rays are launched with a subtended angle to the lens. A default value of 1° increment for a given angular range over a full sphere is acceptable. In the GO hybridization model of the dielectric bodies, mesh size does not matter. The triangular mesh patches can be large as long as it fits with the problem geometry. When a ray hits a surface, the algorithm will compute the magnitude of the reflecting ray as well as the transmission through a dielectric. Thus, there will be two equivalent sources after a ray hits the lens. The algorithm will repeat this for the defined amount of the interactions. However, GO does not account for diffraction effects.

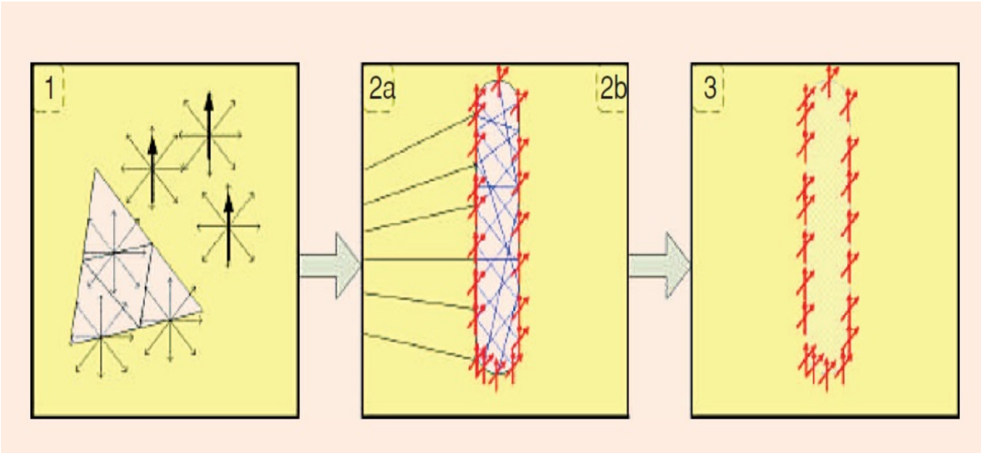

Figure 3.8: The ray launch process is described in the figure. The impressed sources generated by the MOM region are sent over the dielectric body. The GO equivalent Huygens sources are then used to evaluate the field in free space [96].

3.5 PO modelling for dielectric lenses in FEKO

The parameters calculated by MOM and PO are essentially the same, since both methods involve the electric and magnetic field integral equations (EFIE, MFIE) derived from the Maxwell equations for the surface currents. A publication [98] has claimed that a large scale dielectric lens antenna (120λ) could be solved with PO. However, my correspondence with the support service from FEKO suggested this was impossible. The reasons are explained as follow [97].

- PO can not model dielectric EM problems because in PO simulations of dielectric lenses, the mesh triangles are checked for direct illuminations. The PO formulas assume an illuminated current at the front surface of the lens. However, FEKO formulas calculate the currents to be zero in shadow regions of the lens where the back surface of the lens is. Thus, the PO formulation in the FEKO will only account for currents in directly illuminated regions. For this reason, the PO is simply not recommended for dielectric problems.

On the other hand, the other commercial software, GRASP, has been developing a code to adopt the surface equivalence principle (SEP) for PO. The group showed that PO analysis of the dielectric bodies would be possible for dielectric lenses with diameters up to 90λ. However, this method should be verified with experimental data. In the publications [92] and [142], there is also a comparative study for the limitations of MOM, PO and GO. The models are all based on the equivalence principle of the surface currents. The continuing analysis in the same study resulted in that MOM can model dielectric lens antennas up to a diameter of 15λ, with a good agreement to PO and GO.

3.6 Equivalent radiation sources

In most CEM software, radiating elements can be represented by equivalent source inputs. A substantial decrease in the required computational resources could be achieved by the use of spherical wave expansions, aperture field data and radiation pattern data. Stored source data from both far field and near field calculations can be used to illuminate a cascaded antenna system comprising many quasi-optical components that can modify the source beam each time.

3.6.1 Spherical wave expansions (SWE) source data

In FEKO, an advanced option of far field request can be activated to store the data as spherical modes given in detail as follows. In this format, the electric and magnetic fields from a feed source antenna can be expressed as a series of algebraic function given as

$$E(r,\theta,\phi) = \sum_{s=1}^{2} \sum_{n=1}^{N} \sum_{m=-n}^{n} Q_{smn} F_{smn}(r,\theta,\phi) \tag{3.22}$$

where the mode coefficients Q_{smn} and the spherical wave expansions F_{smn} are in the spherical coordinate system. The index s indicates the TE mode for 1 and the TM mode for 2. The indices of m and n are determined by the mode index numbers in the azimuth direction ϕ and in the radial direction respectively, while m ranges from $-n$ to n. The important parameter in this equation is N, the number of spherical wave modes defining the fields. As an upper limit [99], N is calculated by

$$N = kr_0 + 3\sqrt[3]{kr_0} \tag{3.23}$$

where k is the wave number and r_0 denotes the radius of the smallest sphere enclosing the feed-horn antenna body. By using the formula given in Equation 3.23, the enclosing radius of the problem region is around 13λ (λ = 3.09 mm at 97 GHz) leading to 81 modes required to be included for our case of the small lens system.

3.6.2 Aperture (AP) source data

The aperture field source data can be requested from the near field calculations in spherical coordinate systems. The sphere where the near fields are calculated must have a slightly larger radius than the smallest radius enclosing the feed-horn. Angular range of θ and ϕ should be defined with finest angular increment possible for accurate computation. In the case of the corrugated feed-horn antenna model, the radius is defined as 49 mm, considering that the feed horn antenna has a 75.465 mm length. θ and ϕ range from 0° to 180° in $0.1°$ intervals and 0° to 360° in 1° intervals respectively. Similar to the SWE source data, the solution accuracy can be increased by increasing the calculation points of the near field result but it costs more computational resources. Field calculations are recorded with extension files of $*.efe$ for electric field calculations and $*.hfe$ for magnetic field calculations. Data files record the gain results for E_θ and E_ϕ with real and imaginary components.

3.6.3 Radiation pattern point (RAD) source data

Radiation pattern source data is an alternative way to generate an equivalence source as an feed input. In our case, the radiation pattern point source data is specified by the far field pattern of the corrugated feed horn antenna. For this reason, the radiation pattern must be defined in spherical coordinates. The field calculations are recorded with an extension file of $*.ffe$ for far field calculations. Data files record the gain results for E_θ and E_ϕ with real and imaginary components. Field calculations are requested for full angular scale of θ and ϕ. The far field conditions must be met for the computation of the radiation pattern point source. A number of radiation point sources can be used simultaneously to feed a geometric body to be modelled.

3.6.4 Verifications of the equivalent source inputs

In order to verify that source inputs are equal to their own real source, the source data are separately used as the feed input and then re-computed the resulting far-field pattern. Figure 3.9 shows the overlapped radiation pattern plots of the four models: SWE feed input, AP feed input, RAD feed input and the real feed horn. Far-field patterns were calculated for the D plane cut of the co-polarization radiation beam pattern at 97 GHz. Except for AP source input model, three models presented a well overlap. The predicted pattern from the AP source input differed from the others after the first beam side-lobe. The AP its cross-polarization level is also 4 dB higher.

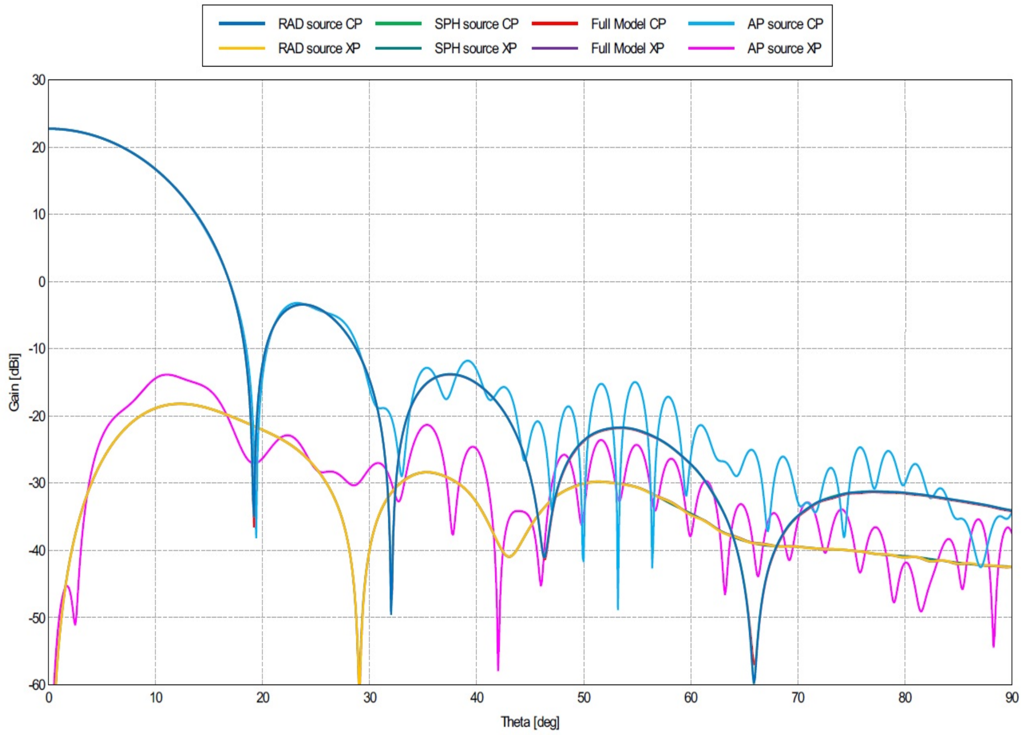

Figure 3.9: Four different models used for far-field calculations of different source inputs. Spherical Wave Expansion (SWE) feed input, Aperture Source (AP) feed input, Radiation pattern point source (RAD) feed input and their real feed input. There is a well overlap of three model plots that look only one blue curve. Radiation pattern of the AP source input starts to fluctuate after first beam side-lobe.

3.7 The W-band corrugated feed-horn antenna

The corrugated feed horn that has been used for the experimental part of this PhD has been designed for the CLOVER experiment to operate between 82-112 GHz, part of the W-band (75-110 GHz) [100]. Throughout the thesis, the Standard Feed (SF) will refer to this corrugated feed horn antenna. For the verification of the predicted results, three different models were employed to investigate the beam properties of the radiation pattern of this horn antenna and then the predicted results were compared to the measured data. The following sections present the model analysis of the feed-horn antenna by employing three different EM codes : mode-matching, MOM and FEM.

A feed operates as a coupler for the radiation beam from a source to a receiver system which may be supported by a reflective and/or refractive element. By taking advantage of the reciprocal nature of the feed, feeds can also be analyzed as a transmitter for the radiation beam, which is propagated to free space. According to this, the coupling properties of an antenna in a receiving position are the same as those of an antenna in a transmitting position. Since they present a nice match to the sky beam with low systematics such as return loss and cross-polarization, corrugated feed horn antennas are often used as the main feed element of the antenna systems. Generally speaking, a corrugated horn consists of four parts as shown in Figure 3.10 [101]. The first part is the aperture diameter which determines the beam-width of the co-polarization radiation beam. The second part, the flare angle and its profile define the main beam shape of the radiation pattern. Thirdly, the corrugation geometry controls the cross-polarization performance and finally the throat region is responsible for the input impedance and mode selection.

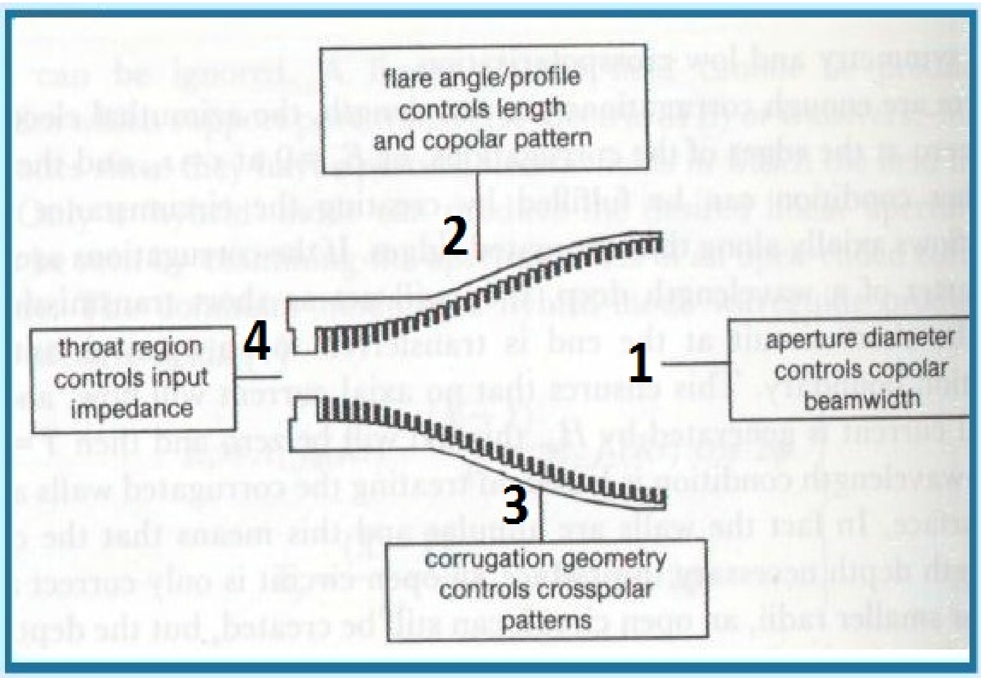

Figure 3.10: The general field behaviour of the corrugated horn antenna with the change of some fundamental horn parameters [101].

In order to meet requirements for a symmetrical radiation beam pattern with a low cross-polarization, a feed-horn should generate a nearly linear electric field. A pure-linearly polarized hybrid mode can only be generated by means of the corrugated structures in a feed-horn profile. In the case of the single mode horn, HE_{11} consists of a combination of %85 TE_{11} and %15 TM_{11}, the smooth circular waveguide modes

[101].

3.7.1 Different modelling of the feed-horn

In order to verify the modelling techniques and validate them with experimentally measured data, some cross-checks between the models are required.

The first code employed was the mode-matching model. A detailed analysis for different types of corrugated feed-horn antennas modelled with the mode-matching model can be found in the PhD thesis of Emily Gleeson [102] for instance. In the model, each waveguide segment of the corrugated profile of the feed-horn antenna is treated as an individual smooth walled part. The model calculates a scattering matrix defined by the interaction between two adjacent waveguide sections. This is repeated for the next waveguide section iteratively until the last waveguide section defining the horn aperture. In the end, the scattering matrix determines the complex coefficients for the modes at the horn aperture and the far-field radiation beam pattern is then predicted by considering the complex coefficients of the mode contribution calculated at the aperture. For our purpose, the model is run with the commercial software tool called CORRUG (Analysis of Circularly Symmetric Waveguide and Horn Structures) [103]. This software analyses corrugated horn antennas with circularly symmetric waveguides. A display of the model geometry is shown in the top photo of Figure 3.11.

The second model used was MOM, the full vector numerical analysis within FEKO. The model was employed in the frequency domain. The model structure was constructed with the perfect electric conductor (PEC) material which was meshed with triangular patch elements in 2D. The external surface has required in the MOM model since there was a clear difference between the radiation patterns, with and without the exterior structure. The real physical structure of the feed-horn was modelled with exterior bodies made up of a cone and cylinder to support the feed structure. In particular, the beam pattern of the horn model without an exterior structure had multiple ripples in the far angles starting from the second side-lobe. These fluctuations were removed by constructing an outside structure for the feed as in the real situation. However, this required a computation time of 21 hours, and 148 GB of memory. The feed was excited by a waveguide port defining the fundamental propagation mode while the selection of the number of the modes propagated was left to the user. By relying on the symmetric structure of the feed horn antenna, symmetric planes of the electric and magnetic fields were assigned to the model. Since the matrix equation to be solved is reduced to half by introducing one of these symmetry operations, the memory requirement was halved.

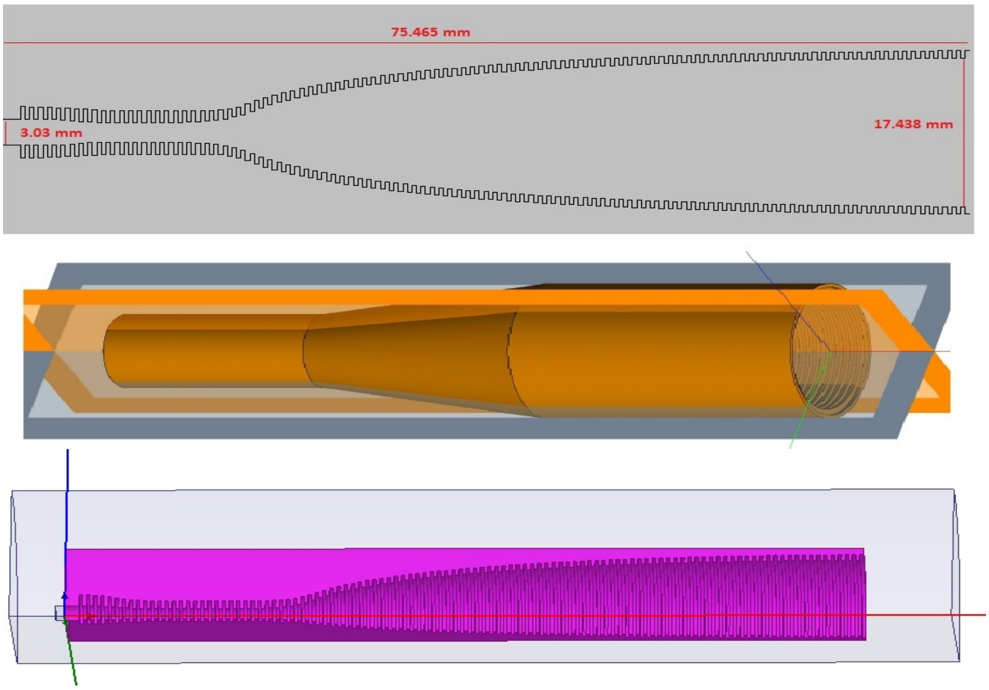

Figure 3.11: The solid models of the corrugated feed-horn antenna constructed in the three different model tools: Mode-matching (CORRUG), the MOM (FEKO) and the FEM (HFSS) from top to bottom. A 1-dimensional model profile of the corrugated feed horn was used in CORRUG. In FEKO model, electric and magnetic symmetry planes are shown with the solid body of the corrugated feed-horn. FEM model of HFSS requires an air box to define a radiation boundary set of the symmetric electric and magnetic planes.

The waveguide port and symmetry operations determine the radiation boundary conditions of the model problem as shown in the center image of the Figure 3.11. Particular attention was paid to meshing the port region and waveguide section. These regions were meshed finer than the other parts of the antenna in order to provide more accurate field calculations. While the edge length of the triangular mesh element defined was specified as $\lambda/8$, this number was decreased to $\lambda/12$ for the port and waveguide section. After the mesh operation was defined on the metallic surface of the antenna profile, the simulation of the model could begin.

The last model used was the finite element model (FEM) employed with HFSS. For the HFSS model, the corrugated surface was made by a PEC structure and effectively coupled to free-space. The solution algorithm is very similar to the iterative solution. A residual parameter (∇S) is set to calculate the magnitude of the S parameters change between two consecutive passes of the simulation. After each iteration, the criteria is checked. If this requirement is met and the results converge, the simulation stops. If a better accuracy is needed, the number of the passes can be increased by using the adaptive solution settings. The number of meshes assigned increases after each simulation pass. The first attempt to model the feed-horn antenna was done quickly, as the ∇S parameter was kept low and the simulation took only 6 hours after 12 consecutive passes. Although the results obtained from this initial model agree with the subsequent model results, the side-lobe level varied between 0.5 dB and 1 dB. Other attempts were made by my colleagues Ho-Ting Fung and Giampaolo Pisano. The HFSS model of the antenna is shown at the bottom image of the Figure 3.11. They modified the model in a similar way to the MOM model from FEKO. In order to couple the radiation from the antenna to the free space, they covered the surrounding feed area with a radiation air boundary. The model was completed after 23 consecutive passes with $\nabla S = 10^{-5}$. The convergence criteria was met at 15th pass by using 24 GB ram in 8 hours. After the 15th pass, the mesh size got finer until it reached $\lambda/8$. The model results matched better after this modification. After all, the HFSS models were found to be strongly depend on the ∇S parameter value.

Simulation details of the three different models are listed in Table 3.2. The predicted and measured results are overlayed in Figure 3.12. Overall, all models presented well matched results with the measured data. The measured data is given with error bars obtained from the standard deviation calculations of many repeated measurements. The HFSS model predicts a maximum cross-polarization level 1.5 dB higher than that of the other models. This level still remains within the error bars of the measurements. The other discrepancy between all plotted data starts from the third side lobe of the co-polarization beam. In order to investigate the beam differences (BD) of the predicted values than the measured values, the beam difference values are calculated for each predicted data as shown in Figure 3.13. The investigation made on the corrugated feed-horn antenna used in our measurements reveals that all the models employed give an accurate calculation based on the comparison results of the beam difference. All model results are consistent with the measurement data up to far angle directions of $\theta = 50°$. The calculated beam differences of different models than the measured data are mostly below -20 dB. Beam difference between two variables is calculated by using the equation given as

$$Beam\,Difference(\theta) = 10 \times \log_{10}\left(\frac{|I_1(\theta) - I_2(\theta)|}{I_2(\theta = 0)}\right) \tag{3.24}$$

where I is intensity. Beam difference is normalized to the peak ($\theta = 0$) of the one

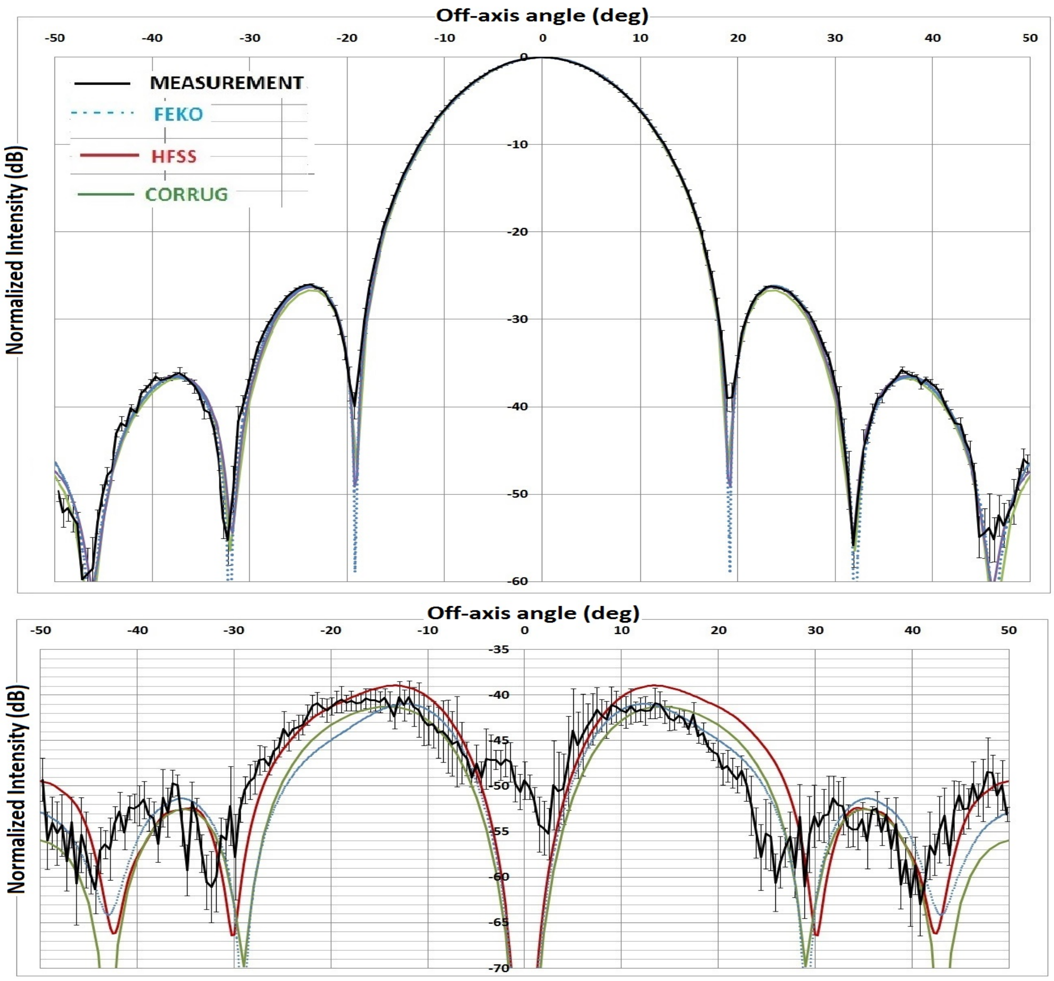

Figure 3.12: The co- and cross-polarization radiation beam patterns are predicted from the three different models and then the results are compared to the experimentally measured data.

variable.

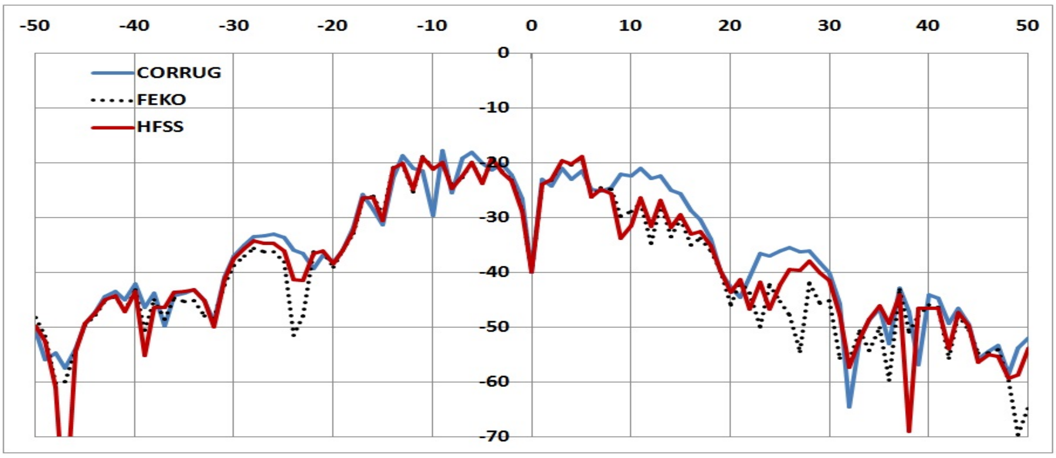

Figure 3.13: The calculated beam difference between the measured data and the calculated data from each model.

Commercial software package	FEKO	HFSS	CORRUG
Solution model	MOM	FEM	Mode-matching
Mesh type	triangular	tetrahedral	-
Mesh size	$\lambda/8$	$\lambda/8$	-
Runtime	21 hours	121 hours	seconds
Memory requirements	148 GB	180 GB	-

Table 3.2: The simulation requirements of the three different codes are listed in the table. A computer with standard qualifications was used to run all model simulations.

3.8 Conclusion

This chapter presented the main software packages and their supplemented optical codes.

As well as full wave modellers (e.g. MOM and MLFMM), approximate models (e.g. PO and GO) were introduced in Sections 3.2, 3.3, and 3.4. These software packages were used to model the quasi-optical components that I used for my research. In particular, capabilities and limitations of the MOM/MLFMM model were discussed in order to model horn-lens systems. The GO hybridization, also called Ray Launching Geometrical Optics (RLGO), with the MOM within the FEKO is recommended for the simulations of dielectric lenses because it can be a very time efficient model to simulate EM behaviour of large scale dielectric antennas. In addition to RLGO, I have decided to model dielectric lenses with MOM and MLFMM models, which are based on the surface equivalent principle (SEP). MOM is the main code that I selected for analysis of the dielectric EM problems in this thesis.

Additionally, three options (SWE, RAD and AP) for equivalent source data were introduced in Section 3.6. It was found that all models overlap very well with the full-wave model of the corrugated feed-horn antenna. Only the AP fed model differed slightly from the overall behaviour outside of the main beam lobe region.

Furthermore, the W band corrugated feed-horn antenna was modelled with three different methods (the mode-matching, the MOM and the FEM) and then the simulation results were compared with measured data in Section 3.7.1. Model comparisons with measured feed data showed a maximum beam difference of -20 dB. The mode-matching model was found to be very time efficient method with only runtime of seconds. However, mode-matching model is limited because it does not take into account ohmic losses due to material conductivity. The software package CORRUG, which employs mode-matching model, can only simulate circularly symmetric feed horns.

Figure 3.14 gives an overall picture of numerical electromagnetic tools used throughout this thesis to model the quasi-optical devices. In this chart, the best suited model for the specific EM problem analyzed in this thesis is boxed in red. For example, the PO modelling was employed for reflective-based components such as CATR system while the MOM modelling was preferred for simulations of dielectric lenses.

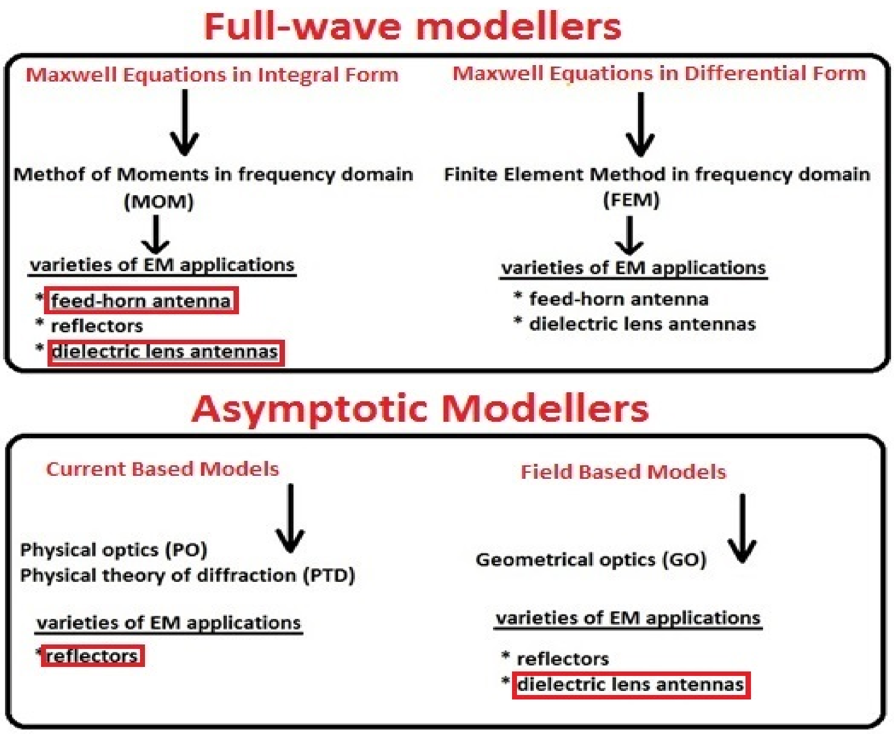

Figure 3.14: The chart explains the calculation method of each model discussed in this chapter. MOM model solves the Maxwell equations in integral form while FEM makes this in differential form. Both are called full-wave modelers because they do not make any approximation when solving the Maxwell equations. Asymptotic modellers (approximate models) can be grouped with two approaches: current based models and field based models. For example, PO modelling uses electric and magnetic currents to calculate scattering fields.

Chapter 4

DESIGN AND CONSTRUCTION OF A FREE-SPACE TEST BENCH

4.1 Introduction

This chapter describes the design, construction and implementation processes of a mirror based quasi-optical free-space S-parameter measurement system operating in the Ka (26.5-40 GHz) and W (75-110 GHz) bands. This project was started as the first step of my PhD research in 2010. Since then, the design, modelling and manufacture have been completed. From October 2012, the project involved two MPhys students, Matthew Robinson and Stephen Legg, helping in the implementation, alignment and characterization of the components. Different measurement systems are reviewed in Section 4.1.1. The description of the test bench and its simulation details are presented in Section 4.2. This research also covers the experimental characterization of the mirror based quasi-optical free-space S parameters measurement system presented in Section 4.9. Finally, the dynamic range of the free-space measurement set-up is determined by the calibration discussed in Section 4.10.

There are two main reasons for developing this test bench. The first is to accurately verify the RF and the optical properties of the quasi-optical components such as interference filters, wave plates or polarisers that are being developed at Jodrell Bank Centre For Astrophysics (JBCA), when located in a collimated beam. These components will be used in instruments dedicated to the study of the Cosmic Microwave Background (CMB) and its polarisation. For instance, dielectric lenses and dewar windows for cyrogenic systems might be used in the next generation of CMB polarization experiments. The second aim is to characterize dielectric materials that will be used to fabricate the quasi-optical components. The reflection and the transmission properties of the components/materials will be measured in order to extract the S parameters. The S parameters are then used to determine the optical properties of the dielectric materials such as loss tangent (δ) and dielectric permittivity (ε). Ultra high molecular weight polyethylene (UHMWPE), High density polyethylene (HDPE), teflon and silicon are the best candidate materials to produce quasi-optical components and millimetre lenses. In order to obtain high accuracy modelling of these components, material properties such as the refractive index and the loss tangent need to be known to four decimal places (see the discussion in Section 5.5). Such parameters could be experimentally characterised, for instance, through the use of free-space S-parameters systems [104].

In order to disentangle systematic effects that might be due to a non-collimated beam (for example testing components between the feed-horns located on an emitter and a receiver), we need to test these components in a collimated beam. Here, an electromagnetic field with very low variations in intensity and phase resembles a quasi-plane wave. For this reason, the test setup was designed to create a test zone, also known as a quiet zone. Throughout the thesis ”test zone”, will also refer to quiet zone (Q.Z.). The Q.Z. is described as an ideal region where the quasi-optical components and the dielectric materials are measured. The general characteristics and performance requirements of the measurement system that we would like to have are given below.

- A Q.Z. dimension of 10x10x20 cm will be generated.

The aim is to generate a beam propagating with a beam-width radius of a maximum 5 cm. This is possible with the quiet zone dimensions indicated above. The beam-size can be reduced with the help of microwave absorbers by defining a circular aperture if needed. The determination of the test zone is explained in Section 4.2.2

- The operating frequency band of the test setup will be optimized for W band (75-110 GHz).

The test bench operates at the wavelengths of the Ka and W bands. While the CMB signals are best probed in the frequency range from 30 to 300 GHz, the frequency range around 100 GHz is the cleanest channel to study the CMB. Therefore, the test bench is optimised for the W band. The Ka band measurements are performed to realise the studies of the polarisation of foregrounds for which the signal is stronger comparatively to the CMB.

- Maximum cross-polarization (XP) should be lower than -40 dB within W-band and -30 dB for Ka-band.

Due to the performance requirements of CMB components, the measurement system should present a typical maximum XP lower than -40 dB [105].

- Intensity and phase variations in the Q.Z. should remain below a few dB and 20°, respectively.

This is important to produce a quasi-plane wave illumination of the components and the materials under test (CUT, MUT). In the literature, a commonly used requirement for the field variations in the Q.Z. is that amplitude variations are less than ± 0.5 dB and phase variations are less than $\pm 5°$ [106].

4.1.1 A review of measurement methods

Depending on the frequencies and materials of interest, several measurement methods exist to measure the dielectric properties of low-loss materials both in the time domain and the frequency domain with one or two ports [107]. In order to extract the parameters that define the optical properties of the material, different algorithms have been developed in the millimeter (mm) and sub-millimeter (sub-mm) ranges [108]. The measurement techniques can be grouped into three categories.

- Transmission-reflection line techniques.
- Resonant techniques.
- Free-space techniques.

The Transmission/Reflection line technique is also known as the waveguide method. A dielectric sample is used to fill a section of waveguide or coaxial line. In the Ka band, several low-lossy dielectric materials have been studied thanks to this method [109]. As the operating frequency increases, the characterisation methods employing the waveguide models become more difficult due to small dimensions of waveguide and hence difficulties of their fabrication. Also, air gap effects that might form inside the waveguide section can limit the measurement accuracy.

Resonant methods using cavities are limited to single frequency even though it is acknowledged to be the most accurate method of low-loss materials characterization.

	Free-space methods	**Transmission/Reflection line methods**
Sample choice	Large flat sample	Waveguide size sample
S parameters	S_{11} and S_{21}	S_{11} and S_{21}
Calibration	TRL, TRM, LRL	TOSM + Background measurement
Advantages	- Easy to prepare samples - Broadband characterization - Good in hostile environment - Plane wave illumination - Q.O. component characterization	- Suitable for high loss materials
Disadvantages	- Multiple reflections - Standing waves - Diffraction effects at the sample edge	- Hard to fabricate samples - Accuracy limited to air gap effect - Waveguide beam

Table 4.1: Two measurement methods in common use are compared in many aspects. Overall, measuring the quasi-optical (Q.O.) components and the dielectric materials under the illumination of the plane wave is the main advantage of the free-space test methods.

Table 4.1 compares two commonly used models in terms of their advantages and disadvantages. Several publications also compare different measurement techniques [110], [111] and [112]. Due to the advantages of wide-band frequency operation, contact-free sample location and available calibration techniques such as Through-Reflect-Line (TRL), Through-Reflect-Match (TRM) and Line-Reflect-Line(LRL) for high frequency applications, free-space method has been chosen among those measurement techniques.

In the simplest scenario of free-space measurements, components can be tested between two feed-horns [105]. We have been using such a measurement system in our RF labs to characterize quasi-optical components. However, the beam is non-collimated and hence the phase fronts of the field propagated to the test zone are not planar. As a result, such system presents phase variations in the plane of the components.

Moreover, free-space lens based compact test ranges are also used as collimating field devices. They transform the curved phase fronts of the feed source into planar phase fronts in order to generate a quasi-plane wave [113], [111]. For this purpose, a lens based free-space S-parameters measurements test bench operating in W band was designed. The optical system comprises two spherical curved lenses fed by the W band corrugated feed horn connected to a four-port Vector Network Analyser (VNA).

The lens based measurement setup developed is shown in Figure 4.1. Gaussian beam transformation method was used to model the lens based measurement setup.

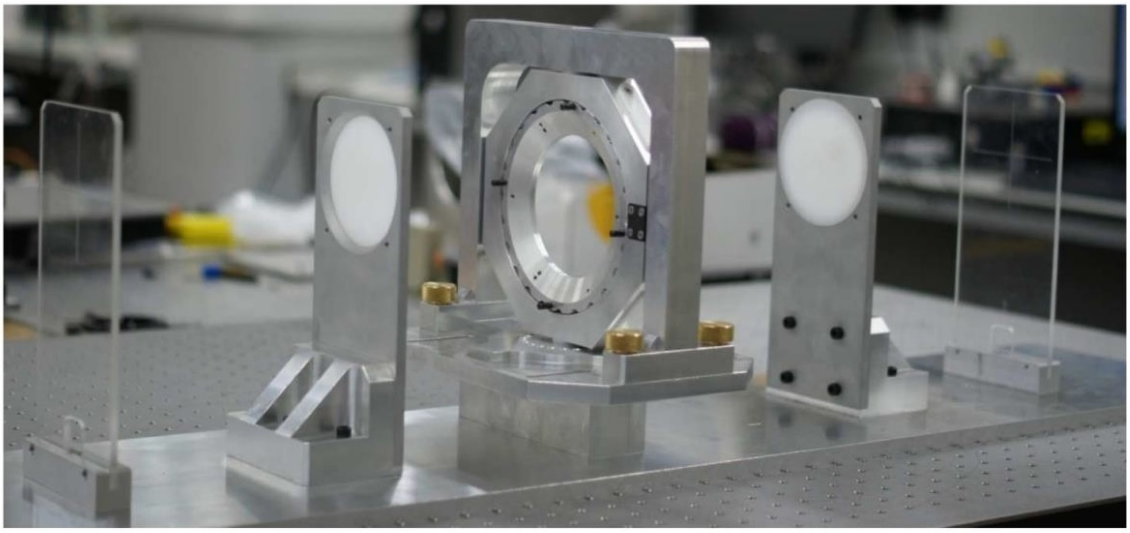

Figure 4.1: Free-space W-band lens based test setup. It comprises two spherical lenses, an alignment plastic and a sample holder in between on a dedicated linear platform. The aperture of the feed antenna connected to the VNA head, not shown in the image, is placed flash against the plastic alignment device, and centered on the cross hair on the plastic.

The lens based setup is not free from problems such as chromatic aberrations and XP. Chromatic aberrations limit the operation bandwidth of the setup. In order to compensate for these problems, an alternative design, a Compact Antenna Test Range (CATR), based on mirrors was developed by the author and manufactured in the workshop facilities of Manchester University. This system allows the characterization of materials, and testing of components under the illumination of a collimated beam with a very low XP. This is not possible with the other measurement techniques mentioned above, apart from a mirror based free-space measurement system.

4.2 Description of the CATR

The mirror based measurement setup discussed in this chapter is inspired by a compact antenna test range (CATR) that has been used for two decade to test electrically large aperture antenas [114], [115]. Single parabolic [117], dual and triple reflector CATRs [116] are the most common. Further test ranges also exist in literature [118]. CATRs

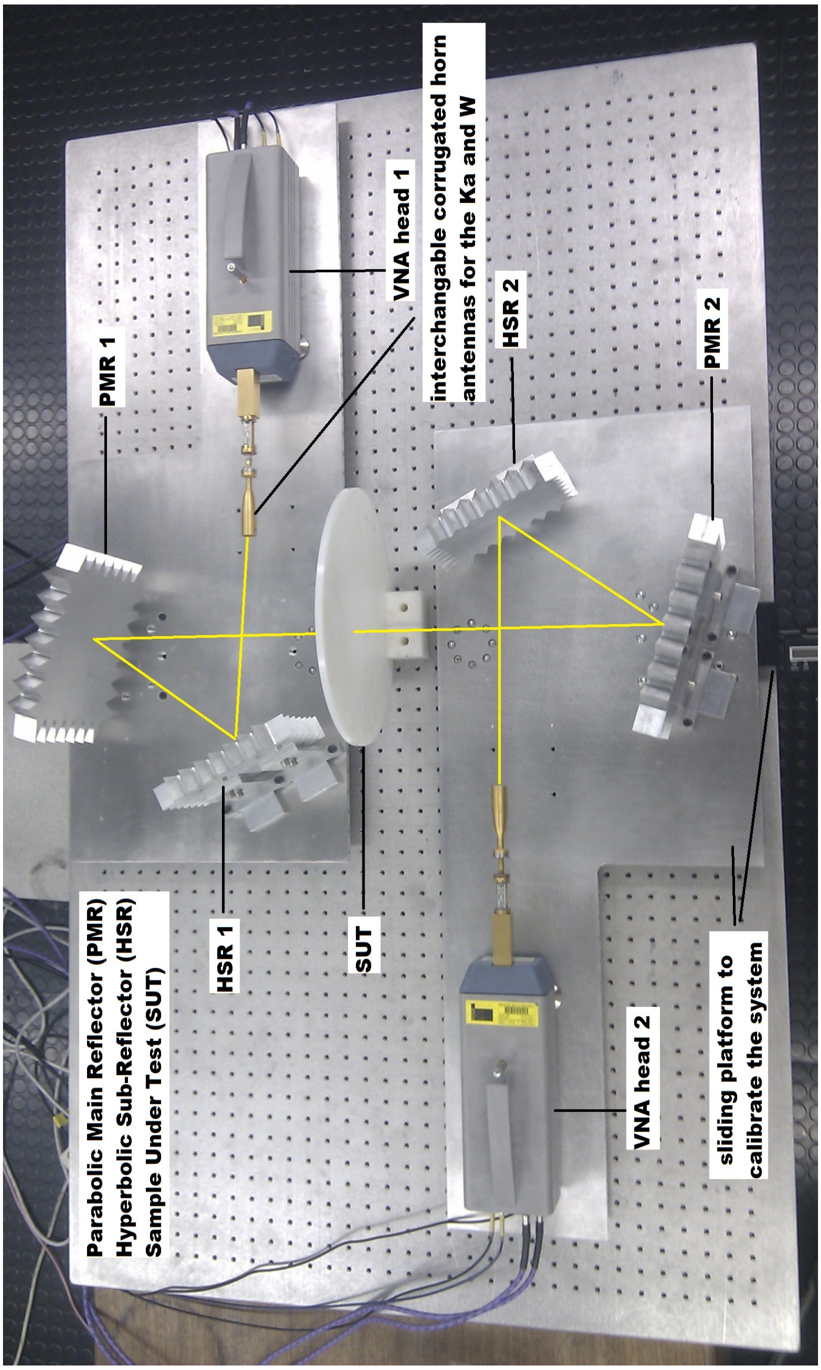

Figure 4.2: The test bench comprising the VNA heads connected to the feed horns are placed on an optical table. Standard feed horns illuminate the mirror systems and create a Q.Z. in between the two CATRs. The abbreviations are explained in the text box provided on the image. A circular-shape dielectric slab is located in the Q.Z. The yellow line shows the light path of the generated beam.

can also be used to develop an experimental test bench as it is in our case. Dual reflector configurations are often preferred due to their effective quite zone region and low cross-polarization (XP) in comparison to single mirror configurations.

The measurement system has two identical CATR system as shown in Figure 4.2. Each of the CATR antenna system comprises two reflectors, a parabolic reflector of 20 cm aperture diameter (60λ for W-band) and a hyperbolic sub-reflector of 17 cm (50λ). These create a quiet zone region of about 10x10x20 cm to test our quasi-optical components. The Q.Z. occupies the region between 20 cm and 40 cm away from the main reflector making a compact system with low XP and low aberration. The sample holder can be located within this range, half way between the parabolic reflectors. The determination of the test region dimensions is discussed in Section 4.2.2.

Figure 4.2 shows the main parts of the free-space quasi-optical bench: the mirrors, the VNA heads with their feed-horns and the optical table. The VNA (Rohde&Schwarz ZVA40 with 75- 110 GHz extensions) has two ports supporting interchangeable corrugated horn antennas (Standard feed horns) for the W-band. For the Ka band applications, another VNA configuration is used.

In order to meet the requirements set for the test bench, the intensity and phase variations in the quiet zone should be reduced as much as possible considering the small size of the system. The phase and intensity ripples of the Q.Z. are dependent on the performances of the feed pattern and diffraction effects. Therefore, reflector edge treatments (serration application) and edge taper analysis were required (Sections of 4.3 and 4.4).

In order to increase the performance of the CATR system, the set-up area is surrounded by absorbers to eliminate direct and multiple reflections through the measurement path. The samples should have a diameter at least twice as large than the quiet zone beam diameter. This will minimise possible diffraction effects that may arise from the edges of the components and materials under test. Depending on the type of tests, the beam size may be reduced, if needed, to compensate for potential higher aberrations such as edge diffractions.

4.2.1 Modelling of the test bench

The basic design parameters, used to define the geometry of the CATR system are listed in Table 4.2. The Mizuguchi-Dragon condition [56] optimizes the tilt angles α and β.

Primary mirror focal length	800 mm
Primary mirror diameter	200 mm
Eccentricity (e) of the hyperbolic mirror	-2
Foci distance	1100 mm
α	65°

Table 4.2: The basic parameters used to define the optical configuration of the CATR. These parameters are indicated in Figure 4.3. e is the eccentricity of the sub-reflector.

$$tan\left(\frac{\alpha}{2}\right) = \frac{e+1}{e-1} \cdot tan\left(\frac{\beta}{2}\right) \tag{4.1}$$

where α is the angle between the rotational axis of the parabola and the rotational axis of the hyperbola and β is the angle between the rotational axis of the hyperbola and rotational axis of the feed horn. e is the eccentricity of the sub-reflector. This condition helps to minimize the XP effects due to the off-axis configuration of the CATR mirrors by arranging the optical configuration according to the condition given in the equation. The optical configuration of the dual-mirror CATR system is illustrated in Figure 4.3.

The intensity and phase variations in the Q.Z were predicted from Physical Optics (PO) and Physical optics Theory of Diffraction (PTD) modelling of the CATR system. PO and PTD methods were employed by using the commercial software package GRASP9. Field calculations in PO modelling are performed in two steps: predicting the equivalent currents induced on the reflector surface due to the radiating field element and using these currents to calculate near fields at any point inside the Q.Z. More detailed theoretical analyses of PO modelling is covered in Section 3.2.1.

The gaussian feed definition was used as the source input of the CATR system. The only parameter of the gaussian feed defined in the simulation was the edge taper. The edge taper of the gaussian beam was set as 12 dB at $\pm 15°$ by default. The optimum operation frequency was selected as 97 GHz. For further investigation, more feed options such as tabulated feed source and real data implementation were also defined and discussed in Section 4.6.2.

4.2.2 Determination of the Q.Z.

The ideal Q.Z. volume is to have dimensions of 10x10x20 cm. Figure 4.4 illustrates the test volume generated by two dual reflector systems.

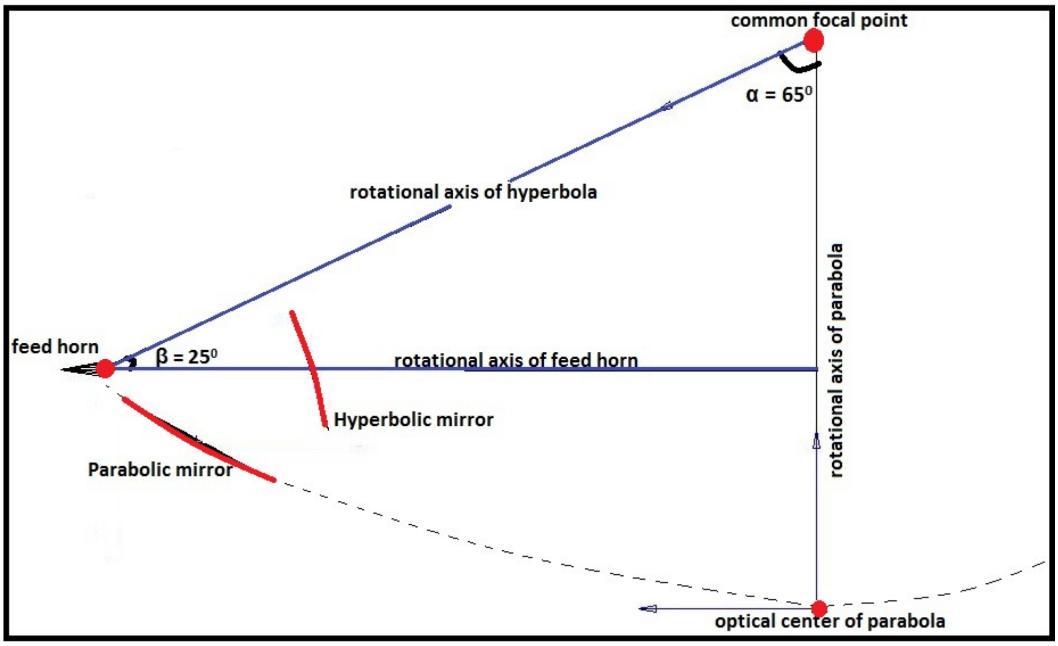

Figure 4.3: The geometrical parameters of the CATR system are shown in the figure. The red indicators are for the mirrors while the blue lines are for the rotational axes of the hyperbolic mirror and the feed horn. Two red dotes show the focal points of the system. The feed horn is located at the first focal point. The second is the common focal point of both reflectors.

The Q.Z. region was scanned to predict the field components starting from the aperture of the main reflector up to 500 mm away. The intensity and phase performances of the test setup in the Q.Z. are indicated on Figure 4.5. This gives the calculated maximum variations in the intensity and phase results calculated for a given distance along the Z-axis. In order to determine the Q.Z. volume generated by the CATR system, a first model assumed an edge taper of a Gaussian feed of 12 dB. The mirrors did not have serrated edges in this basic model. The calculations were conducted for the central frequency of the W-band, 97 GHz. A 2D beam cut of the near field revealed a plane wave. Intensity and phase variations were calculated along the vertical and horizontal planes across the diagonal axis of the Q.Z.. In the calculations, the scattered field from the main reflector is evaluated. If a more accurate analysis is needed, the field contributions to the near field pattern from the feed and the sub-reflector can also be included.

As a result of this analysis, the test zone was selected to occupy the region between 200 and 400 mm away from the main reflector. The optimum distance which gives the

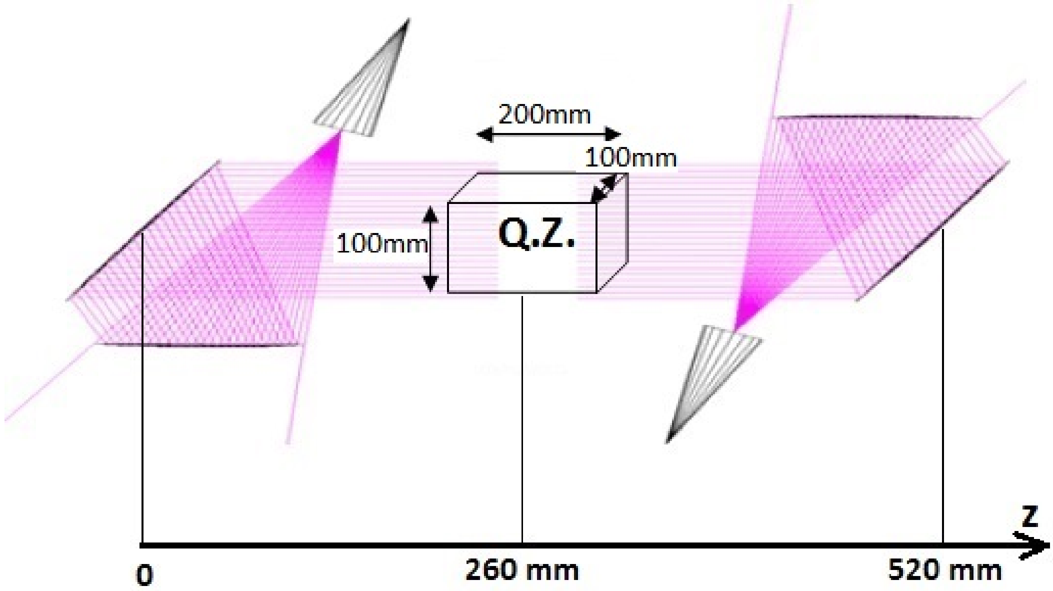

Figure 4.4: The volume of test zone has the dimensions of 10x10x20cm. The generated plane waves by the dual reflector system are collimated in this region which is also known as quiet zone. For the best performance, the CUT/MUT should be located at the predicted position where is 260 mm away from the center of the main reflector.

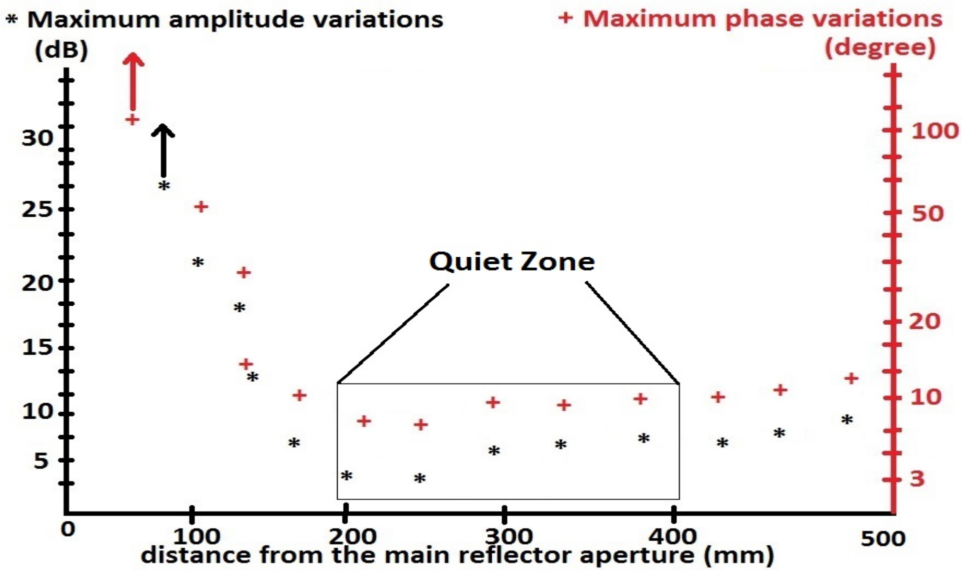

Figure 4.5: The minimum variations for the intensity and phase are calculated at different distances between 200 mm and 500 mm away from the aperture of the main parabolic mirror. The best field performance is presented in the region limited by the square.

lowest intensity and phase variations was found to be 260 mm. Hence, the distance between the center of two main parabolic mirrors was calculated to be 520 mm.

4.3 The serration application

There are two important parameters that have a direct impact on the field diffraction generated in the Q.Z. First, an incident field illuminating a reflector can be generated with an amplitude pattern that falls off suddenly at the edges of the reflector. However, this kind of feed pattern is not easy to model for a wide range of frequencies. The discussion on feed definition with different edge taper values is made in Section 4.4. The second effect comes from the reflector edges. Diffraction can be controlled by modifying the edge of the reflector. A couple of edge treatments may be applied to improve the specifications of the Q.Z.. Several edge treatments exist in the literature [119], [120]. The most popular applications are rolled and serrated edge treatments [119], [121]. These reference publications show the superiority of serrated edges to rolled edges in terms of the manufacturing processes.

Serration is an edge treatment that minimizes the effects of edge diffraction, which can generate distorted fields inside the test zone. By applying the serrations around the reflector edge, the edge fields are scattered away from the Q.Z. region. Therefore, it mitigates the edge impact on the Q.Z. field and also helps to improve the plane wave qualifications in the Q.Z. specified in Section 4.1.

4.3.1 Modelling of the mirror serrations

In this approach, the PO surface currents, which have been calculated for an un-serrated edge reflector model are modified for a serrated edge reflector model. The current distribution is reduced starting from base of the serration. A weight factor, which varies between 0 and 1, is used to multiply by the currents. The weighting factor is 1 for the region inside the inner rim and gradually goes down to 0 for the region between the inner rim and the outer rim where the serration is applied. Of all alternatives for the geometry of the serration edge shapes [122], a linear-triangular serration design has been chosen due to its manufacturing simplicity. For the linear-triangular serration, the variation in the weighting factor is linear as illustrated in Figure 4.6. The model employed does not take into consideration the number of serrations. For this reason, we only provided the side lengths of the inner rim square used to define the

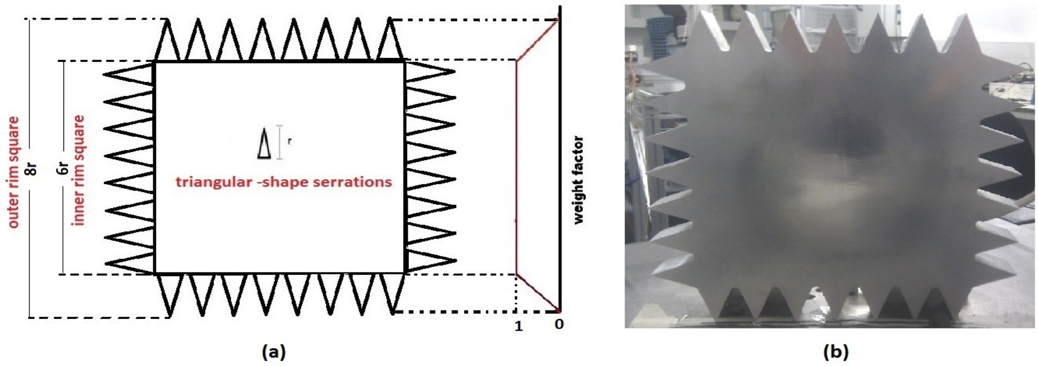

Figure 4.6: The illustration of the serrated mirror geometry. a) Figure shows the dimensions of the inner and outer rim squares. How the weighting factor varies for the region inside the inner rim and the outer rim is also shown. A single triangle-shape serration element is given in the middle of the figure. The ratio of the inner square edge length (6r) to the outer square edge length (8r) is decided as 0.75. b) Right image shows the hyperbolic mirror with its serrated edges manufactured in the school workshop. Both mirror equations are derived in Appendix B.

serration edge. The ratio of the inner square (6r) to the outer square (8r) is calculated as 0.75 as shown in Figure 4.6. The real image of the serrated edge hyperbolic mirror fabricated in the school workshop is also shown in the same Figure 4.6.

Four model cases have been compared: no serration, sub-reflector serrated only, main reflector serrated only and both reflectors serrated. The PTD model can not be employed with the serrated mirrors because the edge geometry is re-structured due to serrations. For this reason, PO analysis is the only model to take account for currents on serrated-edge mirrors. The results can be assessed in terms of maximum XP level and intensity/phase variations calculated in the Q.Z. region for each model. Figure 4.7 shows the co-polarization (CP) and cross-polarization (XP) beam patterns calculated in the Q.Z., at 26 cm away from the center of the main reflector. Figure 4.8 shows how the phase and intensity patterns are modified with a different serration choice. While there was no significant difference between the intensity and phase variations calculated from the models that have at least one mirror serration, the XP level with -50 dB was much lower when both mirrors were serrated. Fluctuations, in particular in the phase pattern, were reduced by 7° through use of the serrations on the sub-reflector and both reflector models. Overall performance results obtained from the different models of the CATR system in terms of the maximum intensity/phase variations and XP are given in Table 4.3.

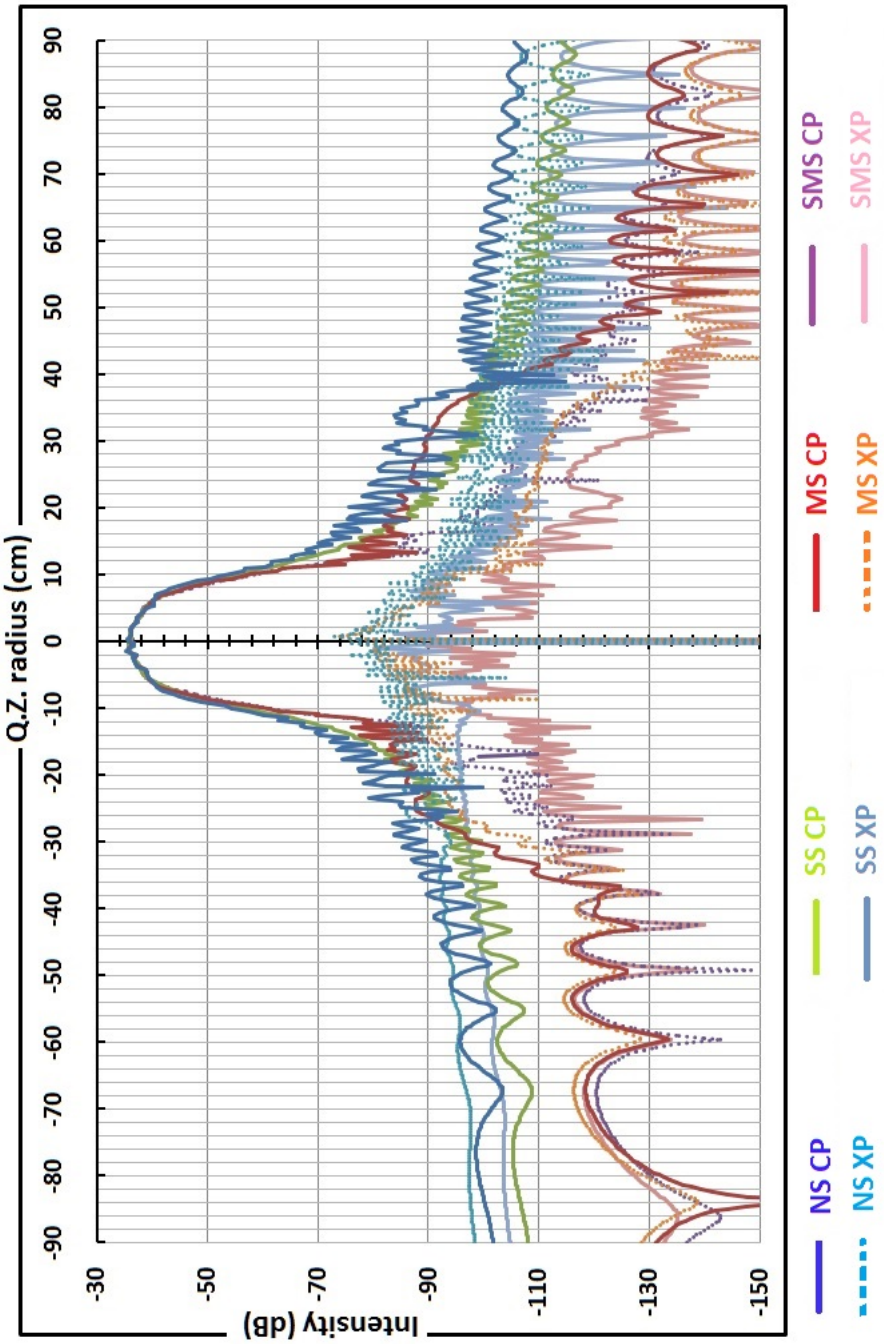

Figure 4.7: Serration application results for the W band. The CP and XP beam patterns were calculated for four model cases: no-serration (NS), sub-reflector serrated only (SS), main-reflector serrated only (MS) and both reflectors serrated (SMS). The calculations were done for a frequency of 97 GHz at the plane cut of ϕ=45 to predict the co- and cross-polarization beam patterns of the CATR system. The near field distance was selected as 26 cm away from the center of the main mirror.

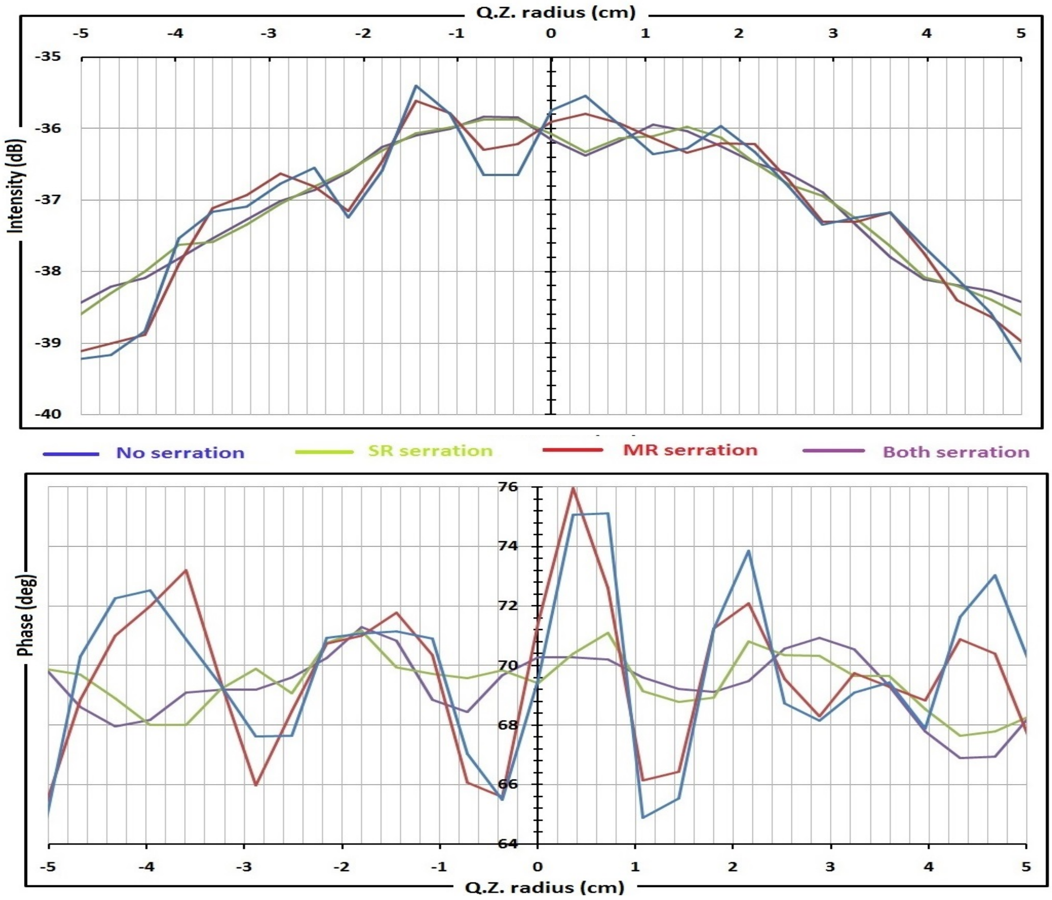

Figure 4.8: Serration application comparison results for the W band. Top: Intensity variation vs quiet zone radius. This is a close up view of the same graph than Figure 4.7 Bottom: Phase variation vs quiet zone radius. In particular, phase variations were reduced considerably by the models which have sub-reflector and both reflectors serrated.

The performance of the test bench was also modelled for 30 GHz, the central frequency of the Ka band. Two model cases have been compared: no serration and both mirrors serration. Figure 4.9 shows the CP and XP beam patterns calculated in near field, at 26 cm away from the center of the main reflector. Figure 4.10 shows how the phase and intensity patterns are modified due to different serration operations. Application of the serrations did not decrease the intensity ripples. On the contrary, the phase variations were increased due to the serrations. The reason is that the inner rim size of the main aperture becomes small compared to the operating wavelengths of the Ka band frequencies. The variations in the intensity and the phase remained within 3 dB and 15° respectively. The maximum XP of the setup for the Ka band is -33 dB.

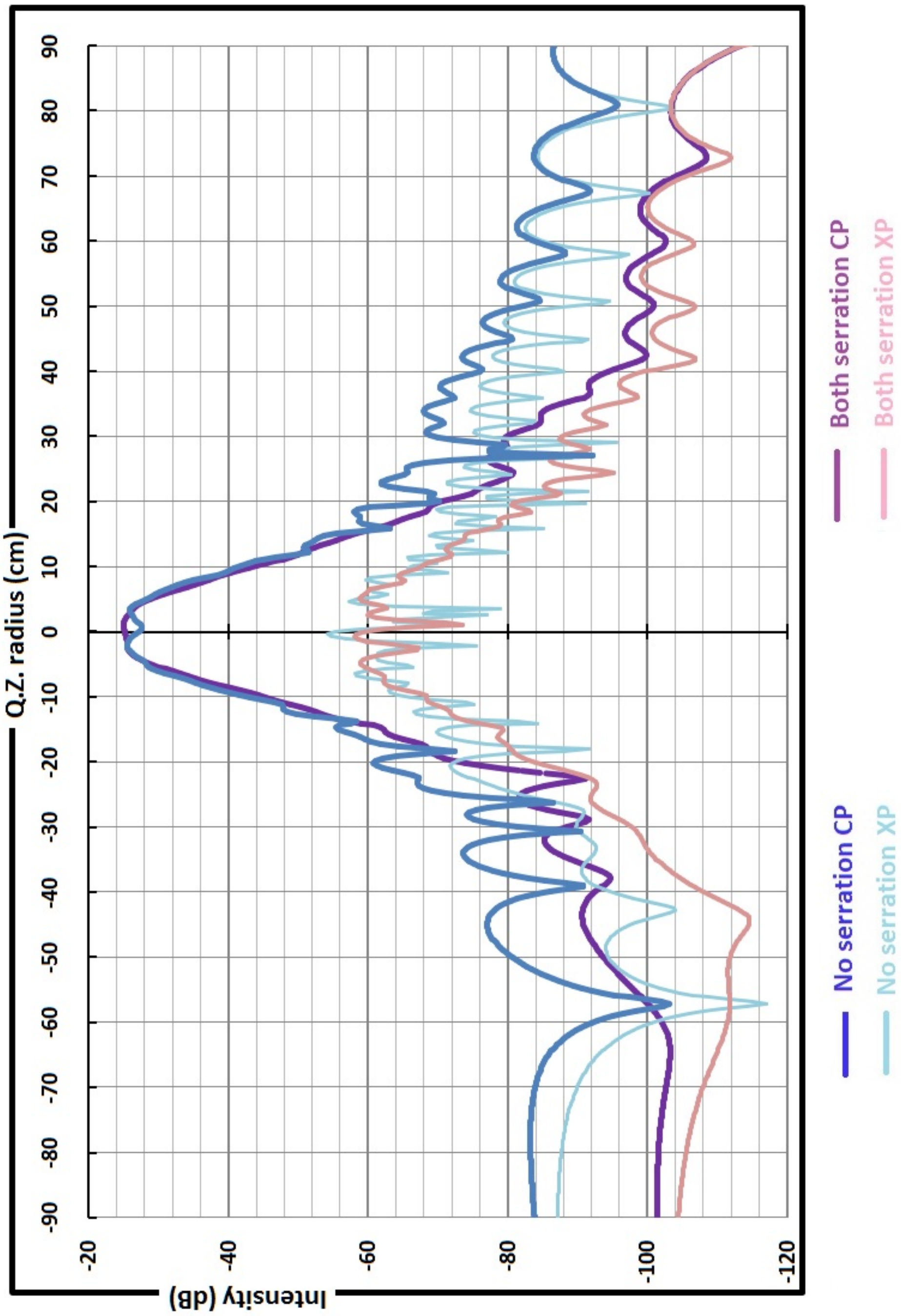

Figure 4.9: Serration application results for the Ka band. The CP and XP beam patterns were calculated for two cases: No serration and both reflectors serrated (Both serration). The calculations were done for a frequency of 30 GHz at the plane cut of ϕ=45 to predict the maximum XP level of the system. The near field distance is selected as 26 cm away from the center of the main mirror.

plane cuts	**NS**(P/A)	**MS** (P/A)	**SS** (P/A)	**SMS** (P/A)
ϕ = 0	9°/3 dB	7°/2.5 dB	2°/2.5 dB	2°/2 dB
ϕ = 45	10°/4 dB	8°/3.5 dB	3°/3 dB	3°/2.5 dB
ϕ = 90	9°/3 dB	7°/2.5 dB	2°/2.5 dB	2°/2 dB
Max. XP at ϕ = 45	-37 dB	-38 dB	-45 dB	-50 dB

Table 4.3: Phase and intensity variations calculated for the different serration models. NS, SS, MS nad SMS are for no-serration, sub-reflector serrated only, main-reflector serrated only and both reflectors serrated. P/A stands for variation values in phase and intensity. The calculations were conducted at three plane cuts for a frequency of 97 GHz.

4.4 Edge taper (ET) analysis

Inherently, both spillover and illumination losses arise from the reflector illumination from the feeds. The spillover is the amount of power from the feed beam falling outside of the reflector edge, and the illumination loss is due to an under-illumination from the feeds. The edge taper can be defined as the ratio of the power at the center of the reflector to the power at the edge of the reflector. While a low edge taper (below -16 dB) might lead to under-illumination, a higher edge tapered illumination of the reflectors results in a higher spill-over as described in Figure 4.11. A trade-off has to be reached through an optimum value for the edge taper. Therefore, an edge taper analysis was carried out.

A direct impact of the ET on the intensity and phase variations was observed in the Q.Z.. During the simulations, four different edge taper values starting from -2 dB to -16 dB have been chosen for comparison. When the ET value was decreased from -2 dB to -16 dB, the intensity variations increased from 1 dB to 3 dB in the W band and 2 dB to 4 dB in the Ka band. On the contrary, the phase fluctuations were improved by 6°, degree from 8° degree to 2° degree in the W band. In the Ka band, the phase fluctuations were improved by 25° from 45° to 20°. There was no considerable change in the XP level with the ET change. The model results are shown in Figure 4.12 for W band and in Figure 4.13 for Ka band.

As a result of the edge taper analysis, the real CATR system should use a feed-horn antenna which has a -12 dB edge taper at $\pm 15°$ for the lowest intensity/phase variations.

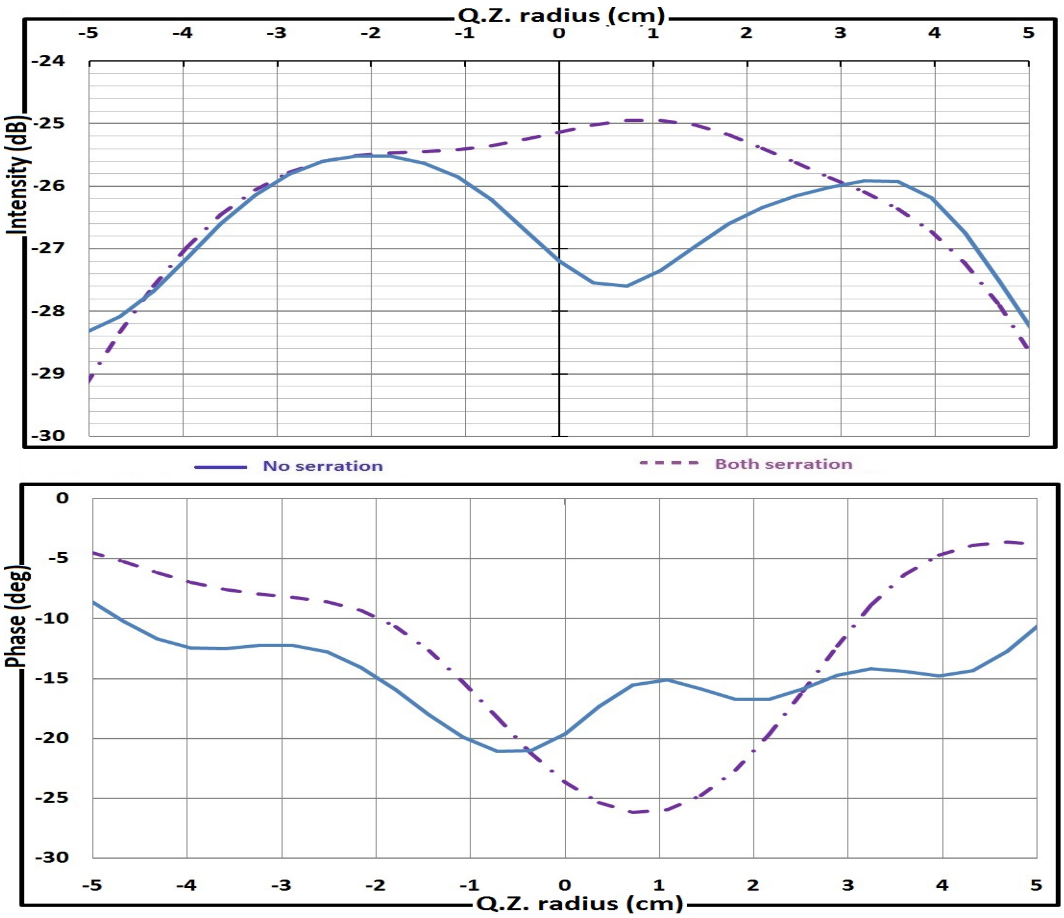

Figure 4.10: Serration application comparison results for the Ka band. Top: Intensity variation vs quiet zone radius. Bottom: Phase variation vs quiet zone radius. The serrations did not have much impact on the Q.Z. beam modifications.

4.5 Model analysis results for Gaussian beam feed

Analyses of the edge taper and the serration operation have been carried out for an optimum CATR design assuming a Gaussian beam with -12 dB edge taper at $\pm 15^{\circ}$ because this model provided a good trade-off between phase and intensity variations for the same ET value of -12 dB. In addition, it was decided that both mirrors would have serrated edges because this design presents the lowest XP level. The overall performance of the CATR system are listed in Table 4.4 for the W band and in Table 4.4 for the Ka band. Two different assumptions are considered for the Q.Z. dimensions: a minimum size of 10x10x20 cm and a larger dimension of 12x12x20 cm if a larger beam size were to be required.

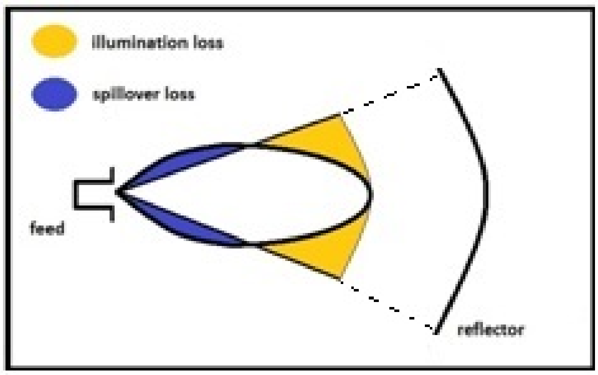

Figure 4.11: The illumination and spillover losses can be explained on an illustration of feed-reflector system illuminated by a low ET (-16 dB). Its opposite, a high ET (-2 dB), concludes more spillover loss.

Table 4.4: The Q.Z. intensity and phase performances for W band. Results are given for two quiet zones dimensions. The calculated values for each parameter are almost identical for each plane cut. A gaussian beam feed with an edge taper of -12 dB at $\pm 15°$ is used to illuminate the sub-reflector of the CATR system. All mirrors of the CATR system have serrated edges.

The Q.Z. region	(10x10x20)cm	(12x12x20)cm
Intensity variations	2 dB	3 dB
Phase variations	2°	5°
Cross-polarization	$\leq$-50 dB	$\leq$-50 dB

4.6 Model modifications of the CATR

Modifications to the CATR model were made to simulate a more realistic system. The first attempt was investigating misalignments of the CATR system components such as mirrors and feed. Secondly, a real feed input was used to obtain higher accurate models.

4.6.1 Misalignment tolerance

An investigation was made in order to determine the sensitivity of the components to misalignment. The effects of the misalignments on the predicted field components such as intensity, phase and XP, in the Q.Z., must be well understood when the system

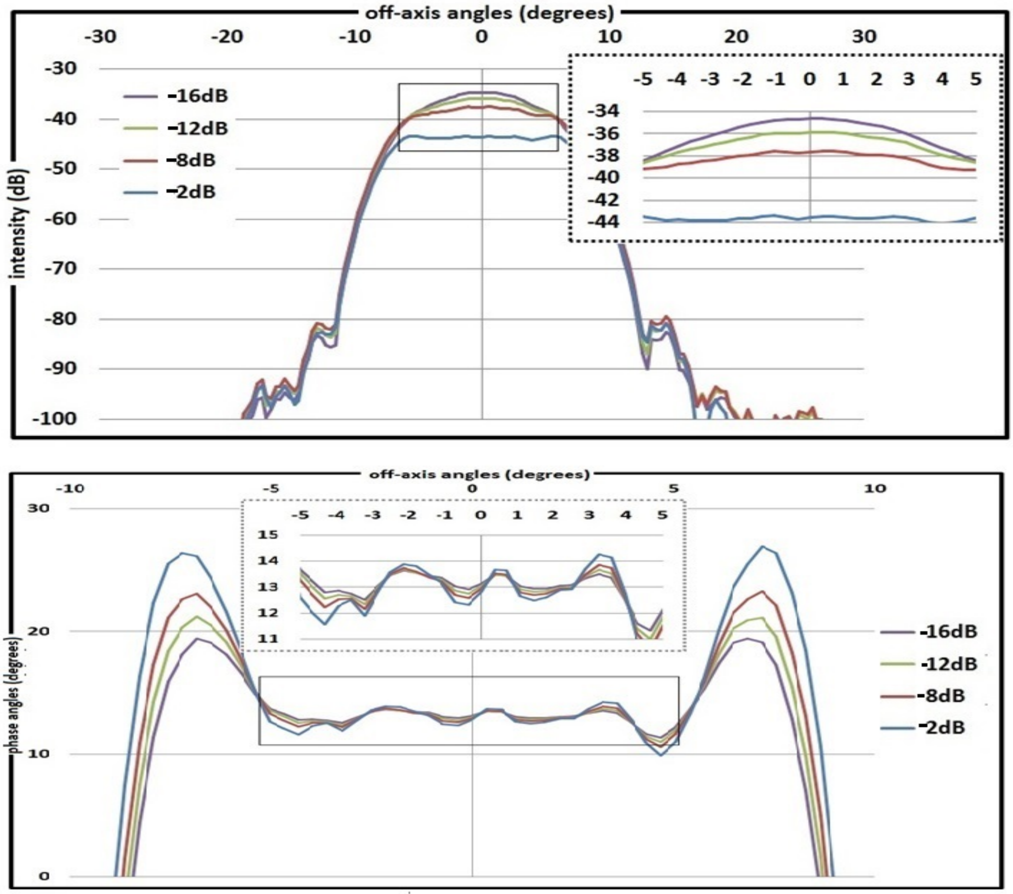

Figure 4.12: Edge taper analysis comparison results for W band. ET varied between -2 dB and -16 dB. Top: Intensity variation vs quiet zone radius. Bottom: Phase variation vs quiet zone radius. The calculations were done for a frequency of 97 GHz for the D plane cut.

components are displaced from their original positions. This investigation puts limits on the CATR alignment accuracy. Each component (feed, sub-reflector and main-reflector) is individually displaced from their original positions to produce a field that still satisfies the Q.Z requirements given in Section 4.1. Displacements up to 3 mm were realized along the X-axis and Z-axis. The coordinate systems for each component displacement are shown in Figure 4.20. Then, variations of the field components in the Q.Z., where the CUT/MUT is placed, were calculated. The simulation results obtained for the displacements across X-axis were almost symmetric to those across Y-axis. The variations of three parameters were investigated: intensity, phase and XP level. Of the three parameters, only the phase was highly sensitive to the component

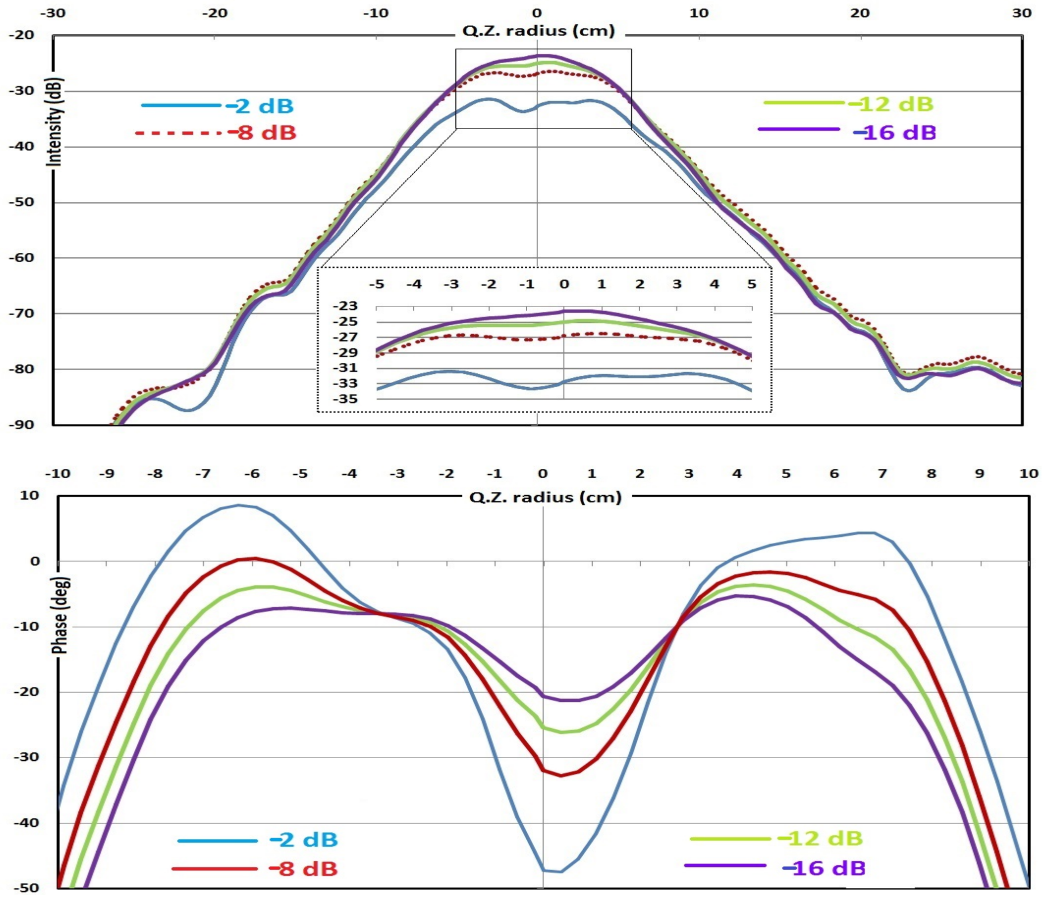

Figure 4.13: Edge taper analysis comparison results for Ka band. ET varied between -2 dB and -16 dB. Top: Intensity variation. Bottom: Phase variation vs quiet zone radius. The calculations were done for a frequency of 97 GHz for the D plane cut.

displacements. Maximum phase shifts of 16°, 22° and 17° were observed by translating of feed, sub-reflector and main reflector separately along X-axis. Translation of the same components from their nominal positions along the Z-axis led to maximum phase shifts of 26°, 24° and 19° respectively. The intensity variations and the XP level for three plane cuts were almost insensitive to the displacements up to 5 mm along both axes. As a result of this analysis, the alignment of the CATR system is tolerant up to displacements of the values listed in Table 4.6.

4.6.2 Use of real feed

For the simplest case (simple CATR model), the CATR system was modelled by using a Gaussian feed beam pattern as the source input in GRASP. The system performance

Table 4.5: Quiet zone intensity and phase performances for Ka band. Results for 2 quiet zones dimensions. The calculated values for each parameter are almost identical for each plane cut. A gaussian beam feed with an edge taper of -12 dB at ±15° is used to illuminate the sub-reflector of the CATR system. All mirrors of the CATR system have serrated edges.

The Q.Z. region	(10x10x20)cm	(12x12x20)cm
Intensity variations	3 dB	15 dB
Phase variations	20°	40°
Cross-polarization	≤ -33 dB	≤ -33 dB

Table 4.6: The tolerance level of each component making up the test bench for displacements. The components are displaced from their original positions until the CATR system still satisfies the Q.Z requirements. Maximum intensity variations by displacements of each component are given in brackets. The calculations were performed for a frequency of 97 GHz at the D plane cut.

Coordinate axis	x	z
Feed	±0.5 mm (16°)	±1 mm (26°)
Sub-reflector	±2 mm (22°)	±2 mm (24°)
Main-reflector	±2 mm (17°)	±2 mm (19°)

for the simple model is summarised in Section 4.5. For more realistic feed definition, a tabulated feed input can be imported for the two CATR models. These models consider that all mirrors are serrated. In the first model, the spherical wave expansion (SWE) source data was used as the feed input. The SWE source input previously discussed in Section 3.6.1 was generated from the far-field calculations of the Standard feed horn by using a full wave modeller (MOM). The second model was using an experimentally measured data as the source input. The measured data was obtained from the far-field measurement of the same feed horn antenna. The measured data includes the CP field measurements taken for the three plane cuts (E, D and H) and XP measurement for the D plane cut. A tabulated feed input used in the GRASP models was generated by Ho-Ting Fung. Use of tabulated feed inputs increased maximum variations in the Q.Z. parameters as given in Table 4.7. The field behaviours of the CATR system predicted

Table 4.7: Quiet zone intensity and phase performances for W band. The calculations were performed in the D plane cut for 97 GHz. The increase of maximum intensity/phase variations and the cross-polarization signal level is listed for different CATR models defined with each feed definition.

The Q.Z. parameters	Gaussian feed	SWE tabulated feed	Measured tabulated feed
Intensity variations	2 dB	4 dB	4 dB
Phase variations	2^o	4.5^o	4.5^o
Cross-polarization	-50 dB	-39.5 dB	-39 dB

from both tabulated feed sources presented similar performances with 4 dB and 4.5° variations in intensity and phase respectively. The CATR system fed by the measured tabulated source input gave half dB higher XP with -39 dB than the first tabulated model. This XP value was also 11 dB higher than the simple CATR model using the Gaussian beam feed.

Finally, the beam contours showing the CP and XP beam patterns for W band frequencies are illustrated in Figure 4.14. A very low XP of -39 dB at maximum is achieved with this quasi-optical free-space S-parameters measurement system.

4.7 Alignment of the CATR system

Once the components of the CATRs have been manufactured, they had to be positioned and aligned on an optical bench. As shown in Figure 4.15, the components were clamped to linear base platforms with brackets, which were not secured to a fixed point on the platform.

Initially, with help of the autocad drawing for the CATR model generated from GRASP, a real scale of the models geometry was printed out and laid on the optical table to indicate to the positions of the setup components. The components were moved to the positions according to the print-out. However, this was not enough to obtain the desired sensitivity for the alignment. For this reason, two approaches were used for the alignment of the CATR system: the laser alignment and the use of the S parameters.

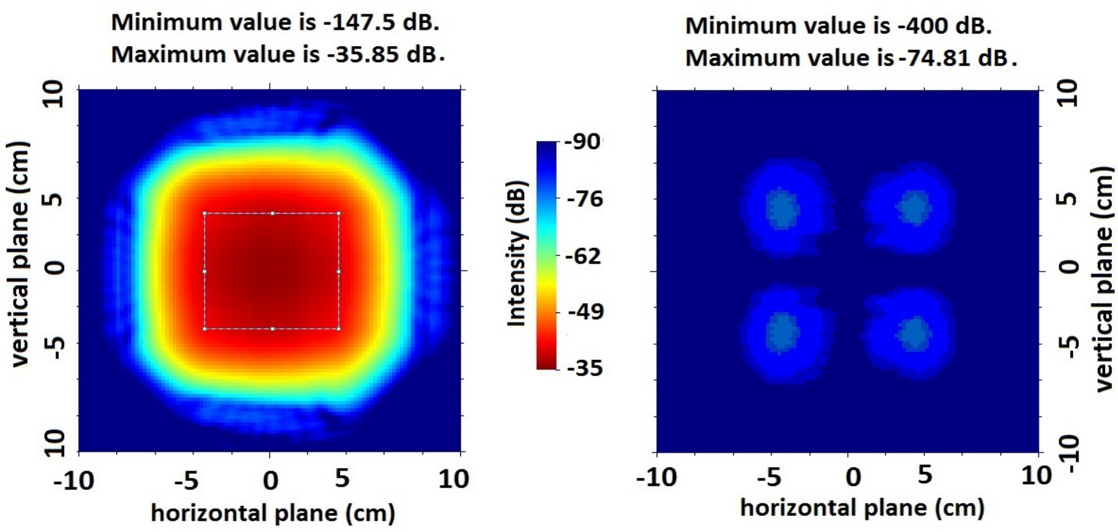

Figure 4.14: Left figure: the beam contour of the CP radiation beam pattern. Right: the beam contour of the XP radiation beam pattern. The square with dashed white lines indicate the extent of the quite zone beam field. The difference between the maximum value (-35.85 dB) of the CP field and the maximum value (-74.91 dB) of the XP field gives the maximum XP value ($\sim$ 39 dB) of the CATR system. The calculations were realized for 97 GHz at near field. The color scale shows the level of the non-normalized beam intensity.

4.7.1 Laser alignment

This alignment technique was attempted by the MPhys students. The CATR system was aligned previously by using a laser beam however the mirror surfaces were too dull to reflect the beam of the 0.95 mW helium-neon laser. The surfaces were polished by using 15 μm grains of Al_2O_3 in order to allow the laser beam to propagate beyond the first CATR system. The test bench was first aligned according to their printed positions from the AUTOCAD drawings. Port 1 was replaced with the laser setup as shown in Figure 4.16. By adjusting the angle of the sub-reflector (SR) axis with respect to the laser (the position of the feed horn), the beam was first directed to the center of the main-reflector(MR). A circular shaped target was placed at the center of the Q.Z.. By adjusting the angle of the MR axis with respect to the SR position, the reflected beam was targeted onto a circular-shape target which was specifically constructed and placed at the center of the Q.Z.. Thanks to the hole at the center of the target, the reflected laser beam generated by the first CATR system was transmitted into the center of the second main mirror which is a part of the second CATR system. This transmitted laser beam was overlapped with the second laser beam which was propagated by the second

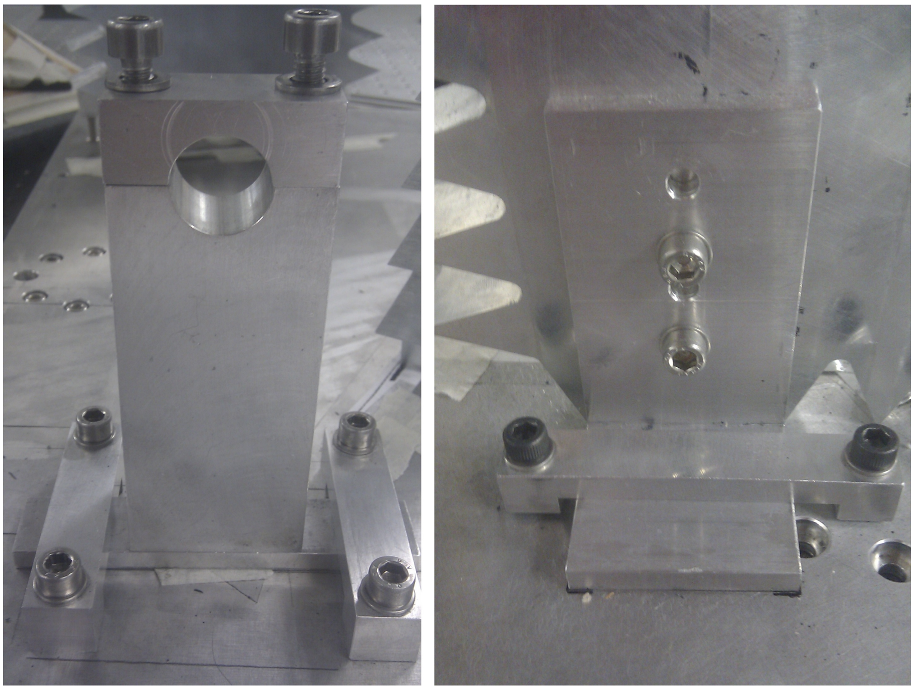

Figure 4.15: The left image shows the feed positioner with its leg brackets. The same clamp system for the mirror is shown in the right image.

laser located at the position of the second feed horn. This alignment was also checked with the mm-wave beam by using the S parameters of the VNA emitter in next section.

4.7.2 Use of S parameters

The analysis results for the misalignment tolerance of the CATR system components given in Table 4.6 showed that the most sensitive component to its location was the feed-horn antenna. The feed position was mostly corrected thanks to the laser technique. Additionally, I used the VNA beam to align the CATR system. The relative position of two mirrors according to each other was kept fixed in order to reduce the number of degrees of freedom in the CATR system. The return and transmission loss parameters, S_{11} and S_{21}, were used to align the test bench. First, the reflected power, S_{11}, was aimed to be maximized by using a reflector. This reflector was located at the sample location in the center of the Q.Z. as shown in the left image of the Figure 4.17. The S_{11} parameter was expected to be 0 dB by changing the feed position. The feed was translated along the X-axis and Z-axis where the coordinate system is defined in

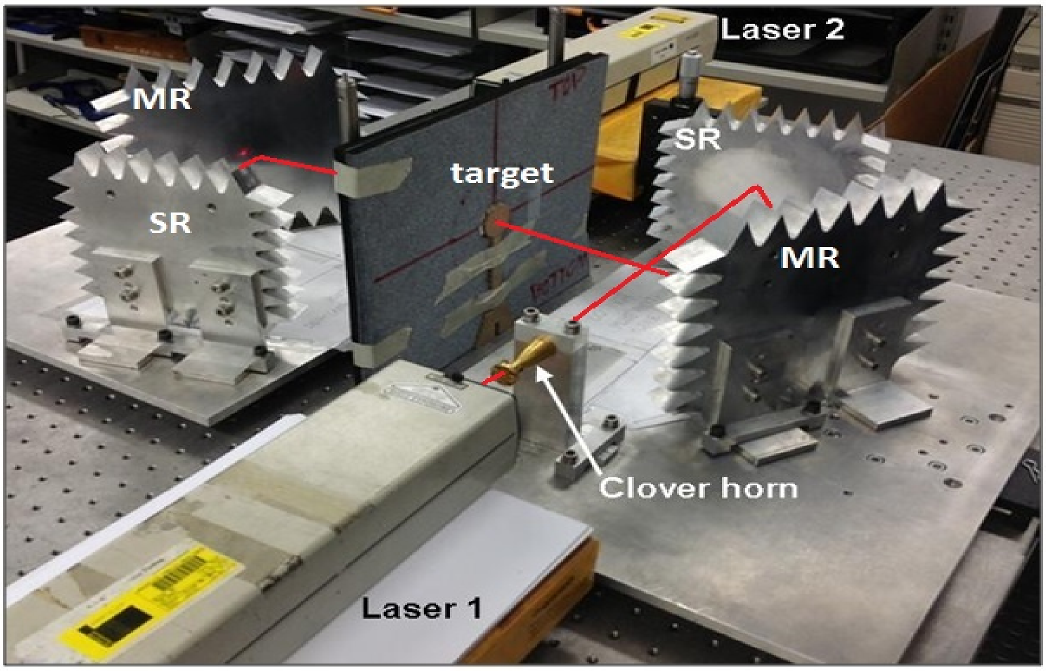

Figure 4.16: The image shows the CATR test bench. The VNA heads were removed and replaced with the lasers. The laser beam was dropped into the center of the target located at the center of the Q.Z.. Then, the laser beam was transmitted from the target hole into the center of the main reflector which is a part of the second CATR system.

Figure 4.17 until the maximum power was obtained by the feed. The feed was eventually secured to a position where the reflected power was maximized. In order to check that we focused the maximum reflected power back into the port 1, the amount of power which was transmitted from the port 1 and was received by the port 1 was compared. Ideally, the values of the transmitted (a_1) and received powers (b_1) should be equal for a lossless system. A power difference of 8.5 dB was observed between a_1 and b_1 as shown in Figure 4.18.

In order to understand where the majority of the power was lost, the aperture of the feed horn antenna was blocked with a circular shape of flat reflector as shown in the right image of Figure 4.17. The power difference between a_1 and b_1 was recorded as 7.5 dB this time. This was the loss between the aperture of the feed horn antenna and the VNA port 1. Compared to the power loss of -8.5 dB which was measured previously, the power difference was assigned as the loss due to the mirror surfaces and the misalignments in the optical configuration of the mirrors. In a similar way, the identical CATR system on the other linear platform was optimized.

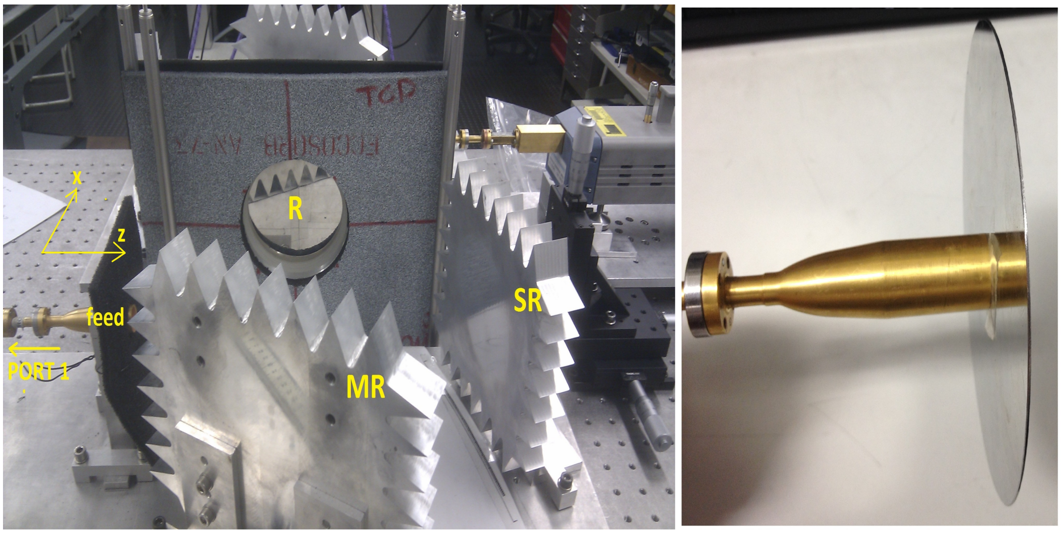

Figure 4.17: The left-image shows the first CATR system with the reflector surrounded with absorbers. The SR, MR, and R are for the sub-reflector, the main-reflector and the reflector. The reflector is located in position the center of the Q.Z. to maximize the reflected power detected by the port 1. The right-image shows that the Standard feed was faced to the small circular-shape reflector.

Once each CATR system was aligned with the use of the return loss maximizing method, the transmission loss parameter, S_{21}, was recorded that there was a loss of less than 1 dB between the two feed-horns.

4.8 Minimizing standing waves

Standing waves occur when radiation propagates in the forward and reverse direction along the same axis of propagation [123]. They are formed between a feed source element and any reflective components in an optical system. The reflections from the components of the system can increase the standing wave magnitude as a result of a superposition principal when the emitted and reflected waves meet at some points throughout beam path. Many publications have been addressed to the problem of the standing waves with different theoretical approaches [124] and their experimental verifications [125].

Figure 4.18: The figure shows the difference between the transmitted (a_1) and the received powers (b_1) by the port 1 as a function of the W band frequencies. The plots of the a_1 and b_1 are shown with the orange line and the red line respectively. The minimum power difference with 8.5 dB was obtained when the mirrors were positioned at the optimum location.

When standing waves show up between the system components, such as the mirrors and the feed horn antennas, fake signals dominate real signal and hence the performance of the quasi-optical system becomes limited. In the RF laboratory, different mm-wave absorbers were used to reduce the possible reflections which caused the standing waves. An investigation was conducted by the MPhys students and concluded that use of thin black absorber (ECCOSORB-HR) surrounding the feed presented best reduction of standing waves [126]. The effect of standing waves present in the S_{12} was characterized and the results were plotted in Figure 4.19. The feed mount surrounded by the thin flat absorber resulted in ~ 2 dB decrease of the standing wave. Eventually, the components were covered by absorbers during the beam scanning of the Q.Z. field as shown in Figure 4.20.

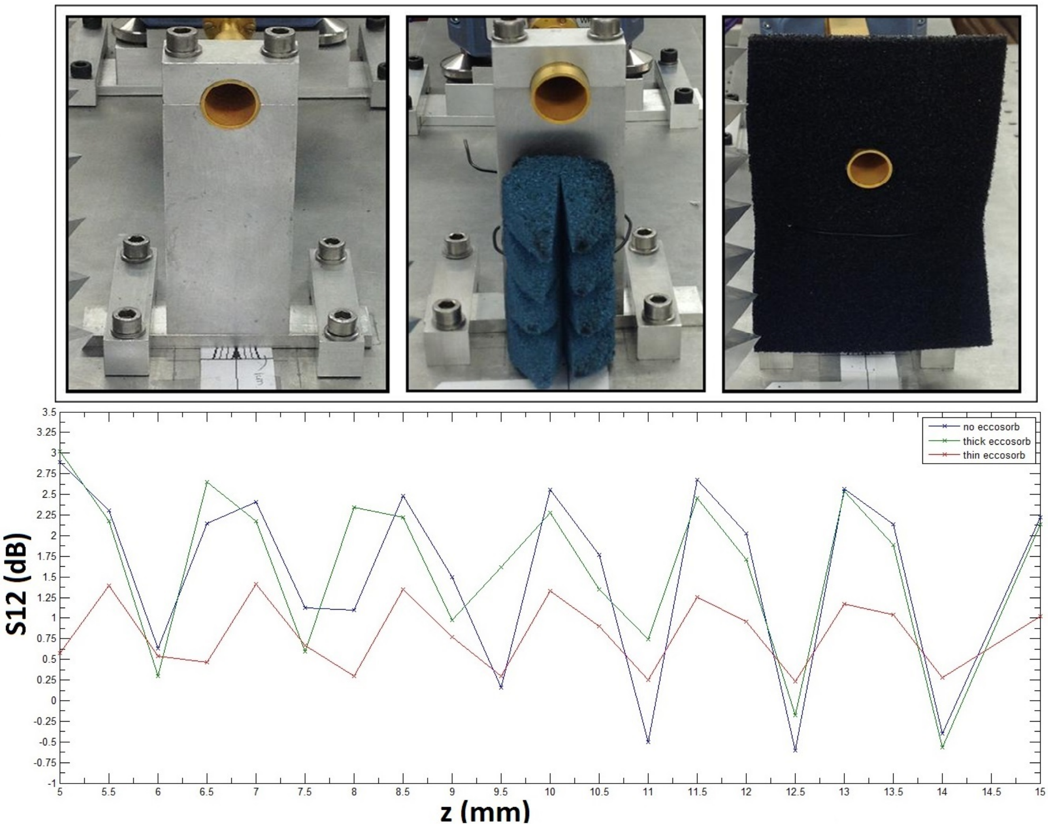

Figure 4.19: The upper-figure shows the three different configuration of the feed absorber use. The S_{12} parameter was measured for each configuration. The lower-figure shows how S_{12} varies as the feed horn is translated along the z-axis with different configurations. Blue line: no absorber, green line: blue pyramid-shape absorber and red line: thin black absorber [126].

4.9 Experimental characterization of the quiet zone

The beam characteristics of each CATR system were investigated by using two measurement configurations. First, the field characteristics have been measured by scanning the Q.Z plane along the horizontal axis in order to be compared with the results of the GRASP models. These preliminary tests were conducted with a linear translational stage. Due to restrictions of the translation stage, only the inner diameter region of the quiet zone was scanned across ± 25 mm in 1 mm intervals. Second, a wider beam scanning for the field characteristics of the Q.Z. was achieved by using the 3D scanner which gave better understanding of field evolution in the Q.Z..

First, the VNA converter head supported by Standard feed was used to scan the Q.Z field. Relying on the comparison study conducted by the MPhys students, the use of the Standard feed as a scanning probe, instead of a waveguide probe, produced much more sensitive results. Therefore, the receiving VNA head integrated to the same feed horn antenna as the transmitting feed source was located at 26 cm away from the main mirror center, half-way between the parabolic main mirrors. The measurement setup shown in Figure 4.20 was prepared for the scans of the field characteristics such as CP and XP intensity and phase along the horizontal axis.

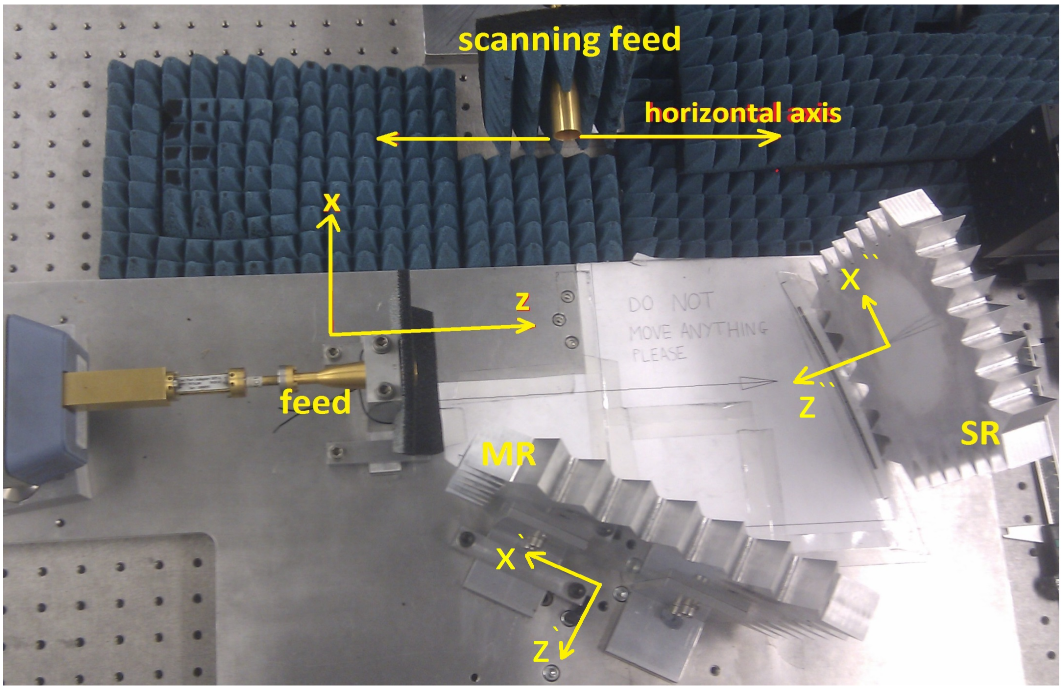

Figure 4.20: The feed source is located at 26 cm away from the centre of the main mirror. By scanning across the horizontal axis, the field intensity and phase data were measured from -25 mm to 25 mm in 1 mm intervals.

4.9.1 Measurements of the CP field intensity and phase

The intensity and phase variations of the CP field in comparison with the model predicted results were investigated in this section. The scanning results are given in Figure 4.21. The plots are for $\phi = 0$ plane cut for 97 GHz. The measured data was verified by repeating the measurements and calculating the error bars. Overall, the measured intensity and phase values with 1.2 ± 0.1 dB and $8^\circ \pm 1.1^\circ$ respectively are in agreement with the simulation data and the Q.Z requirements. Much of the predicted intensity data shown with the blue dot line remains within the error bars of the measured data.

However, the phase variations were measured a few degree larger than the predicted values. The comparison results between the model and the measurements for the field parameters are given in Table 4.8.

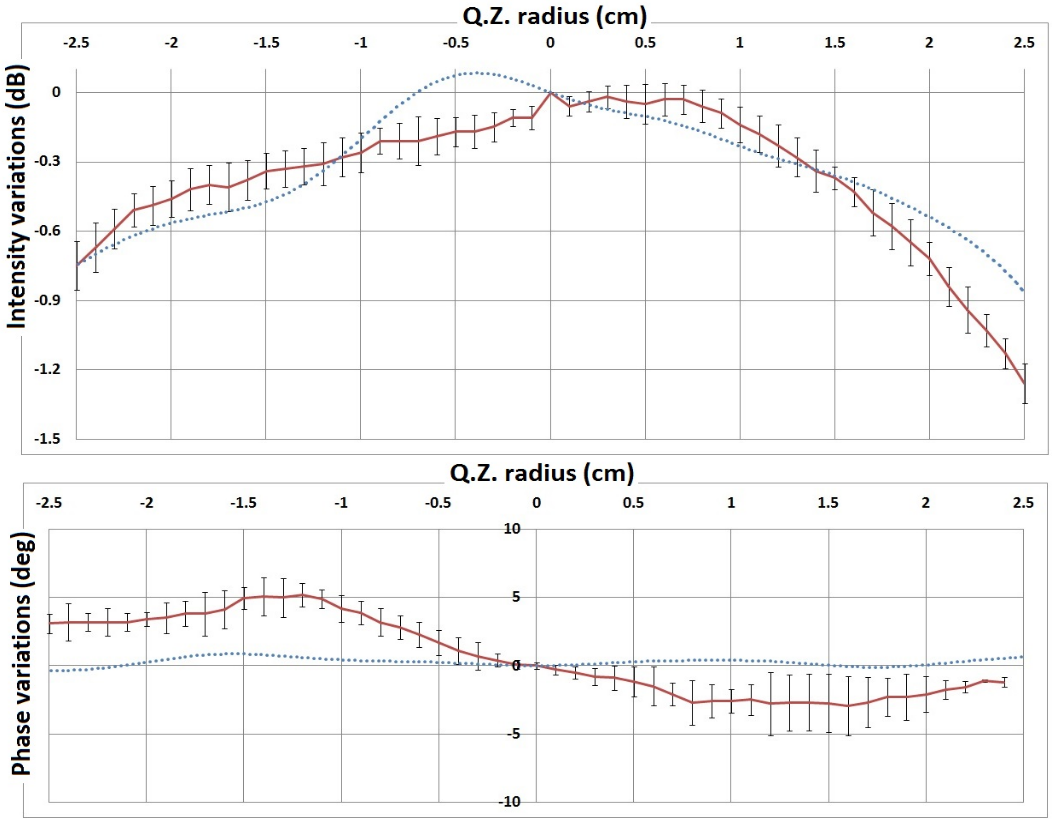

Figure 4.21: The top figure shows the intensity variations while the bottom one shows the phase variations measured for $\phi = 0$ plane cut for the 97 GHz. The blue and red lines denote the model predictions and measured data respectively. The quite zone beam was scanned across the horizontal plane as shown in figure 4.20. The variations are the value relative to the maximum measured value at that point. The error bars were calculated from two measurement readings.

4.9.2 Measurements of the XP field intensity

The XP measurements were first taken at $\phi = 0$ by rotating the scanning feed antenna 90°. Then, the XP measurements were also conducted for $\phi = 45$ plane cut which the highest XP level was expected to be observed. A $\phi = 45$ twist, which allows measurements at the diagonal axis, was connected to both feed horns for the diagonal XP measurements.

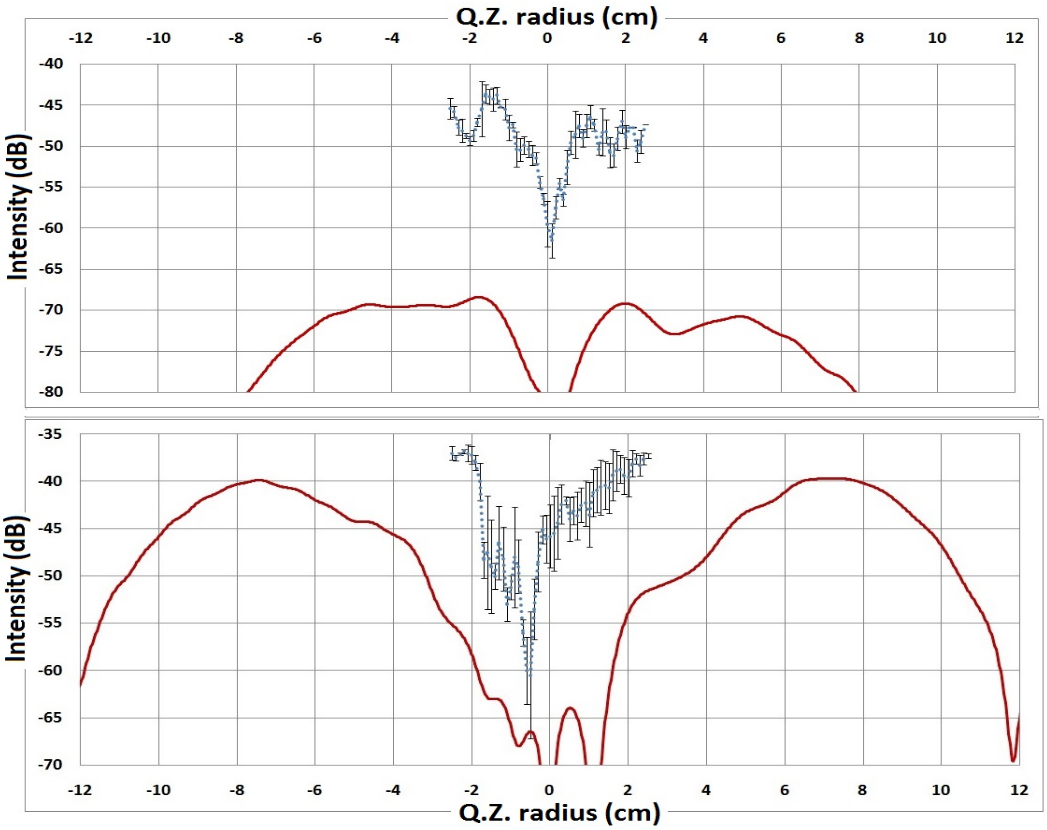

Figure 4.22: The upper figure shows the XP beam pattern both measured and predicted for the H plane cut variations while the bottom one shows the same parameters for the D plane cut for the 97 GHz. All XP data were normalized according to itself CP maximum.

Figure 4.22 presents the measured XP beam patterns of the test system for both H and D plane cuts. In the results for both plane cuts, the general behaviour of the measured XP field plot follows the predicted XP values. A very clear minimum peak was observed below -60 dB in the center of the beam for the H plane cut. Similarly, a very deep peak showed up with a signal level of -61 dB (not normalized scale) in the center of the beam. The maximum XP value with -39.5 dB predicted from the simulations for the D plane cut was expected at around 7 cm. However, the maximum XP level remained out of this measurement range due to restrictions of the translation stage. On the other hand, the D plane cut measurements seemed to be slightly off. This is due to the misalignment problem occurred when the 45° twist was connected to the horn transition.

A substantial improvement by 8±2 dB in the XP level was obtained by use of the

Field characteristics	Predicted values	Measured values
Intensity	0.9 dB	1.2±0.1 dB
Phase	1.3°	8° ± 1°
Max. XP(H/D)	-68 dB / -39.5 dB	-44±1 dB / -37±1 dB

Table 4.8: The measured and calculated variations in the field parameters are listed in the table. Maximum XP values were for the H and D plane cuts. The data was acquired within $\pm 25mm$ along the horizontal axis of the Q.Z..

blue pyramid absorbers surrounding around the Standard feed probe in the Q.Z. as shown in Figure 4.20. Without the absorbers, the XP pattern, with a maximum of -33 dB, varies uniformly across the horizontal axis.

The measurement results are compared to the predicted values for the field parameters listed in Table 4.8. The predictions were obtained from the real feed model (the model that the mirror illuminations were performed by the replacement real feed source data produced from the real measured data). The phase values were not stable enough and fluctuating inside the QZ range. For the data verification, the measurements were repeated and the error calculations were made. Even though the evaluations remain limited due to the narrow displacements along the vertical axis, valuable and comparable data, in particular XP data, were acquired experimentally from the CATR system.

4.9.3 Beam measurements with the 3D scanner system

The beam measurements of the CATR system by using the 3D beam scanner system were performed by MSc students [126]. In these measurements, the scanning feed was a field probe comprising a circular to rectangular waveguide transition. The intensity and phase scanning were performed across $\pm 150mm$ along the x-axis as shown in Figure 4.23. The produced data was compared with the GRASP simulations as shown in Figure 4.24. Overall plots are in agreement, but measured intensity was 1 dB larger than model predictions. Phase pattern measurements were also compared with the model predictions in Figure 4.25. Measured phase plots showed larger fluctuations with a maximum of 7° over a range of ±100 mm. However, overall phase behaviour agrees well. The CP and XP components of the diagonal cut field was also measured and the comparison results are shown in Figure 4.26. Larger deviations from the CP intensity predictions were observed in particular in the beam-size greater than 50 mm. Additionally, XP with a maximum of -19 dB was measured quite higher than model

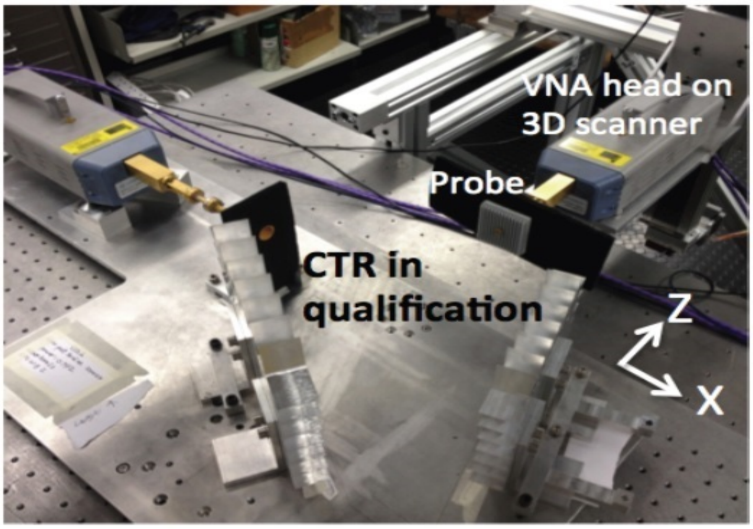

Figure 4.23: The measurement configuration of 3D beam scanner system used to characterize the CATR system. A field probe comprising of a circular to rectangular waveguide transition scanned the field intensity in 3 dimensions.

predictions as shown in Figure 4.26. The main reason for high XP signals might be the use of the field probe used in the 3D scanner. The field probe was not characterized in terms of XP. Last results are for the vertical plane data of the CATR system. These measurements were taken together with my colleague, Peter Schemmel. The effects of mirror serrations on the produced field intensity are clearly observed in Figure 4.27.

4.10 Calibration

In order to remove the systematic errors due to inherent imperfections of the components used within the VNA system such as cables, the system must be calibrated. The calibration accuracy will determine the dynamic range of the free space measurement set-up. Two calibration methods are appropriate here; Through, Reflection and Line (TRL) [110] and Through, Reflection and Match (TRM). These two calibration methods will be implemented and compared in our system. Because TRL needs one VNA head to be translated by $\lambda/4$ for the Line calibration, one of the CTR with the associated VNA head and the sample holder are on a sliding platform.

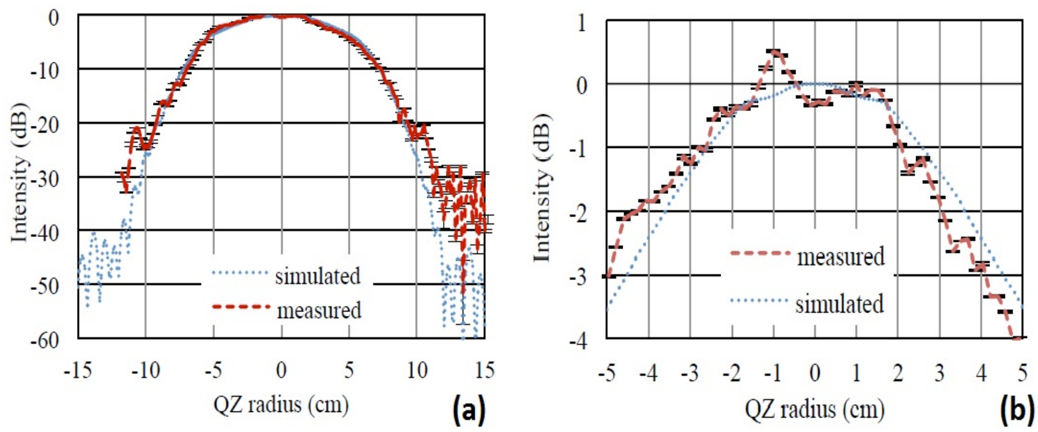

Figure 4.24: Comparison of the GRASP PO simulation and the measured data for the field intensities across the Q.Z.. Left figure shows the large scale plot while right figure shows the close-up view of the same left figure.

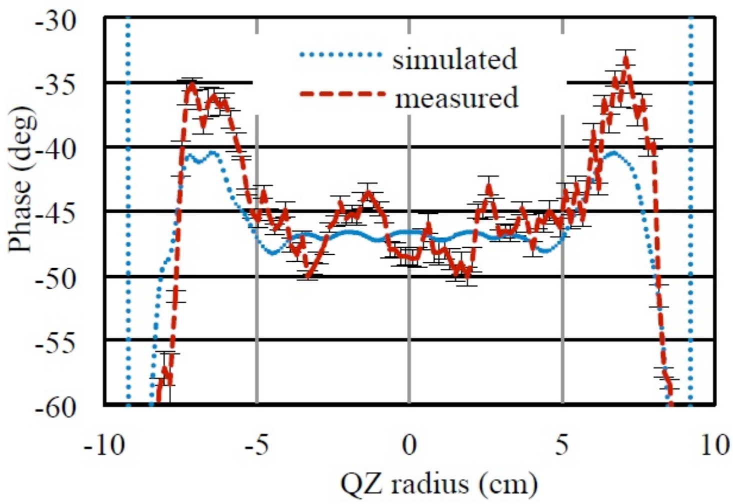

Figure 4.25: Figure compares the simulated and measured phase patterns of the Q.Z.. Both data were taken over a 20 cm diameter of Q.Z..

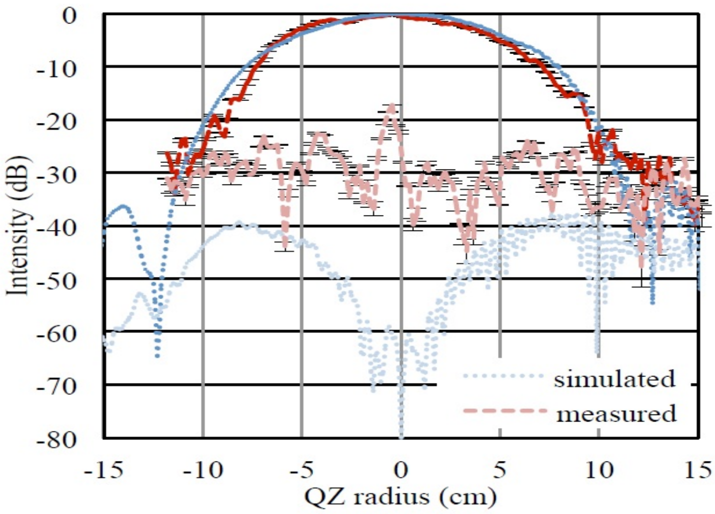

Figure 4.26: Comparison of te D plane cut field intensities predicted from GRASP PO simulations and measured in the RF labs. The CP and XP plots were plotted over a 30 cm diameter of Q.Z..

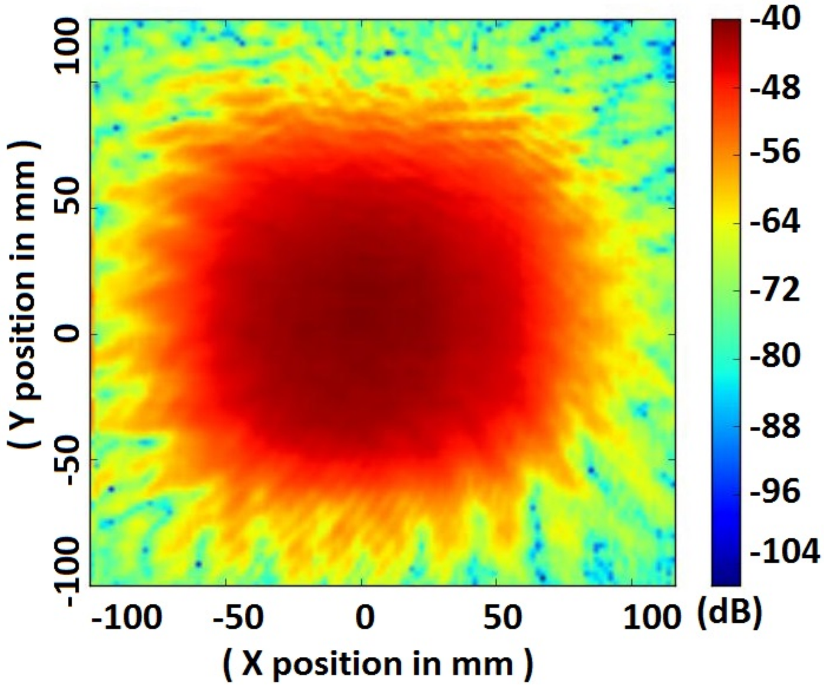

Figure 4.27: Beam evolution of the CATR system for the co-polarization field intensity of the XY plane cut. The field intensity was measured in the Q.Z. where the field probe scanned the beam at 26 cm away from the main mirror center of the CATR system.

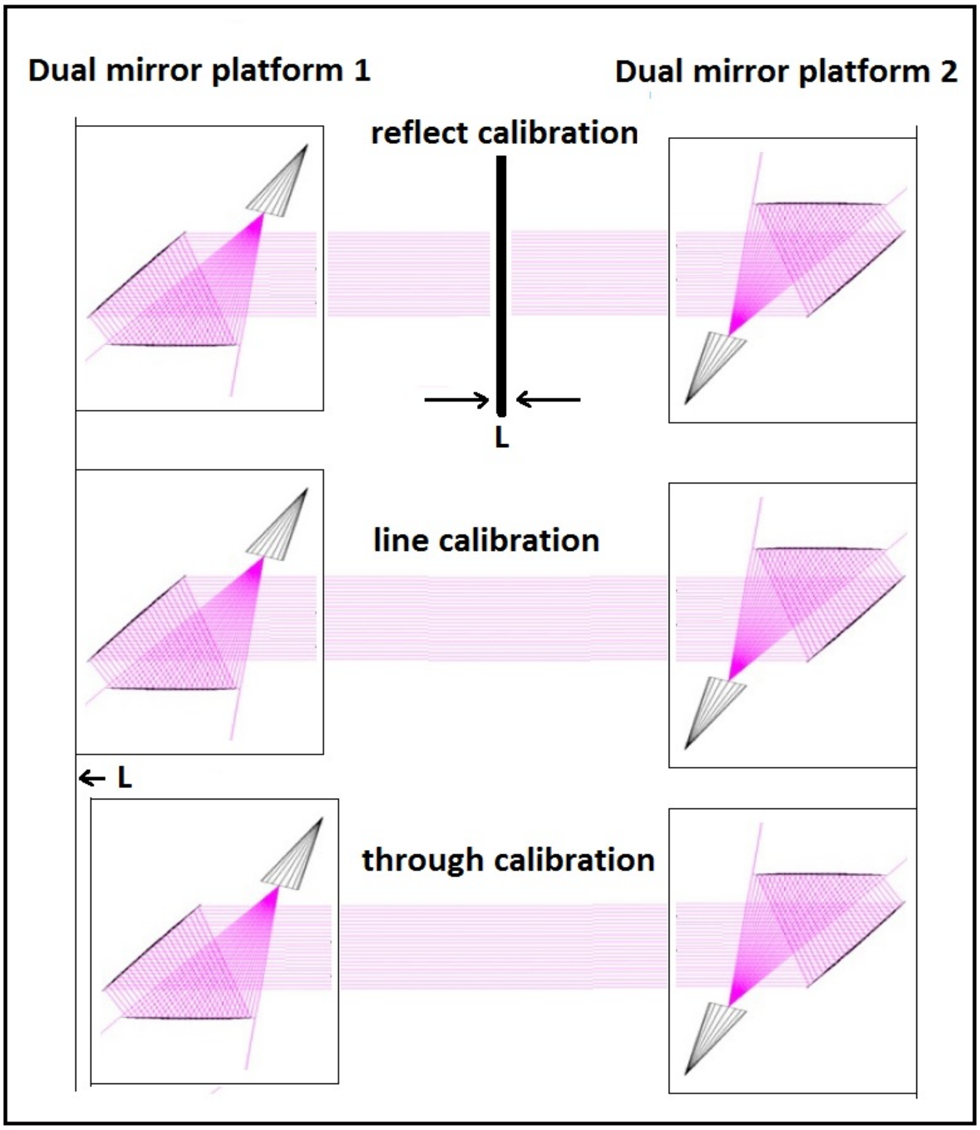

Figure 4.28: The TRL calibration procedure is illustrated in the free-space measurement test bench. From top to bottom: the implementation of the calibration reflector into the CATR system, the line calibration in the same position as the reflect calibration and the translation of the first CATR system for the through calibration. A very accurate translation of L is realized by a linear translational stage with a digital micrometer located underneath the first dual mirror platform.

4.10.1 TRL calibration

First of all, the calibration type is set as TRL in the VNA calibration settings. The calibration process is completed in the three stages: reflect, line and through.

1. **Reflect standard**

   The reflect standard is measured by using a reflector sheet with a thickness L. The reflector is placed halfway between the two main reflectors as shown in Figure 4.28. The dual mirror platform housed on the free translation stage is shifted by a distance L further from the Q.Z. region.

   The crucial point in the TRL calibration process is to overcome a singularity problem. Singularity occurs when two calibrations standards (Line and Through) measure identical phases. In order to avoid this problem, the line thickness is selected as an integer multiple of half-wavelength. The reflector thickness must satisfy the condition given in the following equation [110]

   $$10^\circ < k \cdot L < 170^\circ \tag{4.2}$$

   where k is the wave number in free space and equal to $2\pi/\lambda$. The Standard feed horn used during the test bench measurements operates from 83 GHz to 110 GHz, corresponding to the wavelengths of w_1= 3.614 mm and w_2= 2.727 mm. According to Equation 4.2, a translation by an integer multiple of half wavelength is forbidden because these translations result in either 0° or 180° phase difference between two calibration standards. The allowable thickness of the reflector matching these values is calculated between $0.1mm < L < 1.287mm$. Hence, a reflector with a thickness of 0.9 mm was manufactured in the workshop to be used as the reflect calibration.

2. **Line standard**

   The line calibration is realized by removing the calibration reflector. The positions of the CATR components should stay unchanged.

3. **Through standard**

   The through calibration is done by moving the free CATR stage back to its original position. This position is accepted as the measurement reference location. In order to translate the CATR, the sliding of the linear base platform is achieved by a digital micrometer control.

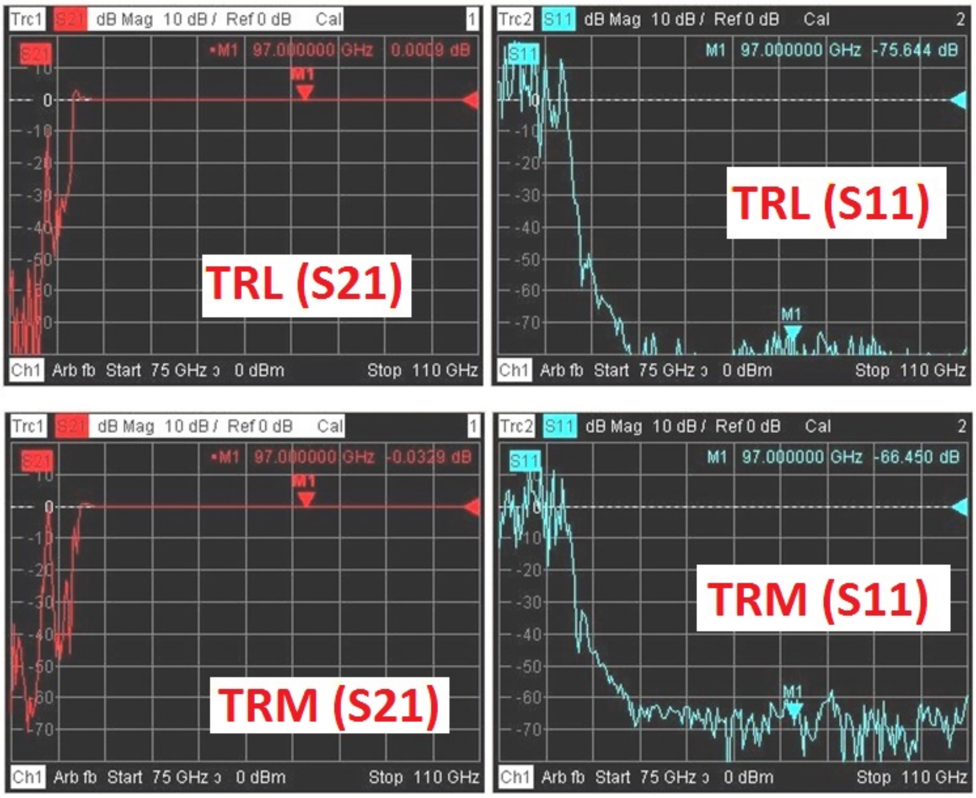

Figure 4.29: The S parameters show how accurately the calibration is processed. The red lines are for the S_{21} parameter while the blue lines are for the S_{11} parameter determined from the TRL and TRM calibration respectively from top to bottom.

S parameter	**Ideal case**	**TRM**	**TRL**
S_{11}	$-\infty$	-66.45 dB	-75.64 dB
S_{21}	0	-0.0329 dB	-0.0009 dB

Table 4.9: The standards are determined after the calibration. The values of the S parameters show the advantage of the TRL calibration over the TRM.

4.10.2 TRM calibration

The TRM calibration is another way to calibrate the free space reflection-transmission measurements using the two port VNA system. It is generally preferred if movement of the test bench is not required. Similar to the TRL calibration, Through and Reflect standards were measured. Then, a thick black MM-wave absorber cut used as a match element was located in place of the sample holder to determine the match standard. The S parameters obtained from both TRL and TRM calibrations seemed to be very accurately calibrated. They present very high accuracy for the S_{11} with -66.45 dB and -75.64 dB S_{21} parameters with -0.0329 dB and -0.0009 dB respectively as shown in Figure 4.29. The S parameters achieved with the calibrations of the TRL and the TRM are compared to those for the ideal case in Table 4.9.

Except for a phase singularity problem with the TRL calibration when the line and through standards were equal, the TRL seemed to be more accurate compared to the TRM calibration.

4.11 First measurements with the test bench

The calibration of the system was successfully performed using a free-space TRL technique. Preliminary measurements were then conducted for the reflection and transmission characterizations of a dielectric slab. An UHMWPE sample (n=1.517 , tanδ=0.0003) was used in this investigation. The details and results of the dielectric slab measurements are presented in Section 6.4.6. Additionally, a spherical curved lens with and without the anti-reflection coating process were characterized and the results are given in Section 6.4.6. Further measurements with the quasi optical components such as wave-plates and filters are still being performed.

4.12 Conclusion

In this chapter, the design and construction of a mirror based free-space S parameters test bench have been described. This test bench is used for the characterization of quasi-optical components and dielectric materials at both Ka and W bands. The optics of the measurement system is based on the dual reflector Compact Antenna Test Range (CATR). The important accomplishments of this project are as follows.

- The PO modelling of CATR system has been simulated by using the software package, GRASP. The model analysis covers the analyses of the edge taper optimization and the serration application. An investigation of misalignments for understanding of the positioning sensitivity of the system components was also made by using the same software tool. In addition, a modification to the CATR model with a real feed feed horn use was made. The Q.Z. beam characteristics of the system were then obtained more realistically. The model results with maximum intensity variations of 4 dB and phase variations of 4.5° remained within the quiet zone requirements. The calculated maximum XP of 39 dB in the Q.Z. almost satisfied the requirement.

- The calibration techniques of the TRL and TRM were successfully performed and understood. After the TRL calibration, the dynamic range of the CATR system was determined as $\leq$-75 dB. Further attempts were made to align the CATR system by using different tools such as laser alignment and maximising S parameters. Substantial progress, in order to understand the system, was obtained by these tools. Additionally, the use of the different mm-wave absorbers was optimized for the different parts of the CATR system such as the feed surroundings. Finally, the beam characteristics were measured in a small range of the Q.Z. due to restrictions of the translation stage with maximum 5 cm translation. The maximum fluctuations in the measured intensity and the phase were 1.2±0.1 dB and $8^\circ \pm 1^\circ$. The maximum XP values measured for the H and D planes were -44±1 dB and -37±1 dB. The intensity and phase measurement results met the Q.Z. requirements. For a larger beam scanning, the 3D beam scanner system was used. Measured intensity was found to be 1 dB larger than model predictions while overall intensity behaviours agree well. Measured phase pattern showed a maximum variation of 7°, which still satisfies the Q.Z requirements. In addition, XP with a maximum of -19 dB was measured quite higher than predictions. The main reason of the high XP level is the field probe that was used during the 3D scanning system. Future plan may be characterizing the field probe in terms of XP.

Based on the above accomplishments, the free-space measurements of the UHMWPE dielectric slab, lens and ARC-lens were performed. The results obtained from the experimental data are quite consistent with the dielectric slab models as you will see in Section 6.4.6. However, improvements of the CATR system are required by replacing some mechanical parts (e.g. sample holder) to allow better confidence on both measurements and alignment. Finally, the specific features of the CATR system should be understood much better in order to characterize the dielectric materials for extracting the dielectric properties such as permittivity and loss tangent.

Chapter 5

SIMULATION OF HORN-LENS SYSTEMS

This chapter focuses on modelling of horn-lens systems. The ability to model and accurately measure (see Chapters 6 and 7) the systematic effects that arise from the optics of refractive telescope systems is investigated with this study. For the first lens prototype, due to the limited space in our RF laboratory, we decided to restrict the far field distance to be $\sim$1.5 m. This distance is consistent with a small sized lens aperture diameter of 47 mm (16λ at 97 GHz). Thanks to its relatively small size, this choice also allowed us to make a full-wave model of the lens with the MOM in FEKO. Based on the model confidence achieved with preliminary analyses, Medium Size Lens with a diameter of 90 mm (30 λ at 97 GHz) was also designed. This lens system was modelled successfully with both the MLFMM and the RLGO approaches in FEKO. The off-axis beam modelling of the medium sized lens system was also carried out (see Chapter 7). Due to the large beam size ($\sim 3\lambda$) of the feed source, compared to the diameter of the small sized lens system (16λ), the off-axis beam characterization of the small sized lens system did not seem to be possible. As a result, only the medium lens design was considered for the off-axis beam study.

In this chapter, basic lens design equations based on conventional ray-based optics are defined in order to calculate the lens parameters. Then, the simulation analyses of the lens systems are performed with a combination of the three main models discussed in Chapter 3: MOM, MLFMM and RLGO.

5.1 Geometrical optics (GO)

As a very first and simple approximation, Geometrical Optics (GO) simplifies wave optics for very small λ. Waves are assumed to be light rays, and polarization, diffraction and interference properties of light are ignored. In GO approach, basic principles can be explained with the reflection and refraction laws of light.

There are two main postulates that a lens design with (GO) is based on: Snell‘s law of refraction and the Fermat‘s principle [127]. The relationship between different mediums that light experiences is ruled by Snell‘s law using refractive index (n_2). Snell‘s law postulates that the angle of the incidence ray and the angle of the transmitted ray should satisfy Equation 5.1 (Figure 5.1).

$$n_1 \sin\theta_1 = n_2 \sin\theta_2 \tag{5.1}$$

This is where n_1 and n_2 are refractive indices of vacuum and a dielectric medium respectively. The refractive index of a material is defined by the light behaviour inside the medium. Light rays travel slower inside a denser matter ($n_2 > n_1$) so its wavelength becomes smaller with a constant frequency.

The physical properties of a dielectric medium (e.g. dielectric permittivity) are extracted from the definition of refractive index, such that

$$n = \frac{\lambda_0}{\lambda_m} = \frac{v_0}{v_m} = \sqrt{\frac{\varepsilon\mu}{\varepsilon_0\mu_0}} = \sqrt{\varepsilon_r\mu_r}. \tag{5.2}$$

The $\lambda_0(v_0)$ and $\lambda_m(v_m)$ are the wavelengths (their corresponding velocities) in vacuum and a dielectric medium, respectively. ε_r and μ_r are relative permittivity ($\frac{\varepsilon}{\varepsilon_\circ}$) and relative permeability ($\frac{\mu}{\mu_\circ}$). ε, μ, $\varepsilon_\circ$ and $\mu_\circ$ are permittivity and permeability of dielectric material and permittivity and permeability of free-space.

Fermat‘s principle requires equality of optical path lengths taken throughout the lens. GO rays are straight lines in free space. However, the same rays in a dielectric medium are the product of the optical path-length and the refractive index of the dielectric medium. According to the Fermat‘s principle given in Equation 5.3, the optical paths of both ray traces should be equal. This is the requirement for generating rays in phase after they are refracted on an interface as shown in Figure 5.1.

The geometry of the lens surface is formed by using the two principles. Supposing that the rays enter from the air to the dielectric lens medium with a refractive index n_2 and a focal length (f), Fermat‘s law states

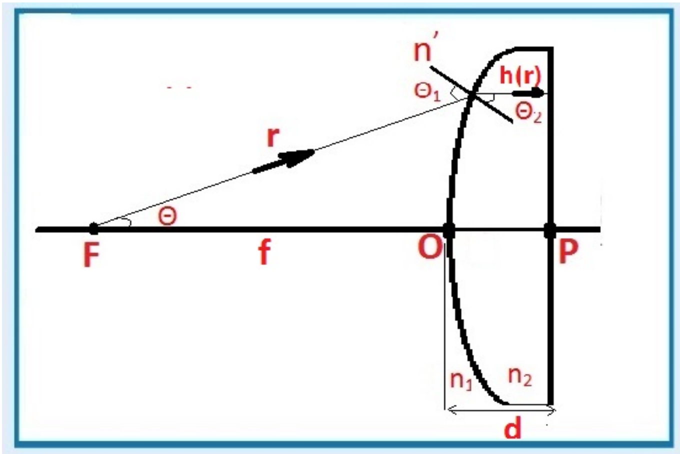

Figure 5.1: Two fundamental principles to explain the ray-based behaviours of the dielectric lens: the Snell‘s refraction law and the Fermat‘s principle. f denotes the focal length of lens geometry with a central thickness of d and refractive index of n_2.

$$r + n_2 \cdot h(r) = n_1 \cdot \mid FO \mid + n_2 \cdot \mid OP \mid . \tag{5.3}$$

Equation 5.4 is the hyperbola equation for an eccentricity value of $\varepsilon = n > 1$ in terms of polar coordinate systems. For the asymptotic condition, r goes to infinity for the angle θ.

$$r = \frac{(n-1)f}{n\cos\theta - 1}. \tag{5.4}$$

$$\theta = \cos^{-1}\left(\frac{1}{n}\right) \tag{5.5}$$

By using Equation 5.3, the lens thickness is described by [128]

$$h(r) = \frac{f}{n+1}\left[\left(1 + \frac{r^2(n+1)}{f^2(n-1)}\right)^{0.5} - 1\right]. \tag{5.6}$$

Lastly, the phase shift introduced by the lens as a function of distance from its symmetrical axis is given by [128]

$$\phi(r) = -\frac{2\pi}{\lambda}(n-1)[d - h(r)] \tag{5.7}$$

where d is the central thickness of the lens and the expression [*d-h(r)*] defines the optical path length difference between the two ray cases. The equality of the path length for two different ray paths is satisfied with this equation. For different dielectric materials having a specific index of refraction, the asymptotic angle given in Equation 5.5 takes a specific value. For example, this angle becomes $48.75°$ for the UHMWPE dielectric with the refraction index of 1.517. Incident rays propagating with larger angles than asymptotic angle value do not intercept lens surface. As a result, the ideal profile of a planar lens should be a hyperbola. For my research, we have chosen to use spherical curved plano-convex lenses over hypberbola curved lens because this lens profile is easier to fabricate in the school workshop.

5.2 Focal distance definitions

The curved surfaces of both lenses have spherical geometries. The design equations for a thick lens are

$$\begin{aligned} \frac{1}{f} &= (n-1)\left(\frac{1}{R_1}-\frac{1}{R_2}+\frac{(n-1)d}{nR_1R_2}\right) \\ BFD &= f\left(1-\frac{(n-1)d}{nR_1}\right) \\ FFD &= f\left(1+\frac{(n-1)d}{nR_2}\right). \end{aligned} \tag{5.8}$$

In the most general case, a lens is defined by the refractive index n, the center thickness d and three focal distances. The Front Focal Distance (FFD) is the distance between the first lens vertex (V1) to the focal point of the lens (F1) while the Back Focal Distance (BFD) is the distance between the second lens vertex (V2) and the focal point of the lens (F2). The radii of lens curvatures are R_1 and R_2. The intersection points of the principal planes with the lens show the effective focal length (f). These planes are where the rays actually refract as shown in Figure 5.2.

5.3 Models for Small Lens Prototype

Initially, the plano-convex lens with spherical surface as shown in Figure 5.3 was designed by using the thick lens formula. The lens has an aperture diameter of 47 mm

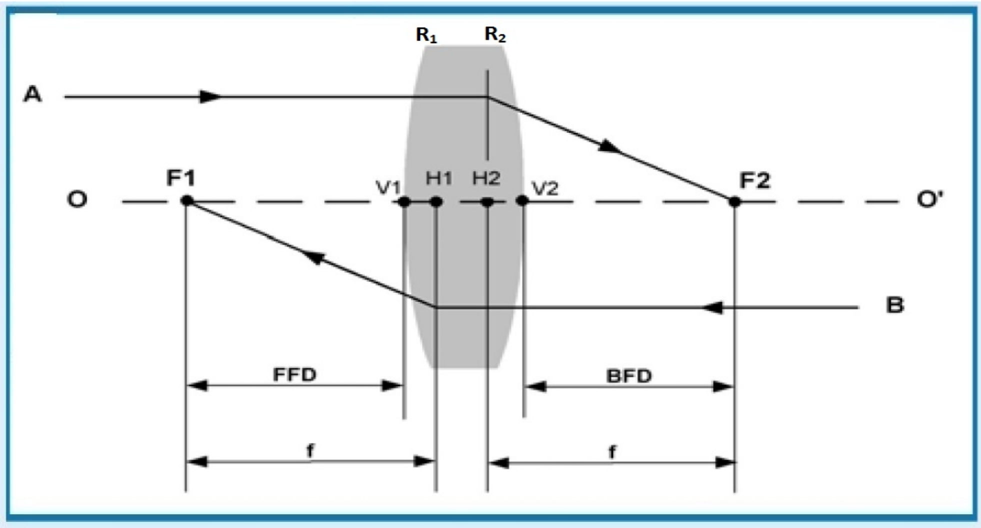

Figure 5.2: This diagram shows the lens parameters for a thick lens. The Front Focal Distance (FFD) is the distance between the first lens vertex (V1) to the focal point of the lens (F1) while the Back Focal Distance (BFD) is the distance between the second lens vertex (V2) and the focal point of the lens(F2). The Effective Focal Distance (F) is the distance from the principal planes(H1,H2) to the focal point(F1,F2) [129].

(16 λ at 97 GHz). Its effective focal length of 69.85 mm is providing a F number of 1.48. F number is defined as the ratio of effective focal length to lens diameter (f/D). More than 99% power concentration is achieved with the specifications indicated above, considering the use of the Standard Feed (SF) horn as feed source (see Section 3.7). The lens is made from a low-loss dielectric, Ultra High Molecular Weight Polyethylene (UHMWPE). According to the manufacturer information, it has a dielectric constant value that varies between 2.30 and 2.34 with a tangent loss of $3x10^{-4}$ at W-band frequencies [14]. The refractive index of the UHMWPE dielectric was measured as $1.517/pm0.001$ corresponding to a dielectric permittivity of 2.301. The lens parameters are listed in Table 5.1.

5.3.1 FEKO Modelling of the Horn-Small Size Lens system

A preliminary simulation was carried out to illustrate the field and phase propagation of the near field propagation. The modelling issues regarding to the full-wave simulations of the horn-lens system are discussed in Appendix C. Figure 5.4 shows that the curve wave-fronts are converted to the planar wave-fronts by means of the dielectric plano-convex lens fed with the Standard feed horn antenna. The lens modifies the phase

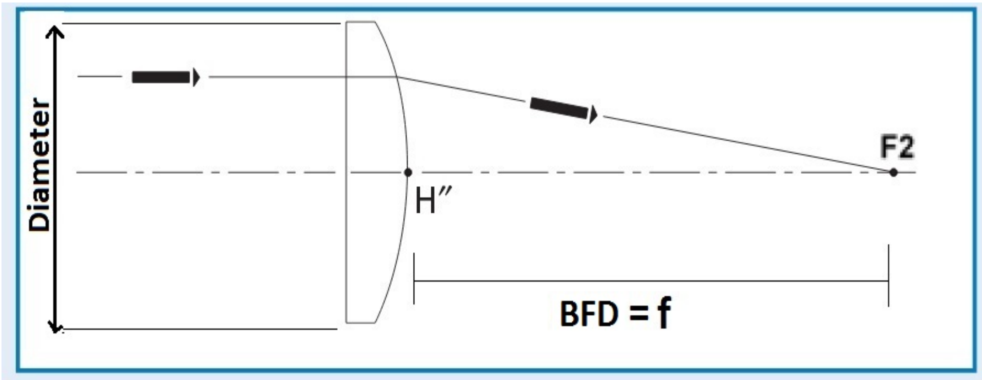

Figure 5.3: Model geometry of the plano-convex lens. $H^{''}$ is the principal point and determines the distance from the focal point (F2). In this thick lens configuration, the effective focal distance of the lens is equal to the back focal distance [92].

Parameters	Small Lens
f number	1.48
Radius of curvature(R_1)	∞
Radius of curvature(R_2)	-36.112 mm
Lens thickness (d)	11.11$\pm$0.03 mm
Refractive index (n)	1.517 $\pm$0.001
Effective focal length(f_{eff})	69.85 mm
Back focal length(f_b)	69.85 mm

Table 5.1: The lens parameters of the small size lens. Lens has a plano-convex spherical curve geometry. f number of the lens is the ratio of effective focal distance to diameter of the lens. The refractive index of the UHMWPE dielectric was measured by using a free-space measurement test bench discussed in detail in Chapter 4.

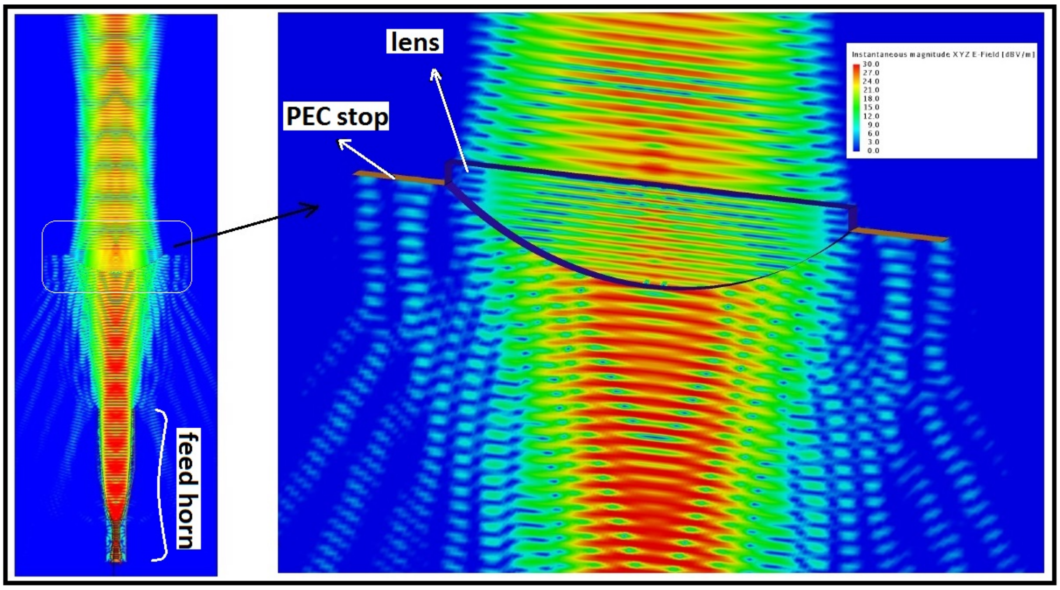

Figure 5.4: Electric field evolution through a horn-lens system. Logarithmic scale field magnitude was amplified 2 times to make wave-fronts visible. MOM modelled dielectric lens is illuminated by the Standard feed horn. Lens aperture is defined by an perfect electric conductor (PEC) stop. A close-up view of the field propagation shows how curve wave-fronts are converted into almost planar wave-fronts.

of the incident field by introducing a phase delay at its surface so that it generates a uniform phase variation inside the lens and after the transmission from the lens.

Four different procedures illustrated in Figure 5.5 and Figure 5.6, have been used in the simulations to model the feed horn-lens system. The Method of Moments (MOM) based on the Surface Equivalence Principle (SEP) within FEKO was the main solving method for the dielectric lens. The purpose of using the other three models was to attempt to create efficient models in terms of time and memory. These additional models were compared to the full MOM simulation. By doing so, the verification of different models was achieved.

- **Model 1**: **Full MOM Model**

  In this model (Figure 5.5), both Standard feed horns and dielectric lens antenna were modelled with the full-wave model of the MOM. Model 1 is expected to present the most accurate results of the simulations so it is taken as the reference model.

- **Model 2**: **SWE + MOM**

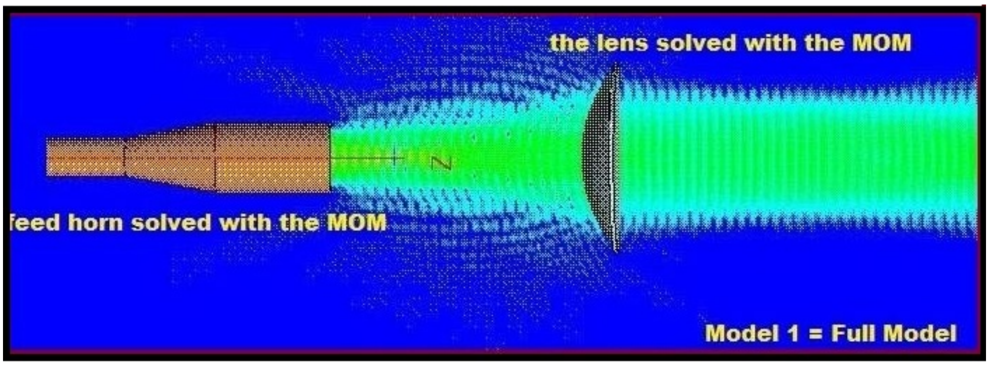

Figure 5.5: The illustration of Model 1. In this model, both horn and lens antennas were modelled by the MOM method. This full analysis is the reference model of the small lens design.

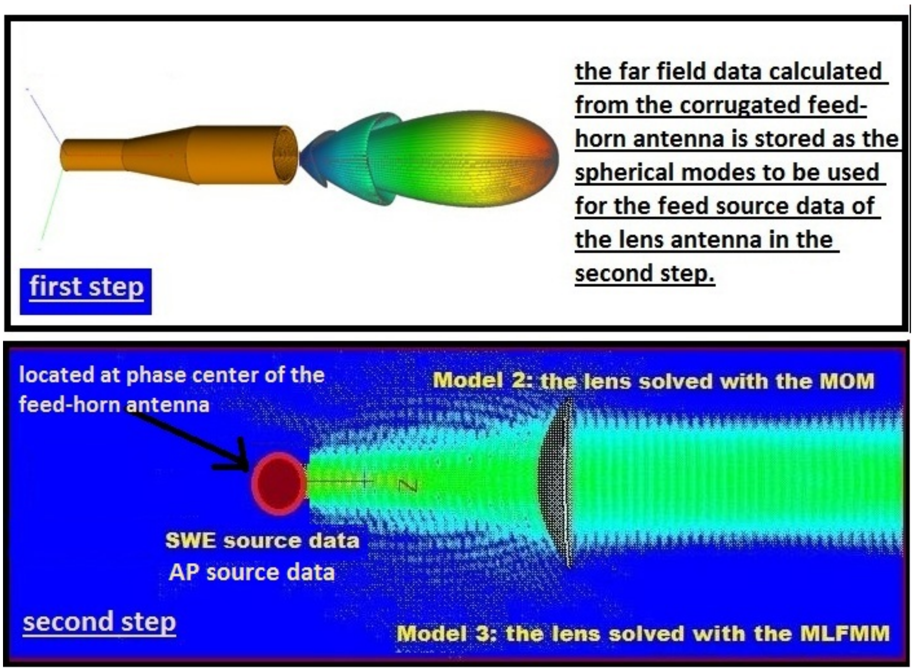

Figure 5.6: The illustration of Models 2,3 and 4. Upper figure demonstrates the far-field data of Standard feed horn antenna calculated in the first step of the simulation. Lower figure shows the locations of equivalent source inputs to the pre-calculated far-field solutions of the feed and dielectric lens. Model 2 used a SWE source input to illuminate the MOM modelled lens. Model 3 had the same feed input to illuminate the MLFMM modelled lens. AP source input was used in Model 4 as the feed of the MLFMM modelled lens in Model 4.

In this model, the equivalent source of the Standard feed horn was first generated by calculating the far-field from the full-wave MOM simulation. A spherical wave expansion (SWE) source was then created by storing the far field data in the file format of *.sph. This input was then used as the feed source of the second part of the simulation. MOM was then used to model the lens with the SWE input as shown in Figure 5.6.

- **Model 3**: **SWE + MLFMM**

  The accelerative version of the MOM, the MLFMM was used to model the lens. Similarly, the lens was illuminated with the SWE source generated in the first part of Model 2.

- **Model 4**: **AP + MLFMM**

  In this approach, the Aperture Source (AP) was used as the feed input. More information on the AP source can be found in Section 3.6.2. It was in turn used to illuminate the MLFMM modelled lens.

5.3.2 Model Results

The modelled phase and intensity results are presented here.

- **Phase calculations**

A well designed lens system should present a uniform phase behaviour in far-field. This phase uniformity shows that coherent field propagation is achieved. In the models, the feed was located at the focal point of the lens, considering the phase center of the feed-horn. The location of the phase center for the feed horn is known from its previous feed measurements. This location is 1.1 mm inside the feed aperture. The phase center of the entire horn-SL system is the second beam-waist of the lens beam as shown in Figure 6.16. The second beam-waist position was calculated to be 62 mm away from the plane surface of the lens by using the Gaussian beam transformations. The first beam-waist position is assumed as the phase center location of the feed-horn. Both phase centers are the locations where the wavefronts are planar ($R \to \infty$). The far-field samples were requested to calculate the field over a sphere to be defined. The centre of this sphere corresponds to the phase center of the horn-small lens system, the second beam-waist position. The phase calculation results from four different models are given in Figure 5.7. The data for the D plane cut of the calculated field phase at

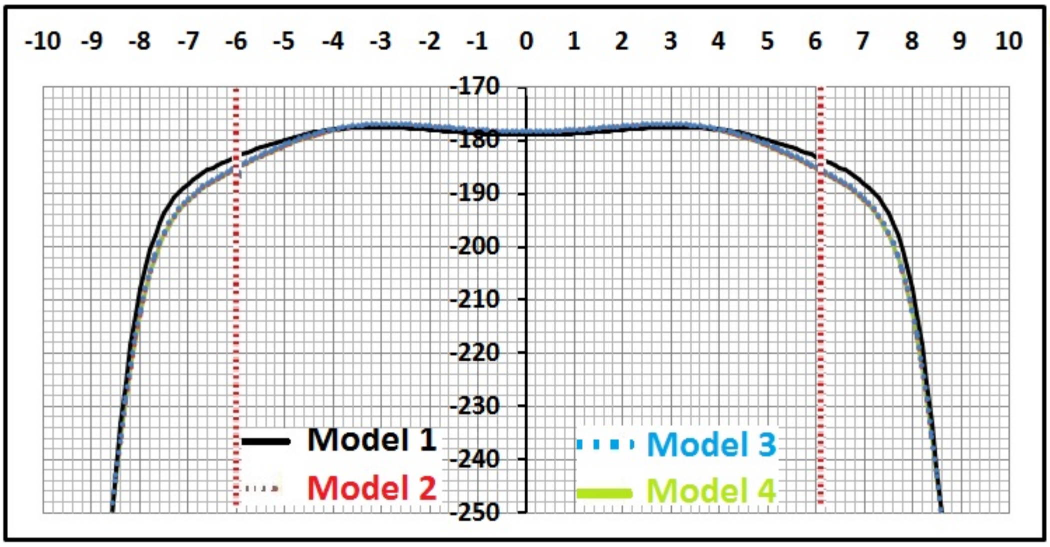

Figure 5.7: D-plane ($\phi = 45°$) phase patterns of the small lens design calculated from 4 different models for 97 GHz. The dashed red lines indicate the extent of the HPBW. The plots of Model 2, 3 and 4 overlap well so all lines are not visible.

97 GHz is given. Apparently, the phase patterns calculated from each model behave in a similar way. There is maximum 2° difference between the phase value of the main model and those of the other three models within the extent of the HPBW.

- **Intensity calculations**

The intensity pattern results obtained from the four simulations are plotted in Figure 5.8. The calculations were done at 97 GHz. The superimposed plots of the co-polarization (CP) and cross-polarisation (XP) beam predictions computed with each model show the variations due to the modelling methods. It is obvious that the simulations from Models 2, 3 and 4 give almost identical results for the CP beam. However, the Model 1 presents a different CP plot behaviour than the other model plots. Two important discrepancies in the side-lobe and XP levels between the Model 1 and the other models are observed. The difference between the side-lobe levels remains maximum 1 dB. In addition to this, the predicted XP levels from the model 1 are different from the other models. However, the closest prediction of the XP level to the Model 1 prediction came from the Model 4 (AP+MLFMM) with a difference of 0.69 dB.

Figure 5.9 shows the beam difference (BD) between the intensity patterns calculated from the full MOM (Model 1) and the other three models (Models 2, 3 and 4).

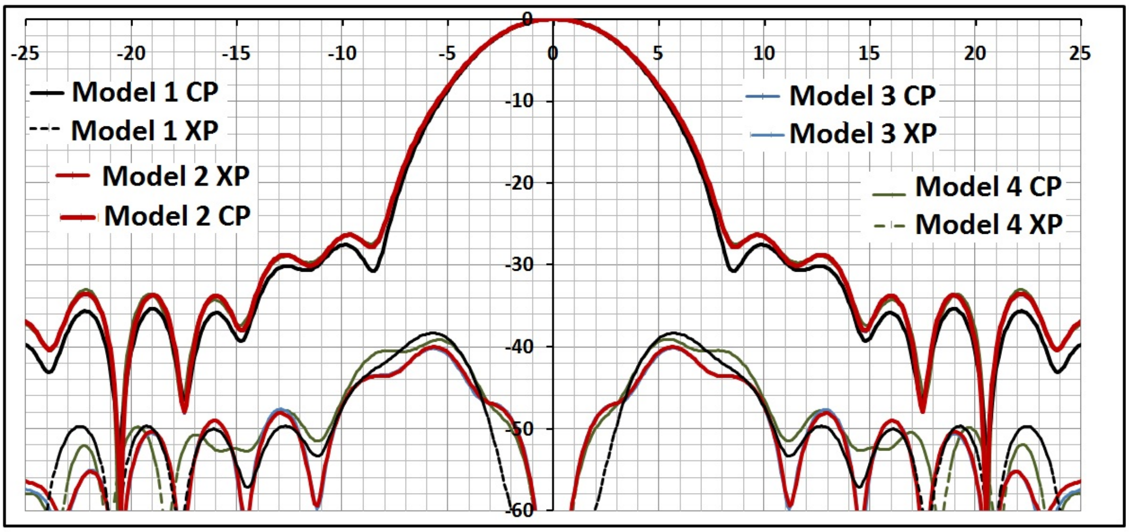

Figure 5.8: Intensity radiation patterns calculated with four different models of the horn-lens system. The calculations are for a frequency of 97 GHz at D plane cut.

These three models are quite consistent with the full model. The maximum beam difference was calculated to be -23 dB. Model 4 gives the best match with the full model. Overall, the feed definition was found to have a major impact on both the CP and XP beam patterns as seen from the equal level of the beam differences between Models 2-3 and Model 1. The MLFMM and the MOM were also quite consistent for the simulations of the dielectric lenses as it can be understood from the comparison of Model 2 and Model 3 for the radiation beam pattern.

The beam patterns calculated at $\phi = 0°$, $\phi = 45°$ and $\phi = 90°$ with Model 1 are shown in Figure 5.10. Only very minor variations show up in the side-lobes for different cut planes. This shows that the lens design leads to an almost symmetrical beam pattern.

5.3.3 Summary from the small lens models

At this stage, we do not know which model is more accurate without comparing the model predictions to experimental data. Supposing that the full-wave model analysis predicts the highest accuracy in comparison with the other models, we can make the following comments:

1. Based on the discussion of equivalence source data in Section 3.6.4, models using SWE and RAD source inputs predicted almost identical far-field patterns

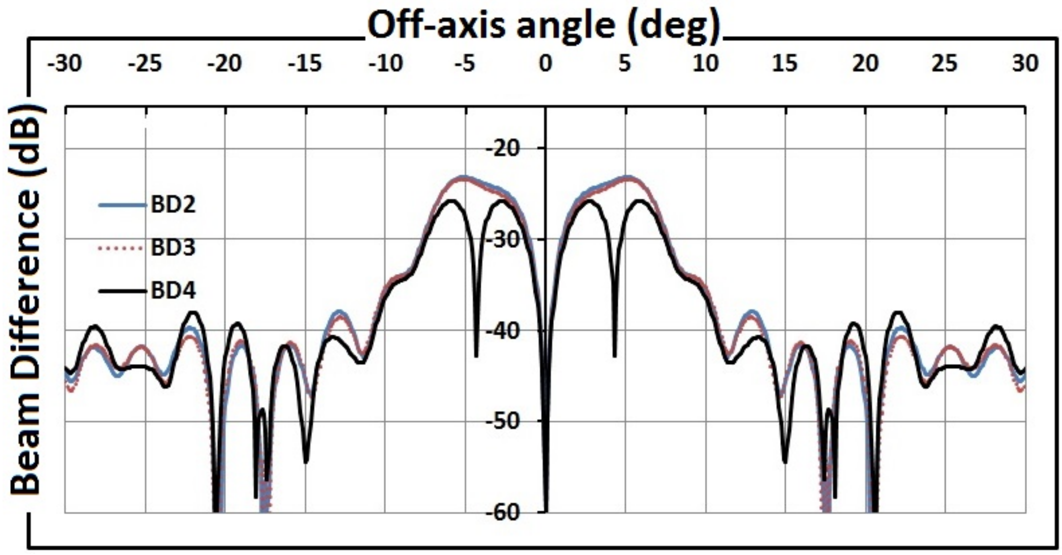

Figure 5.9: BD is normalised to the peak of the beam for the Model 1. The three plots compare the best matched approximation (Model 2, 3 and 4) to the full model (Model1).

to that of the real feed model. AP source input was the only model that deviated from the real feed model. However, all model data were in a well agreement within the region of the main beam lobe. Edge taper illumination of the lens remained inside the beam region of the feed. Figure 5.8 showed that all three lens models (Models 2, 3 and 4) using equivalence source inputs presented maximum 1 dB side-lobe difference than the full model results of lens simulation (Model 1). The beam difference between Model 4 and Model 1 was the lowest, at -26.5 dB. The maximum beam difference between the beam pattern predictions of the Model 1 and those of the Model 2,3 and 4 remained below -23 dB. The predicted maximum XP and side-lobe levels of the Model 1 differed by less than 1 dB from the other model predictions. The closest XP prediction to Model 1 prediction came from Model 4. This similarity can be attributed to the AP source behaviour. As it can be remembered from the equivalence source analysis in Section 3.6.4, the AP source input showed 4 dB higher XP than the other feed source models.

2. Second, there is a tremendous difference between the computational requirements of the four different models highlighted in Table 5.2. Three far less computation intensive methods of 2,3 and 4, with runtime reduced by a factor of

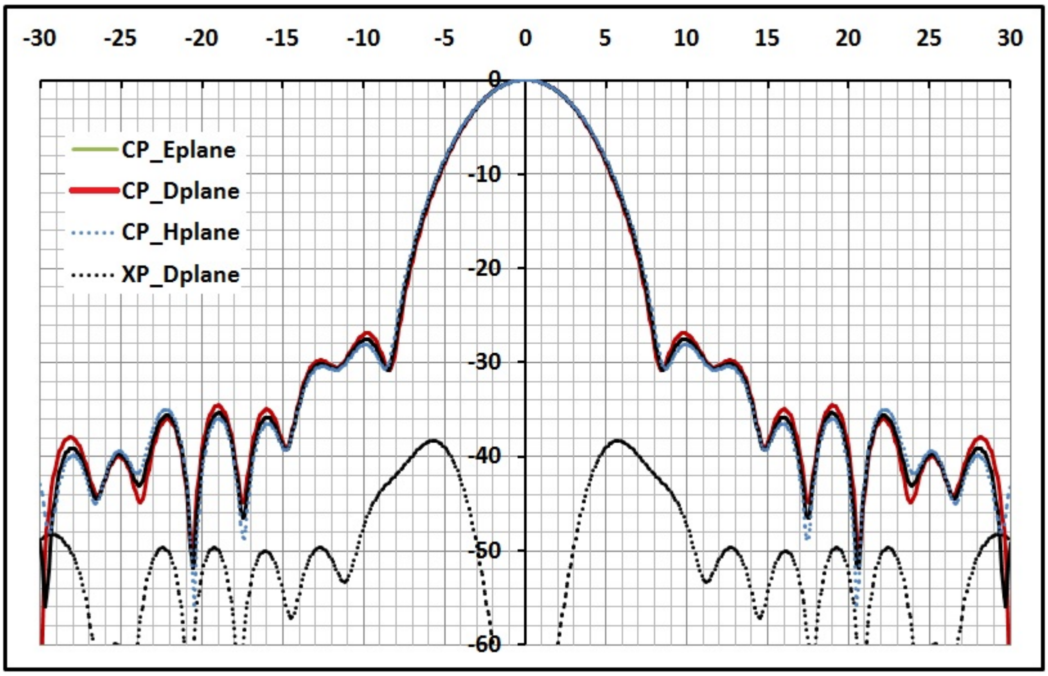

Figure 5.10: Beam patterns for E,D and H plane cuts at 97 GHz. The pattern results are calculated with the full MOM model of the horn-lens system illuminated with a real Standard feed horn beam (Model1).

24 and memory reduced by a factor of 44, gives reasonable predictions. Model 4 required 50% more time than Models 2 and 3 to complete. In the full model, a model feature provided by the FEKO allows the simulations which requires a memory usage up to 1 TB to be divided into the sub-simulation domains. However, this feature does not allow the symmetry options to be assigned to the model simultaneously so run-time may be an issue.

5.4 Models for Medium Lens Prototype

Here, initial design of the Medium Size Lens is detailed. For the reasons explained in the introduction of this chapter, an investigation of a second lens design was required. This study aimed at obtaining further information not only for on-axis pixel performances of the horn-lens systems, but also for its off-axis pixel performances.

The plano-convex lens with spherical surface (Figure 5.11) was designed by using the thick lens formula. This distance is consistent with an aperture diameter of 90 mm

Models	Feed/Lens (Model tool)	Solution times	Memory requirements
Source data	MOM	21 hours	150 GB
Model 1	MOM/MOM	141 hours	508 GB
Model 2	SWE/MOM	29.5 hours	122.5 GB
Model 3	SWE/MLFMM	16 hours	11.5 GB
Model 4	AP/MLFMM	24 hours	11.8 GB

Table 5.2: The computational requirements of the different models are detailed in terms of solution times and memory requirements.

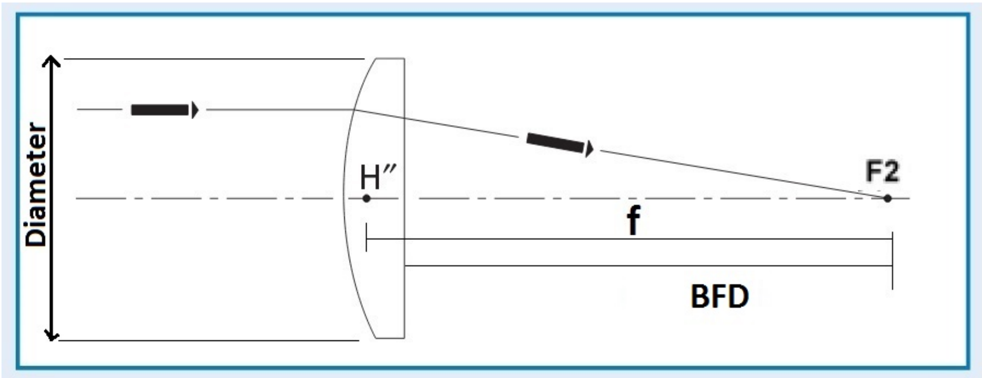

Figure 5.11: Model geometry of the plano-convex lens. $H^{''}$ is the principal point and determines the distance from the focal point (F2). In this thick lens configuration, the effective focal distance is larger than the back focal distance as given in Table 5.3 [92].

lens (30 λ at 97 GHz). Its effective focal length is 216.6 mm, providing a F number of 2.4. More than 90% power concentration is achieved with the specifications indicated above, considering the use of the Standard feed horn. The lens was made of UHMWPE dielectric with material properties has been given in Section 5.3. The lens parameters are listed in Table 5.3.

5.4.1 Modelling of the Horn-Medium Size Lens Systems

Due to the requirements of the high computational resources of electrically large structures (Medium Lens = 30 λ in our case) at high frequencies, the horn-lens antenna system could not be solved with full MOM. Without model validations, the model analyses remain always questionable. To this end, I used five different models with a combination of the feed inputs (e.g. Spherical Wave Expansion (SWE), Aperture Source (AP) and Radiation Pattern (RAD)) and dielectric models (e.g. MLFMM and

Parameters	Medium Lens
f number	2.4
Radius of curvature(R_1)	112 mm
Radius of curvature(R_2)	∞
Lens thickness (d)	12.28±0.03 mm
Refractive index (n)	1.517±0.001
Effective focal length(f_{eff})	216.6 mm
Back focal length(f_b)	208.5 mm

Table 5.3: The lens parameters of the medium size lens are given in the table.

GO) to calculate the CP and XP radiation patterns. In the lens simulations employed in this section, new source data, radiation pattern point source is introduced. Some details on the use of this source data is given in Section 3.6.3. For the dielectric lens simulation, the outputs of the MOM and MLFMM were almost identical (see Figure 5.9). Therefore, the MLFMM can replace the MOM in the simulations.

Equivalent source inputs to the real Standard feed horn with different definitions were used to illuminate the lenses in all five models. In the first three models, the MLFMM was used to model the dielectric lenses. The last two models used GO hybridization with the equivalent sources to model the dielectric lenses. The model descriptions are presented in Figure 5.12.

- **Model 1: SWE + MLFMM**

  In the first model, the SWE feed was used as source input. This source was generated from the far-field solution of Standard feed horn was used as the feed source of the MLFMM modelled lens.

- **Model 2: RAD + MLFMM**

  In the second model, a RAD source was used to illuminate the MLFMM modelled lens.

- **Model 3: AP + MLFMM**

  Here, the AP source was used. The aperture source (AP) was first formed with the near-field solutions. The near field of Standard feed horn was requested to be calculated in spherical coordinates. In turn, it was used to illuminate the lens which was modelled by MLFMM.

- **Model 4: SWE + GO**

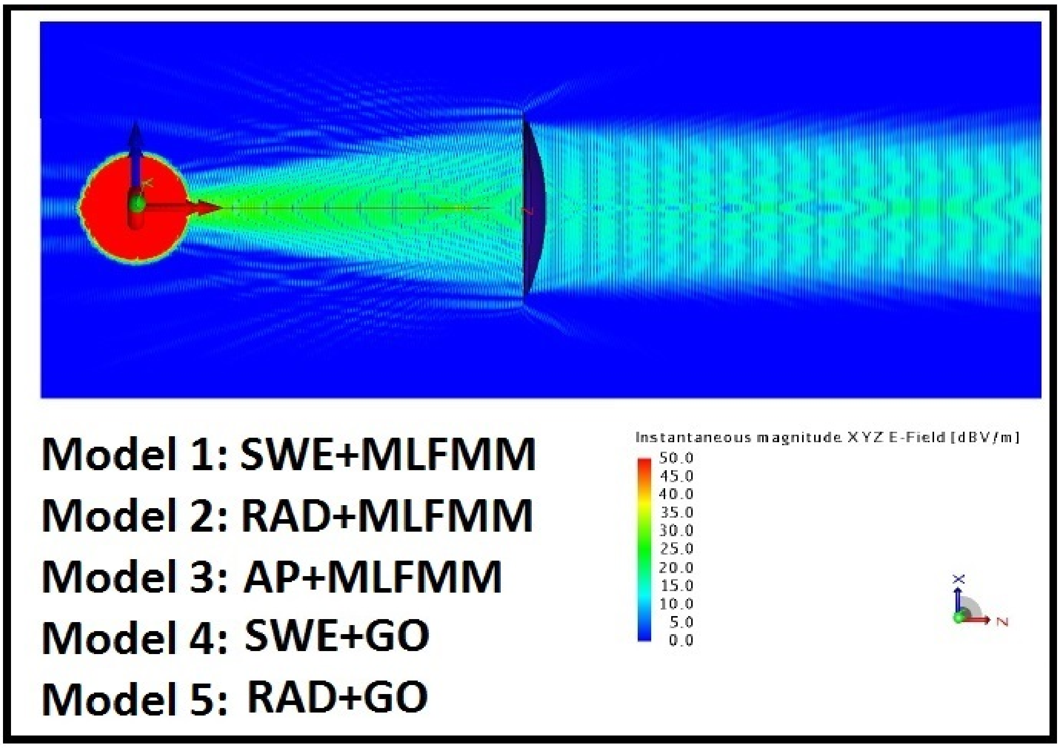

Figure 5.12: The illustration of Models 1,2,3,4 and 5. A combination of equivalent feed sources (SWE, RAD and AP) and lens models (MLFMM and GO) generated 5 different models as listed in left corner of the figure. In all models, lenses were surrounded with PEC lens stop.

The fourth and fifth approaches are based on the use of the other modelling method of the dielectric lenses. RLGO model was chosen because the aperture diameter of the lens with 30λ at 97 GHz is considered large enough to employ this model. Here, the SWE source data was used to illuminate the lens which was modelled by RLGO model.

- **Model 5: RAD + GO**

  Here, a RAD source was used to illuminate the lens which was modelled by RLGO. This model was not employed for the simulations of the small size lens because the far-field conditions could not be met with the specifications assigned for the small lens design.

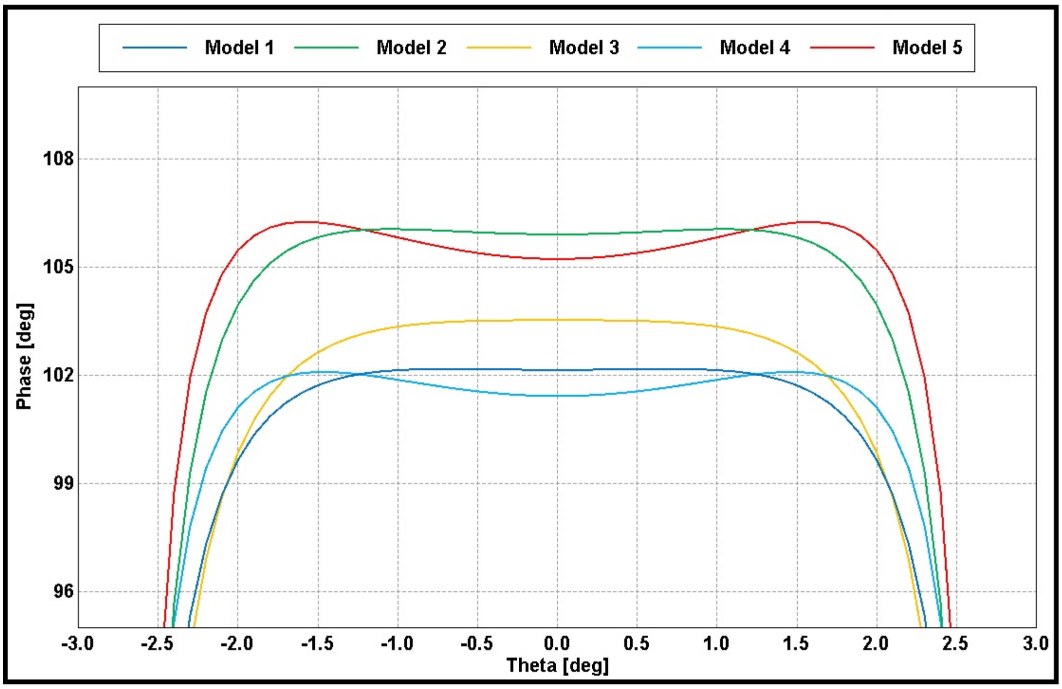

Figure 5.13: Calculated phase patterns of the medium lens design from 5 different models for 97 GHz are shown. The line conventions are given in the figure frame.

5.4.2 Model results

The model results are presented under three headlines: phase, CP and XP field calculations.

- **Phase calculations**

Ideally, the phase center of the horn-medium size lens system (horn-medium lens system) is the second beam-waist of the lens beam. However, we chose the phase center of the horn-medium lens lens system as the middle point of the lens center as shown in the measurement schematics in Figure 6.26. The phase uniformity is still satisfied by using this location. In all models, far field samples were requested over a defined sphere. The center of the far field sphere corresponds to the phase center of the horn-medium lens system. Figure 5.13 shows the predicted phase patterns from the models. A maximum phase difference of 4° was observed between the different models. This is likely due to the difference between the excitation locations of the feed source inputs. In order to determine the exact location of the focal distance of the lens system theoretically, a plane wave was propagated through the lens and the focal spot was noted. The beam was focused within ±0.5 mm of the calculated focal distance of the lens.

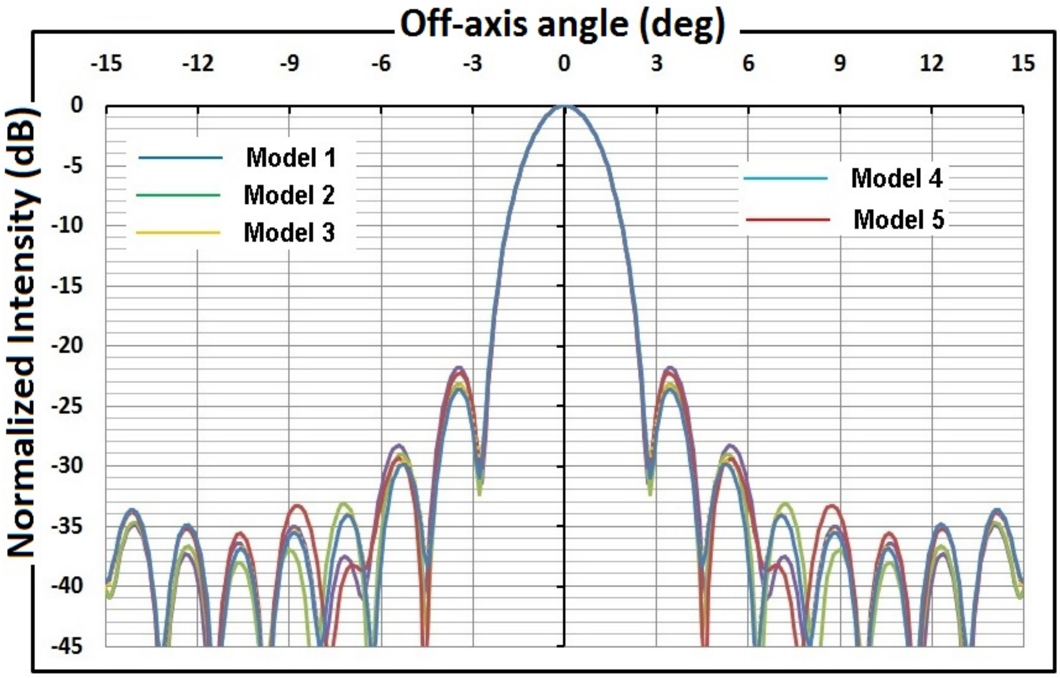

Figure 5.14: Predicted CP radiation pattern calculated with five different models of the horn-lens system. The calculations are for D plane cut for a frequency of 97 GHz. The line conventions are given in the figure frame.

- **CP beam calculations**

The superimposed plots of the CP beam predictions computed with each model show the variations due to the modelling methods are presented in Figure 5.14. The beam patterns were calculated at D-plane for a frequency of 97 GHz. The general agreement between all model results is good. While the lens models (Model 1 and 4) fed by the SWE source gives similar results, the lens models (Model 2 and 5) fed by the RAD sources give similar results for the CP beam intensity patterns. This means that simulation results for the intensity beam patterns are mostly determined by the type of the source data. In general, there is a maximum difference of 1.5 dB between the first side-lobe levels of the different models.

- **XP beam calculations**

The superimposed plots of the XP beam predictions computed with each model show the variations due to the modelling methods are presented in Figure 5.15. The beam patterns were calculated at D-plane for a frequency of 97 GHz. A comparison

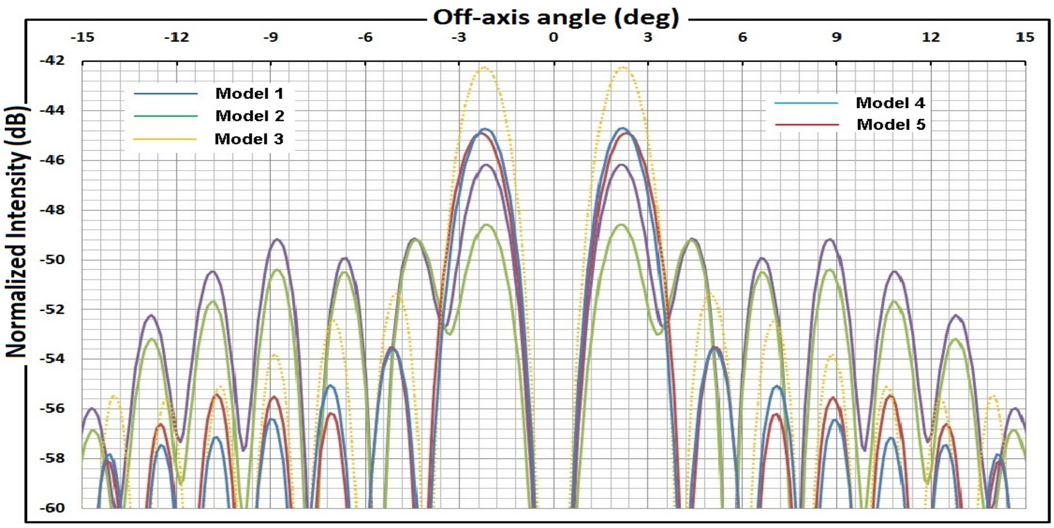

Figure 5.15: Predicted XP radiation pattern calculated with five different models of the horn-lens system. The calculations are for D plane cut for a frequency of 97 GHz. The line conventions are given in the figure frame.

of all model predictions for the maximum XP levels reveals that there is a maximum 6 dB difference. The XP were calculated at the values between -42.2 dB (Model 3) and -48.6 dB (Model 4). While the MLFMM based models give a higher XP, the GO modelled lenses present a lower XP level.

5.4.3 Near-field (NF) models of the medium lens system

A further investigation was made by modelling the near field behaviour of the medium lens system in FEKO. The near field simulation results were then compared to the measurement results given in Section 6.4.6. In the near field lens model, a radiation pattern (RAD) feed input was used as the source of the lens system. The RAD source data was generated from the far-field calculations of the Standard feed horn for 97 GHz. Near field evolution of the lens system for three plane cuts (XY, YZ and XZ planes) are shown in Figure 5.16. The XY plane axis has a range of 250 mm (125 mm to either side of the centre of the propagated beam) and is located at a distance of 405 mm from the phase center of the feed input. Each plane data was calculated with a resolution of 1.8 mm. The resulted beam is almost symmetric and the beam size is limited to the lens diameter with 90 mm.

Figure 5.17 shows the XZ plane cut across z-axis (propagation axis). The distance on the z-axis is measured from the feed location. The electric field is plotted in

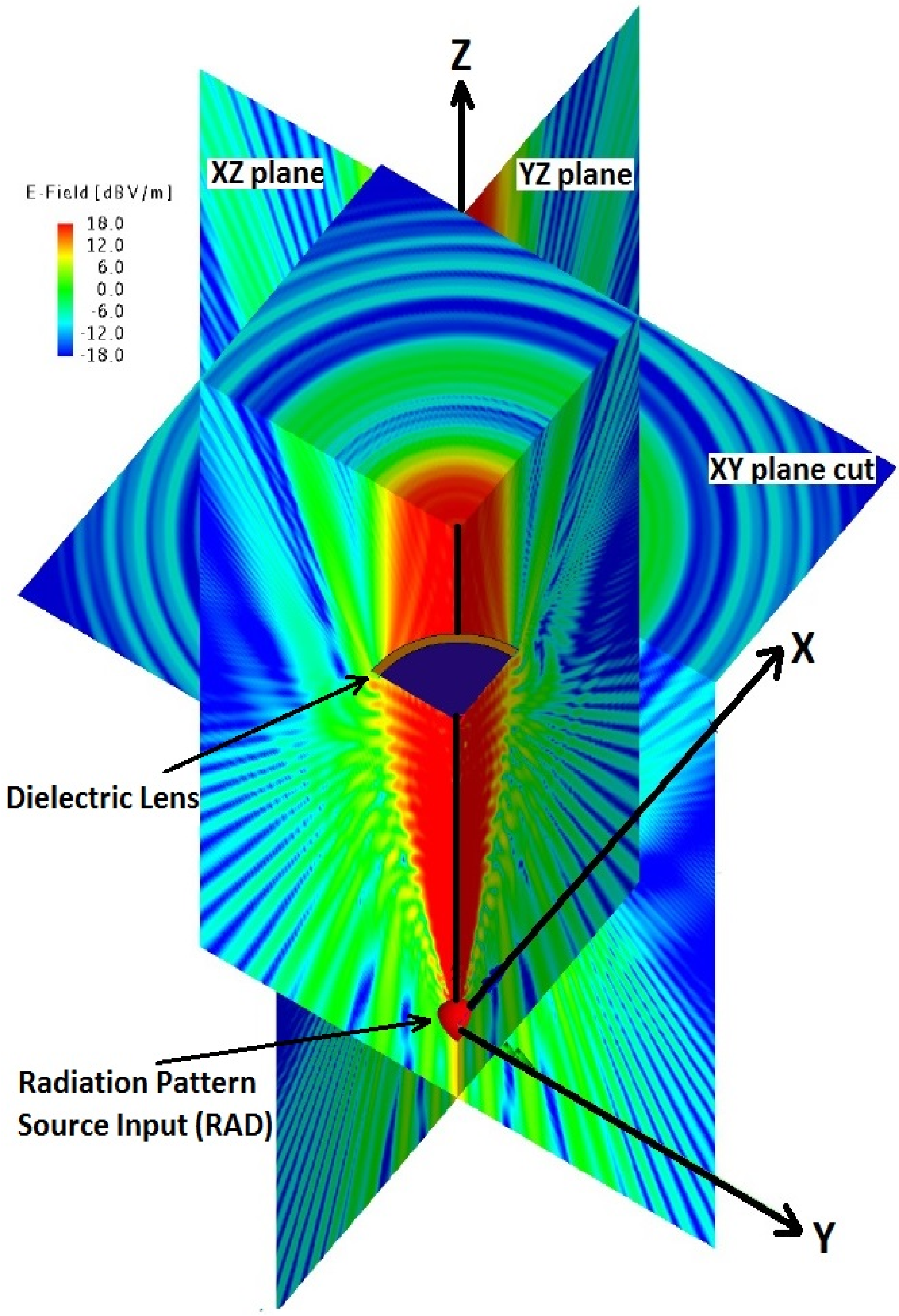

Figure 5.16: Near field evolution of the lens system for three plane cuts: XY, YZ and XZ planes). XY plane cut was taken at 405 mm away from the location of the source input. Field magnitude was amplified until wave-fronts are made visible.

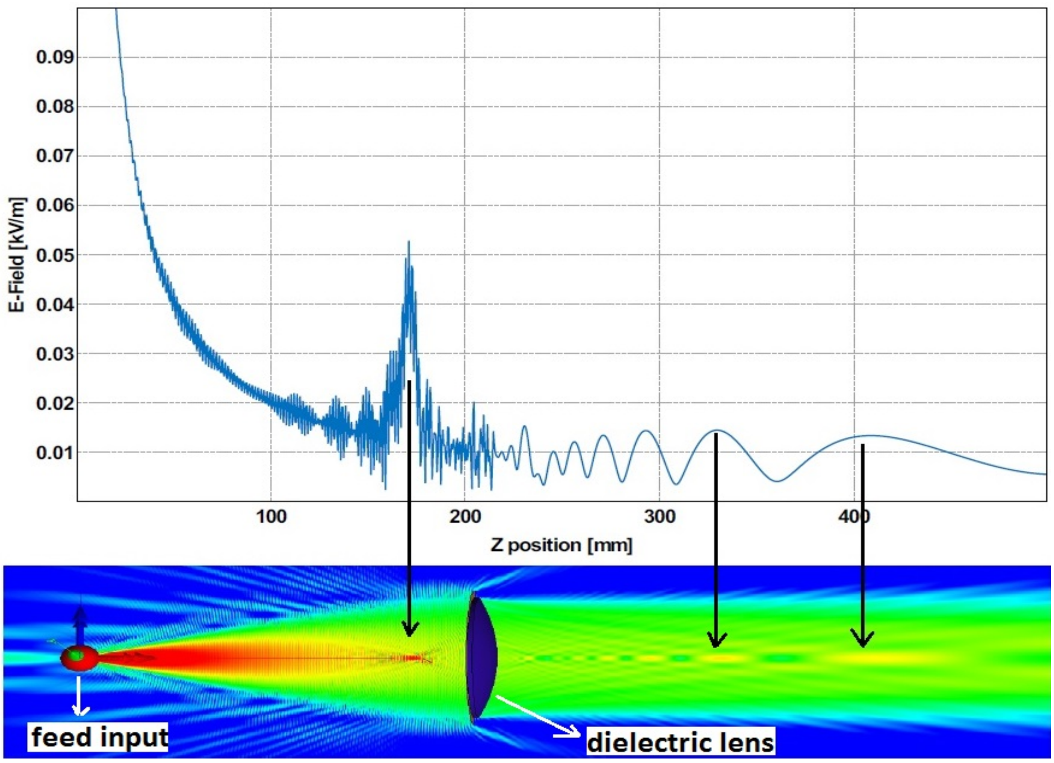

Figure 5.17: The XZ plane cut of lens system across z-axis. Upper figure shows the electric field magnitude in linear scale while lower figure shows the same field propagation on the XY plane. The peak field points in upper figure corresponds to more dense field regions in lower figure and are shown with black arrows.

linear scales and the peak values observed at 329 mm and 405 mm (in upper figure) corresponds to yellow regions (in lower-figure) are shown with black arrows. Largest peak observed at 169.5 mm are resulted from superposition of incidence and reflection beams. Overall, the lens beam has a uniform field magnitude throughout the propagation axis in near field and hence gives rise to a symmetric radiation beam pattern.

Field data calculated for the XY plane cut are plotted in Figure 5.18 for different field peak locations on the Z-axis. All modelled data are compared with the measured lens data in Section 6.4.5.

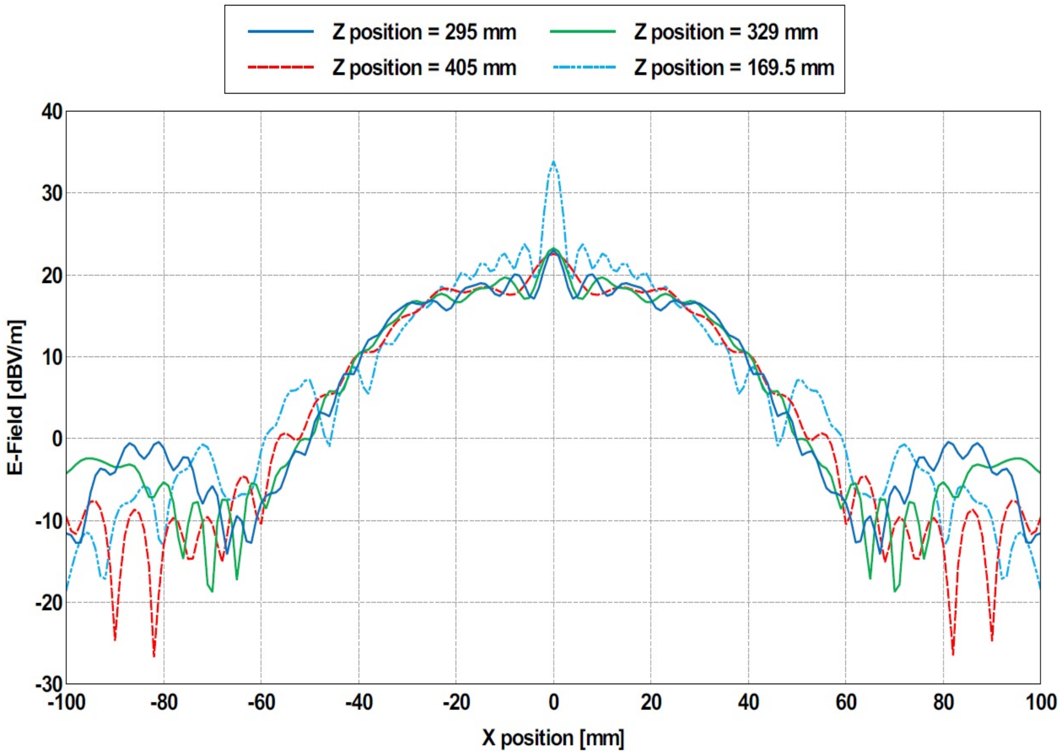

Figure 5.18: Near field plots of the lens system for the different locations on the XY plane cuts. The locations where the near fields are calculated corresponds to the peak field locations observed in Figure 5.17.

5.4.4 Summary from the medium lens models

The simulation details showing the runtimes, memory requirements and the number of meshes are given in Table 5.5. Due to the limited computational resources such as runtime and RAM usage, the full MOM of the feed-horn lens system was not able to run with a memory requirement of 2.2 TB. Therefore, the MLFMM and GO were

Models	BW(E/D/H)	SL (E/D/H)	Max. XP (D)
Model 1	2.176° / 2.189° / 2.201°	23.43 / 23.64 / 23.80	44.7 dB
Model 2	2.169° / 2.179° / 2.189°	22.08 / 22.27 / 22.45	44.9 dB
Model 3	2.167° / 2.181° / 2.196°	23.02 / 23.32 / 23.63	42.2 dB
Model 4	2.195° / 2.199° / 2.203°	22.93 / 23.19 / 23.47	48.6 dB
Model 5	2.185° / 2.191° / 2.196°	21.63 / 21.84 / 22.06	46.2 dB

Table 5.4: Some beam parameters obtained from the model results are given in terms of BW, SL and Max.XP.

Models	Feed/lens model	Runtime (in hours)	Memory req.	# of triangle meshes
Full Model	MOM / MOM	No result	2.2 TB	457736 (λ/6.75)
Test Model	SWE / MOM	447.5	800 GB	221684 (λ/6.75)
Model 1	SWE/MLFMM	41	29 GB	221684 (λ/6.75)
Model 2	RAD/MLFMM	3.8	29 GB	221684 (λ/6.75)
Model 3	AP/MLFMM	25.5	15 GB	221684 (λ/6.75)
Model 4	SWE/GO	12 mins	15 MB	27711 (λ)
Model 5	RAD/GO	1-2 mins	27 MB	27711 (λ)

Table 5.5: The computational requirements of the different models are detailed in terms of solution times and memory requirements. The table also gives information on the mesh numbers used to model the medium lens system.

used to model the horn-medium size lens system. A substantial difference between the computational requirements of the MLFMM and the GO models should be noticed.

In all models, the lens was encircled by a perfect electric conductor (PEC) ring as a lens stop defining the clear aperture of the lens to simulate the mount used in the far-field measurements. This increased computation requirements by 20%.

Table 5.4 presents the calculated beam parameters from each model for the E,D and H plane cuts for 97 GHz. The accuracy of the calculated parameters given in the table can be assessed after they are compared with the experimentally measured data. However, the most significant difference to emerge from the data is that XP levels calculated from the different models deviate up to 6 dB. In particular, the models that the dielectric lens was simulated with the GO give very small values of XP with -48.6 dB. The model investigation shows that the XP results are mainly governed by the lens model while the main beam shape of the CP is determined by the feed source model.

5.5 Simulation details

- **Effect of the metallic lens stop**

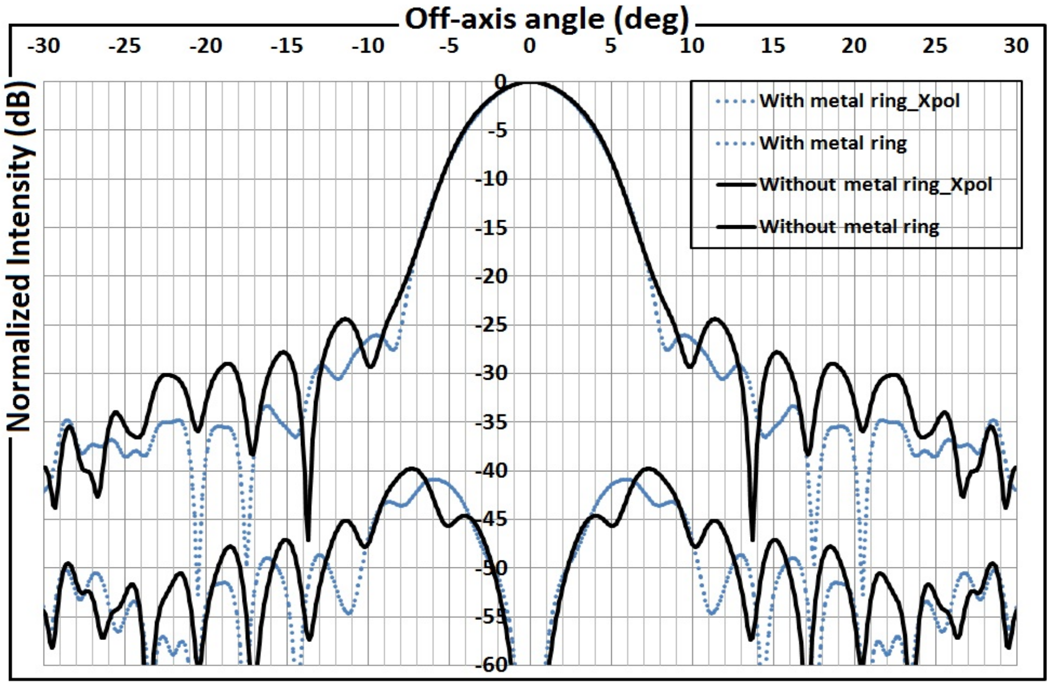

Figure 5.19: The logarithmic scale plots of the intensity beam patterns. The far-field CP and XP field intensity of the horn-small size lens system were predicted for the models with and without metal ring used as the lens stop.

In all models, the lens was encircled by a perfect electric conductor (PEC) ring as a lens stop, defining the clear aperture of the lens. It was aimed at simulating the lens mount used in the measurements. The run-times and memory requirements of the feed horn-lens simulations with and without the metal ring are given in Table 5.6. Both models are the same as those of the small lens models. The introduction of the metal ring increased the computation requirements, in particular the runtime, by 25% to 35%. The calculated intensity patterns from the model 2 with and without the metal ring are compared in Figure 5.19. As seen in the comparison of the measured beam patterns with the simulated beams in the next section, the agreement between the measured and predicted beam patterns was considerably improved with slightly lower side-lobe and CP levels thanks to the introduction of the PEC lens stop. Therefore, all lens models discussed previously had a PEC lens stop.

Models	Solution times (with/without ring)	Memory requirements (with/without ring)
Model 2	(29.5 / 21.1) hours	(122.5 / 78.7) GB
Model 3	(16 / 12) hours	(11.5 / 11.25) GB

Table 5.6: The computational requirements (e.g. solution time and memory requirement) are compared for the models with and without a metal stop ring around the dielectric lens.

Additionally, the effect of the metal stop diameter on the beam pattern was investigated. The modified model had a lens stop with a %20 larger diameter than the lens stop of the nominal model. A beam pattern difference of 0.4 dB in the first side-lobe level was observed and there were beam differences by a few dB in second and later beam side-lobes. Also, a very low level difference with 0.016% between two model predictions for HPBW values was calculated.

- **Tolerances on lens thickness and refractive index**

Setting $\frac{\lambda}{32}$ rms in the optical path length as the upper limit on wavefront irregularities, the corresponding phase shift becomes 11.25° [130]. Thickness tolerance for a given dielectric in terms of free space wavelength becomes $\Delta t = 0.06\lambda_0$ for this phase shift value. The corresponding tolerance on refractive index is $\Delta n = \frac{0.03}{t}$ where t is the lens thickness.

For example, this value becomes 180 microns for the UHMWPE material with a refractive index of 1.517 at 97 GHz (λ_0=3.09 mm). The thickness of the medium lens designed for my research was measured as 12.28$\pm$0.03 mm. An uncertainty of 30 microns in the thickness measurements remains within the thickness requirement calculated above (180 micron) for the UHMWPE dielectric. Correspondingly, the tolerance on refractive index variation was calculated as 0.0025 for this dielectric thickness. The refractive index of the same dielectric was measured as 1.517 ± 0.001 and acceptable for the criteria given above. Errors in the refractive index calculation are calculated from the combination of the dielectric thickness and measurement variations.

The effect of thickness accuracy was simulated by comparing two lens models in FEKO. The lenses of two models have a 30 micron thickness difference. The analysis showed that the HPBW value of the comparison model differed by 0.073% from the nominal model. The levels of the XP and the side-lobes were identical up to the off-axis angles of 60°. After this angular level, there were minor variations between two beam patterns below 0.4 dB.

The other analysis was made to determine the tolerance on the refractive index in [131]. The analysis showed the power coupling loss of an optical system with refractive index variation as shown in Figure 5.20. The power coupling efficiency at the nominal focus position between the nominal focused beam and the defocus beam at the same position of the nominal focus was calculated. A change of 10^{-4} in refractive index results in a drop in power coupling efficiency of 1%. Therefore, knowing the refractive index to four decimal places is mandatory for high performing optics.

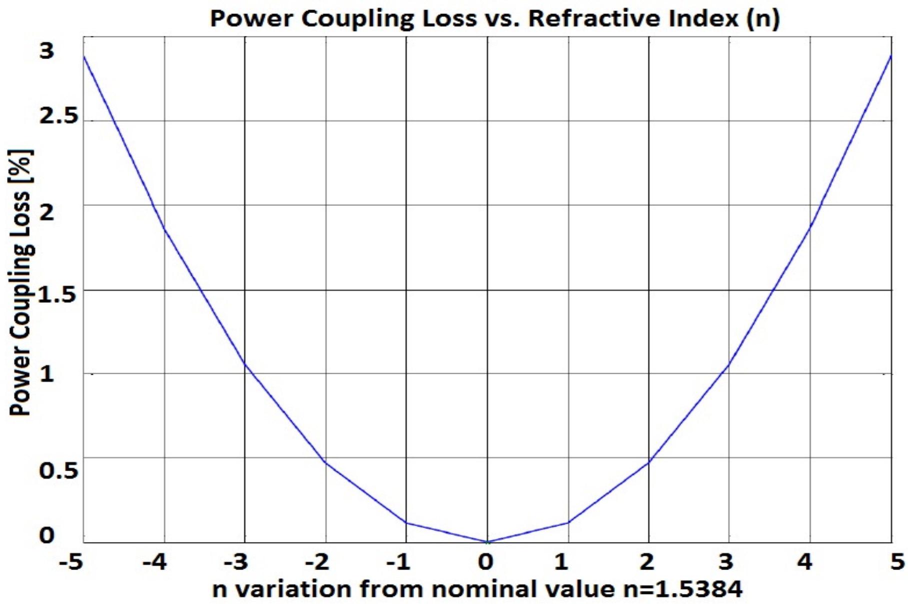

Figure 5.20: Power coupling loss versus refractive index variation. The nominal value for refractive index is 1.5384 and varies by 10^{-3} along x-axis.

- **Mesh size dependence**

In all lens simulations the mesh size was kept fixed. Edge length of triangular mesh element was selected as $\lambda/6.75$ to reduce the computational requirements. The recommended value from the FEKO tutorials was $\lambda/8$. Two different models were compared for beam pattern shape. It was found that mesh size change from $\lambda/6.75$ to $\lambda/8$ did not have a significant impact on the beam pattern. The two models were different with less than 0.5 dB at very far off-axis angles of the radiation beam pattern ($\geq 60°$). Also, a difference of 0.016% was calculated in the predicted HPBW values.

5.6 Conclusion

In this chapter, the model analysis of the horn-lens systems was investigated. First, the use of the lens stop for the dielectric lens was found necessary to define the beam size precisely and to mimic the same configuration used in the measurements. The computational resources increased by 20% by the introduction of the stop.

Second, the full-wave model calculations of the entire lens system (a standard feed horn + dielectric lens) by using the Method of Moments were only possible up to $D \cong 20\lambda$ considering the design frequency of 97 GHz ($\lambda = 3.09mm$). The maximum diameter of the dielectric lens which can be modelled by MOM can be increased by using a smaller size feed antenna. The full model (Model 1) results were also compared with the approximate models (Model 2,3 and 4) of the lens system. In these approximation models, the equivalent sources to the Standard feed horn were preferred. Thanks to these new approaches, the computational requirements were dramatically decreased with a factor 24 in runtime and a factor 44 in memory requirement. The beam difference between the results was calculated as below -23 dB. The most striking result to emerge from this model investigations is that the MLFMM and the MOM were consistent for the simulations of the dielectric lenses.

MLFMM and RLGO can also be used for analysis of lenses with diameters larger than 30λ. These lens simulations can be achieved by using the equivalent feed-inputs to the Standard feed horn (e.g. the SWE, the AP and the RAD). In this investigation, I first questioned the consistency of the MLFMM and GO model calculations. Also, I studied what the maximum lens size can be modeled with the existing models considering the model limitations such as computational requirements.

- **Lens diameters** $\sim 75\lambda$

A spherical surface plano-convex lens with a diameter of 225 mm has been modelled with both MLFMM and RLGO. This lens size corresponds to $\sim 75\lambda$ in terms of wavelength of 3.09 mm (97 GHz). The metallic lens stop was not used in the lens design because I aimed at studying only maximum lens diameters that can be modelled with the existing models. The first side-lobe and the XP levels were predicted to be 0.5 dB and 1 dB lower by RLGO. Except for this difference, general agreement between two models was very good up to very far off-axis angles (50°) as shown in Figure 5.21.

- **Lens diameters** $\sim 90\lambda$

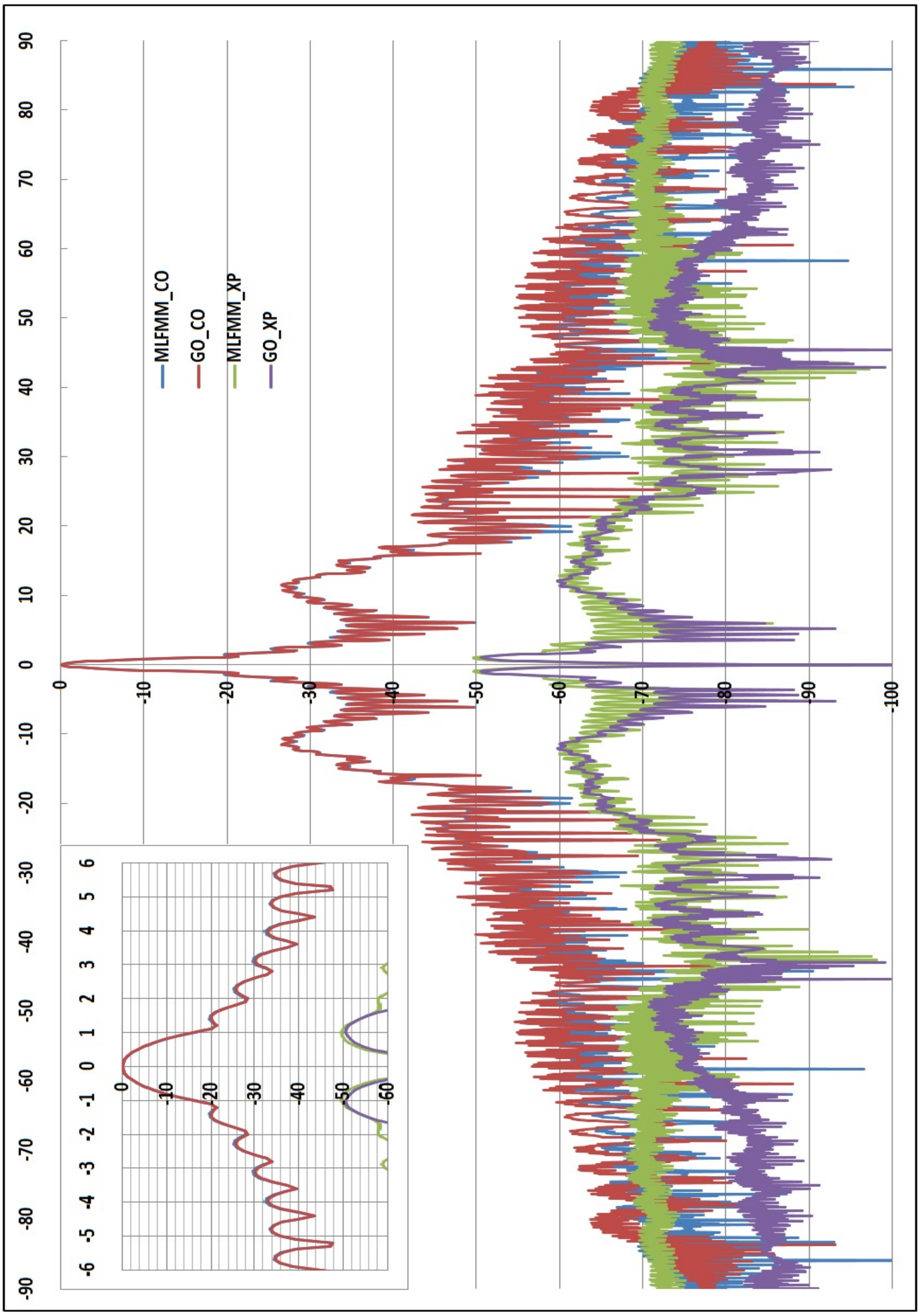

Figure 5.21: Figure shows the overlapped intensity beam patterns predicted by the MLFMM and the RLGO models. The large figure shows the general agreement between the model results extending up to very far off-axis angles. The small figure zooms out the detail in the directed beam angles.

Depending on the different feed inputs and the mesh size defined for lens simulations, the MLFMM model was used to model the lenses with diameters up to 90λ. For instance, the MLFMM simulation of 75λ size lens with the illumination of the SWE and the AP feed inputs could be successfully modelled. The simulation took ~ 200 hours. When the RAD source input was used, the diameter of the MLFMM modelled lens could be increased up to 90λ.

- **Lens diameters** $\geq 150\lambda$

There is no measurement validation of these results. However, it is very promising to know that RLGO model is in agreement with an approximate model of the MOM, MLFMM. As the lens size increases up to $\geq 150\lambda$, the GO model becomes more suitable for lens simulations. In order to sustain this agreement, the ray launching process, which is the basis of RLGO model in FEKO, requires more rays to accurately define the interactions between the source and lens. This increased the simulation runtime considerably. For example, a simulation of 75λ lens took ~ 100 hours.

In order to save time and memory in the simulations, the symmetric planes were defined in FEKO models. This was only possible with the on-axis lens models. Therefore, a clear benefit of symmetric planes in the simulation performance achieved with the on-axis lens models could not be identified in the off-axis lens models.

Chapter 6

CHARACTERIZATION OF ON-AXIS HORN-LENS SYSTEMS

This is the first of two chapters that discuss the characterization of the horn-lens systems. Following the introduction of the measurement setups used for the lens characterization, far-field measurements of an on-axis horn-lens system were studied using a small size lens. Based on the experience acquired from the small lens study, the characterization procedure is repeated for a medium size lens with and without anti-reflection coating (ARC). The subsequent chapter presents the results for the characterization studies of the off-axis horn-medium lens system. The simulations of the lenses were presented in Chapter 5. Instead of optimizing the lens design, this chapter compares the present lens model with measured data.

6.1 Description of the Measurement Setups

These simulations are validated through experimental measurement.In order to perform the measurements of the electric field, test facilities dedicated to measurements of horn-lens systems were specifically needed. There were two lens systems (horn-small size lens and horn-medium size lens) to be measured. Far field measurements of both lens systems were realized with a far-field test facility. The far-field test setup was developed using the existing beam-scanning system, a part of the RF laboratory of the technology group at JBCA. The existing system was used as a test arrangement for azimuthally scanning beam measurements in horn-to horn systems. With the modified test system, on-axis co-polarization and cross-polarization beam pattern measurements

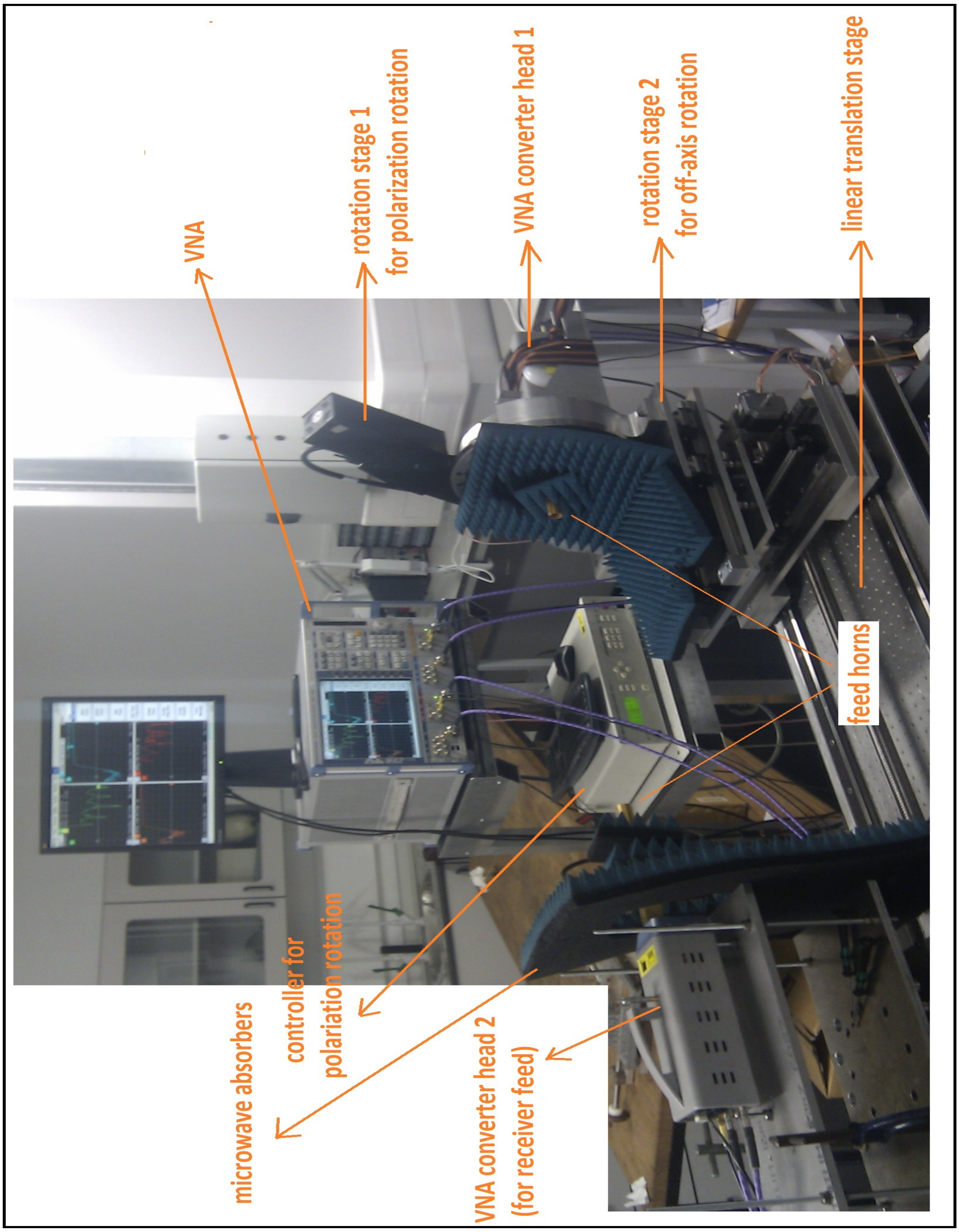

Figure 6.1: The image shows the arrangement of far-field measurement test setup. The entire system is located on a sliding linear platform. The VNA converter heads the VNA set feed two Standard feed horn antennas. Two rotary stages are for controlling the polarization and off-axis rotations. The metal parts in the path of the beam and around the transmitting and receiving horns are surrounded with MM-wave absorbers. This test facility allows the co- and cross- polarisation measurements of an antenna system to be performed.

of two lens configurations have been conducted. Additionally, the far-field test facility was partly modified so that off-axis pixel measurements of the horn-medium lens system could be taken. Also, the field measurements of the second lens system were performed through the use of a near field 3D scanner.

Here, the far-field measurement system and the near field 3D scanner system are introduced with their related system components e.g. Vector Network Analyzer (VNA) and feed-horn antenna.

6.1.1 Far-field measurement set-up

The experimental arrangement is shown in Figure 6.1. This system consists of two parts: electronic components and mechanical components.

The main electronic component is a VNA set. A VNA is capable of characterizing any complex electrical system, by measuring the amplitude and phase of the electric field over a frequency range. JBCA RF lab has the VNA model of the Rohde&Schwarz (RS) ZVA-40 [131]. This model has a frequency range of 300 kHz to 40 GHz. For our measurements, the VNA set is supported with two converter heads (RS ZVA-110) that increase the frequency range of the VNA to the W band (75-110 GHz). Each converter head is connected to a feed horn antenna via a WR10 waveguide. The VNA system has two port elements that measure S parameters, which give the reflectivity and transmittance of the components under test (CUT). The relationship between the incident and the reflected voltages at each port is

$$S_{ij} = \frac{V_i^-}{V_j^+}\Big|_{V_k^+=0, k\neq j}. \tag{6.1}$$

The S parameters can be converted into decibels, for convenient plotting of transmission and return loss patterns,

$$RL_{ii} = 10log_{10}(|S_{ii}|^2) = 20log_{10}|S_{ii}| \tag{6.2}$$

$$IL_{ij} = 10log_{10}(|S_{ij}|^2) = 20log_{10}|S_{ij}| \tag{6.3}$$

For a two-port VNA system, the scattering matrix below yields $V_1^- = S_{11}V_1^+ + S_{12}V_2^+$ and $V_2^+ = S_{21}V_1^+ + S_{22}V_2^+$.

$$\begin{pmatrix} V_1^- \\ V_2^- \end{pmatrix} = \begin{pmatrix} S_{11} & S_{12} \\ S_{21} & S_{22} \end{pmatrix} \begin{pmatrix} V_1^+ \\ V_2^+ \end{pmatrix}$$

The physical system described by the scattering matrix is illustrated in Figure 6.2.

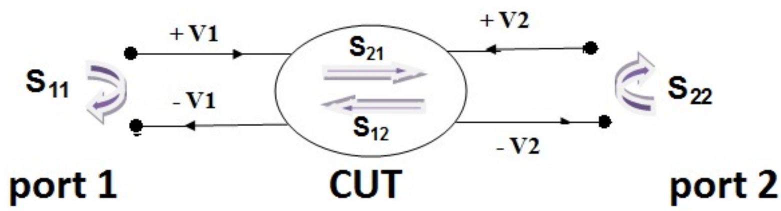

Figure 6.2: The figure illustrates the signal flow for a 2-port VNA system. The CUT (Component Under Test) modifies the incident voltage signal and generates the reflected and transmitted voltage signals. The incident and reflected voltages are indicated by + and - respectively.

The mechanical parts of the measurement setup comprise a sliding linear stage and two rotary stages shown in Figure 6.1. The sliding linear stage is used to move the feed horn-lens system, or the components, with respect to the receiving antenna. The transmitting feed-horn antenna assembly is mounted to two rotary stages. The rotation stages perform off-axis angle (θ) and polarization angle (ϕ) rotations. A gear system performs the beam spanning by rotating the feed horn-lens system around its phase center. Gear motor scanning, data acquisition and real-time data display are accomplished through a labview code.

Various views from the measurement setup are also given in Figure 6.3. The far-field distance (FFD) of an antenna system is calculated by Equation 6.4.

$$FFD = 2 \cdot \left(\frac{D^2}{\lambda} \right) \tag{6.4}$$

D is the aperture diameter of the antenna, and λ is the operating wavelength. For example, the far field beam pattern measurements of the Standard feed horn-small size lens antenna system require the horns to be separated by 150 cm. Figure 6.4 shows a schematic of the test set-up for the horn-lens systems. The phase centre of the feed-horn antenna is located at the focus of the dielectric lens.

- **Measurements of the radiation beam pattern cut**

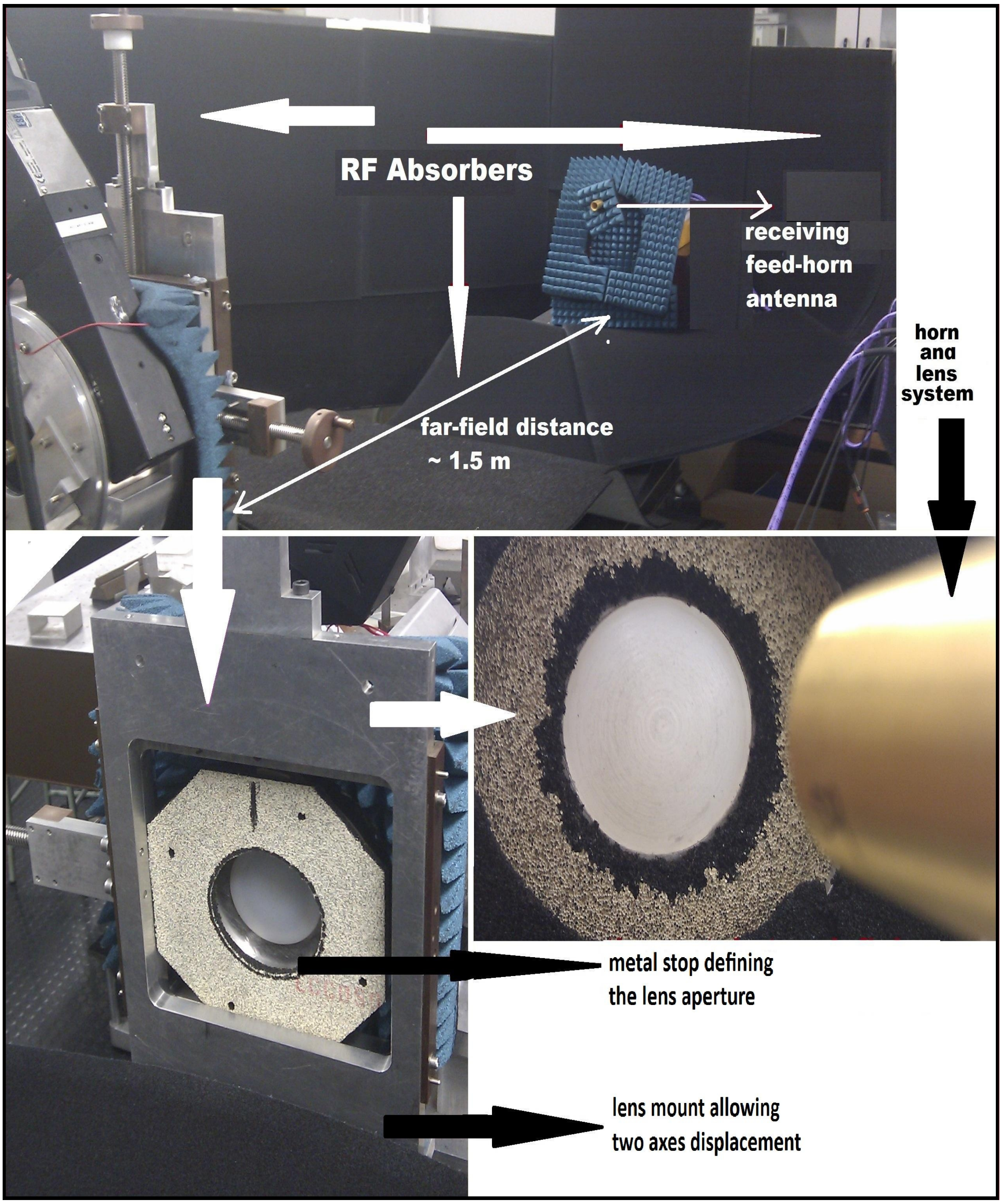

Figure 6.3: Various views of the horn-lens beam pattern measurement set-up. Upper image shows a wide angle view of the far-field measurement setup of the horn-small size lens system. The entire system is surrounded with MM-wave absorbers to generate a low-noise measurement environment. The distance between the lens aperture and the receiver horn antenna is greater than 1.5 m. The bottom-left image shows the metal frame lens mount. The frame allows dual axes displacements for lens alignment. All metal surfaces of the metal frame are covered with absorber during measurements. The bottom-right image shows the horn-small lens system and the MM-wave absorber used around the lens.

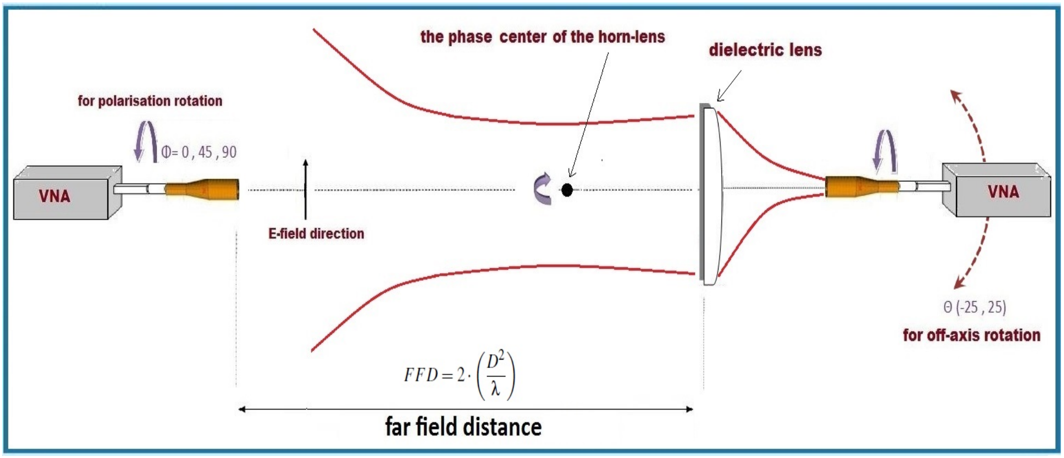

Figure 6.4: The figure shows the polarization orientation (ϕ) and the off-axis angle orientation (θ) of the measurement set-up. The VNA head coupled to the dielectric lens is the transmitter and the other VNA head is the receiver. The polarization orientations of the receiver can be changed by inserting 45° and 90° waveguide twists. Two rotary stages shown in Figure 6.1 are used to realize these polarization and off-axis angular orientations. For off-axis rotations, the system is rotated around the phase center of the horn-lens system shown by a thick black dot in the figure. The far-field distance is set by the lens diameter D, and the operating wavelength λ.

For the polarization measurements of the lens system, six plane cuts of the angular beam pattern are required: three co-polarization cuts and three cross-polarization cuts. Each VNA head has a rectangular waveguide which sets the direction of the electric field. The horns mounted on each of the VNA heads is matched through a rectangular to circular waveguide transition (TRC). The transmitting and receiving antennas have a parallel polarization orientation when the co-polarization measurements are performed. The cross-polarization measurement are taken when the transmitter and receiver have an orthogonal linear polarization orientation. Pattern cut orientations can be changed by inserting waveguides with 45° and 90° twists. The measurements of the far field radiation patterns are taken across off-axis angles of $\pm 25°$ with an increment of $0.1°$. Four S-parameters (S_{11}, S_{12}, S_{21} and S_2) are recorded over all frequency values of the W-band.

- **Antenna Beam Parameters**

  Figure 6.5 shows a three dimension (3D) antenna beam pattern. The beam pattern is composed of the MOM model results of the Standard feed horn discussed

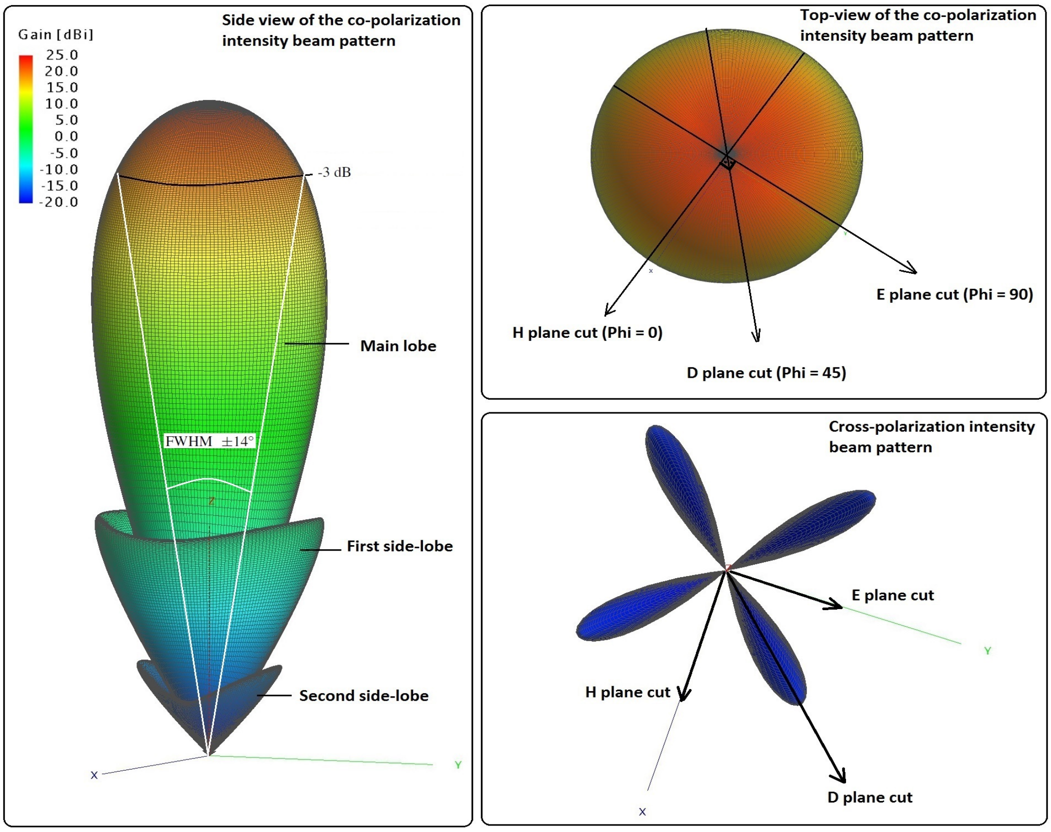

Figure 6.5: A typical 3D intensity beam pattern with the main characteristics of the antenna beam: Main-lobe, FWHP and side-lobes. The beam pattern is from the Standard feed horn. The upper-right figure shows the top view of the 3D beam pattern with plane cuts. The lower-right figure shows the cross-polarization beam pattern of the Standard feed horn. The cross-polarization is maximum at the D plane cut and should not exist for the E and H plane cuts.

in detail in Section 3.7.1. A radiation beam pattern shows the field/power distribution of an antenna or an antenna system with respect to the off-axis angle. The left hand side figure shows a 3D view of the co-polarization intensity beam pattern. In the diagram, the main beam lobe describes the region radiating the maximum power. The region is limited between the first nulls of the antenna power. The characteristic of the main beam is determined by the Full Width at Half Maximum (FWHM). This is also called the half-power beam width (HPBW). This value corresponds to the angle value read at 3dB level of the normalized intensity pattern. The 3 dB level is where the power is one half the maximum value of the beam. For a simple circular aperture antenna, FWHM (in radians) is approximated by $\frac{\lambda}{D}$. However, a more general description for the FWHM of a circularly symmetric antenna illuminated by a Gaussian beam is given by Equation [128] as

$$FWHM = [1.02 + 0.0135T_e(dB)]\frac{\lambda}{D} \tag{6.5}$$

where T_e is the edge taper value of the antenna aperture for a given Gaussian beam illumination. The side-lobes are defined as any lobe other than the main lobe. They are expected to have very low relative power compared to the main lobe for a very effective antenna system. The upper-right part of Figure 6.5 shows the top-view of the 3D beam pattern with plane cuts, which represent reference planes for a linearly polarized antenna. For example, the E-plane is parallel to the polarization direction of the antenna and H-plane is the orthogonal plane of the E-plane. The H-cut, E-cut and D-cut are the planes for $\phi = 0°$, $\phi = 90°$ and $\phi = 45°$, respectively. The bottom right part of Figure 6.5 shows the cross-polarization pattern of the Standard feed horn. The feed generates a single hybrid mode, HE_{11}. The maximum cross-polarization is observed at the diagonal plane cuts $\phi = 45°$ and $\phi = 135°$.

6.1.2 Near-field measurement set-up

Near field space is defined as a region between the antenna aperture and the far field distance. Due to large space requirements of far-field measurement space, a near field 3D beam scanning system for MM waves was developed at JBCA [132]. The scanner system has a scanning volume of 50 cm x 50 cm x 50 cm as shown in Figure 6.7. The system generates a map of the 3D near field beam with a mechanical positioning accuracy better than 0.1 mm. The W-band VNA set used for the far-field measurement setups was used for feeding the 3D scanner system.

The 3D near-field scanner system comprises two parallel Z-axis and one X-axis belt driven rails supported by an aluminum frame. The VNA converter head is mounted to the Y axis carriage. This carriage system is movable and translates the VNA converter head along Y-axis. This Y-axis screw driven rail is mounted to the X-axis rail.

A WR-10 rectangular to circular transition waveguide is used as measurement probe. The circular aperture probe has a clear aperture size of 3 mm. It presents a

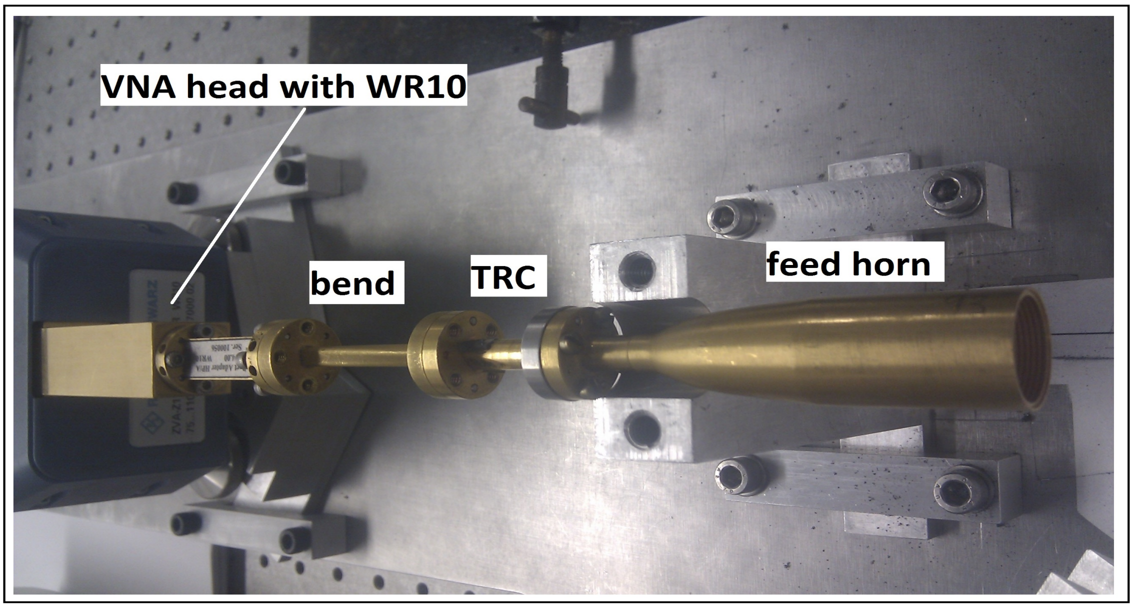

Figure 6.6: A transmission chain for a VNA converter head. Standard feed horn is coupled to the VNA converter head through the rectangular to circular waveguide transition and a 45° twist.

return loss of -34.4 dB at 100 GHz. A dielectric piece of plastic absorber with a pyramidal shape was used to surround the probe in order to reduce reflections.

The stability of the VNA used for the 3D scanner system was tested by Peter Schemmel. The system was left in a scanning position and S_{21} and phase data were recorded for 18 hours at one minute intervals. Figure 6.8 shows that peak to peak signal varies within 0.6 dB in intensity and 4.5° in phase at 100 GHz.

6.1.3 Alignment procedure

Alignment was the most difficult part of the measurement process because both transmitting and receiving antenna systems were not located on the same translation platform. The transmitting antenna, which illuminates the lens, was kept on the linear sliding platform. The receiving antenna system was moved to an optical table. The lens and feed are separated by the focal length. A laser pointer was then used to align the setup. A metal reflector was placed in front of the metal frame holding the lens as shown in Figure 6.9. A point on the reflector matching up with the center of the lens aperture was marked. On the other side of the setup, the receiving VNA converter head was removed from the horn and the laser beam was shone through the horn directly

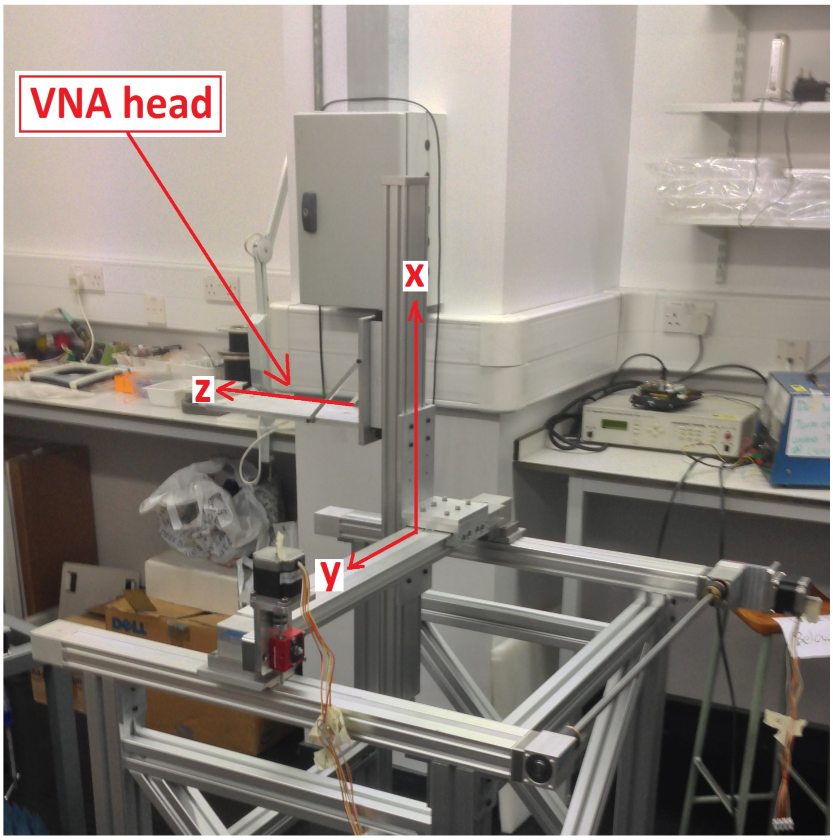

Figure 6.7: 3D scanner system used for near-field measurements. The system has a scanning volume of 50 cm x 50 cm x 50 cm. The VNA head is located at the position indicated in the photo. The 3D near field scanner system is supported by a 1 metre high aluminum frame.

along the propagation axis. The antenna mount was adjusted until the laser beam was reflected back from the marked point on the reflector and dropped into the exit aperture hole of the laser beam. In this fixed position of the Standard feed horn, the reflector and the laser system were removed and replaced with the VNA converter head. This is of course not a sophisticated way to align the antenna system. However, the uniform phase and the symmetric beams in the measured beam patterns show that this method was adequate.

The linear micrometer was used to make the final touches to align the measurement setup. Basic indicators of the setup alignment on the beam pattern are phase and symmetric beam patterns. The target of phase uniformity is achieved by adjusting the feed position relative to the lens position with very fine shifts. This last alignment attempt can also help to mitigate the positioning errors of the components.

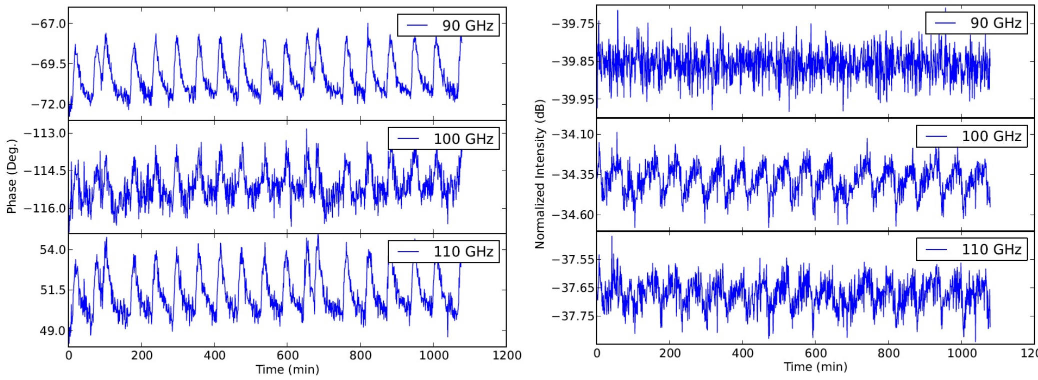

Figure 6.8: Stability tests applied to the VNA used for the 3D scanner system. Left figure shows the phase variations while right figure shows the variations in S_{21} (transmission intensity) over a time period of longer than 1000 minutes. Each graph has three plots for frequency values of 90, 100 and 110 GHz.

6.1.4 Calibration

The components used in the measurements induce errors in the measurement data. For an accurate measurement, the measurement system requires calibration to remove these errors. Performing calibration carefully, with high performance tools such as test cables and adaptors, is extremely crucial. A prerequisite list to perform an accurate measurement is given below.

- A stable temperature environment should be generated. The variations in temperature may result in expansion of the waveguide components that give rise phase drift in data.
- The cables should be fixed both during the calibration and the actual measurements. Moving the cables cause phase variations.
- The power on the VNA converter should be kept fixed during the calibration.
- Reducing the IF bandwidth to 100 Hz may help to suppress the noise figure and increase the dynamic range to around 120 dB. The IF bandwidth should be fixed from the calibration through the actual measurements.

The measurement accuracy depends strongly on the calibration choice. Various calibration techniques are available [131]. However, the best methodology, considering the measurement setup and the device under test should be chosen. Through, Short,

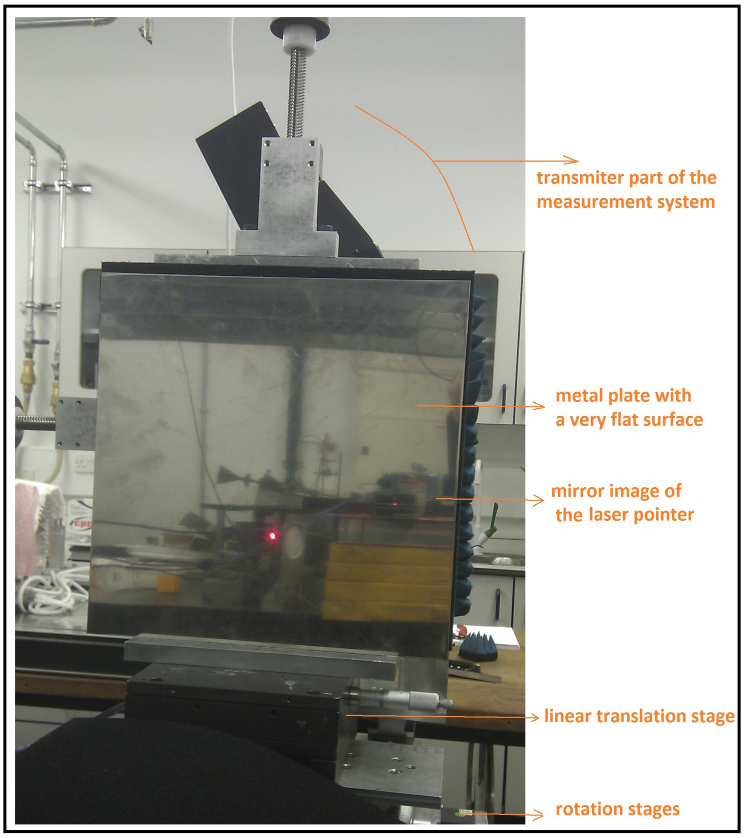

Figure 6.9: An image shows how the far-field measurement setup was aligned using a laser beam. A metal reflector was used to reflect the laser beam back and to drop the beam into the exit aperture of the laser beam.

Offset short and Match (TOSM) calibration standards were chosen for the calibration of the two-port network. Seven measured standards are required. They are Short, Offset short and Match on each port, and one Through measurement done by connecting the two waveguide flanges directly. This calibration choice is suitable for transmission and reflection measurements of the components under test. Through standard calibrates the insertion loss of the system. The Short and Match calibrations determine the reflection coefficients. A shim for offset short calibration allows a 180° phase shift in the reflection coefficient by introducing a transmission line of $\lambda/4$. This calibration is achieved by connecting the offset shim to the short. An accurate reflect standard is achieved by differentiating these two calibration standards. The sliding match can also be replaced by the fixed match for an accurate calculation of the systematic errors. The calibration kit for Rohde-Schwarz ZV-WR10 was used in the calibration process shown in Figure 6.10. After the calibration is completed, the error terms are calculated

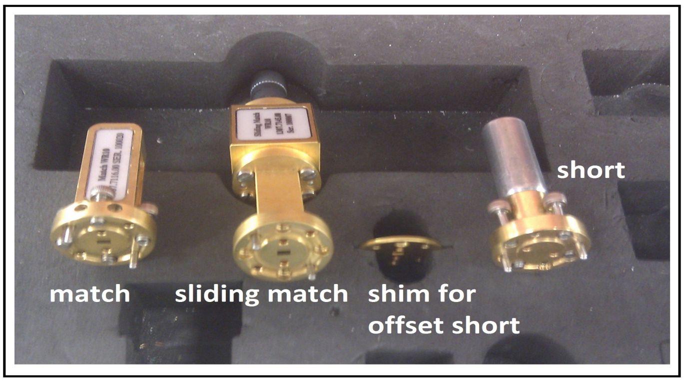

Figure 6.10: The image shows the calibration kit of Rohde-Schwarz ZV-WR10. The calibration kit was used to calculate the 7 calibration standards for the TOSM calibration. Pins fabricated around the waveguide flanges help to align the components correctly.

by the VNA.

6.1.5 Error analysis

On the one hand, full-wave model solutions of an electromagnetic problem (EM) simulate the propagation of EM energy under very ideal conditions such as homogenous and isotropic media. On the other hand, measurements of the equivalent EM system to the EM model problem in real world applications suffer from hostile and anisotropic measurement environments. The measurement accuracy can be improved by repeating the measurements multiple times. The following points discuss how to conduct more accurate measurements by understanding the measuring instruments better.

- **Error bars**

The measurement results of the horn lens system given in all sections are presented with its associated error bars. These error bars show the standard deviation between measurements. Measurements were repeated 3 to 10 times according to variations in measured intensity results. This error analysis was performed for each measurement, in order to compare the data with the model predictions.

- **Signal to noise ratio (S/N)**

The error bars become large due to signal variations at low signal level. The quality assessment of a measurement system is described by the signal to noise ratio (S/N). The

S/N is different for different measurement systems since the radiation power attenuates with distance and each lens system has different far-field distance. The noise level of our measurement system can be determined by blocking the radiation coming out of the transmitting feed-horn with microwave absorbers. In particular, the S/N ratio is important for XP measurements, which have very low signal strength.

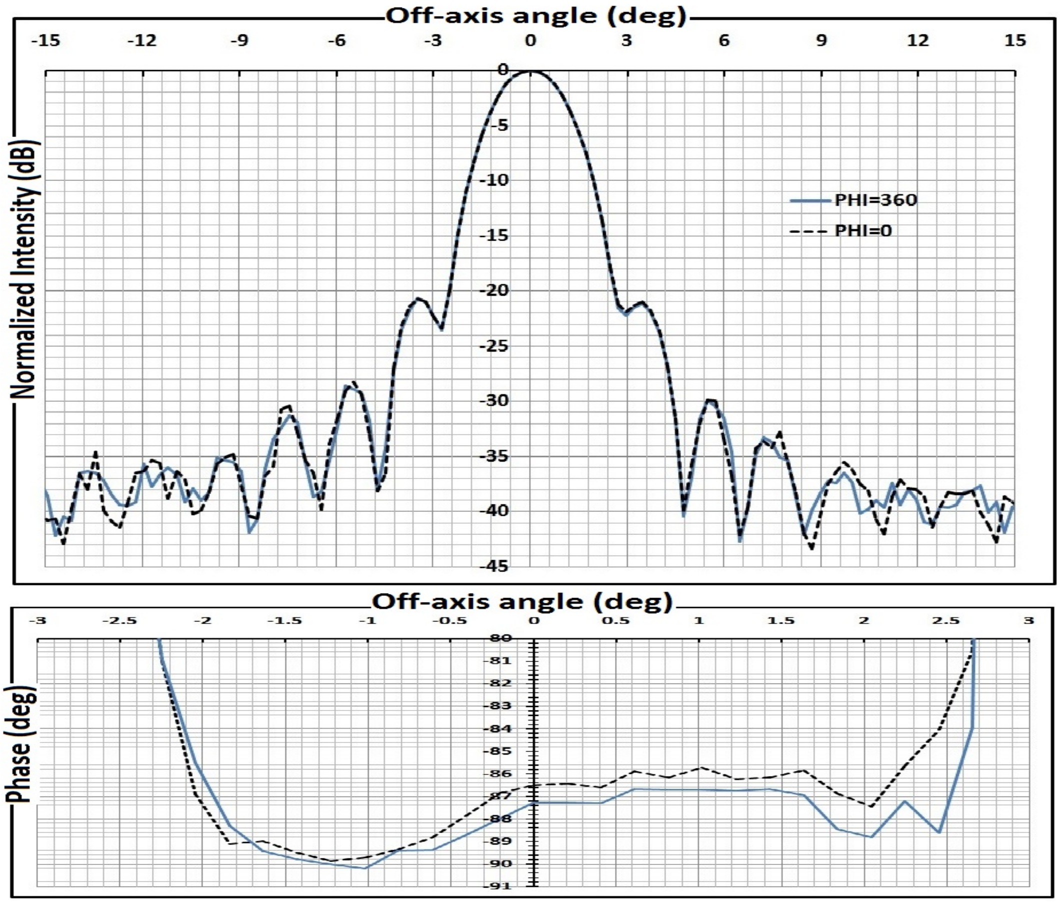

Figure 6.11: Upper-figure: the intensity beam patterns measured at $\phi = 0°$ and $\phi = 360°$ for 97 GHz. Bottom-figure: the phase patterns measured at $\phi = 0°$ and $\phi = 360°$ for 97 GHz.

- **Component misalignments**

The polarization measurements require a very accurate component alignment. For this reason, the effects of the components and the misalignments on the beam pattern should be determined. This requires high positioning accuracy for the components (e.g. rotary stage controlling the polarization state of the system and rotary stage used for beam scanning as shown in Figure 6.1). For example, the positioning accuracy of the polarization rotary stage is specified as $\leq 1^\circ$ by the seller company. However, the angular position of the rotary stage is controlled by a Labview code via a stepper motor. The horn-medium size lens system was measured twice, first at $\phi = 0^\circ$ and second at $\phi = 360^\circ$. Comparison of measured data is shown in Figure 6.11. After 360° rotation, this signal should be the same. Intensity patterns are almost identical and a phase shift of 1° was observed. Possible source of this phase shift might be movement of the RF cable when the polarization rotary stage was repositioned.

Similar to the polarization rotary stage, the positioning accuracy of the linear micrometer stage where the lens is located should be investigated. The seller company specifies its accuracy in each axis as 50 microns. A test has been conducted for investigating the misalignments through the X-axis. The mount accommodating the lens was displaced by ± 0.5 mm along the X-axis. Intensity beam patterns, taken for three configurations at $x = -0.5, 0$, and $+0.5$ mm are plotted in Figure 6.12. An off-centred beam by $\pm 0.11^\circ$ was observed by ± 0.5 mm translation, respectively.

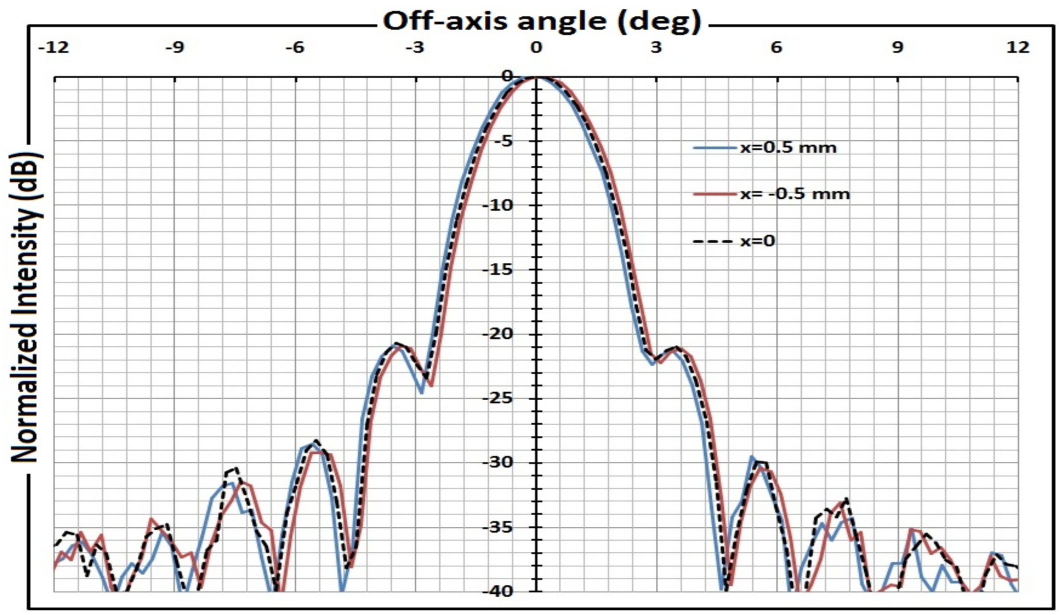

Figure 6.12: Figure shows the intensity patterns measured in the far-field of the horn-medium size lens system. Three measurements were taken for three different positions of the lens mount. A small shift of ($\frac{\lambda}{6} \simeq 0.5mm$) results in an off-centred beam pattern with 0.11°.

- **Focal distance shift**

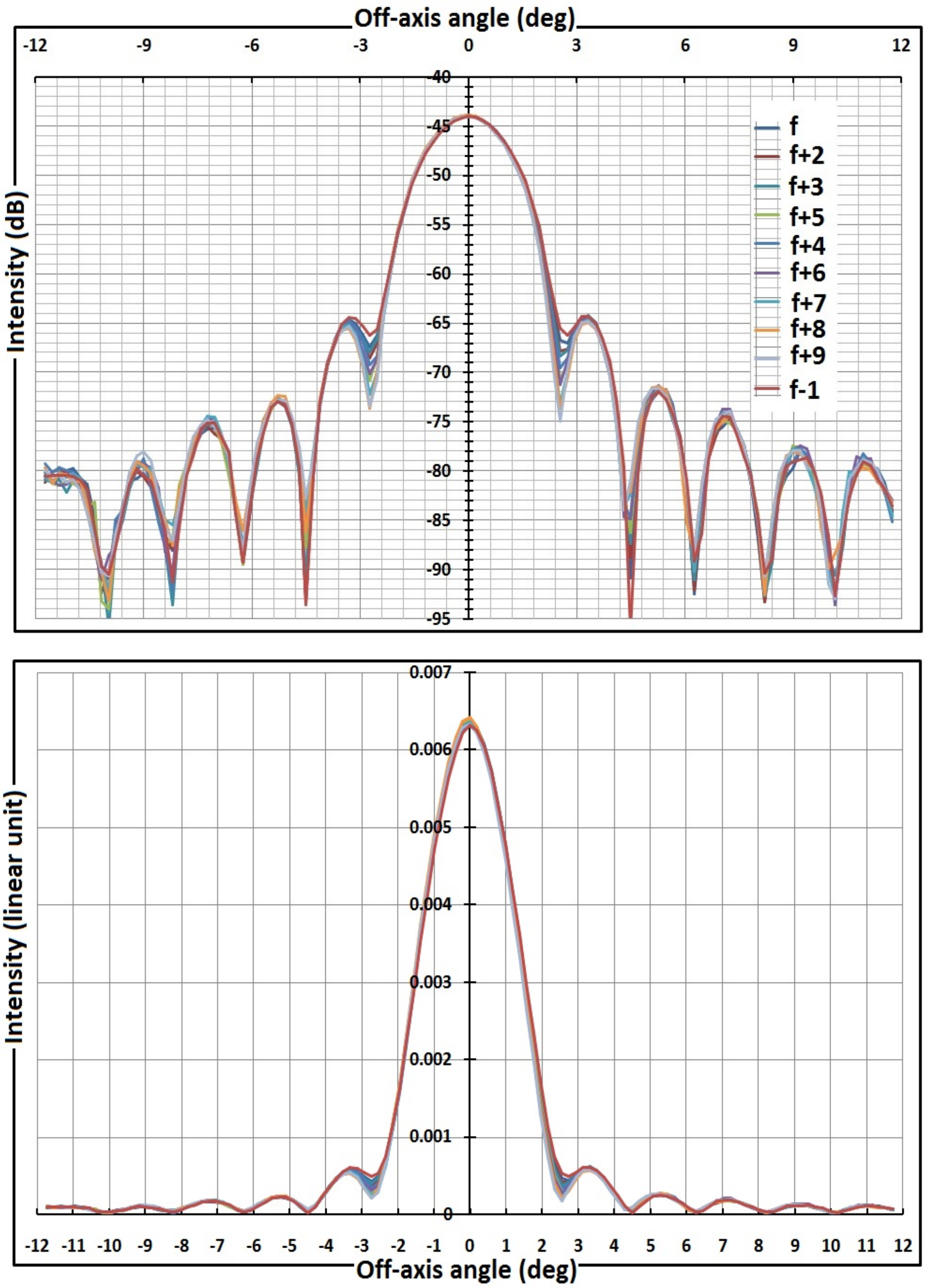

Figure 6.13: Intensity beam patterns for different focal positions. The focal length varies from f-1mm to f+9mm (f=203mm). Intensity patterns are not normalised in order to show the variation in the gain.

The sensitivity of the horn-lens system to the feed location has been investigated. This analysis was conducted by changing the focal distance along the focal axis (f-axis). Measurements of the horn-lens system for the co-polarization radiation beam pattern were taken at the different positions along the f-axis. The impact of the feed-lens distance on the co-polarization radiation patterns is shown in Figure 6.13.

The change in gain was insignificant but a substantial side-lobe decrease of 1 dB was observed at a distance of 211 mm. Also, the beam size gets narrower at further distances. Results obtained from this investigation was used to determine the measurement inaccuracies due to the misalignments of the feed position relative to the lens position.

6.1.6 Time Domain Gating (TDG)

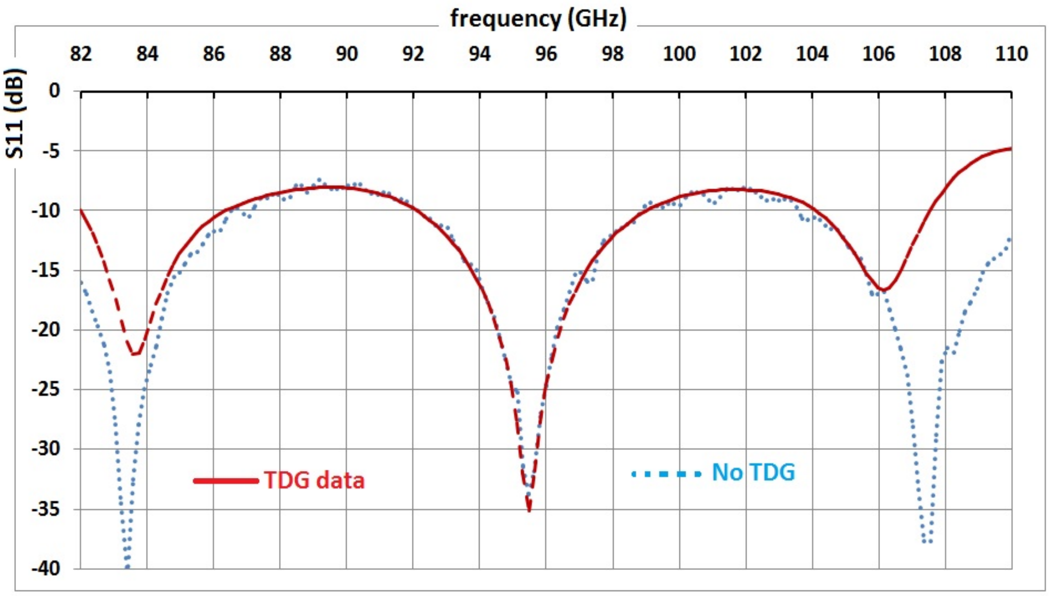

Figure 6.14: The return loss (S_{11}) measurements of the dielectric slab as a function W-band frequencies. The measurements were conducted with and without the Time Domain Gating (TDG) by using the CATR free-space test bench. The time domain gated data presents a smooth plot line while the operating bandwidth of the test bench reduced.

Time Domain Gating (TDG) is used to improve the measurement accuracy by detecting the signal response of CUT. In this method, the measured S parameters are modified by using a gating function in the time domain. Special gating functions [133] are used to suppress reflections from components in the measurement setup. From the time domain spectrum, impulses of the measured component can be identified, and all signals that reach the receiving port can be localized. The filtered data in the time domain is then converted back to the frequency domain, so that the S parameter includes a gating frequency data. The relation of the time domain to the frequency domain is accomplished by the fourier transformation.

For example, the S_{11} parameter with and without the TDG in the frequency domain is shown in Figure 6.14 when there is a dielectric slab located at the center of the CATR test bench. The same data is plotted in the time domain spectrum with and without the TDG as shown in Figure 6.15. The reference distance shown in the time domain with zero location corresponds to the central position of the dielectric slab. There are two peaks representing reflections from the dielectric slab. The first reflected peak is from the front surface of the slab and the second is from the back surface of the slab. The thickness of the slab is 8.248 ± 0.004 mm, which agrees with the peak locations in the time domain spectrum. Other signals with small magnitude peaks are reflections coming from different locations of the test bench. In this way, more accurate results with less fluctuations in the S parameter can be obtained by filtering reflections not associated with CUT.

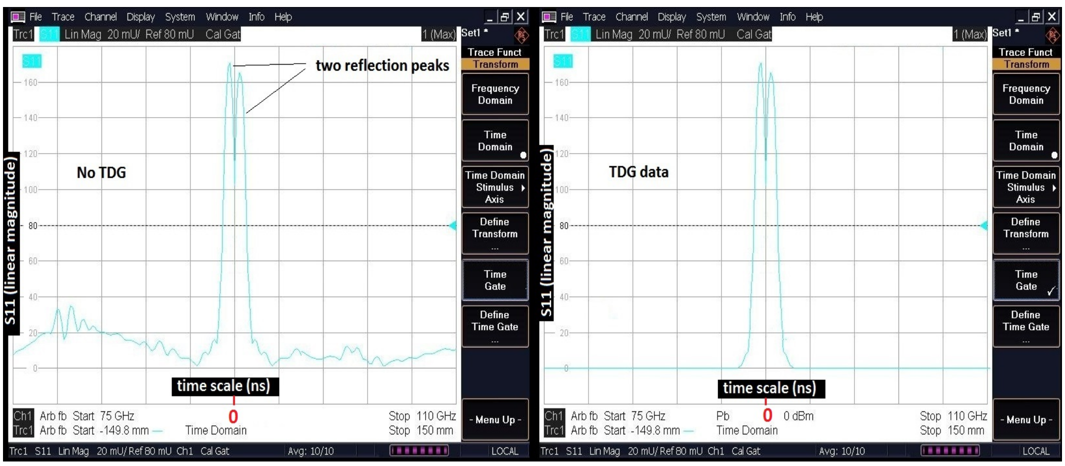

Figure 6.15: Linear scale plots of the S_{11} magnitude of a dielectric slab. Two peaks corresponding to the reflections from the two surfaces of dielectric slab are observed. After time gating was applied to the data, the unwanted reflections (shown in the left hand side figure) with small magnitudes were removed.

This operation also helps to attenuate high frequency fluctuations, however it reduces the usable frequency range of the measurement setup from 82-110 GHz to 86-106 GHz. This is related to the gate definition which limits the width of the impulse in the time domain. As the power in the time domain is attenuated, the frequency range of the test system is reduced.

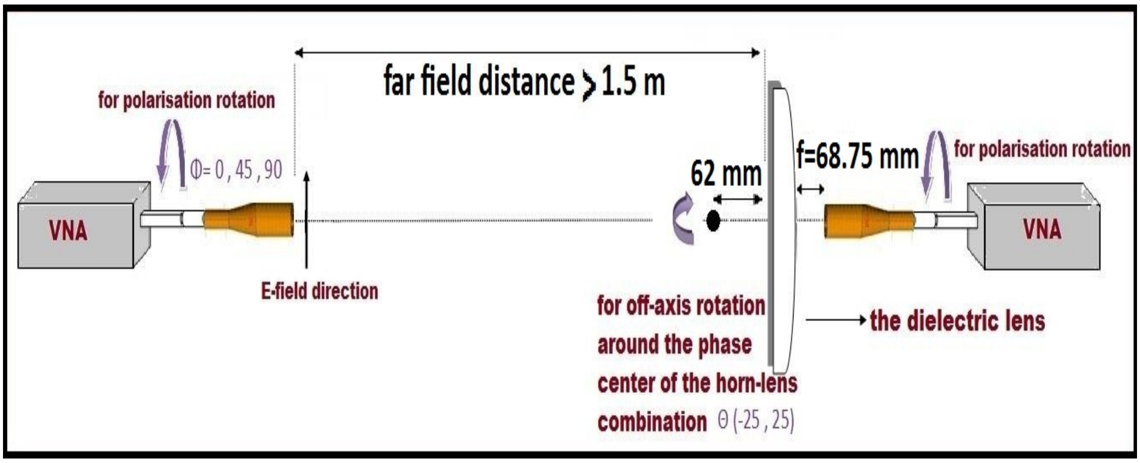

Figure 6.16: Optical arrangement used to perform the far-field measurements of the horn-small size lens system. The VNA head coupled to the dielectric lens is the transmitting part and the other VNA head is the receiving part of the measurement system. Two rotary stages shown in Figure 6.1 are used to realize the polarization orientation (ϕ) and the off-axis angle orientation (θ) of the measurement set-up for the co- and cross polarization beam pattern measurements in free-space. For off-axis rotations, the system is rotated around the phase center of the horn-lens system shown by a thick black dot in the figure. The far-field distance is set to be greater than 1.5 m ($2D^2/\lambda$).

6.2 Measurements of Horn-Small Lens System

The far field setup used for the measurements of the horn-small size lens system was described in detail in Section 6.1. The model analysis of the horn-small lens system was conducted in Chapter 5. Here, the experimental studies of the horn-small lens system are presented. Figure 6.16 shows how the beam scanning was carried out. RF modelling and preliminary experimental studies of this system has been already published in [134]. The horn-small lens system was rotated around the phase center of the entire lens system, where the second beam-waist of the lens beam was located. This location was calculated by Gaussian beam analysis.

6.2.1 Fabrication of the lens and the lens mount

The lens was fabricated from a cylindrical slab of Ultra High Molecular Weight Polyethylene (UHMWPE) by using a Computer Numerical Controlled machine (CNC) in the school workshop. The UHMWPE material is a low-loss dielectric, which has a dielectric constant of 2.3 and a tangent loss of $3 \cdot 10^{-4}$ over W-band [135], [136].

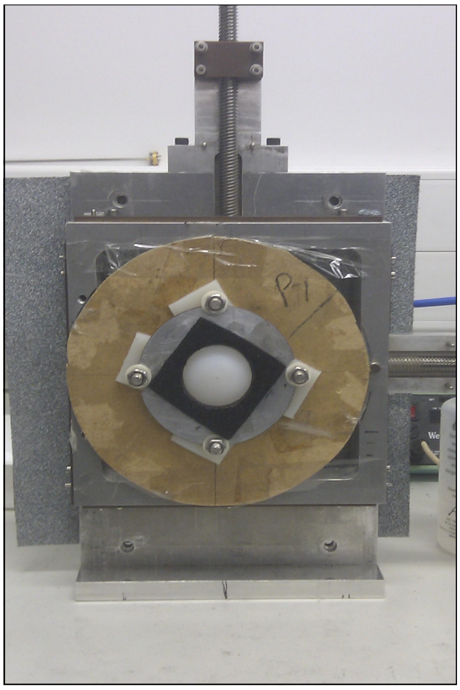

Figure 6.17: A metal frame used to hold the lens mount. The base system provides with dual axes displacements.

The central thickness of the lens was measured as 11.11 ± 0.003 mm. A lip of 1.5 mm, around the lens, was used for mounting purposes. This extension was used as the lens stop in order to define the clear aperture of the lens. After the manufacture of the lens profile had finished, a rough surface was present. This was removed by applying grading paper so not to destroy the original geometry of the lens.

One of the very crucial issues regarding the lens mount was defining the clear aperture of the lens. This is because the outgoing beam width is directly dependent on this parameter. In order to support the lens design during beam scanning, I prepared an in-house lens mount. The mount is originally made up of a wooden circle. This wooden piece has a hole fitting with the inner diameter of the lens. This piece was then covered by an aluminium tape in order to block the radiation from penetrating the other side. Then, an absorber was used to cover around the lens to minimize reflections from the aluminium taped face. Lastly, the lens mount was placed in a rectangular metal plate base allowing dual axes displacements, which are up-down and left-right. This plate is independent from movement of the feed-horn antenna. The complete design of the lens assembly is shown in Figure 6.17.

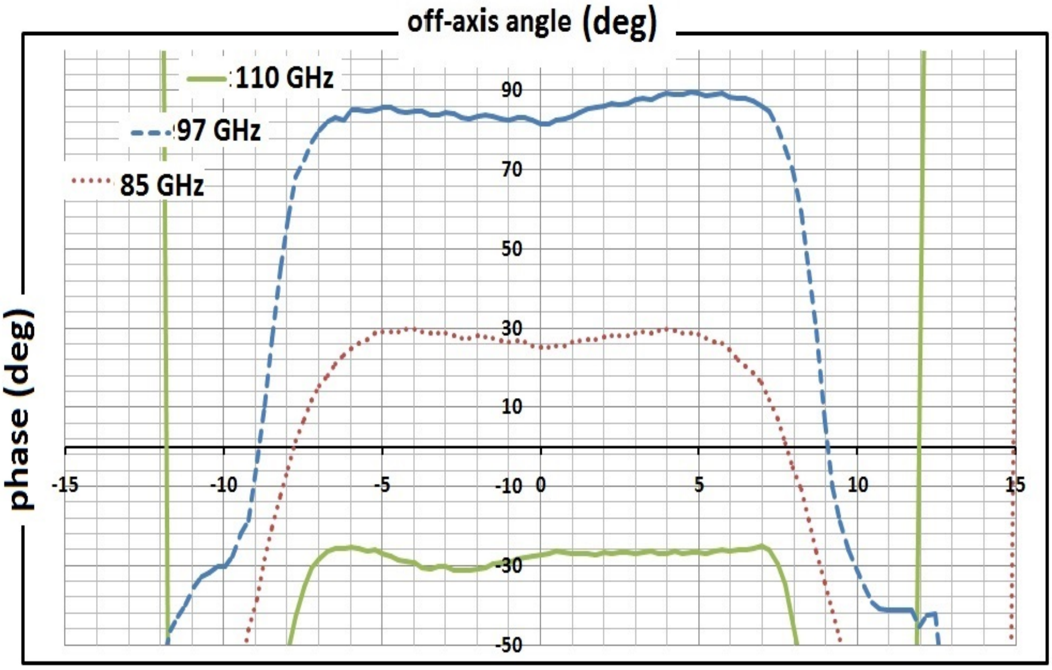

Figure 6.18: D plane cut phase pattern measurements for the horn-small lens system. The measurements were performed for three different frequencies of 85 GHz, 97 GHz, 110 GHz.

6.2.2 Measurement Results

- **Phase Measurements**

Figure 6.18 shows the measured phase patterns of the co-polarization beam. D plane cuts were taken for the edge and the central frequencies of W band (85, 97 and 110 GHz). Each phase plot is uniform with maximum variations of $\pm 4°$ inside the extent of the main beam. There is $\sim 50°$ phase shift between each plot. This value corresponds to the difference between the phases measured for 85, 97 and 110 GHz. This phase uniformity ensures that the beam scanning of the horn-small lens system was achieved around the phase center of the entire lens system.

- **Intensity measurements**

Intensity pattern measurements were performed for both co-polarization (CP) and cross-polarization (XP) beams. Figure 6.19 gives the CP and XP beam patterns measured for the D plane cut across the W band frequency range. The CP and XP patterns show little variations across the band. The XP beam pattern measurements were challenging to perform because the emphasis was put on obtaining a null level of the XP at

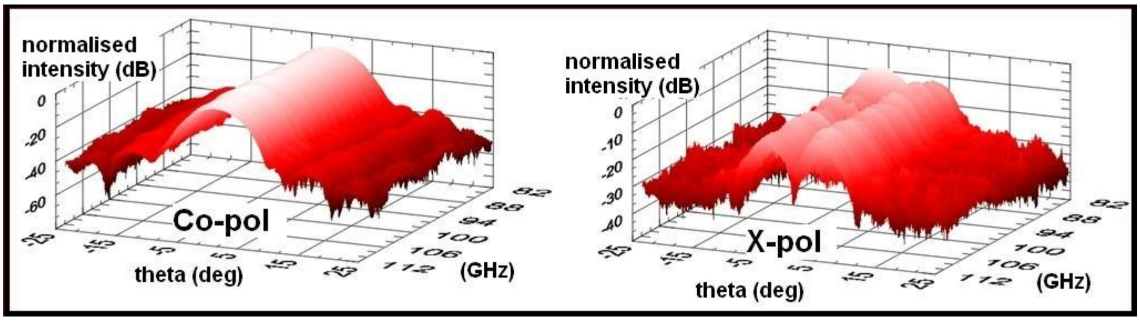

Figure 6.19: Left: normalised intensity distribution of the co-polarisation radiation pattern across the band 82-110 GHz. Right: cross-polarisation radiation pattern normalised to its maximum.

boresight angle. However, small deviations up to 5 dB in the XP signal were observed in a few frequency measurements. These deviations were inherent from the XP of the feed-horn pattern. Figure 6.20 shows the CP and XP polarization patterns, for each reference frequency, which have been extracted from the intensity map given in Figure 6.19. The CP data was normalized to its own peak value while the XP cuts were normalized to the CP peak. Measured beam pattern cuts for the upper edge frequency (110 GHz) exhibits a very symmetric pattern below -35 dB at $\sim 11^{\circ}$. However, there is a small asymmetry between the beam patterns of different plane cuts measured for the frequencies of 85 GHz and 97 GHz. The central frequency has the lowest XP signal measured with -31.6 dB, while the XP patterns gives an apparent minimum dip at the beam center of the edge frequency beams.

6.2.3 Comparison: Model and Measurement

- **Co-polarization results**

Figures 6.21, 6.22 and 6.23 compare the measured beam patterns with the simulated beams performed with full MOM (Model 1) at 97 GHz. The figures also present the calculated beam difference due to disagreement between the modelled and measured data.

Modelled and measured results for all three plane cuts are in a good agreement for the shape of the main beam lobe down to -30 dB. A slight discrepancy at the edges of the main lobe, for the D plane cut was observed. Additionally, the side-lobe structures differed by 3 dB at maximum, particularly in the E plane cut. Correspondingly, the measured side-lobes presented a large level of measurement errors. It was deemed that

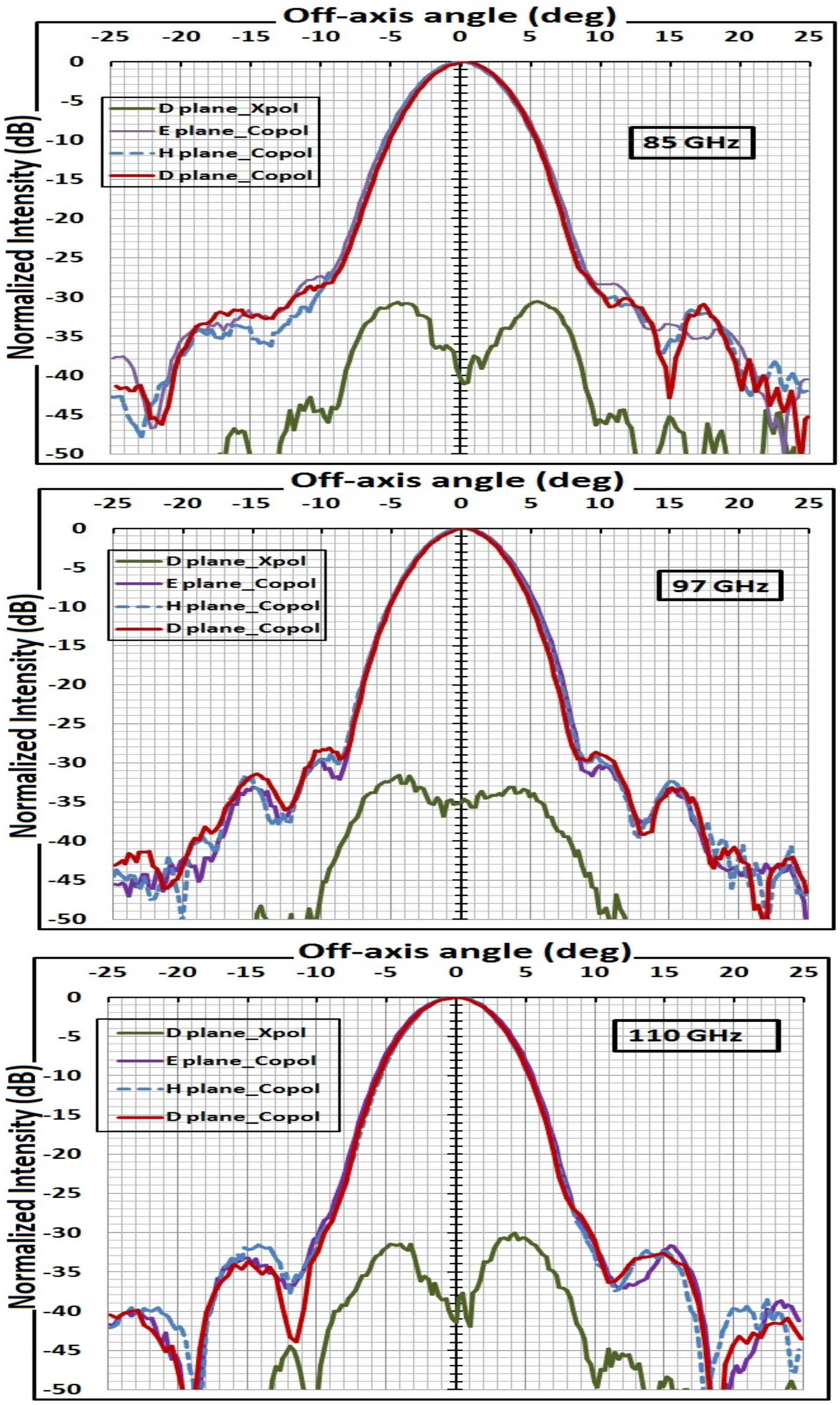

Figure 6.20: From top to bottom: the far-field beam patterns of the horn-small lens system were measured for 85 GHz, 97 GHz and 110 GHz. Each plot has the co-polarization intensity patterns measured for three plane cuts and the cross-polarization patterns measured only for the D plane cut.

there were two possible reasons for the side-lobe differences and fluctuations. First, the lens size is small compared to the beam-width of the feed horn. Such a small size lens may suffer from diffraction effects. We will see that the side-lobes of the medium size lens can be measured with higher precision. The second reason was the poor fabrication of the lens stop. Therefore, the present set-up, which has produced these preliminary measurements, is in need of improvement for far-field measurements of the second lens prototype.

- **Cross-polarization Results**

Figure 6.24 shows the comparison plots. The XP measurements of the horn-small lens system were carried out only for the diagonal plane cuts for the reference frequency values. The comparisons reveal good agreement between the measured and simulated data. The behaviour of the measured XP beam pattern is very similar to that of the simulated XP pattern for the three frequencies. However, the maximum level of the measured XP beam is 4 to 6 dB higher than the simulated XP values. The XP pattern measured for the central frequency showed no significant central dip. The other frequency patterns present a minimum dip of the XP signal at the center of the main beam.

6.2.4 Conclusion for the small lens design study

Model 1 (the full Model) produced the best matched simulations with the measured data of the horn-small lens system. For this reason, Model 1 was selected as the reference model to compare with the experimental data. The beam difference calculations with a maximum of -13 dB and an average of -31.2 dB, which were plotted in Figures 6.21, 6.22 and 6.23, show the confidence level of the models.

A summary Table 6.1 is given for a comparison between the calculated and measured beam parameters. Beam parameters were computed for three different cuts for each reference frequency. The beam parameters are full width half maximum (FWHM), side-lobe (SL), maximum cross-polarization (Max. XP), and integrated cross-polarization (Int. XP). As the operating frequency increases, the errors in the measurements become higher. For example, the measurement error in the FWHM of 110 GHz was determined to be $\pm 0.13°$, while the same parameter was measured with an error of $\pm 0.05°$ for 85 GHz. The variations in the obtained FWHM values across the band are shown in Figure 6.25. The best agreement between the simulated and measured FWHM was observed between 92 to 103 GHz. The values for the maximum

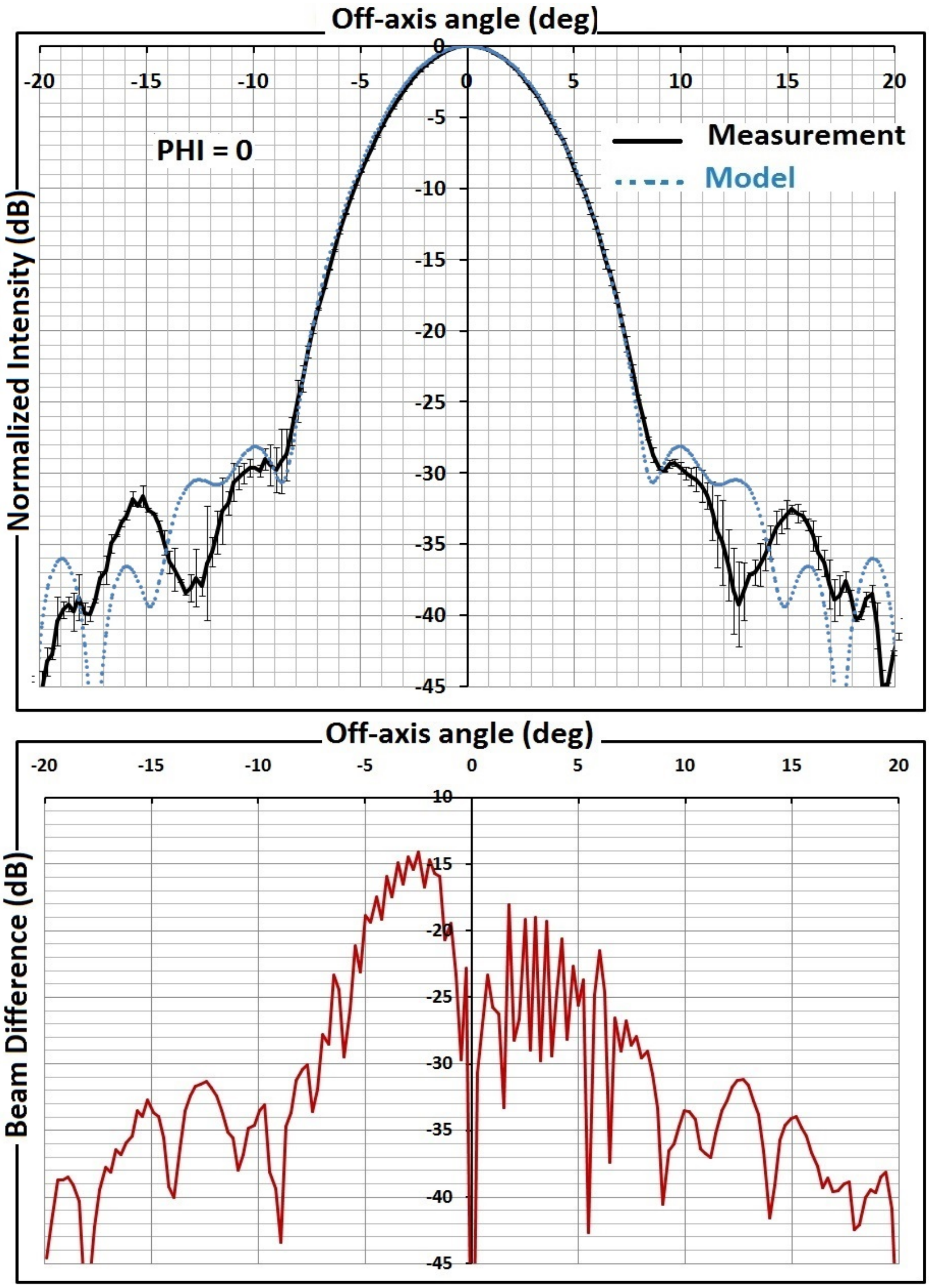

Figure 6.21: The comparison of the full MOM model (Model 1) predictions and the measurements of the feed horn-small lens system for intensity beam patterns. Far field co-polarization measurements were performed for the H plane cut ($\phi = 0$) for 97 GHz. The bottom figure shows the beam difference between the model and measurement. The minimum difference was calculated as -15 dB.

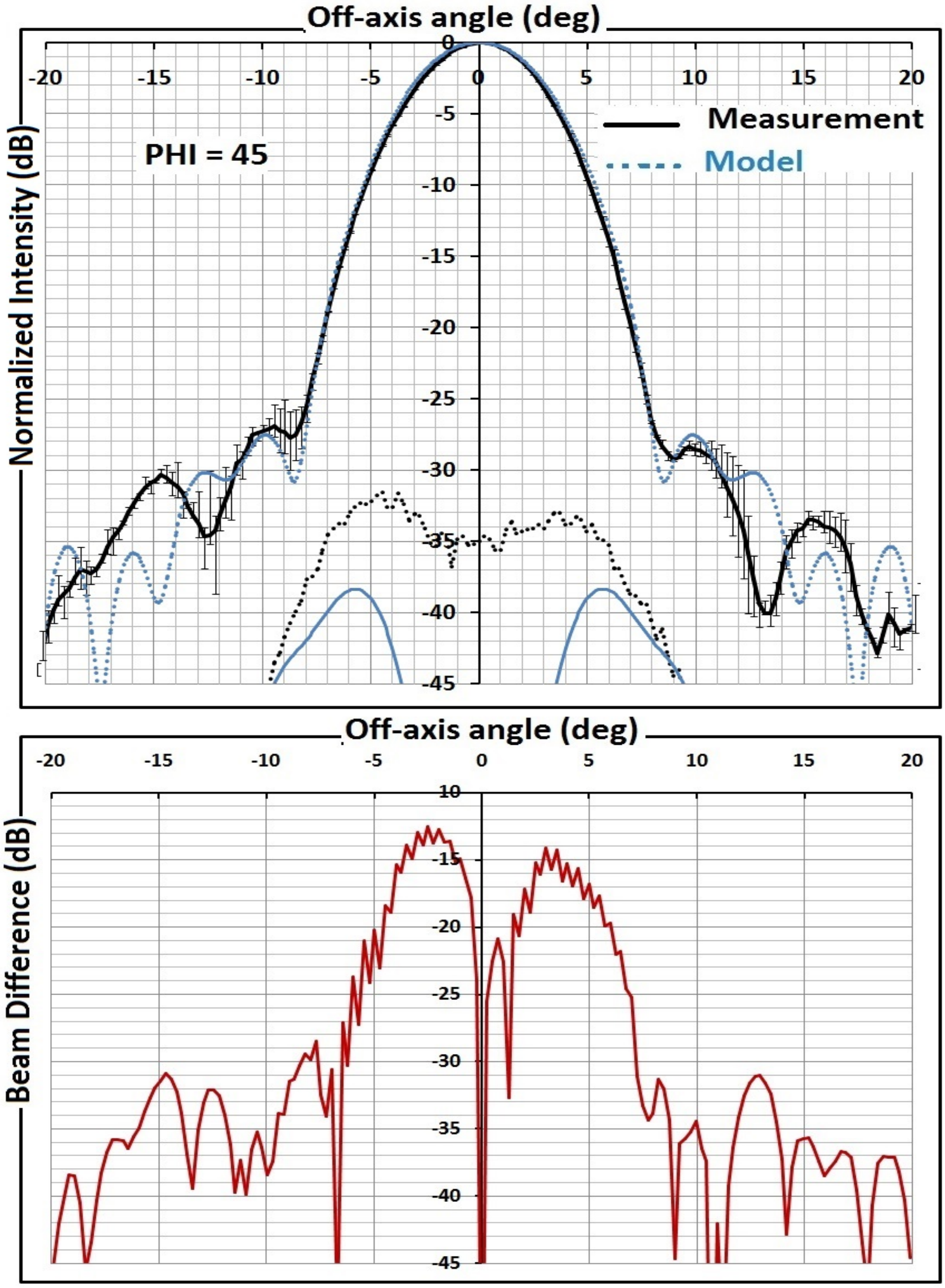

Figure 6.22: The comparison of the full MOM model (Model 1) predictions and the measurements of the feed horn-small lens system for intensity beam patterns. Far field co- and cross-polarization measurements were performed for the D plane cut ($\phi = 45$) for 97 GHz. The bottom figure shows the beam difference between the model and measurement. The minimum difference was calculated as -13 dB.

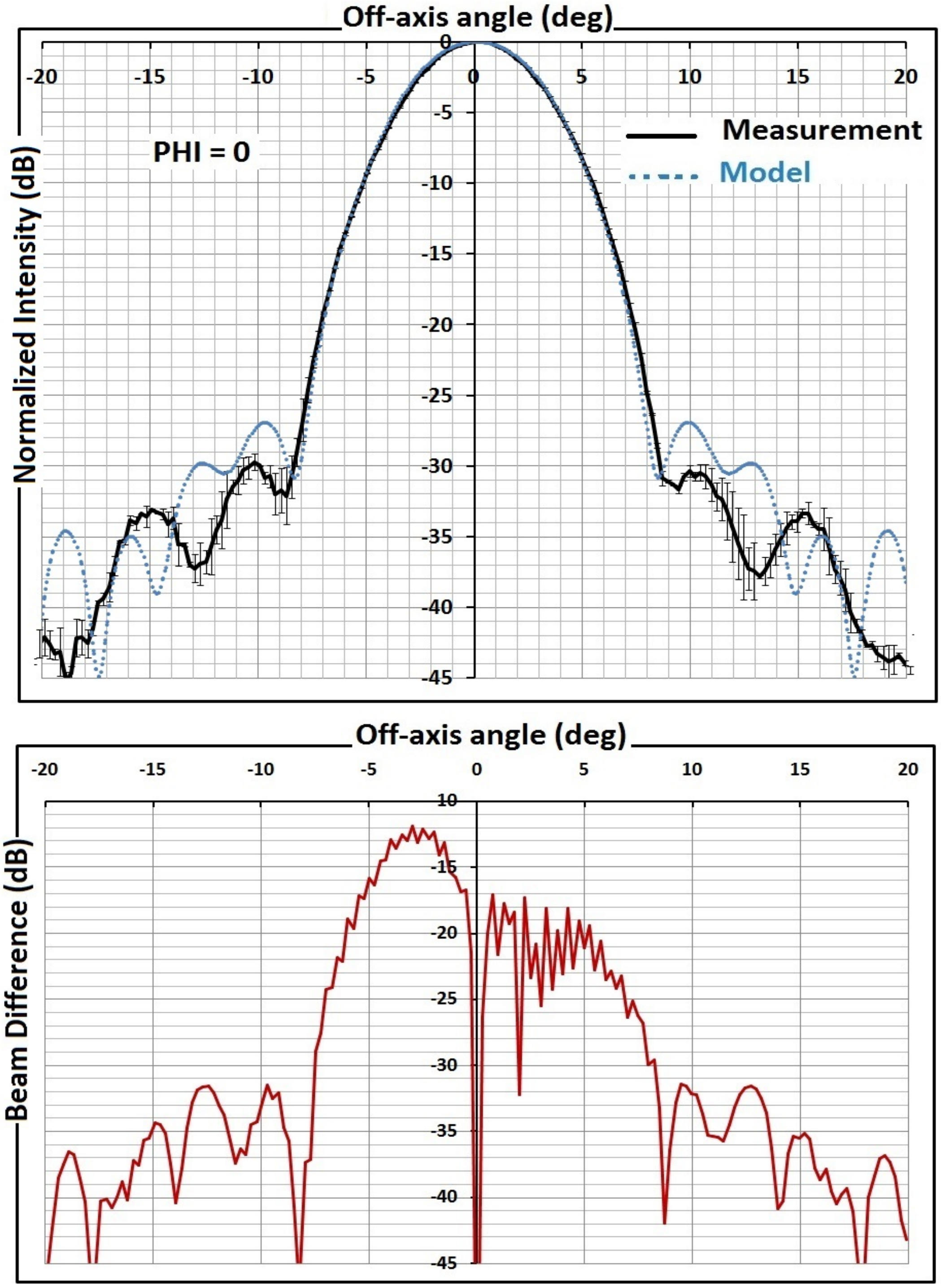

Figure 6.23: The comparison of the full MOM model (Model 1) predictions and the measurements of the feed horn-small lens system for intensity beam patterns. Far field co-polarization measurements were performed for the E plane cut ($\phi = 90$) for 97 GHz. The bottom figure shows the beam difference between the model and measurement. The minimum difference was calculated as -12 dB.

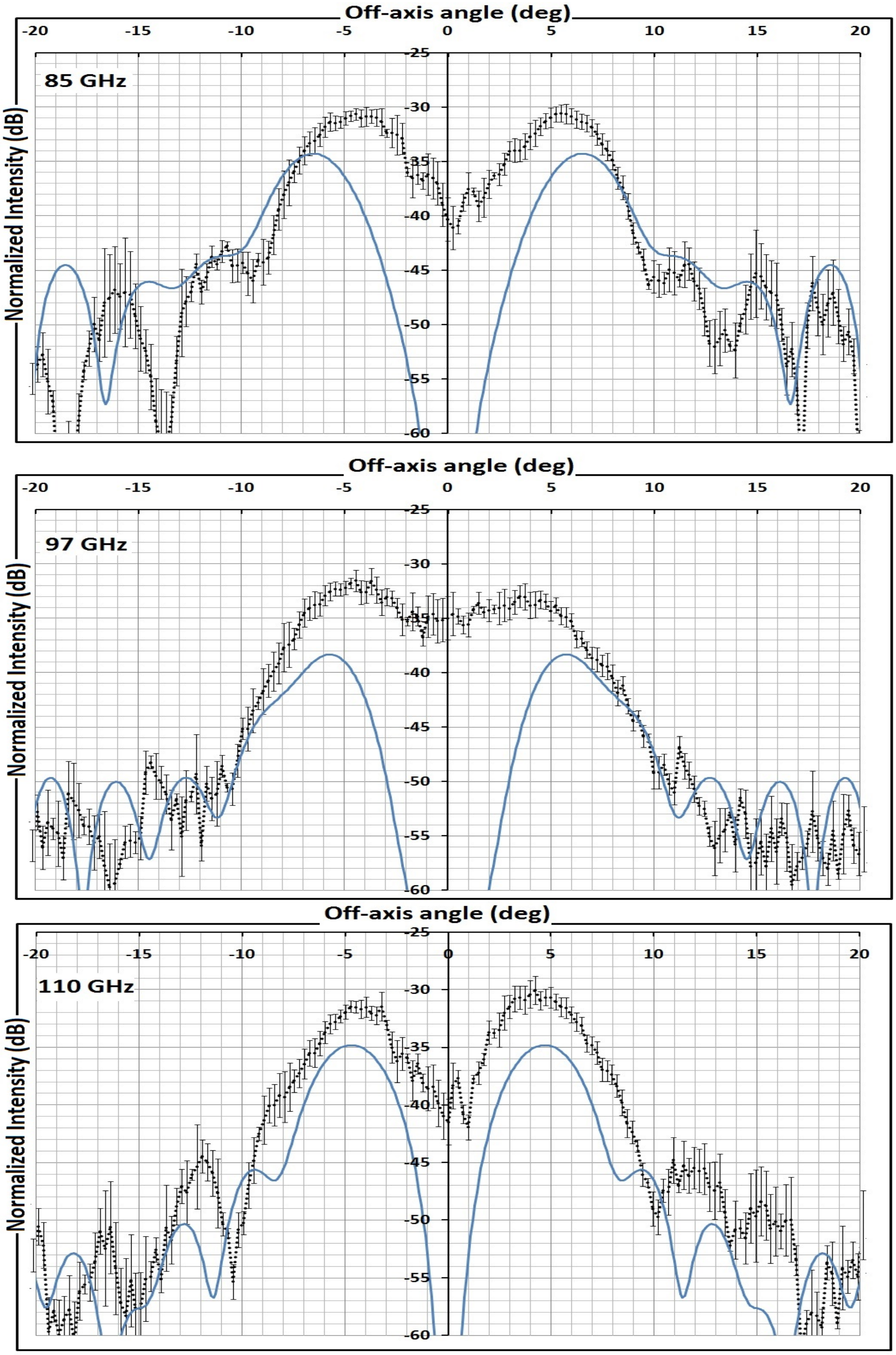

Figure 6.24: The comparison of the full MOM model predictions and the measurements of the feed horn-small lens system for cross-polarization beam pattern. D plane cut cross-polarization measurements were performed for there reference frequencies of the W band: 85 GHz, 97 GHz and 110 GHz. All measured and predicted cross-polarization plots show a very similar change in beam shape.

Parameter	Model(H)	**Exp.(H)**	Model(D)	**Exp.(D)**	Model(E)	**Exp.(E)**
BW (85 GHz) deg	6.42	**5.9**±0.05	6.36	**5.8**±0.05	6.48	**6.22**±0.05
BW (97 GHz) deg	6.16	**5.95**±0.06	6.12	**5.76**±0.06	6.1	**5.9**±0.06
BW (110 GHz)deg	6.02	**6.02**±0.13	6.06	**6.3**±0.13	6	**6.61**±0.13
SL (85 GHz) dB	-25.5	**-30**±0.3	-24.8	**-29**±0.2	-26	**-27**±0.2
SL (97 GHz) dB	-28.12	**-29.5**±0.3	-27.53	**-28.6**±0.2	-26.91	**-28.8**±0.2
SL (110 GHz) dB	-30.2	**-32.1**±0.3	-29.6	**-32.5**±0.3	-30.8	**-31.8**±0.3
Max. XP (85 GHz) dB	-	**NM**	-34.28	**-30.06**±0.56	-	**NM**
Max. XP (97 GHz) dB	-	**NM**	-38.38	**-31.6**±0.56	-	**NM**
Max. XP (110 GHz) dB	-	**NM**	-34.8	**-30**±0.56	-	**NM**
Int. XP dB	-	**NM**	-	**-30.08**	-	**NM**

Table 6.1: The beam parameters calculated from the best matched model (Model 1) are compared to the experimentally measured values for the frequencies of 85, 97 and 110 GHz. Theoretically, there is no XP at both E and H planes. The XP signal was only measured in the measurements of the D plane cut and was not measured (NM) for the other plane cuts. The integrated cross-polarization (Int. XP) was calculated over the main beam extent ($-9^\circ \leq \theta \leq 9^\circ$).

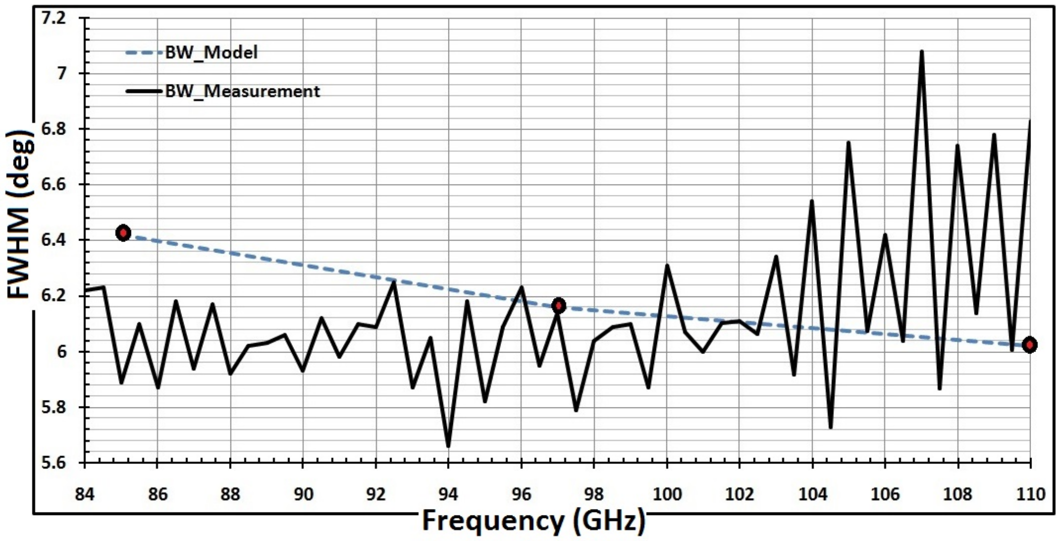

Figure 6.25: The comparison of the full MOM model (Model 1) predictions and the measurements of the feed horn-small lens system for FWHM parameter. The FWHM was calculated only for the three frequency values (85, 97 and 110 GHz) as shown with red dots in the figure while it was measured across the W band.

XP shows a difference 4 dB to 6 dB between the model and the measurement data, in the central part of the beam, but are otherwise showing in fairly good agreement with respect to beam shape. The integrated XP over the main beam lobe ($-9^{\circ} \leq \theta \leq 9^{\circ}$) is -30.08 dB. The instrumental polarization due to component imperfections can contribute to the XP signal measured experimentally. The discussion on its contribution is made in Section 6.3.3.

In conclusion, the tests provided rich knowledge of the representative refractive system. This means that we can use the models reliably in further investigations. Due to the large beam size ($\sim 3\lambda$) of the feed source compared to the diameter of the small lens (16λ), the off-axis beam characterization of the small lens system did not seem to be possible. To this end, further research presented in next section includes beam studies of off-axis pixels, by using a larger diameter lens system (Medium Size Lens).

6.3 Measurements of Horn-Medium Lens System

In this section, the far-field measurements of the horn-medium lens system are presented. The measurements were performed in the same way as before. Unlike the horn-small lens system analysis, further research was included. For example, the XP beam patterns were measured for three plane cuts (E, H and D). Additionally, off-axis pixel measurements of the horn-medium lens system discussed in Chapter 7 was performed.

The far-field distance was arranged to be $\sim 5.4m$, which is consistent with an aperture of 90 mm lens for a frequency of $\sim 97GHz$, by using the far field equation $(2D^2/\lambda)$. For this reason, the beam pattern measurements for the frequencies over 97 GHz, which requires $\sim 6m$ far field distance, can be slightly varied from the far-field simulations.

The lens has an f-number of 2.3 and therefore the feed illuminates the lens at an edge taper of 10 dB. Almost ten percent of the feed radiation power is not intercepted by the lens. This power enters to the system by being diffracted from the lens edges. In order to absorb this radiation and reduce its impact on the far-field beam, both sides of the lens mount were surrounded by MM-wave absorbers.

6.3.1 Modification of the far-field measurement schematic

The only difference between the medium lens measurement setup and the small lens measurement setup was the rotation point of the feed horn-lens system. The medium lens system was rotated around the lens centre as described in Figure 6.26 since the focal length of the medium lens was longer than that of the small lens. The platform carrying the rotary stage does not have enough space to take the beam scanning measurements around the second beam-waist location of the horn-medium lens system. Wave-front deviations still remained acceptable when the system was rotated around the lens center. This shift in the phase centre did not therefore cause much impact on the beam pattern measurements.

Many of optical components, e.g. lens mount and linear metal platforms, used in the measurement setup were fabricated in-house when the first lens prototype was measured. However, their machining accuracy was not adequate for our measurement purposes. These components were reconsidered and renewed with suggestions of the school workshop.

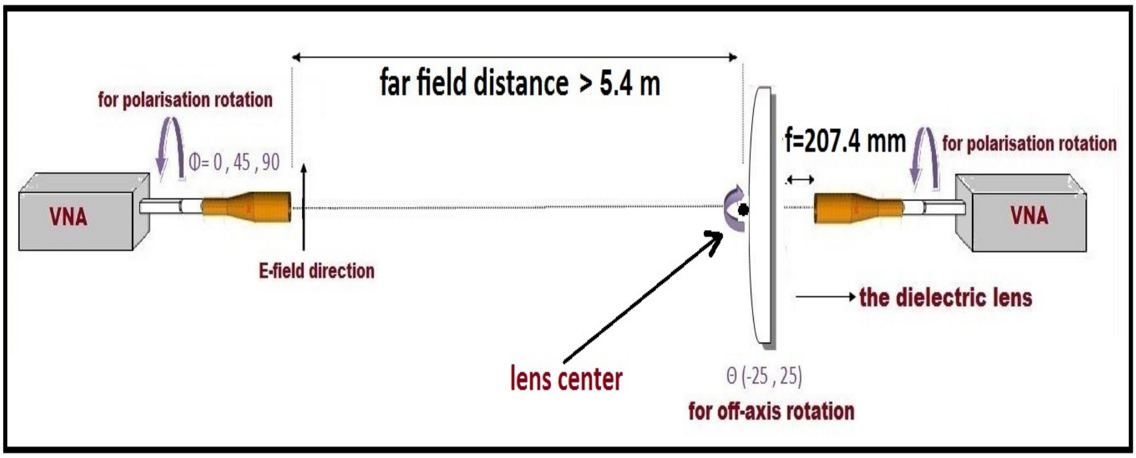

Figure 6.26: Optical arrangement used to perform the far-field measurements of the horn-medium size lens system. The VNA head coupled to the dielectric lens is the transmitting part and the other VNA head is the receiving part of the measurement system. Two rotary stages shown in Figure 6.1 are used to realize the polarization orientation (ϕ) and the off-axis angle orientation (θ) of the measurement set-up for the co- and cross polarization beam pattern measurements in free-space. For off-axis rotations, the system is rotated around the phase center of the horn-lens system shown by a thick black dot in the figure. The far-field distance is larger than 5.4 m.

6.3.2 Fabrication of the small lens

Similar to the small lens, the medium lens was fabricated from a cylindrical shape of the UHMWPE dielectric slab. The central lens thickness was measured as 12.28 mm. A lip of 2.5 mm, around the lens, was used for mounting purposes. A lens mount was made to be the lens stop as shown in Figure 6.27.

6.3.3 Measurement results

- **Phase measurements**

Figure 6.28 shows the phase patterns measured for the three plane cuts. The results for each reference frequency are presented. There are phase shift values varying between 45° to 60° between each cut plot. This was due to the displacement of the feed horn when the VNA converter head was being rotated. The phase variations over off-axis angular scale are otherwise uniform in the extent of the main beam, between $-2.5°$ to $2.5°$. Uniform phase change shows that the beam scanning was successfully achieved.

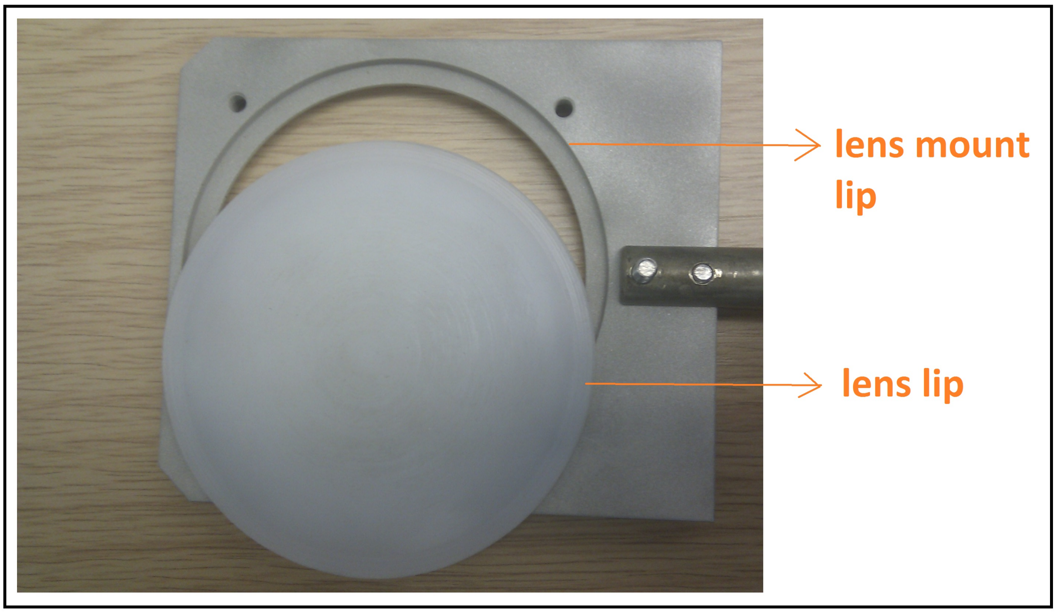

Figure 6.27: The lens mount was fabricated in the school workshop. It was used to hold the lens in place tightly by means of lips.

- **Co-polarization beam measurements**

Intensity pattern measurements of the horn-medium lens system were performed for both CP and XP beams in far-field. From top to bottom, Figure 6.29 shows the beam patterns measured for the E, H and D planes for each reference frequency, respectively. Different cut plots exhibit very well symmetric patterns up to angular range of $\sim 10^{\circ}$ which corresponds to the fourth side-lobe at around -40 dB.

- **Cross-polarization beam measurements**

Unlike the first lens system, the XP measurements of the horn-medium lens system were taken for three cut planes across the W band. Measured intensity patterns are given in Figure 6.30 in normalised form. As far as the XP due to the optics is concerned, there is no cross-polarization at the H plane cut and a very low level at the E plane cut. However, it is expected to be maximum at the D plane cut as explained in Section 6.1.1. In the beam shape of the D cut patterns, a minimum signal dip was obtained at around the central beam direction. The level of the cross-polarization signals measured for E, H and D plane cuts at 97 GHz were -37 dB, -37 dB and -38 dB, respectively. The likely source of the XP signal was the effect of the instrumental polarization discussed in Section 2.3. Also, the maximum level of the measured XP

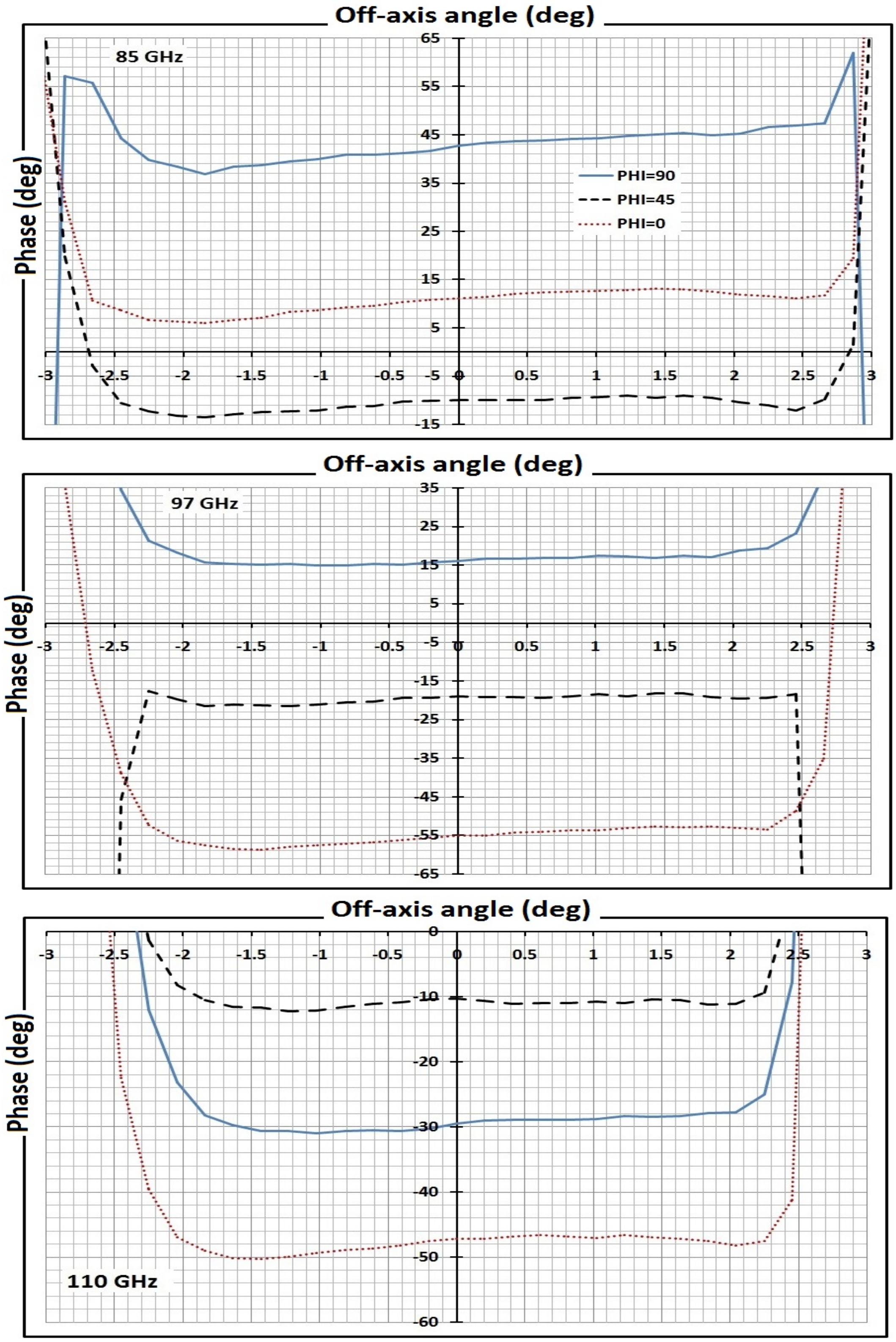

Figure 6.28: Phase pattern measurements for the horn-ML system. From top to bottom: The measurements were performed for the E, H and D plane cuts for 3 different frequencies of 85 GHz, 97 GHz, 110 GHz.

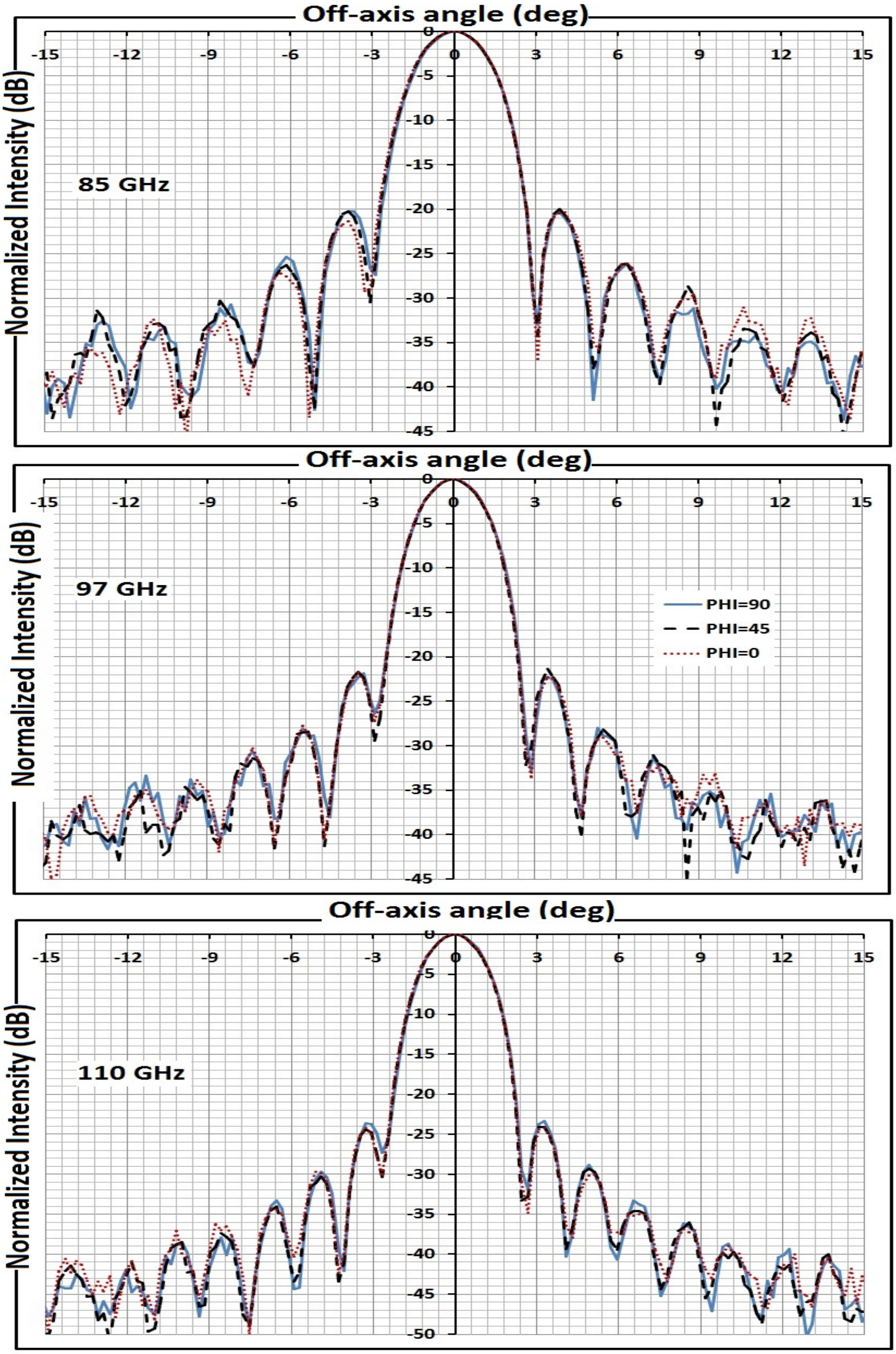

Figure 6.29: From top to bottom: the far-field beam patterns of the horn-ML system were measured for 85 GHz, 97 GHz and 110 GHz. Each plot has the co-polarization intensity patterns measured for three plane cuts and the cross-polarization patterns measured only for the D plane cut.

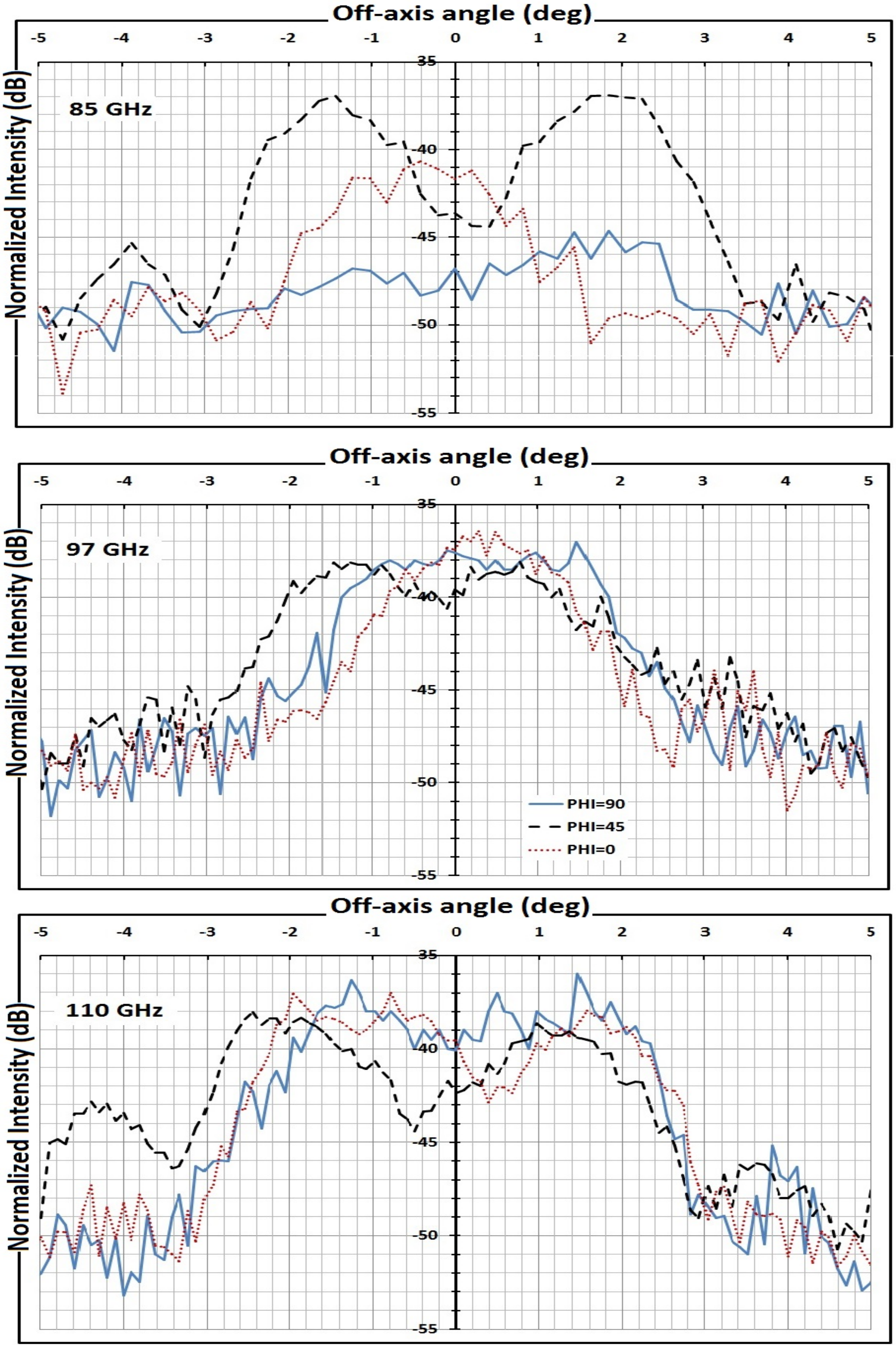

Figure 6.30: Measured cross-polarization beam patterns of the horn-ML system. From top to bottom: The measurements were performed for the plane cuts of E, H and D for the frequencies of 85 GHz, 97 GHz and 110 GHz.

signal varied a lot from one frequency value to another. Therefore, the integrated XP value for each cut measurement was determined and listed in Table 6.2.

6.3.4 Comparison: Model and Measurement

- **Co-polarization Results**

Figures 6.31, 6.32 and 6.33 give the comparison plots. The comparison was made between the measured data and the simulated data from all models for the reference frequencies. Beam patterns show a very good agreement for the main co-polarization beam down to -30 dB. The measured side-lobe levels match with the calculated values from Models 2 and 5 much better than the other models. The sidelobe-predictions of the other models differ from the measured values by up to 2 dB. It is difficult to ascertain the reasons of this discrepancy because a large beam extent of all model predictions is still within the error scale of the measurements. An alternative assessment is to calculate the beam differences due to disagreement between the modelled and measured data. From the beam difference plots, the maximum beam difference was shown to be -17 dB for each model comparisons. Additionally, the average beam difference across the angular range varied -35 to -37 dB depending on the model used and the plane cut taken.

- **Cross-polarization Results**

Figure 6.34 shows the comparison between the measured and simulated data for the XP beam pattern. D cut patterns only are plotted at 97 GHz. Overall, the behaviour of the measured XP beam pattern is similar to that of the predicted XP pattern for the three frequencies. A close-up view shown in the lower part of Figure 6.34 details the difference between the beam patterns. A minimum dip was observed at -42 dB at bore-sight. In the extent of the main beam, the measured XP deviates by 4 dB from the model predictions. The overall beam shape of the measured XP is consistent with that of the model predictions.

6.3.5 Determination of the noise level

The far-field distance of the horn-medium lens system is 5.4 m so the noise level for such a large distance must be determined. Results of two measurements were compared: the signal level measured when the horn-lens system is in the cross-polarization

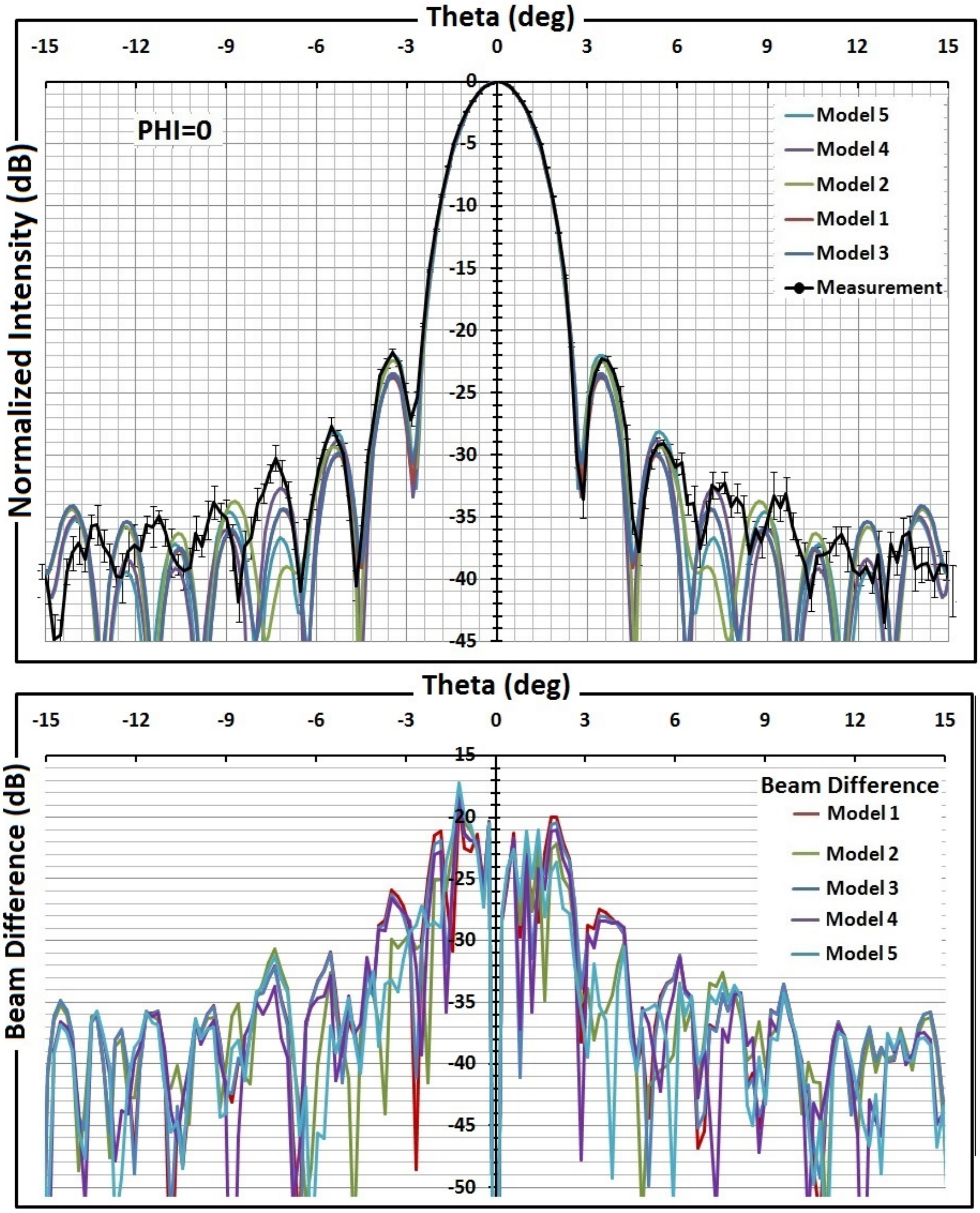

Figure 6.31: The comparison of all model predictions and the measurements of the feed horn-medium lens system for intensity beam patterns. Far field co-polarization measurements were performed for the H plane cut ($\phi = 0$) for 97 GHz. The bottom figure shows the beam difference between all models and measurement. The maximum beam difference was calculated to be -17 dB.

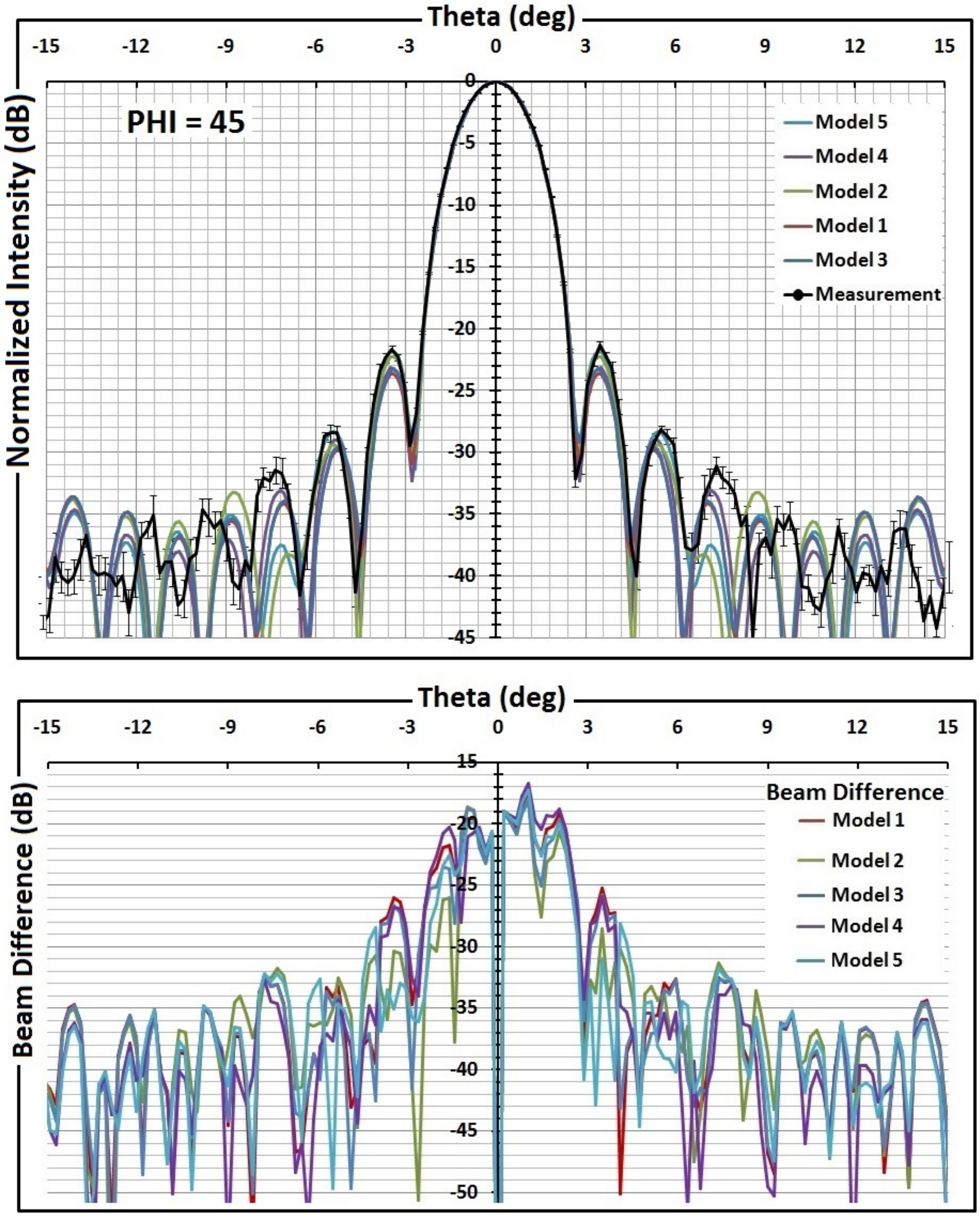

Figure 6.32: The comparison of all model predictions and the measurements of the feed horn-medium lens system for intensity beam patterns. Far field co-polarization measurements were performed for the D plane cut ($\phi = 45$) for 97 GHz. The bottom figure shows the beam difference between all models and measurement. The maximum beam difference was calculated to be -17 dB.

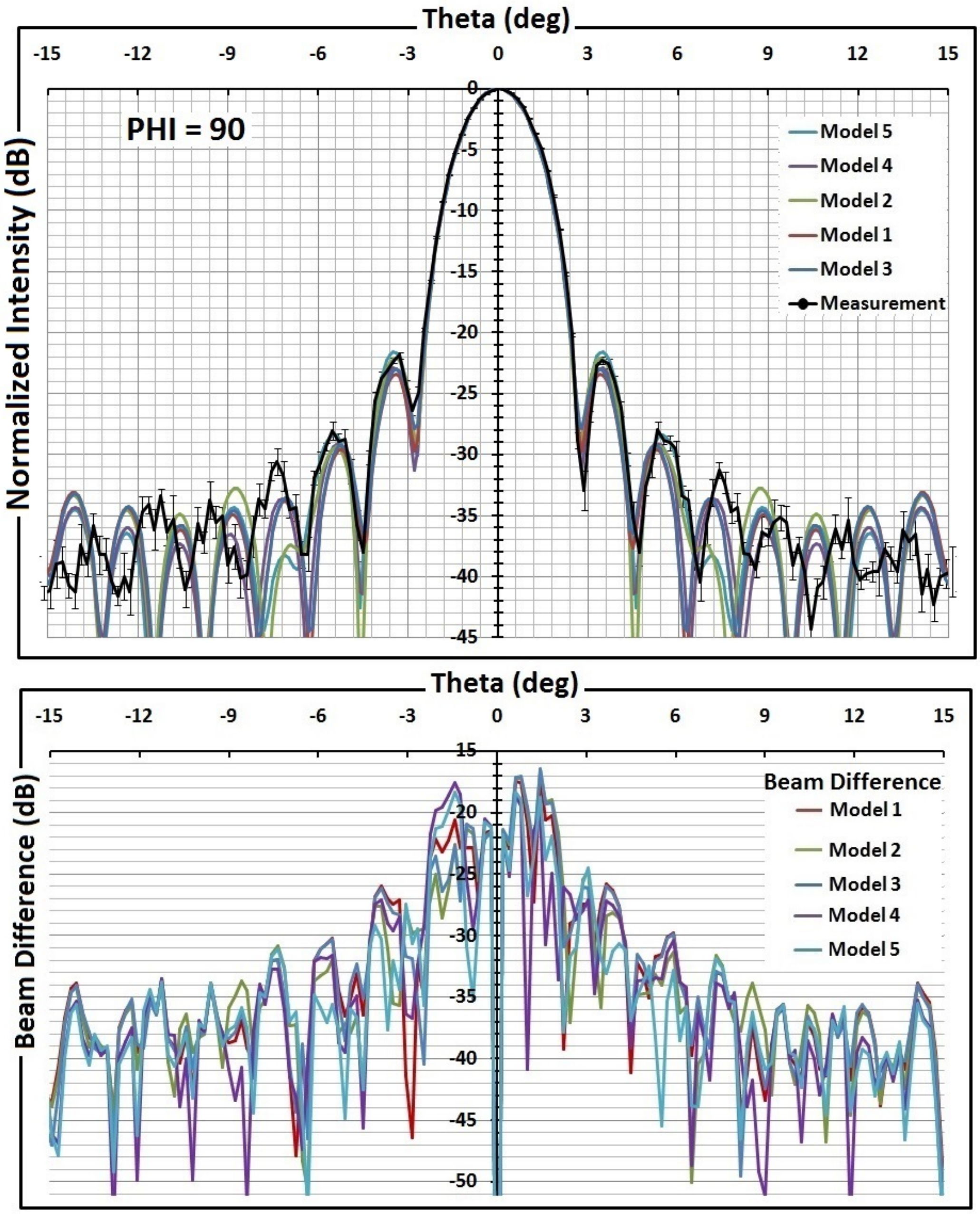

Figure 6.33: The comparison of all model predictions and the measurements of the feed horn-medium lens system for intensity beam patterns. Far field co-polarization measurements were performed for the E plane cut ($\phi = 90$) for 97 GHz. The bottom figure shows the beam difference between all models and measurement. The maximum beam difference was calculated to be -17 dB.

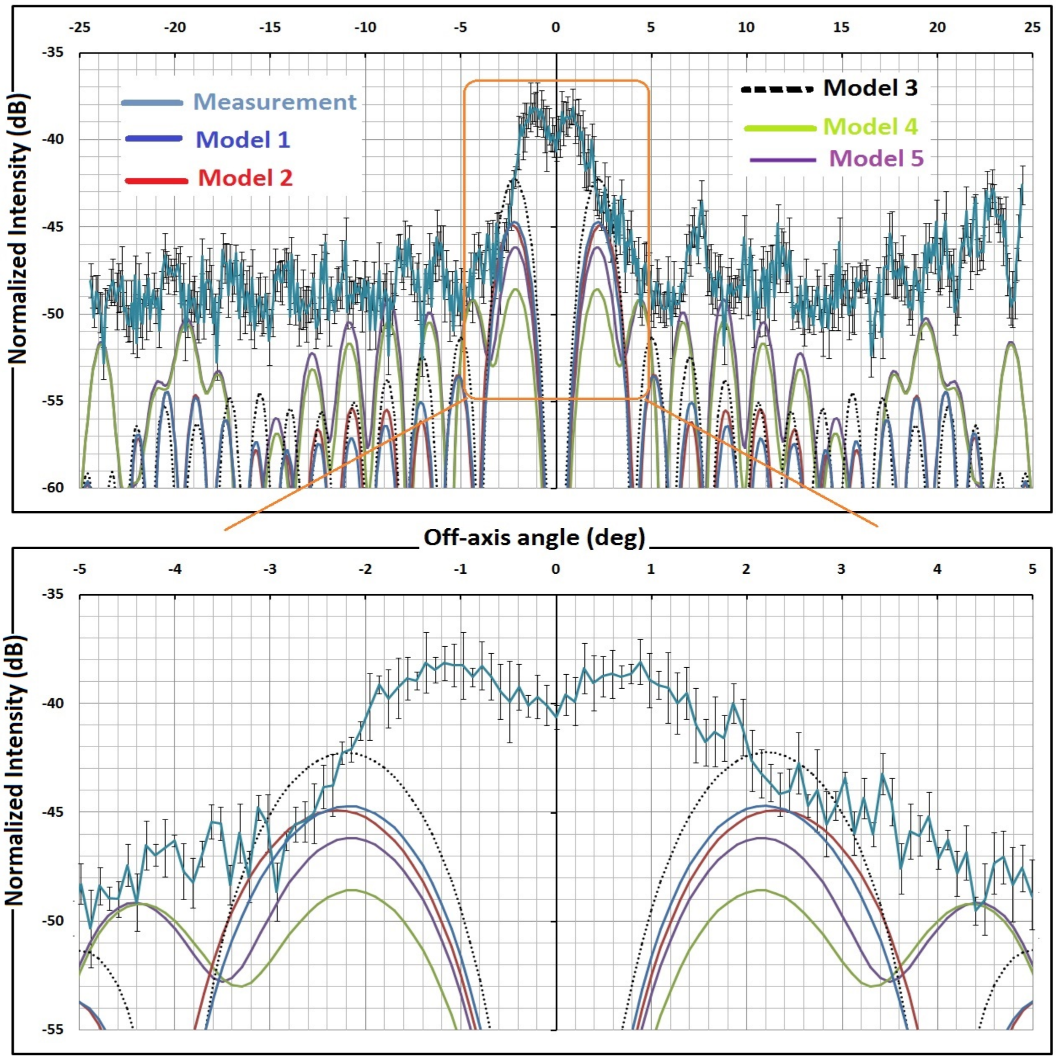

Figure 6.34: The comparison of all model predictions and the measurement of the feed horn-medium lens system for cross-polarization beam pattern. The plotted data only shows the measured cross-polarization pattern for the D plane cut. The bottom figure shows the zoomed image of the upper figure.

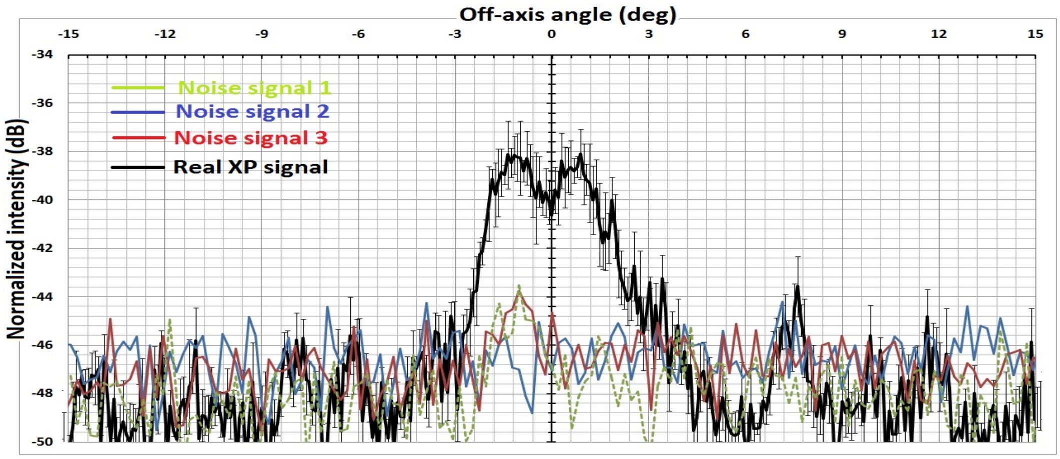

Figure 6.35: Figure shows the comparison of the measured cross-polarization pattern for the D plane cut and the noise measurements. Three different noise measurements were performed by blocking the transmitting feed aperture with a MM-wave absorber.

orientation for the D plane cut and when the path of the horn-lens beam is blocked by a thick MM-wave absorber. Measured signals are normalized to the same co-polarization pattern as shown in Figure 6.35. The comparison shows that the signal level below -44 dB is fluctuating randomly and can be accepted as background noise. In particular, the cross-polarization signal varies from the noise signal in the main beam region.

6.3.6 Conclusion for the medium lens design study

Beam predictions from all models differed from the measurement results almost equally as shown in Figures 6.31, 6.32 and 6.33. Maximum beam differences between the measured and the simulated data were calculated to be -17 dB for the comparisons of each plane cut.

Maximum XP signals for the E, H and D plane cuts were measured as -37 dB, -37 dB and -38 dB, respectively. In particular, the source of the cross-polarization measured for the E and H plane cuts must be separately investigated. This is associated with the instrumental polarization effects due to dielectric material imperfections. The best matched XP values with the measured data was obtained from the Model 3 predictions. Therefore, the Model 3 was chosen as the reference model and its results were compared with the measured beam parameters given in Table 6.2. Table gives that the measured values of the beam-width at 3 dB (FWHM) could be predicted by FEKO simulations very well. Also, Models 2 and 5 are in a well agreement with the measured data for the side-lobe level. Lastly, maximum and integrated XP values show the polarization performance of the horn-lens for each cut over the W band. Integrated XP was also plotted in Figure 6.36 as a function of frequency over the main beam. Many measured values vary between -30 dB and -40 dB over the band frequencies with two exceptions. These are the peaks of -21 dB and -26 dB at $\sim$89 GHz and $\sim$95 GHz. Standing waves cause these spikes.

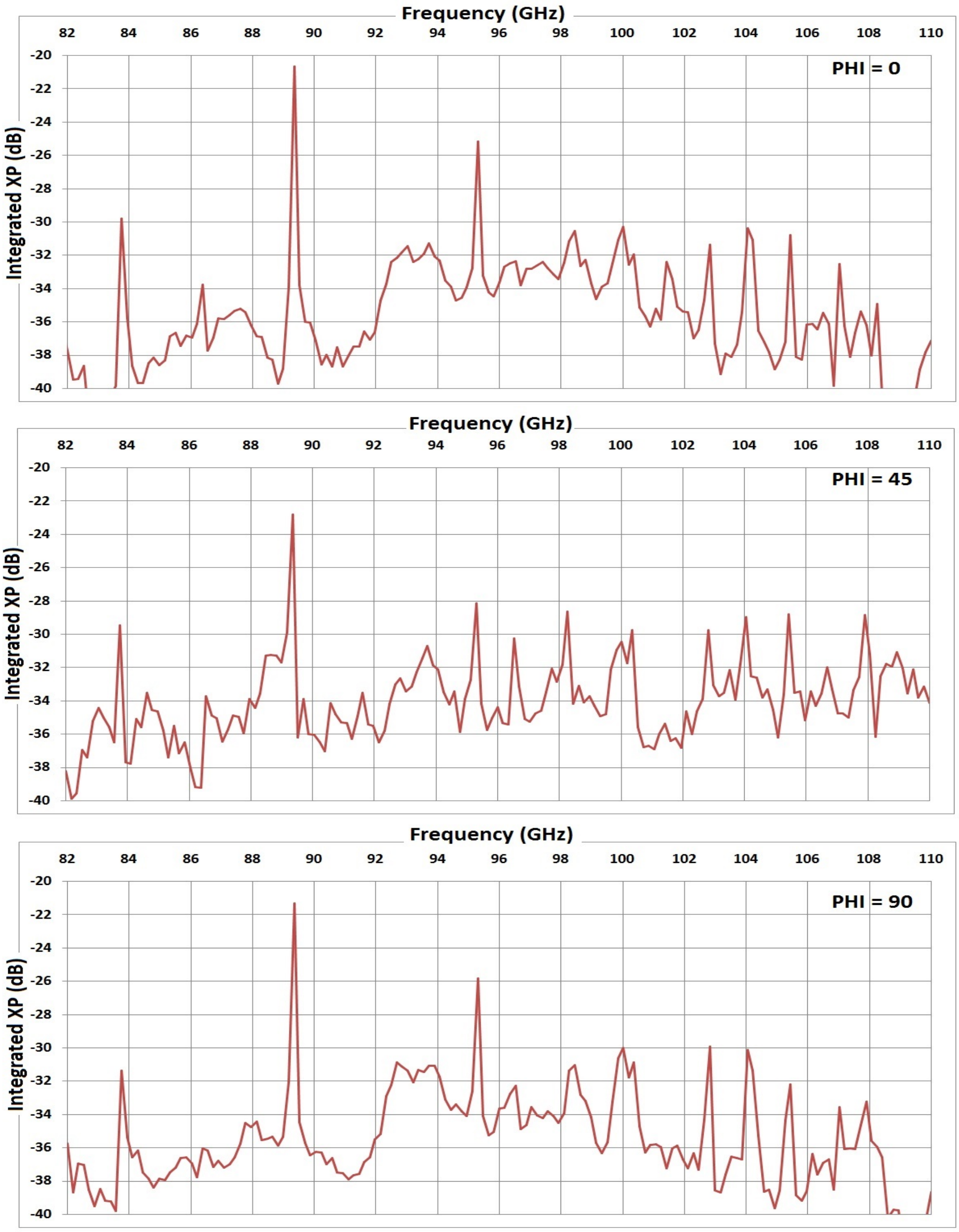

Figure 6.36: Integrated XP values as a function of frequency. The plots are given at H, D and E plane cut from top to bottom.

Parameter	Model(H)	**Exp.(H)**	Model(D)	**Exp.(D)**	Model(E)	**Exp.(E)**
BW (85 GHz) deg	2.42	**2.425**	2.44	**2.485**	2.45	**2.504**
BW (97 GHz) deg	2.167	**2.251**$\pm$0.014°	2.181	**2.213**$\pm$0.01°	2.196	**2.251**$\pm$0.007°
BW (110 GHz)deg	2	**2.05**	1.98	**2.04**	1.97	**2.05**
SL (85 GHz) dB	-22.3	**-21**	-22.2	**-20**	-22.1	**-20.2**
SL (97 GHz) dB	-23.6	**-22**	-23.3	**-21.5**	-23	**-22**
SL (110 GHz) dB	-24.8	**-24.2**	-24.5	**-24.2**	-24.1	**-23.5**
Max. XP (85 GHz) dB	-	**-45**$\pm$0.75	-41.9	**-37**$\pm$0.47	-	**-41**$\pm$0.67
Max. XP (97 GHz) dB	-	**-36.6**$\pm$0.61	-42.2	**-38.1**$\pm$0.56	-	**-37**$\pm$0.61
Max. XP (110 GHz) dB	-	**-36**$\pm$0.6	-41.5	**-38**$\pm$0.6	-	**-37**$\pm$0.41
Int. XP (W-band) dB	-	**-35.3**	-	**-34.1**	-	**-35.5**

Table 6.2: The beam parameters calculated from the lens model are compared to the experimentally measured values for the reference frequencies. The XP were measured for all plane cuts however it was compared to only modelled data at the D plane cut because the XP is not expected to be in the E and H field cuts. The bold characters denote the measured values while the others are for the predicted values.

6.4 Study of Anti reflection coated (ARC) lens

This section describes the simulations and measurements of the UHMWPE dielectric slab and the medium size lenses with and without the anti-reflection coating (ARC). The ARC manufacture process, based on the single layer method, is also explained. The performance of the ARC medium sized lens is compared to the un-coated lens by measuring the reflection, transmission and far-field beam patterns.

ARC is a process used to reduce reflections and increase the transmission in an refractive optical system. Reflections from the lens surfaces lead to systematic effects in the return loss, transmission loss and instrumental polarization. Transmission losses increase the noise in the optical system and therefore reduce the sensitivity. To this end, an effective ARC technique is expected to reduce reflections considerably while increasing transmission.

6.4.1 A brief literature review of ARC

With increasing interest in the use of refractive components for CMB polarization instrumentation, reliable techniques for ARC of large aperture lenses have been studied for the millimeter and sub-millimeter frequency ranges. There are well established techniques employed to coat lenses with a set of anti-reflection materials. The basic technique is the single layer coating process, which has also been used, for instance, for the coating HDPE lenses and PTFE filters on the BICEP instrument [74] and for the coating of the silicon lenses on the ACT instrument [137]. In addition, multi-layer ARC can be manufactured to increase the bandwidth performance of lenses by carefully repeating the single layered procedure. One example for multi-layer AR coating is the silicon lenses of CMBPol mission made by the UC Berkeley group [55]. It is also worth mentioning that there is a simulated dielectric ARC technique which produces a layer of graded-index ARC dielectric. In this technique, the refractive index of the ARC material is varied from 1 to n_{ARC} which is the refractive index of the ARC material. The technique has already been used for the DASI, CAPMAP, SPT lenses [55]. The bandwidth and polarization performances of the ARC lenses designed with the simple quarter wavelength method were highly improved by the graded-index method. However, machining technology is limited to a group of materials: HDPE, LDPE and Rexolite.

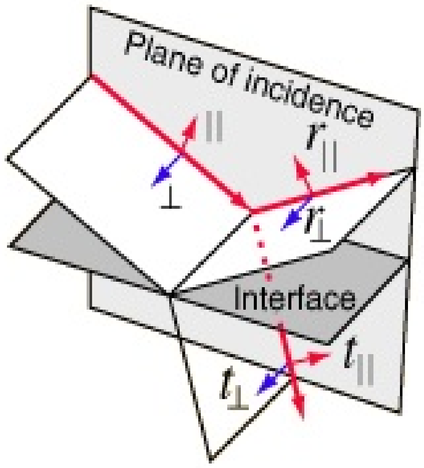

Figure 6.37: Rays parallel and perpendicular to the plane of incidence [138]. Each ray has two polarization components. The s polarization (||) is parallel to the plane of incidence and the p polarization ($\perp$) is the perpendicular to the plane of incidence.

6.4.2 Reflection and Transmission Models

As the starting point of the model analysis, transmission and reflection properties of a dielectric slab were modelled. Calculated parameters were verified by using two models: the fresnel equations and the transmission-line model. The transmission-line model was also used for an (ARC) dielectric slab. Following these slab predictions, two lenses (ML and ARC-ML) were modelled for simulations of co- and cross-polarization radiation beam pattern in both far and near field in FEKO.

1. **Fresnel equations**
   Figure 6.37 shows reflection and refraction of an incident ray on an interface. The reflectance from each surface element and transmittance over a dielectric interface with the refraction index n_m can be calculated by fresnel equations 6.6-6.9 for two polarization states [139]. The s polarization (||) is parallel to the plane of incidence while the p polarization ($\perp$) is the perpendicular to the plane of incidence. The fresnel equations are independent of wavelength and the behaviours of the calculated parameters are predicted by only the incident angle.

$$R_s = \left(\frac{n_1 \cdot \cos\theta_1 - n_m \cdot \cos\theta_m}{n_1 \cdot \cos\theta_1 + n_m \cdot \cos\theta_m} \right)^2 \tag{6.6}$$

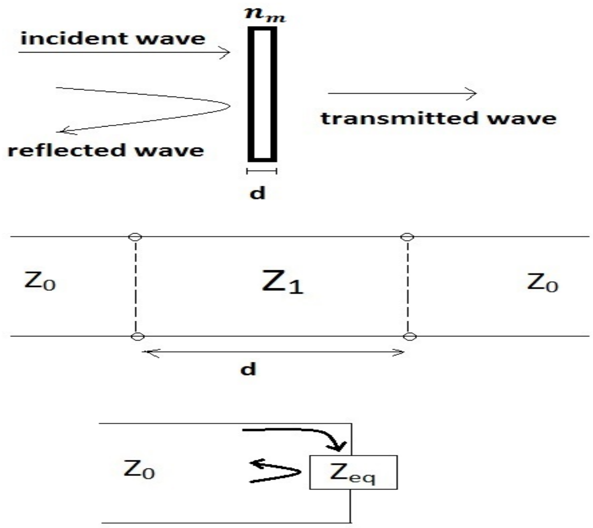

Figure 6.38: Upper figure: A plane wave travelling along the free space and entering the slab at normal incidence. Middle figure: The representation of the optical system in the upper figure with a transmission line model. Bottom figure: An equivalent load impedance is generated thanks to the free-space impedance of Z_0 and the dielectric slab impedance of Z_{eq}.

$$R_p = \left(\frac{n_1 \cdot \cos\theta_m - n_m \cdot \cos\theta_1}{n_1 \cdot \cos\theta_m + n_m \cdot \cos\theta_1}\right)^2 \tag{6.7}$$

$$T_s = \frac{n_m \cdot \cos\theta_m}{n_1 \cdot \cos\theta_1}\left(\frac{2 \cdot n_1 \cdot \cos\theta_1}{n_1 \cdot \cos\theta_1 + n_m \cdot \cos\theta_m}\right)^2 \tag{6.8}$$

$$T_p = \frac{n_m \cdot \cos\theta_m}{n_1 \cdot \cos\theta_1}\left(\frac{2 \cdot n_1 \cdot \cos\theta_1}{n_1 \cdot \cos\theta_m + n_m \cdot \cos\theta_1}\right)^2 \tag{6.9}$$

2. **Transmission-line model for single-layer interface**
   This model is used to determine the wavelength dependency of reflection and transmission parameters. The model can be employed for modelling of both un-coated and coated dielectric slabs. Its algorithm is based on the impedance definitions of the mediums. Once a medium is defined in terms of the refractive index, the equivalent impedance of layered mediums can be determined. For instance, a generator in a circuit is represented by a plane wave source propagating through an isotropic dielectric medium. The schematic of the circuit can be staged as shown in Figure 6.38.

The dielectric impedance is defined as $Z_1 = \frac{Z_0}{n_m}$. The equivalent impedance is given in the equation as

$$Z_{eq} = Z_1 \left(\frac{Z_0 + jZ_1 \tan \beta d}{Z_1 + jZ_0 \tan \beta d} \right) \tag{6.10}$$

where β is the wave-number of the propagating wave inside the dielectric. Z_0 is the free space impedance and its value is 377Ω .

Due to the discontinuity in free-space, the propagating wave meets an impedance and thus some power is reflected. The fractions of the reflected power (Reflectance) and the transmitted power (Transmittance) can be calculated from Equations 6.11 and 6.12 given as follows.

$$R = \left| \frac{Z_{eq} - Z_0}{Z_{eq} + Z_0} \right|^2 \tag{6.11}$$

$$T = 1 - R \tag{6.12}$$

Equation 6.12 is for non-lossy dielectrics. The maximum transmission and the minimum reflection can be obtained for specific thickness values defined in Equation 6.13. From Equation 6.10, the condition dictates that the thickness of the dielectric slab should be an integer number m of half wavelengths.

$$d_m = m \frac{\lambda}{2n_m} \tag{6.13}$$

This is where λ is the free-space wavelength and d_m is the m_{th} thickness of dielectric slab.

3. **Transmission-line model for multi-layer interfaces**
   The transmission-line model can also be employed for the multi-layer structures such as the ARC slab. The scenario can be represented as shown in Figure 6.39. For each dual impedance system, the equivalent impedance is reformulated until the left-side free-space impedance meets the impedance of Z_{eq2}. The expressions for the Z_{eq}, Z_{eq1} and Z_{eq2} are given in Equations 6.14, 6.15 and 6.16 respectively.

$$Z_{eq} = Z_{arc} \left(\frac{Z_0 + jZ_{arc} \tan \beta d_{arc}}{Z_{arc} + jZ_0 \tan \beta d_{arc}} \right) \tag{6.14}$$

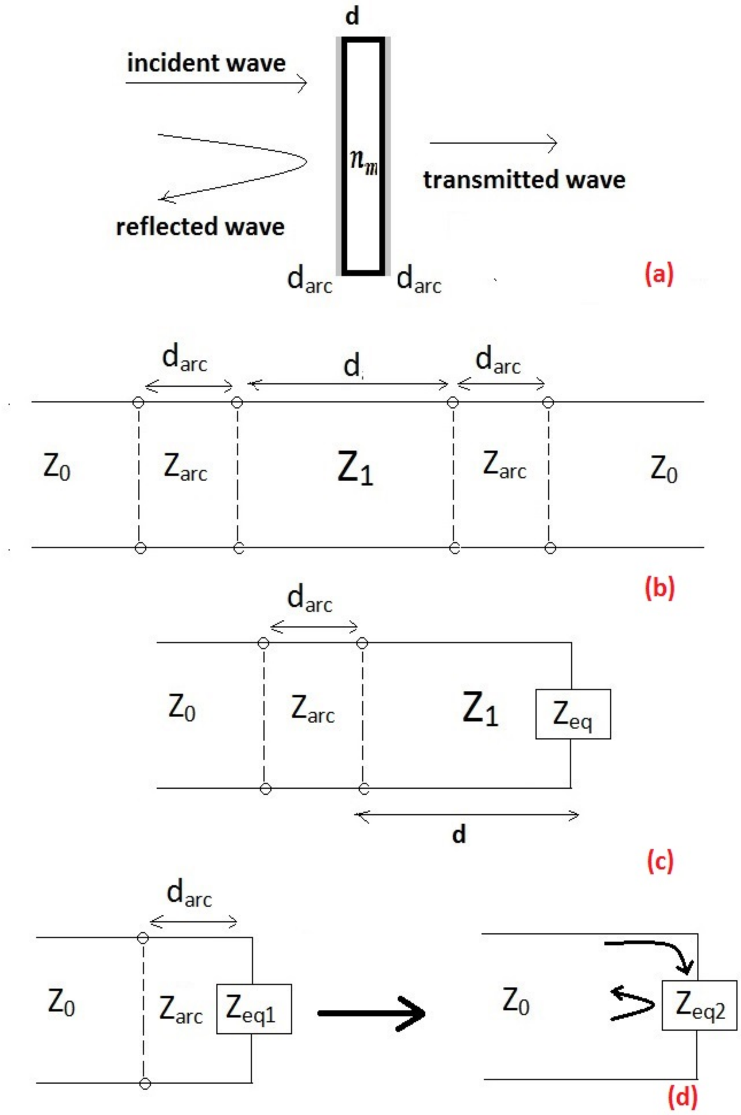

Figure 6.39: Similar to Figure 6.38, the upper figure shows five mediums with three different impedances. A plane wave travels along the free space (free-space medium), enters the slab at normal incidence (ARC material and dielectric mediums) and finally leaves the slab (dielectric and ARC material mediums). The second figure is the representation of the equivalent transmission line model of the optical system in the upper figure. While d is the thickness of the dielectric slab and another transmission line of d_{arc} matches with the thickness of the ARC layer. From the second figure to the bottom right figure, an equivalent load impedance is eventually generated in terms of the free-space impedance of Z_0 and the final equivalent impedance of Z_{eq2}.

$$Z_{eq1} = Z_1 \left(\frac{Z_{eqn} + jZ_1 \tan \beta d}{Z_1 + jZ_{eqn} \tan \beta d} \right) \tag{6.15}$$

$$Z_{eq2} = Z_{arc} \left(\frac{Z_{eqn1} + jZ_{arc} \tan \beta d}{Z_{arc} + jZ_{eqn1} \tan \beta d} \right) \tag{6.16}$$

The impedance for the ARC layer is defined as $Z_{arc} = \frac{Z_0}{\sqrt{n_m}}$. Also, the reflectance and transmittance are given in the equations 6.17 and 6.18.

$$R = \left| \frac{Z_{eq2} - Z_0}{Z_{eq2} + Z_0} \right|^2 \tag{6.17}$$

$$T = 1 - R \tag{6.18}$$

6.4.3 Single layer ARC model

Single layer ARC method is the simplest model used to coat dielectric structures such as lenses and filters. Predictions of reflection and transmission coefficients are obtained by achieving zero reflectance for an optimum wavelength value. However, this can be obtained only at normal incidence.

There are two requirements to select a suitable ARC material that provides minimum reflection. Firstly, the refractive index of the ARC material should satisfy Equations 6.19 and 6.20 given for two polarization states [140],

$$n^s_{ARC}(\theta)^2 = \frac{n_m^2 + \sqrt{n_m^4 - 4 \cdot n_m^2 \cdot \cos\theta \cdot \sin^2\theta \cdot \sqrt{n_m^2 - \sin^2\theta}}}{2 \cdot \cos\theta \cdot \sqrt{n_m^2 - \sin^2\theta}} \tag{6.19}$$

$$n^p_{ARC}(\theta)^2 = \sin^2\theta + \cos\theta \cdot \sqrt{n_m^2 - \sin^2\theta} \tag{6.20}$$

where n_{ARC} is the refractive index of the ARC material. The indexes of s and p denote the orthogonal polarization states.

Secondly, the thickness d of the matching ARC layer is fixed by Equation 6.21

$$d_{s,p}(\theta) = \frac{\lambda}{4 \cdot \sqrt{n_{s,p}^2 - \sin^2\theta}} \tag{6.21}$$

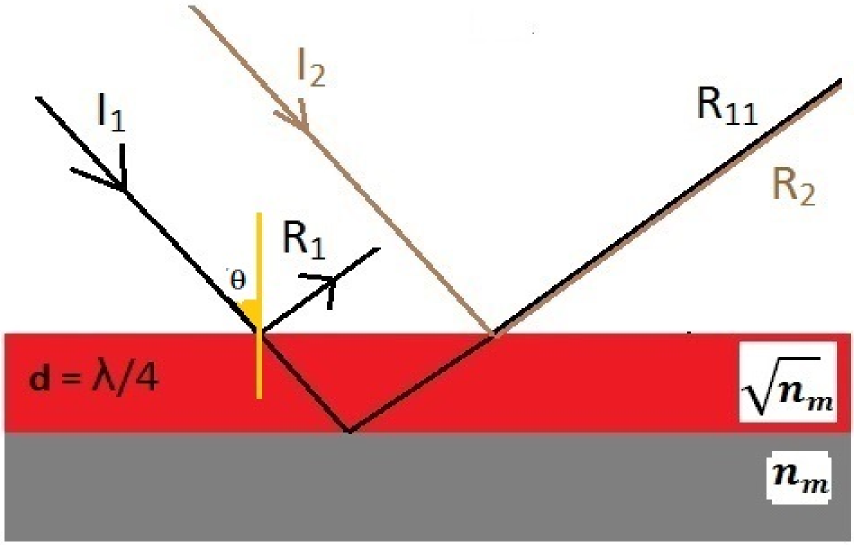

Figure 6.40: The grey layer indicates the dielectric slab while the red layer indicates the matching ARC layer. The reflected beams of R_{11} and R_2 are out of phase and hence destroy each other for a given wavelength λ. α shows the incidence angle.

The requirement of the quarter wavelength thickness for the zero reflection is illustrated in Figure 6.40. The quarter wavelength thickness of the ARC layer results in destructive interference between two reflected beams of R_{11} and R_2.

For the special case of Equations 6.19, 6.20 and 6.21, the normal incident wave gives the relations as follows.

$$n_{ARC}^{p,s}(\theta = 0) = \sqrt{n_m} \tag{6.22}$$

$$d_{s,p}(\theta = 0) = \frac{\lambda}{4 \cdot \sqrt{n_m}} \tag{6.23}$$

For the UHMWPE material ($n_m = 1.517$), the values for refractive indexes and the corresponding thicknesses of the matching ARC material are calculated and plotted as a function of incidence angle in Figures 6.41. The requirements are satisfied up an the angle of $\sim 20°$, while the performance of the ARC with the calculated specifications is reduced by higher incidence angles. In practice, the differentiation of the calculated refractive index and thickness values between two linear polarization states leads to power leakage and hence increases the instrumental polarization systematics. In our case, the lens has a f-number of 2.4 corresponding to the divergence angle of $\sim 12°$

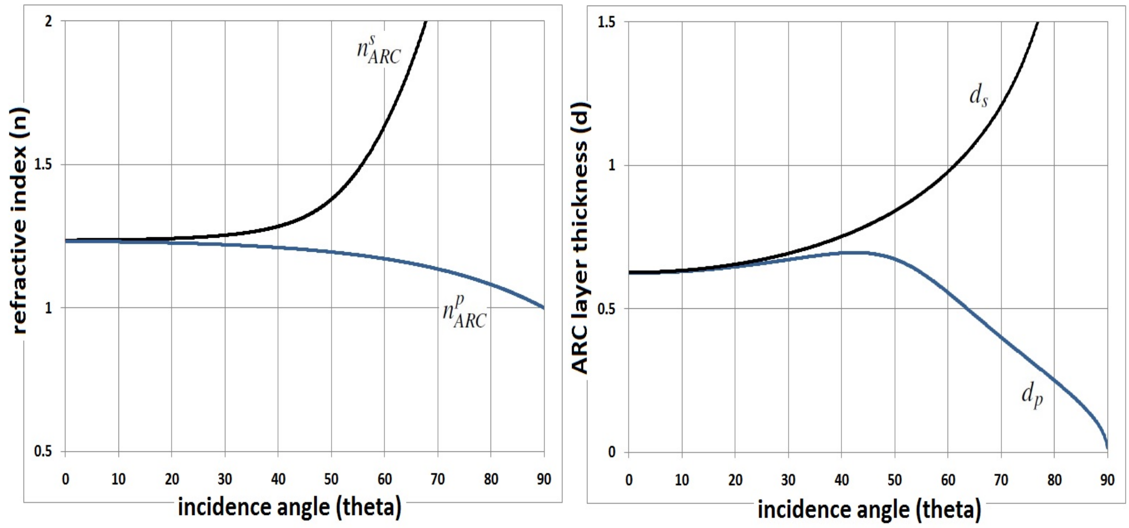

Figure 6.41: The left figure shows the calculated refractive indexes of the ARC material while the right figure shows the change in the thickness of the ARC layer as a function of incidence angle for both linear polarization states. Blue and black lines are for the polarization states of the s and the p respectively.

so the effectiveness of the ARC model employed will not suffer from large angular divergence up to $\sim 20°$.

6.4.4 Model results for the UHMWPE dielectric slab

Reflection and transmission equations of dielectric materials were extracted by using two model approaches highlighted in Section 6.4.2. Here, the verification of models are carried out by comparing calculated parameters from both models.

By using the fresnel equation for two internal reflections, the reflected power (R_1) at normal incidence ($\theta = 0$) from the first surface of the dielectric slab is calculated as 4.22% of the incident power (I_1). The rest of the power (T_1) is refracted and again reflected (R_2) from the second surface of the dielectric slab. As illustrated in Figure 6.42, some fraction of the reflected power T_3, penetrates from the first surface of the dielectric slab to the system. After three reflections (R_1, R_2, R_3), 8.1% of the incident beam power ($R_1 + T_3$) reflects back due to the dielectric slab with a refraction index of 1.517. This corresponds to a maximum return loss of -11 dB and a transmission loss of -0.36 dB. In these calculations, the only parameter used was the refractive index, which was measured and discussed in Section 6.4.6.

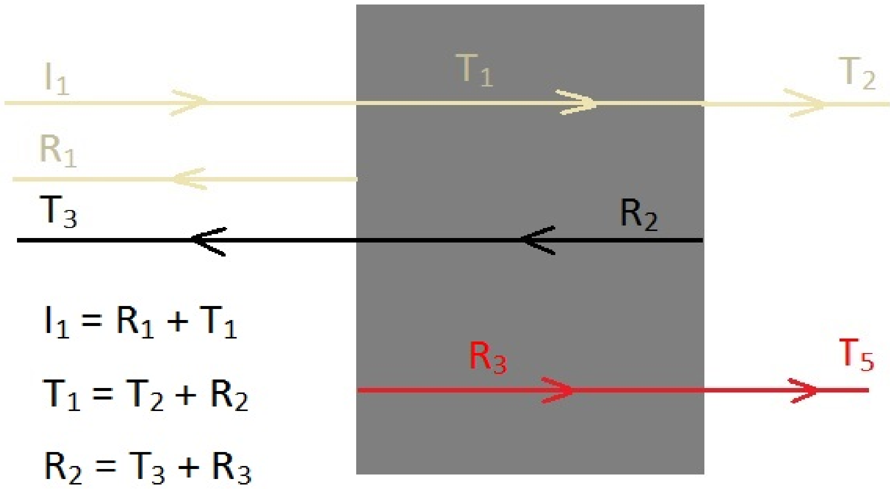

Figure 6.42: The incidence beam I_1 refracts from the dielectric boundary at normal incidence. After three reflections, the total reflected power is the sum of R_1 and T_3.

Alternatively, reflection and transmission parameters of a dielectric slab are calculated in terms of wavelength by using the transmission-line model. An IDL code was written to calculate these parameters for the frequencies between 50 GHz and 150 GHz. Parameters predicted from the transmission-line model are averaged over the frequency band (82-110 GHz). Band average values for return loss and transmission loss was calculated to be -11.6 dB and -0.32 dB respectively.

For a given dielectric thickness, a frequency value will be optimized for maximum transmission and minimum reflection. To this end, the tolerance of the slab thickness was also studied with the transmission-line model. This is to investigate how errors in the measurement of the dielectric slab thickness effect the minimum locations in the return loss parameter S_{11}. These locations give the optimum frequency values of dielectric slab for given dielectric thicknesses. The sample thickness was measured as 8.284 ± 0.004 mm by using a very accurate micrometer. Therefore, a change of 0.004 mm in the slab thickness was modelled. The optimum frequency value shifted by 0.075 GHz. Table 6.3 gives the material specifications extracted from Figures 6.41 and set in the IDL code.

In addition to the calculations of the dielectric slab, the return and transmission losses of the ARC UHMWPE dielectric slab were also calculated by using Equations 6.17 and 6.18. The calculated results for both slabs are overplotted in Figure 6.43.

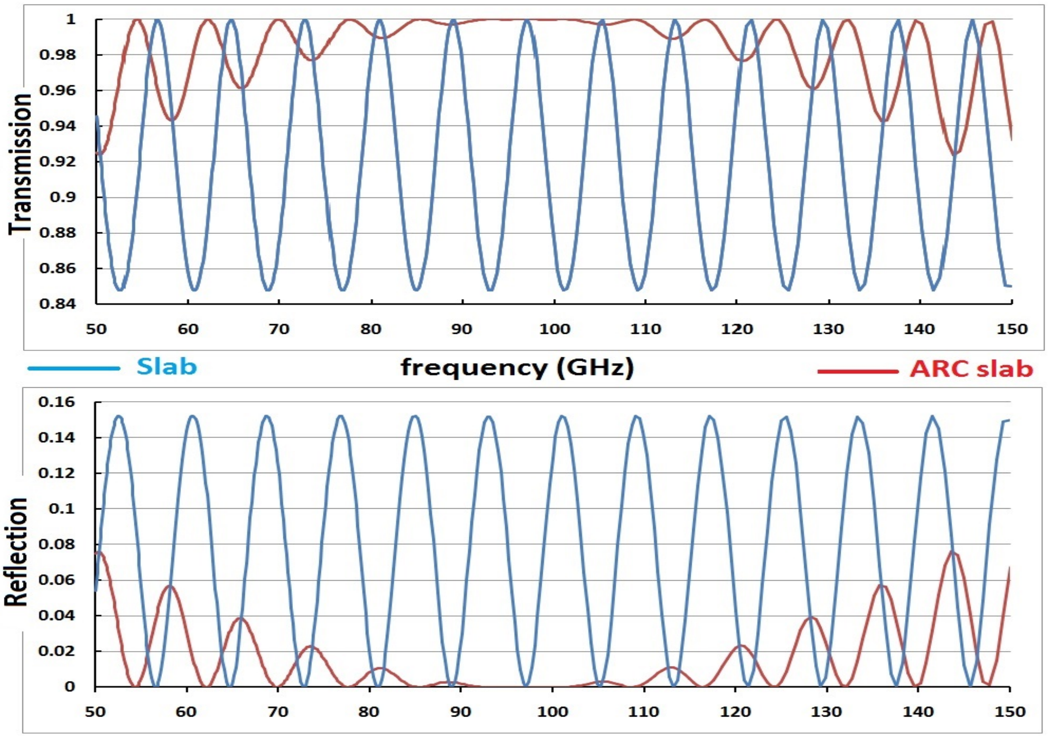

Figure 6.43: Assuming that there is no absorption loss in the dielectric, the top figure gives the model results for the transmission of the slab and the ARC slab versus frequency. The bottom figure compares the calculated reflection coefficients for both slabs. The best performance is obtained in the optimum frequency range, the W-band (75-100GHz).

6.4.5 Modelling of the ARC lens with FEKO

- **Far-field models**

Far-field simulations of the ARC lens were conducted using the MLFMM modelling in FEKO. Predicted beam results were compared with its corresponding un-coated lens model. Figure 6.44 shows the overplotted beam patterns of both lens models computed for the D plane cut at 97 GHz. Two significant differences between two patterns are clearly visible. ARC lens presents 1.5 dB lower side-lobe level and 1 dB higher cross-polarization. Linear scale plots of electric-field pattern for both lenses is shown in Figure 6.45. ARC lens increased transmission of the lens system by 2.64 % as observed in the linear scale field patterns. In the FEKO models of the medium lens and ARC-medium lens, the return loss of the lens system could not be predicted because there was not a port defined in the source model. An equivalent feed input was

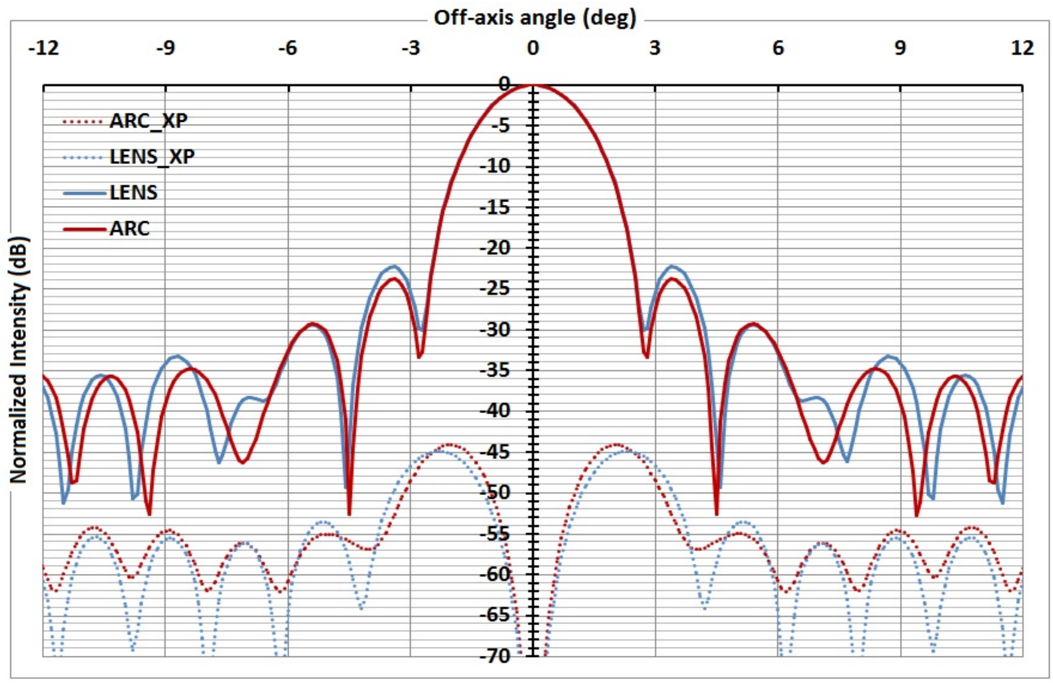

Figure 6.44: The comparison of the lens and the ARC lens model predictions for the intensity beam pattern. the far-field patterns were computed for the D plane cut for 97 GHz.

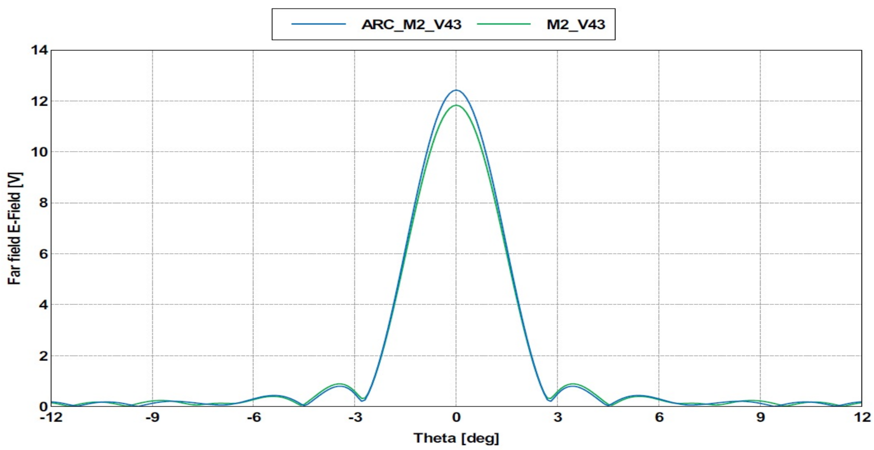

Figure 6.45: Linear scale plots of the electric field. the calculations are conducted in far-field for 97 GHz. The increase in transmission due to the ARC model is visible.

used as a source, instead.

- **Near-field models**

The near field calculations of the medium lens and ARC-medium lens lenses were predicted by using the MLFMM modelling technique. The XY plane cut fields were calculated at a distance of z=329 mm from the phase center of the source input. This distance of z corresponds to the maximum of the XZ plane cut shown in Figure 5.17. Figure 6.46 shows the electric field calculation of the lens system in logarithmic scales. Both lenses have the same level of transmission at this z distance. Additionally, Figure 6.47 shows the field propagation of both lenses along Z-axis. The decrease of reflected power due to the ARC layers is clearly visible at points along the z-axis. For instance, the amount of reflected power was decreased by 4 dB at the distance of z=171 mm as shown in Figure 6.48.

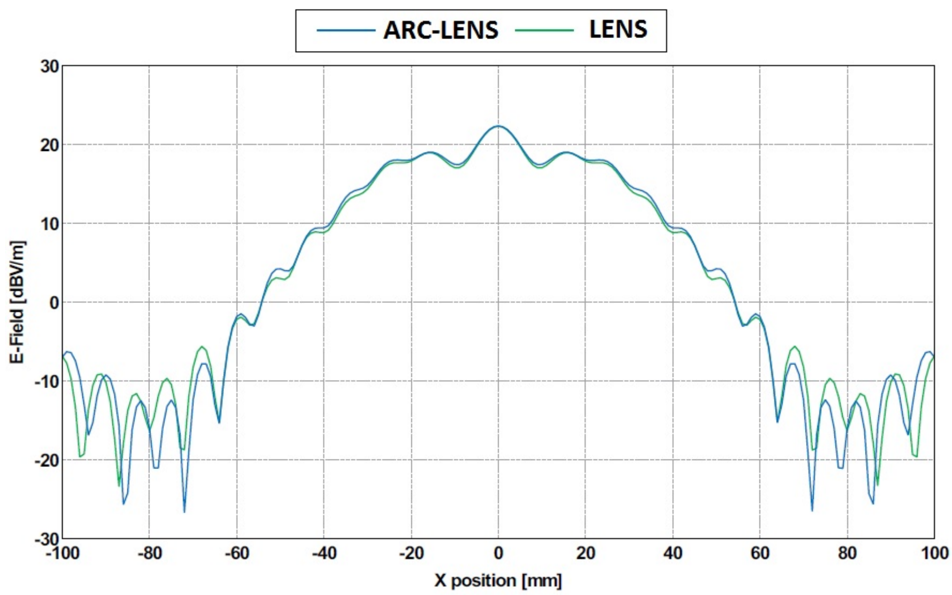

Figure 6.46: Electric field plots of the lens and the ARC lens computed for 97 GHz. The field calculations were conducted on the XY plane cut at a distance of z=329 mm.

6.4.6 Experimental studies

First of all, the experimental determination of the refractive index from the return loss measurements is described in this section. Secondly, the transmission measurements

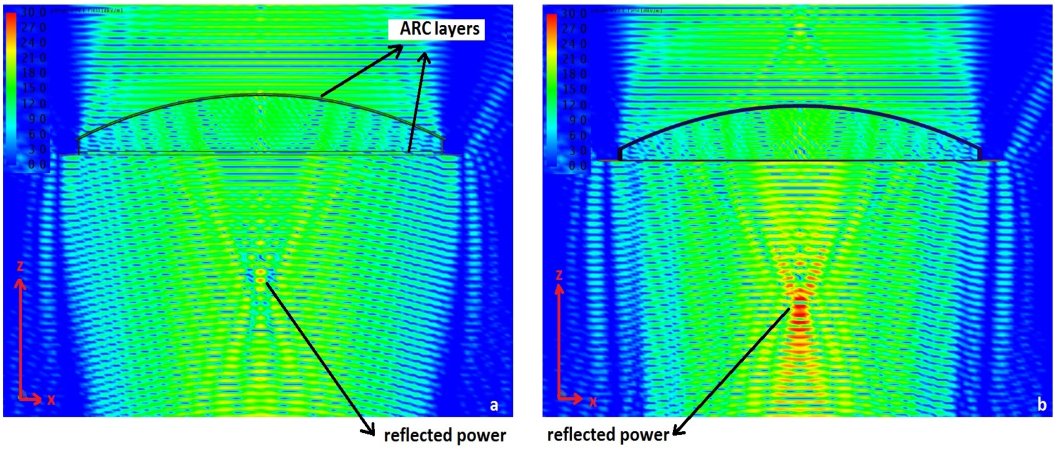

Figure 6.47: The illustration of the field propagations of a) the ARC lens and b) the lens along the z-axis. The reflected power is reduced thanks to the ARC process.

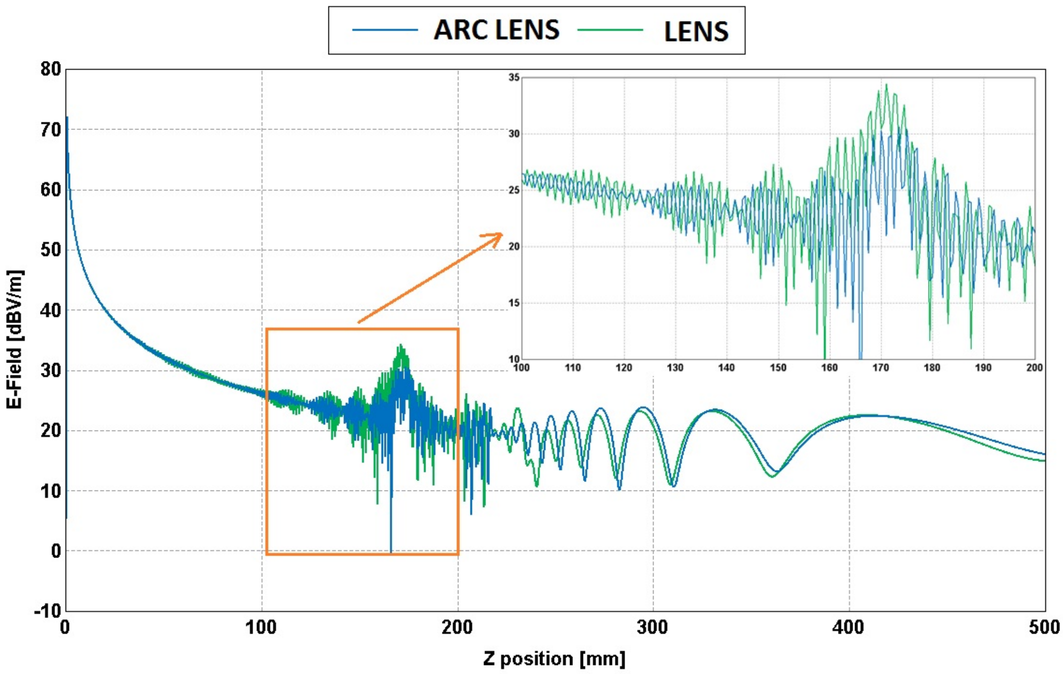

Figure 6.48: Electric field plots of the lens and the ARC lens along the z-axis. Peak reflected power of the ARC lens model computed at a distance of z=171 mm is 4 dB lower than that of the lens model.

Table 6.3: The specifications of the materials used in the IDL code developed for the transmission-line model

Material	Physical thickness	Refractive index
dielectric slab	8.284 ± 0.004 mm	1.517 ± 0.001
ARC material	0.63 mm	$\sqrt{1.517}$

Table 6.4: The refractive index of UHMWPE dielectric was determined by the minimum reflection method. Three frequency values giving minimum return loss as shown in Figure 6.49 were extracted and the corresponding refractive index values were calculated. By referring to the dipping frequency value in the middle, the refractive index was calculated as 1.5170 ± 0.001 for the slab thickness of 8.284 ± 0.004 mm.

Wavelengths	Frequency values	Refractive indexes
$3.592 \pm 4.6x10^{-6}$ mm	83.51 ± 0.1 GHz	1.5176 ± 0.002
$3.141 \pm 2.8x10^{-6}$ mm	95.5 ± 0.08 GHz	1.5170 ± 0.001
$2.794 \pm 0.5x10^{-6}$ mm	107.36 ± 0.02 GHz	1.5178 ± 0.00026

of the dielectric slab are presented and then compared with the model results given in Section 6.4.4. In addition to the slab measurements, the measurements of the ARC lens were realized and the results were compared with those of the un-coated lens. Lastly, the co-polarization radiation beam patterns taken for both lenses are discussed.

1)Determination of the refractive index

The material information provided by the company from where the dielectric slab was bought indicates that the refractive index of the UHMWPE is between 1.51-1.53. This is a quite large range of refractive index so a more precise determination of the material‘s refractive index is required. This can be performed by measuring the scattering parameters (S_{11} and S_{21}) in the CATR test setup. The characterization of both S parameters also provides accurate information of dielectric loss, tangent loss.

Alternatively, the minimum reflection technique (maximum transmission) provides a quick determination of real refractive index for low-loss dielectric materials. In this method, a series of minimum return loss values at specific wavelengths, due to field interference, are determined for an arbitrary dielectric slab thickness.

S_{11} parameter, the return loss of the dielectric slab, was measured in the CATR free-space measurement test bench presented in Chapter 4. There were three minimum wavelength points (λ_1, λ_2 and λ_3). The calculated refraction index values are listed in Table 6.4. Also, the corresponding frequency values are shown clearly in the bottom plot of Figure 6.49. The equation 6.13 was used to calculate refractive index values for UHMWPE. The frequencies corresponding to λ_1, λ_2 and λ_3 were very close to the edge frequencies of the W-band in the CATR setup. Therefore, the second minimum was chosen as the reference point and the corresponding refractive index was calculated as 1.517 ± 0.001 for the slab thickness of 8.284 ± 0.004 mm.

There were two error factors when the refractive index was being calculated. The first was the error in slab thickness determined from the slab measures by using a micrometer. The second was the statistical measurement error obtained from the measurement repetitions.

2)Measurements of the dielectric slab

The transmission and the reflection behaviors of the UHMWPE dielectric slabs with and without ARC were modelled. In order to validate the model results, the slab was measured under the illumination of the plane wave by using the CATR free-space test bench. Figure 6.49 shows the return loss and the transmission loss predicted from the transmission line model and compares them with the experimentally measured data over the W-band frequencies. The plots show the measured data with and without Time Domain Gating (TDG) (see Section 6.1.6). The model data are consistent with the measured data. The measured minimum reflection dips were observed exactly at the same frequency values as predicted from the model. The band average values calculated for the reflectance and transmittance are within the measured error. Table 6.5 gives the measured and the calculated reflectance and transmittance values from the two models for the dielectric slab.

3)Fabrication of ARC lens

The steps of the ARC fabrication process are detailed in this section. The process of the single layer ARC in this section has been developed by Vic Haynes from Jodrell Bank Observatory (JBO) in the Technology Group.

Two identical lenses were manufactured and characterized. Table 6.6 gives the differences in the beam pattern, transmission and the FWHP between two lens measurements. There is 0.88% difference in the FWHP values between two lenses. The intensity difference remains below -17 dB in angle range between $-25^\circ \leq \theta \leq 25^\circ$. The transmittance power difference was calculated as 0.085 dB corresponding to 0.2% transmission loss, while they present almost same reflection performance. All these differences are assigned as manufacturing errors.

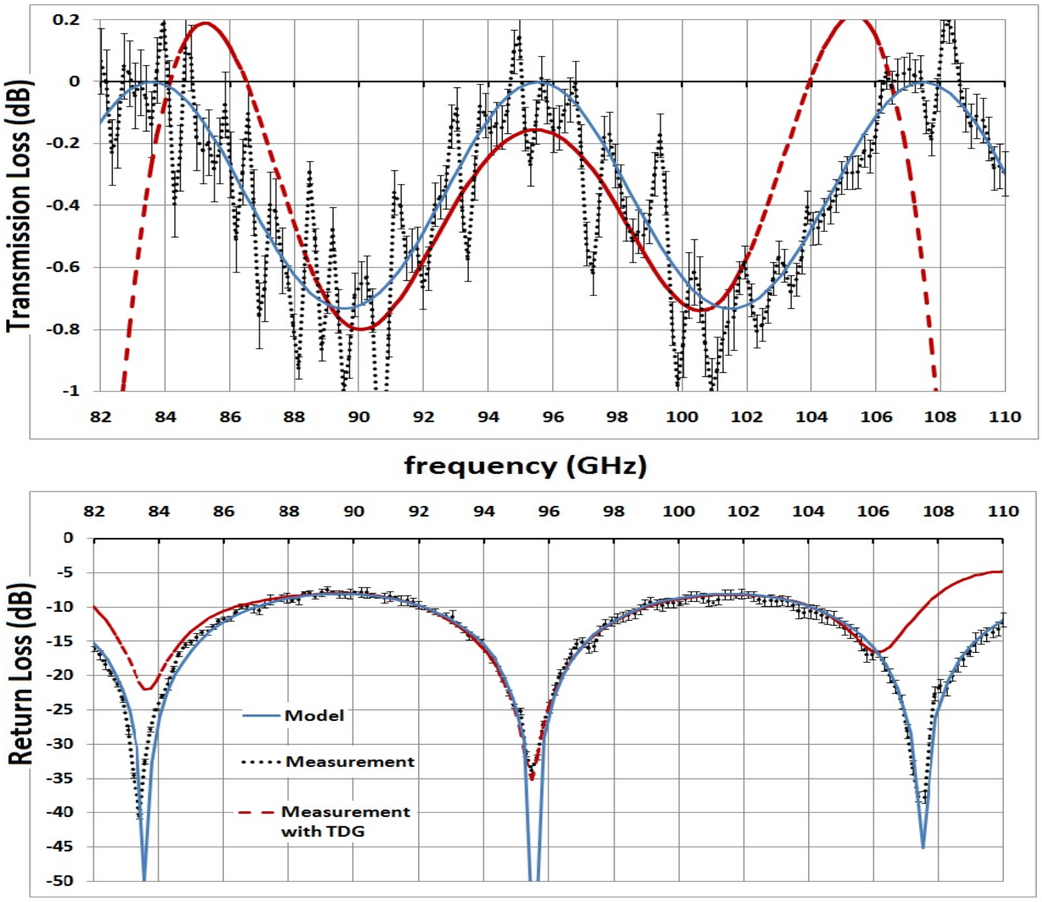

Figure 6.49: The overlapped plots of the predicted and measured data with and without the TDG for the return and transmission losses of the dielectric slab. The UHMWPE slab has a thickness of 8.284 ± 0.004 mm. The frequency range is for the W band frequencies (82-110 GHz) while the parameters are given in the logarithmic scale (dB).

According to the comparison results, the less transparent one was preferred to make the ARC lens. The ARC process is detailed as follows. Figure 6.50 shows the stages of the ARC process starting from the upper-left image to the bottom-right corner.

- An aluminium **mould** fitting the curved surface of the lens was manufactured in the school workshop. It was used to apply the ARC material on the lens surface uniformly as shown in Figure 6.50b.

- The porous Polytetrafluoroethylene (pPTFE), also known as Teflon, was selected as the **ARC material**. The pPTFE has a void volume of 50% that provides the right refraction index with n$\sim$1.22 to coat the lens. The thickness of the

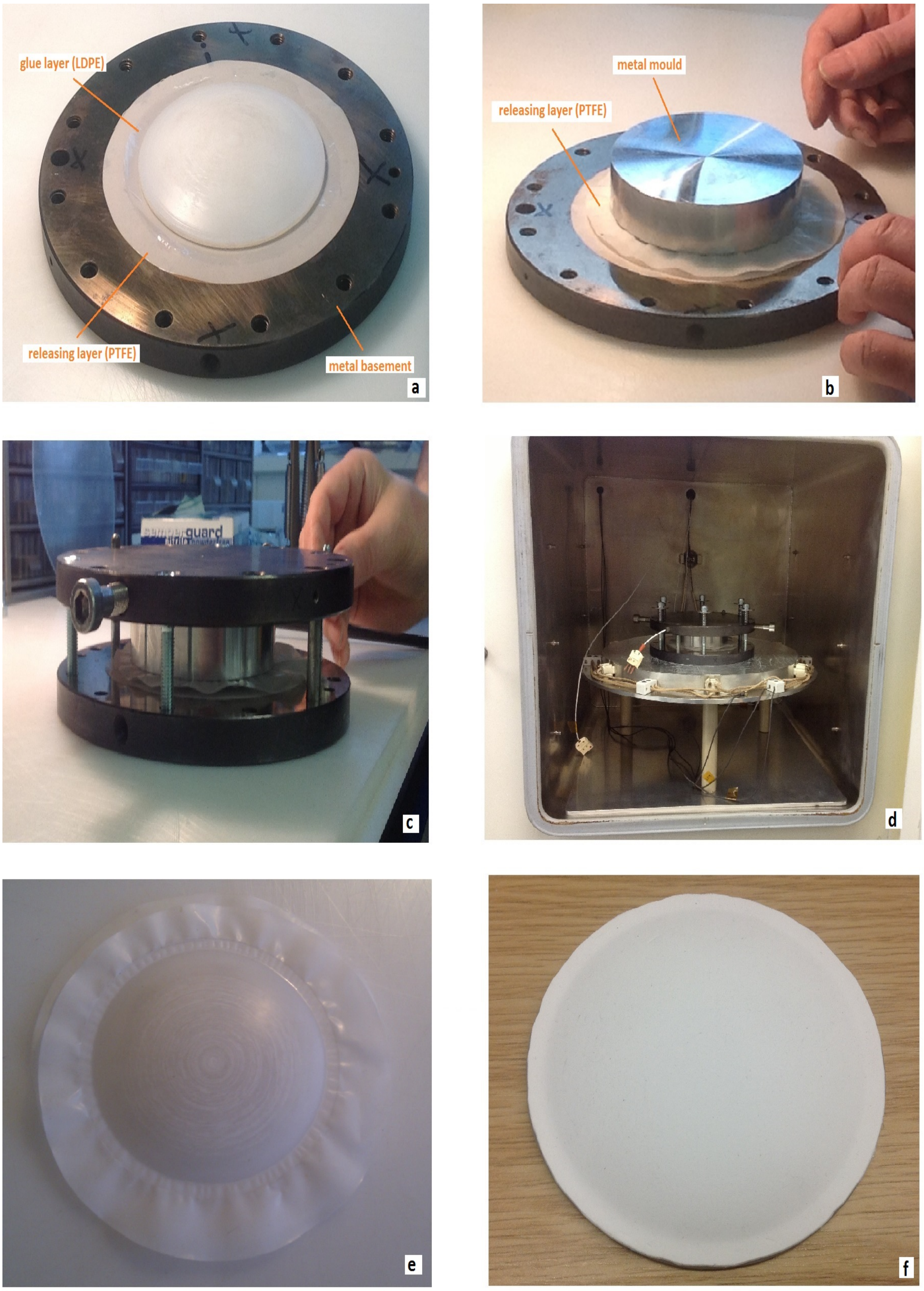

Figure 6.50: The preparation consists of glue layer (LDPE), releasing layer (PTFE) and lens. From the upper-left image to the bottom-right figure: the preparation laid on the metal basement, the aluminium mould left on the preparation, the upper metal basement used to press the preparation, the screwed preparation left in the oven chamber, the glued lens and the ARC lens are photographed respectively.

	Measured data	**Fresnel equations**	**Transmission-line**
Reflection	-12.2±0.2 dB	-11 dB	-11.6 dB
Transmission	-0.358±0.02 dB	-0.36 dB	-0.32 dB

Table 6.5: The band average for the return loss are calculated from the two models and then compared to the measured data. Also, the transmission losses are predicted from the two models.

Table 6.6: The beam difference between the radiation beam patterns measured for both lenses is calculated. Transmission losses and the FWHP of both lenses are also compared.

Beam difference	Transmission difference	FWHP difference
$\geq$ 17 dB	0.085 dB	0.88 %

pPTFE layer was calculated as 0.63 mm from the equation 6.21 for an optimum frequency of 97 GHz.

- Low density polyethylene (LDPE) was used as **glue material** to adhere the lens to the ARC material. Its thickness was measured as 0.2 mm.

These material layers were stretched down in order of the UHMWPE lens and the LDPE glue on the aluminum base as shown in Figure 6.50a, 6.50b and 6.50c, and then they were put into the purpose-built evacuated oven (6.50d).

- All prepared materials were cleaned from any contaminants left on their surfaces before they were combined. A dielectric layer of PTFE was used as an intermediate material by being left between the LDPE and the metal surfaces to be used as a releasing material. Otherwise, the glue part might be sealed off together with the metal. The pressure applied by the aluminum mould helped the glue melt (LDPE layer) evenly over the lens surface. The metal basement was left in an oven at 130° overnight as shown in Figure 6.50d. In the beginning of each heating process, the oven chamber was depressurized to ensure that no air gaps were left between the layers.

Then, the metal basement system was taken out from the oven and left to cool down to room temperature. Figure 6.50e given in the bottom right, shows the glued lens. The PTFE layer was sealed from the surface.

- The system was then prepared for a second heating process. The same steps photographed in the first four images of Figure 6.50 were repeated for the pPTFE ARC layer. The metal basement system was left at 130° in the oven overnight. The last photo of Figure 6.50f, in the bottom-right, gives the final view of the ARC lens.

4)Beam pattern measurements of the ARC lens

- **Far-field measurements**

  The co-polarization radiation beam patterns of both lenses (the medium size lens(ML) and anti-reflection coating lens (ARC-ML)) were measured for W band frequencies in far-field. The results of the overlapped beam patterns are shown in Figure 6.51. The measured lens data remain within the error bars of the ARC lens data for many angular values. Obviously, there is not a significant difference between two lens data so that beam difference was below -16 dB level at maximum.

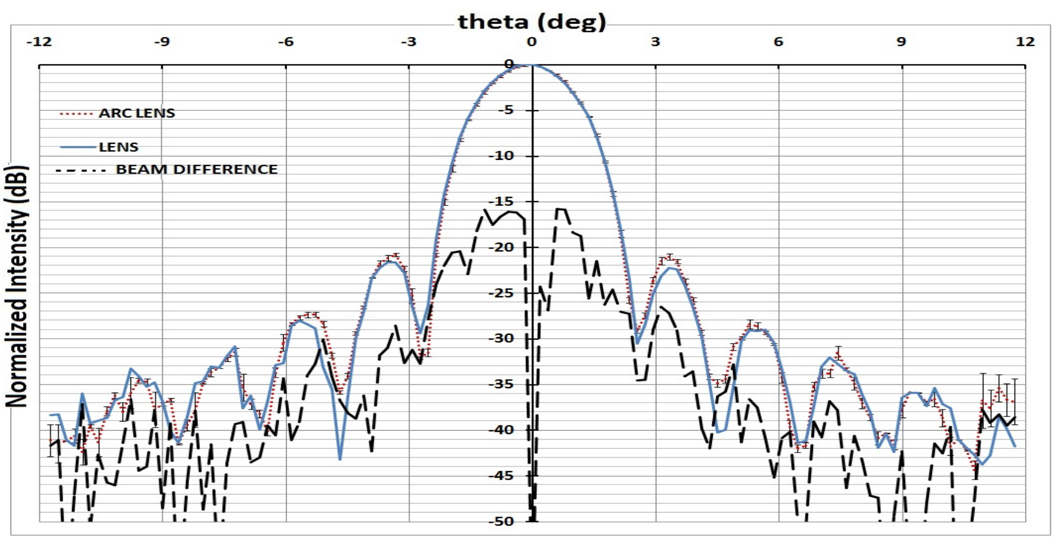

Figure 6.51: Intensity radiation patterns of the lens and the ARC lens measured at far-field. Data were plotted for a frequency of 97 GHz at H plane cut. The calculated beam difference between two plotted data remained below -16 dB.

- **Near-field measurements** The near field of the medium lens was also measured using the 3D scanner together with my colleague, Peter Schemmel [132].

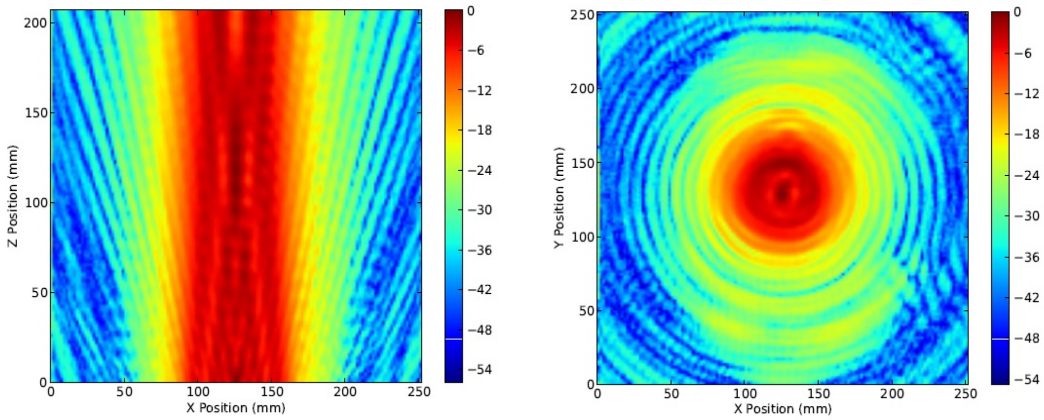

Figure 6.52: Left figure shows the near-field measurements of the lens beam taken at the XZ plane while right figure shows the same field measurements taken at the XY plane. The XZ cut field was performed at the distances between z=103.75 mm and z=311.25 mm. The XY cut field was measured at z=208.15 mm. The measurement resolution is 1.8 mm.

The measurements were performed in two plane cuts (XZ and XY) for co-polarization beam pattern. Left plot of the Figure 6.52 shows the near-field beam evolution along the Z-axis (XZ plane) starting from z=103.75 mm to z=311.25 mm from the front surface of the lens. The fields were measured up to 125 mm to either side of the centre of the beam with a resolution of 1.8 mm. Similarly, right figure of the Figure 6.52 shows the near-field beam evolution at the XY plane. Field measurements were taken at z=208.15 mm. Along the X and Y axes, the scanner measured the lens field from x=y=0 to x=y=252 mm. Display of the phase evolution for the same beams are shown in Figure 6.53. The resulting beam presents uniform phase variation along the Z-axis, seen in the left hand side pattern. Similarly, the measured phase pattern along the XY plane was shown at the right hand side pattern. The phase ripples are getting larger starting at 54 mm from the center of the main beam. The comparison of the FEKO model predictions and the measured data obtained from the lens system for the XY plane cut is given in Figure 6.54. The near field measurements were taken at z=208.5 mm In the central extend of the beam, the both data matches with a maximum beam difference of -7.9 dB. No data correction was applied to the probe beam. Finally, the last plot (Figure 6.55 shows the measured near field along the Z-axis at the centre cut of the XZ plane. We aimed at finding

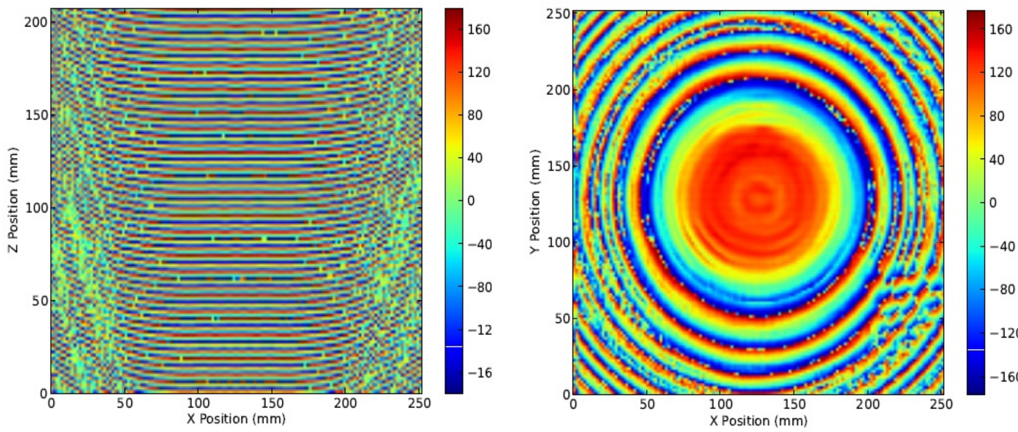

Figure 6.53: Left figure shows the phase measurements of the lens beam taken at the XZ plane while right figure shows the same phase measurements taken at the XY plane. The XZ cut field was performed at the distances between z=103.75 mm and z=311.25 mm. The XY cut field was measured at z=208.15 mm. The measurement resolution is 1.8 mm.

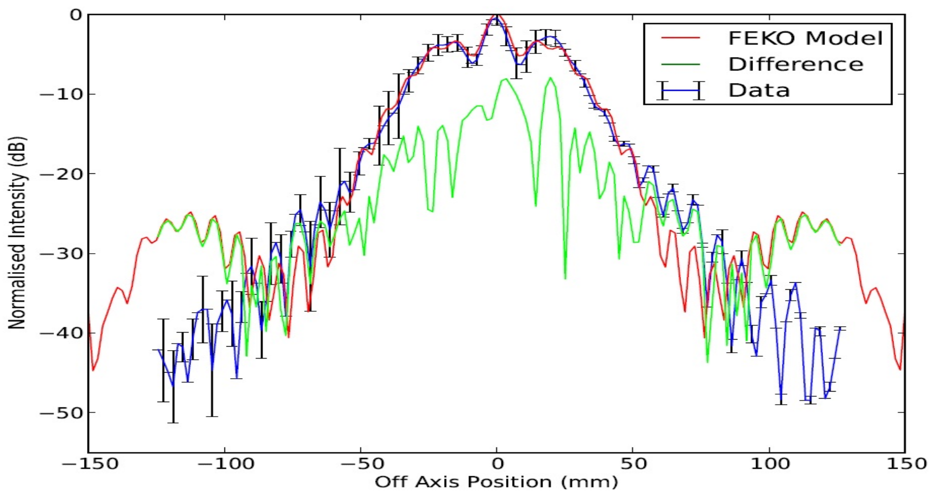

Figure 6.54: The comparison of the measured and the FEKO model data. Green line shows the maximum beam difference between two data to be -7.9 dB.

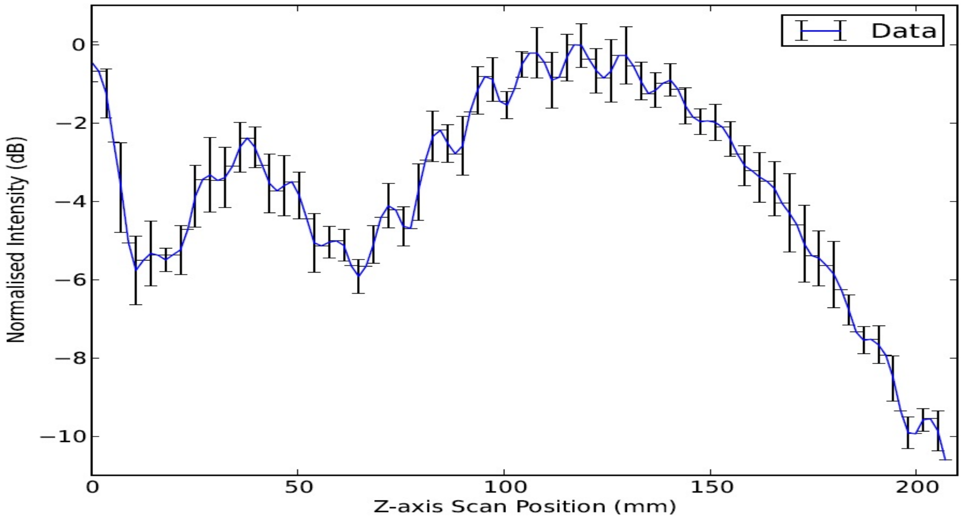

Figure 6.55: The near-field measurements of the lens beam taken at the centre cut along the XZ plane. The maximum of the XZ cut field shows the second beam waist location of the lens system.

the second beam waist position of the beam. The maximum of the XZ plane cut was calculated at z=214.75 mm. From the Gaussian beam model, this value was predicted to be 215 mm.

5)Return and transmission loss measurements

The reflection and transmission measurements of the medium sized lens were compared to those of the ARC medium sized lens. The CATR free-space mirror based S-parameters test bench was used for these measurements. The lenses were measured twice to verify the validity of the experimental data after the TRL calibration had been carried out.

The return loss measurements have been successfully realized by measuring the S_{11} parameter. The plane surface of the lens faced the feed horn during the measurements. Figure 6.57 shows the return loss results of the lens measurements in terms of the W band frequencies. Significant improvements in the measured return loss values were observed. The reflected power decrease due to the ARC lens was between 8 dB to 20 dB over the band. The band average values for the measured return losses of the lens and the ARC lens became -15.93 dB and -29.91 dB respectively. Namely, the amount of average returned power over the band was reduced to one fifth. The interference oscillations appearing in the return loss patterns of the slab disappeared in those of the lens. However, the overall RL pattern for the ARC lens still has an interference

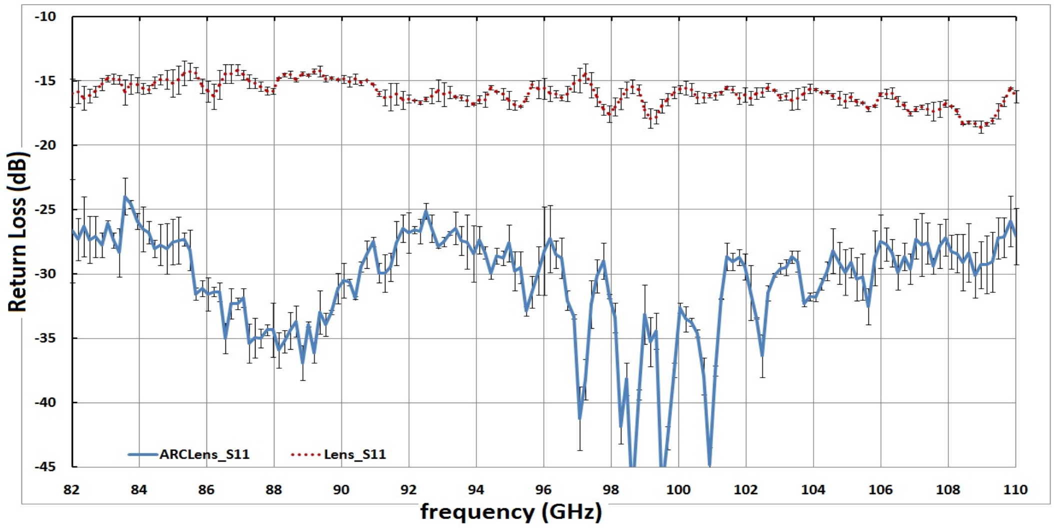

Figure 6.56: The return loss patterns are shown for both lenses with and without anti-reflection coating. The return loss value for the lens is below -15 dB while it is below -25 dB for the ARC lens for many of the W band frequencies.

behaviour. This is probably resulted from the beam modification due to the curve geometry of the second surface of the lens. The other reason can be explained by the multiple reflections from the other components in the test bench. The treatment of TDG on the raw data was intended however this resulted in the loss of the multiple reflections from the lens.

In addition, the transmission loss measurements were attempted with the same measurement setup as the return loss. Since the CATR setup can not focus the lens beam at the receiver feed, the absolute transmission measurements of the medium lens could not be realized with this test bench. The relative transmission measurements obtained for the medium lens with and without ARC were taken over the W band, instead. The transmission loss plots are compared in Figure 6.57. There was no significant increase in transmission introduced by the ARC lens. Slight difference between two plots shows the improvement in the transmission due to the anti-reflection process.

6.4.7 Overall results

Following a brief literature on use of the ARC processes for CMB instrumentation, two approaches (Fresnel equations and Transmission-Line model) were introduced to model the reflection and transmission behaviours of the dielectric slabs. Single layer

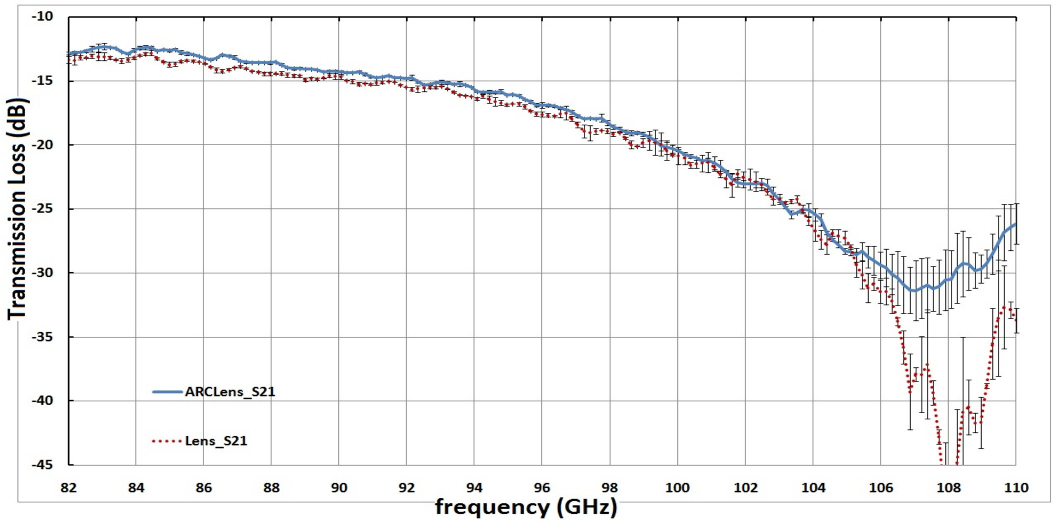

Figure 6.57: The relative transmission loss patterns are shown for both lenses with and without anti-reflection coating. Due to the ARC process, There is a slight improvement in the transmission performance of the lens by 0.5 dB to 1 dB up to a frequency value of 100 GHz.

ARC model was also presented for dielectric slab investigation. Additionally, the far-field and near field calculations of the coated and un-coated lenses were carried out using FEKO simulation package.

Furthermore, the experimental studies of the dielectric slab and the lenses were performed. Initially, the UHMWPE dielectric slab was used to determine the refractive index (n) of the material. It was measured as 1.517 ± 0.001. Then, the obtained n value was used to verify the models with the experimentally measured data. For the same slab, the results shown in Figure 6.49 are well consistent. The average return loss over the W band frequencies (82-110 GHz) was predicted to be -11.6 dB and measured -12.2 dB. Similarly, the transmission loss was predicted to be -0.32 dB and measured -0.358 dB. Relying on these comparison results, the UHMWPE lenses with and without ARC were measured by using the same free-space measurement setup. The co-polarization beam pattern obtained at the H plane cut for both lenses were measured and compared as shown in Figure 6.51. The maximum beam difference between both lens data was calculated to be -16 dB. Other measurements were conducted for the return and the transmission losses. The band average values of the return loss for the lenses with and without ARC were measured -15.93 dB and -29.91 dB respectively. Also, the relative transmission measurements of both lenses showed an improvement by 0.5 dB to 1 dB thanks to the ARC.

6.5 Conclusion

This chapter investigated the characterization of on-axis horn-lens systems. The purpose of this investigation was to compare the present lens simulations (see Chapter 5) with experimentally measured data obtained in RF labs. Measurements of these two horn-lens systems were performed by using three measurement configurations: a far-field measurement setup, a free-space CATR setup (see Chapter 4) and a 3D near field scanner system. The establishment of these measurement setups and the associated technical details were described in the beginning of this chapter. In order to minimize the possible measurement errors, the tolerancing analysis was also carried out. Phase figures helped to align the lens measurement systems in beam scanning.

In the first lens prototype (horn-small size lens system with a diameter of 16λ), a full wave model analysis (MOM) was used and the simulation results were compared to measured data. As a result of comparisons between the simulated and measured data, the maximum beam difference was calculated to be -12 dB at maximum. However, the lens beam suffered diffraction effects due to its relatively small size compared to the beam size of the feed source (3λ). As a result of this, it was found that the lens stop had a significant impact on the diffracted beam pattern. This resulted in poor comparisons of beam characteristics at the edges of the main beam lobe. The comparison of beam parameters between the full model simulated and measured data was given in Table 6.1. Comparison results showed that predictions remained out of measurement errors.

By relying on consistency between the MOM and MLFMM models (also between the MLFMM and RL-GO models, see Conclusion of Chapter 5) used for the first lens, a second lens prototype (horn-medium size lens with 30λ) was considered. MLFMM and RL-GO, which required much less memory requirements than the MOM simulations, were used to model dielectric lens body. The lens was illuminated by different types of equivalent source inputs (SWE, AP, and RAD). Maximum beam difference of -17 dB between the simulated and measured data was observed. Accordingly, beam parameters, e.g. FWHM, side-lobe, and XP, were predicted in close agreement with measured beam parameters as shown in Table 6.1. The difference between the highest and the lowest values of the maximum XP predictions was 6 dB. The measured maximum XP was 4 dB higher than the highest predicted value. What exactly causes this XP signal difference is unkown but this is associated with the instrumental polarization effects due to dielectric material imperfections.

Furthermore, ARC studies of dielectric slab and the medium size lens with and without anti-reflection coating were carried out. Transmission-line model was used to extract the reflection and transmission properties of the dielectric slab. Simulation results were then compared to measured data. Predicted band-average values for both return and transmission losses match very well with measured values as shown in Figure 6.49. Also, the refractive index of the UHMWPE dielectric slab was determined to be 1.517±0.001 by measuring return loss parameter in the CATR measurement setup.

Additionally, an identical lens to the medium lens was produced for ARC studies. Single-layer ARC model was employed to coat the medium lens. The reflection and transmission measurements of both lenses were taken using the CATR setup. Considerable decrease in return loss was obtained by the ARC lens. The relative transmission measurements of both lenses were measured and no significant improvement in transmission was observed. Moreover, modelling of the medium lens and ARC-medium lens for radiation beam patterns in both far and near fields was also conducted using the MLFMM in FEKO and then compared to measured data. The calculated beam difference between two plotted data remained below -16 dB across the full angular range.

Overall, the comparisons of the model predictions with measured data presented high-confidence to analyzing horn-lens systems.

Chapter 7

CHARACTERIZATION OF OFF-AXIS HORN-LENS SYSTEMS

As explained in the introduction of this thesis, the overall sensitivity of a CMB polarimetric instrument can be increased by using more receivers. Large focal-plane arrays supporting the polarimetric detectors, with thousand-pixel elements, need to provide a well designed diffraction limited field of view optical (FOV) system. Such a system accommodates many off-axis pixels. These off-axis pixels have lower RF performance due to their locations. To this end, the systematic effects of off-axis optical configuration such as cross-polarization (XP) and beam shape should be characterized. This section characterizes the off-axis performance of the horn-medium size lens system. This lens is the same as the un-coated lens used for the on-axis beam characterizations. The lens system was initially designed using GO model in ZEMAX and then refined through full-wave modeler tool of FEKO. In GO analysis, the focal plane geometry of the horn-medium lens system was determined. For the selected configuration, FEKO models were employed to obtain the beam pattern characteristics of the horn-medium lens system. Finally, this chapter compares the present FEKO lens model with measured data for main beam parameters, e.g. FWHM, XP, and side-lobe.

7.1 Lens design study with ZEMAX

As the starting point of the off-axis horn-medium lens analysis, the ray-based formulation of ZEMAX was used to optimize the focal plane curvature of the medium lens. The chosen lens material did not exist in the lens catalogue of ZEMAX so the UHMWPE dielectric material was inserted into the catalogue. The parameters that have to be defined in the formula are the refractive index (n=1.517) and the design wavelengths from 2.27 mm to 3.53 mm, which corresponds to 110 GHz to 85 GHz, respectively. The only free parameter in the design was the radius curvature of the focal plane and the rest of the lens parameters were kept fixed in the simulation.

Diffraction will impose a theoretical limit on the angular resolution of an optical system. These systems are known as diffraction limited FOV systems. In the lens analysis of ZEMAX, Strehl ratio is used as the figure of merit to design an achievable diffraction limited FOV lens system. The Strehl ratio compares the performance of the optical systems with and without aberrations. An optical system with a Sthrel ratio value larger than 0.95 could be considered as a perfect imaging system while one with a SR of 0.8 is acceptable as diffraction limited system. It shows how perfect a lens can focus the incoming rays in the diffraction limit. ZEMAX analysis was made to optimize focal plane geometry. Wave-front errors due to the optical design are directly related to the Strehl ratio [141].

$$SR = \left(1 - 2 \cdot \frac{\pi^2}{W^2}\right) \tag{7.1}$$

where W is the wavefront error. A wavefront denotes rays in phase. Therefore, different phase points on a wavefront will form wavefront errors.

7.1.1 Focal plane optimization

In the measurement setup that we performed the far-field measurements in the labs, the feed horn attached to the VNA converter head was fixed, and the feed position could not be shifted. For this reason, it was decided that the lens to be rotated in order to make the relative angular move instead. The lens is rotated around its center. For a fixed focal length distance, the feed draws a circle with a radius of focal length (f=207.4 mm) whose center is coincident with the lens center.

In ZEMAX analysis, three different focal plane designs with different radius of curvature were investigated. Figure 7.1 shows three focal plane options: a flat focal plane , an optimised focal plane and a realistic focal plane. The radius of curvature of the RFP is 207.4 mm, which is consistent with the focal length of the medium lens. The performance results obtained from each focal plane option were compared in terms of the Strehl Ratio versus the FOV.

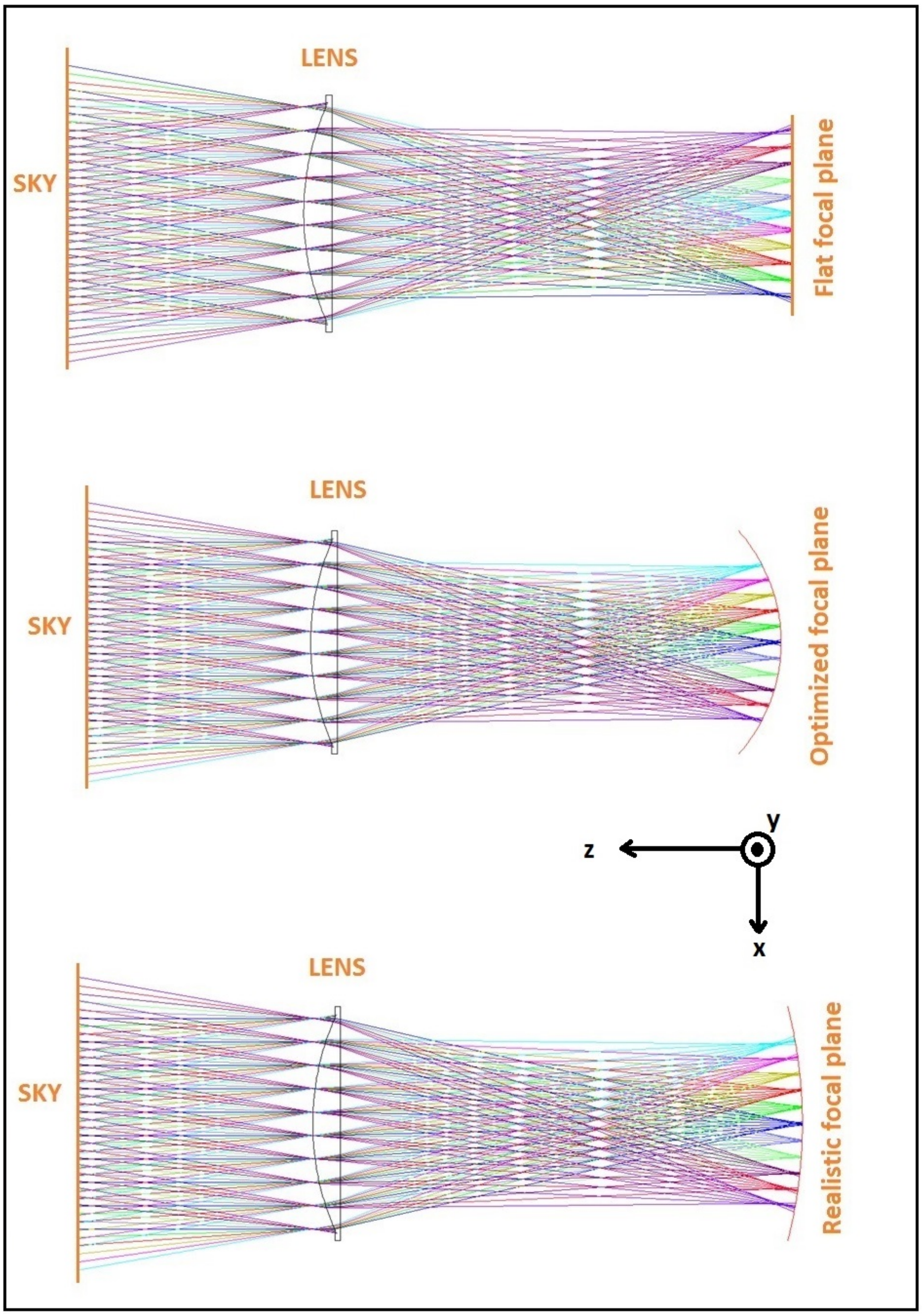

Figure 7.1: Three design options for focal plane geometry of the lens design: a flat plane (FFP), an optimised focal plane (OFP) and a realistic focal plane (RFP). All designs have the same design parameters except for the focal plane geometry.

7.1.2 ZEMAX model results

The optimization analysis of the focal plane geometry of the lens was conducted by leaving the image plane radius as a free parameter. The optimum radius of curvature was calculated as 75.1 mm (Optimised Focal Plane). Figure 7.2 shows the calculated Strehl ratio values from three different options over W band. The system was optimised for 97 GHz (λ = 3.09 mm) which can be considered the central frequency of W band. The Flat Focal Plane option (radius of curvature is infinite) shows the worst performance for the Strehl ratio while the Optimised Focal Plane shows the best as expected. Initially we considered the Flat Focal Plane option because it is easier to manufacture. The Realistic Focal Plane presents acceptable results up to $\pm 20^\circ$ because its Strehl ratio values remain below diffraction limits up to $\pm 20^\circ$. The other Figure 7.3 shows the Strehl ratio values calculated for each focal plane option versus the resulting FOV.

In conclusion, it was decided that the configuration of the Realistic Focal Plane could be used in both FEKO simulations and measurements because the radius of curvature of the Realistic Focal Plane is consistent with the focal length of the medium sized lens. The lens configuration is symmetric due to its spherical geometry of the curve surface. For this reason, the Strehl ratio analysis done only for half-angle is valid for the entire (full-angle) FOV.

7.2 FEKO Model results

A standard model was used for all off-axis simulations. The MLFMM modelled lens was illuminated with a radiation pattern (RAD) source input. Unlike the on-axis models, the symmetric plane settings could not be assigned because geometrical symmetry is broken by off-axis configurations. Therefore, off-axis simulations took at least one third longer than the on-axis simulation of the same horn-lens configuration.

7.2.1 Phase calculations

The lens is tilted around the Y-axis as described in Figure 7.4. Figure 7.5 shows the phase patterns simulated at 97 GHz, for different off-axis angles, which starts from 0° to 22°. As a result of the off-axis configuration, the phase patterns calculated for the H and D planes are distorted. However, the pattern shapes are not affected in shape but a phase shift of 12° was observed at the E plane cut due to symmetry.

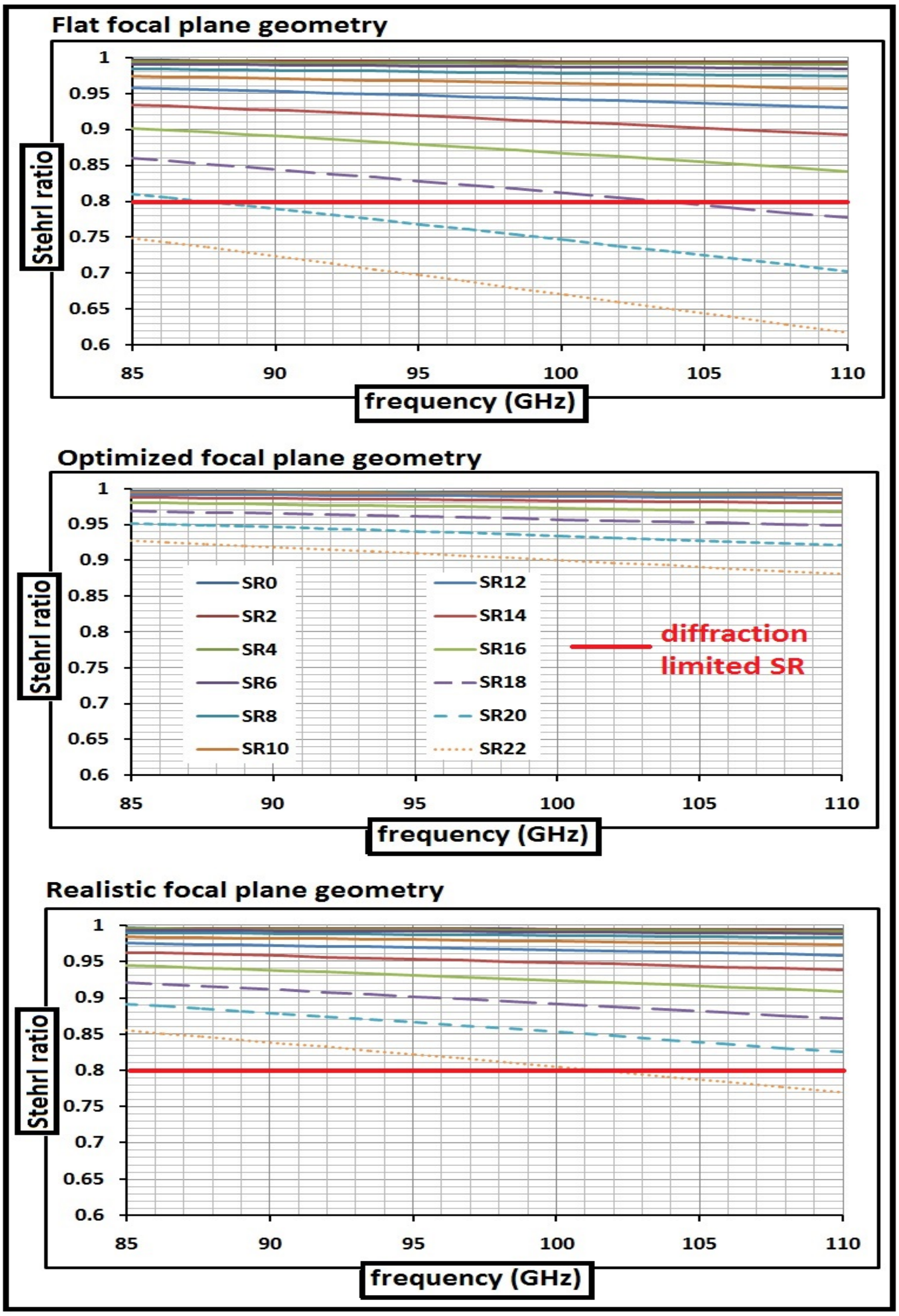

Figure 7.2: The strehl ratio values as a function of frequency for different focal plane options. Each plot shows the off-axis angle performance of the propagated ray in the system. For example, SR22 denotes the strehl ratio plot for an off-axis angle of 22°. The field angles of the incident rays were determined with respect to the centre of the lens from 0^0 to $\pm 22^0$ showing the FOV of the optical system. Red thick line indicates the diffraction limited FOV level for a strehl ratio value of 0.8.

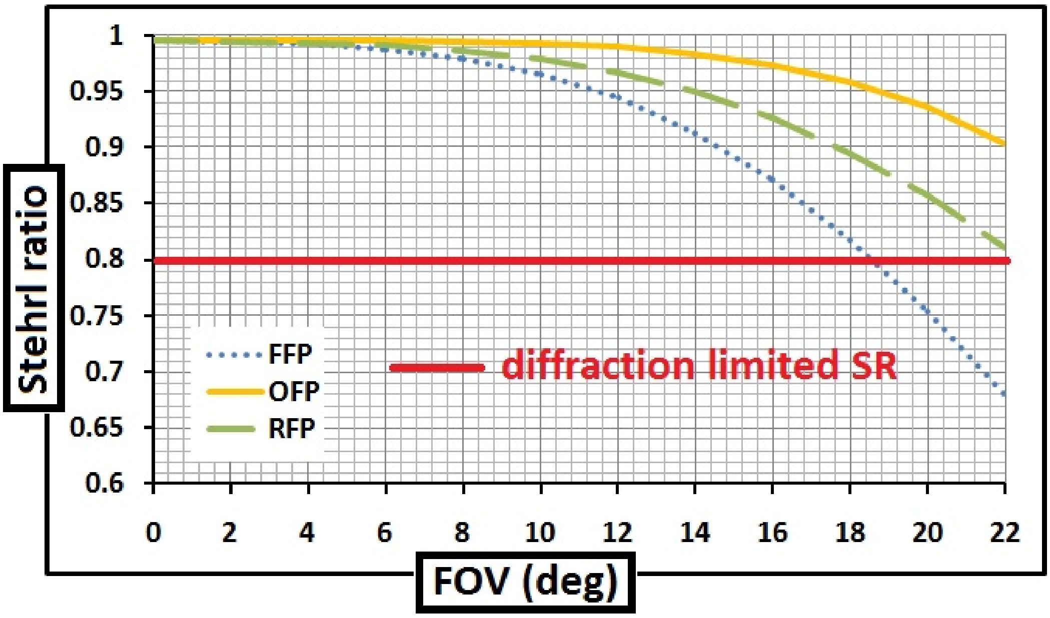

Figure 7.3: The strehl ratio against field of view. The performances of there focal plane options are shown for a frequency of 97 GHz. The red line indicates the diffraction limited SR.

7.2.2 CP and XP beam calculations

Figure 7.6 shows the CP and XP beam patterns calculated at 97 GHz for different off-axis angles starting from 0° to 22°. The beam patterns are not normalized in order to make the decrease in gain with increasing off-axis angle visible. Similar to the phase results, the E cut intensity patterns are not distorted in beam shape but the H and D cut patterns experience shape distortion. For each plane cut, the reduction of gain with increasing off-axis (up to 22°) angles reaches 3 dB with respect to on-axis model. The XP values for H plane cut is below -100 dB. However, the XP values computed at the D and E plane cuts grew quickly with increasing off-axis angles. The maximum XP calculated at the on-axis E plane cut soared to -60 dB at 2° off-axis horn-lens configuration. For the higher off-axis angles, the maximum XP was calculated to be -40 dB. The distortion of the beam parameters, due to the off-axis movement, are symmetrical with respect to the axis that the lens is tilted around. Namely, tilting the lens around the X-axis, instead of tilting the lens around the Y-axis, gives rise to beam distortions in the E plane cut, instead of those in the H plane cut.

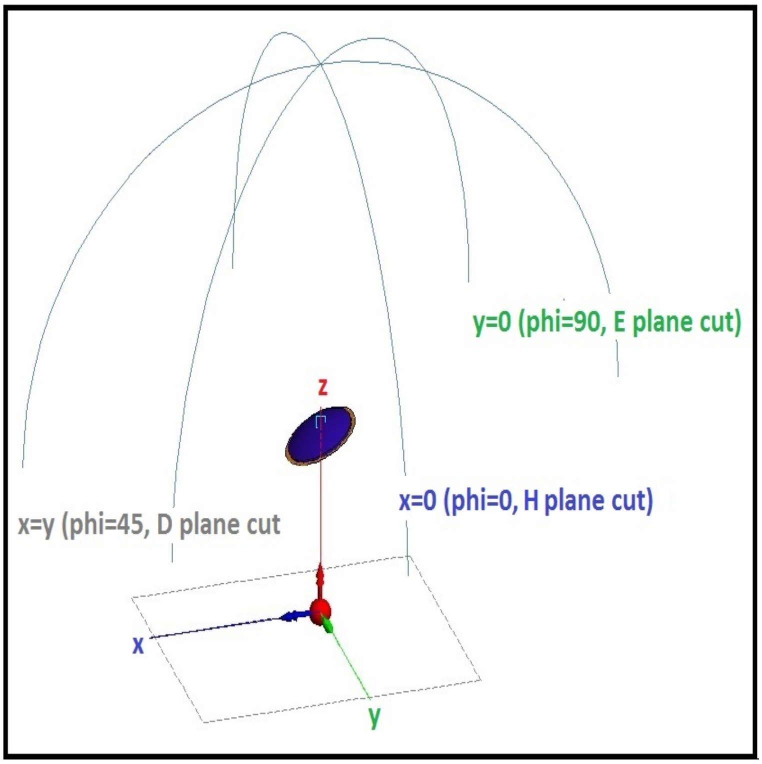

Figure 7.4: The figure shows the lines representing the plane cuts of H, D and E for a beam propagating along the z-axis. The lens is tilted around y-axis.

7.3 Experimental study: Off-axis pixel measurements of the medium lens system

7.3.1 Measurement setup

In this section, off-axis measurements of the horn-medium lens system are presented. Based on the ZEMAX analysis conducted in Section 7.1.1, a realistic focal plane configuration was selected. The relative position between the feed horn and the lens is shown in Figure 7.7. This relative orientation is equivalent to the feed positioning in the realistic focal plane.

A small rotation platform was bought in order to rotate the medium lens around its center. The off-axis angles can be arranged accurately by means of this rotation platform clamped to the lens mount. Angular scale of the rotation platform is marked in 2° increments and labeled every 10°.

The H plane cut measurements were carried out by starting between 2° to 22° in 2°

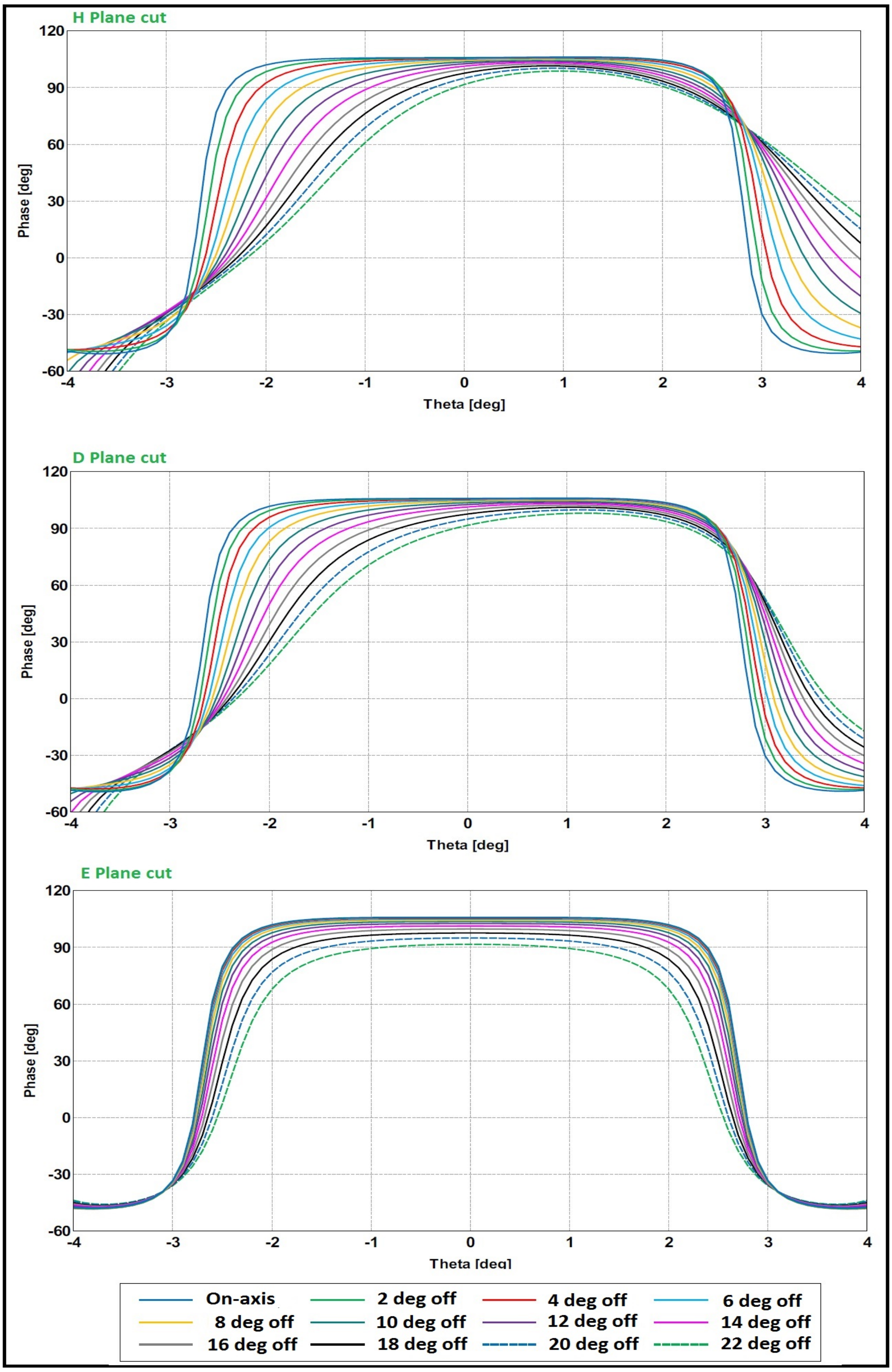

Figure 7.5: Model predictions of phase pattern for the horn-medium lens system. The RFP option was used in the simulations. From top to bottom: Phase calculations of the co-polarization E-field for 97 GHz at the plane cuts of H, D and E are plotted for different off-axis angles starting from 0° to 22°.

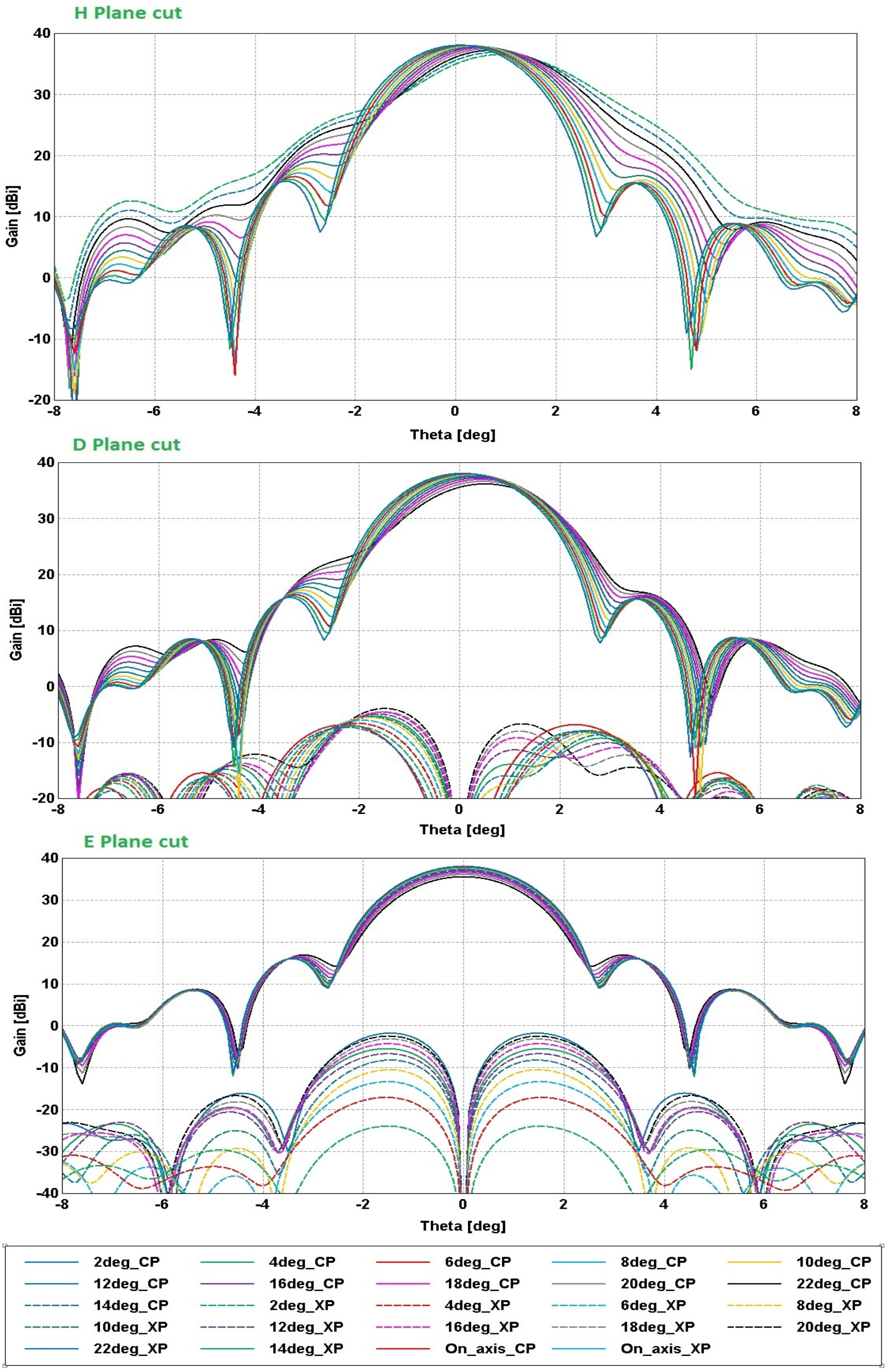

Figure 7.6: Model predictions of the radiation beam pattern for the horn-medium lens system. The RFP option was used in the simulations. From top to bottom: Intensity patterns calculated for 97 GHz at E,D and H plane cuts are plotted for different off-axis angles starting from 2° to 22°. The cross-polarization level for the H plane cut results are almost negligible level while they show up for the D and H plane cuts.

intervals. Additionally, the measurements at the D and E plane cuts were conducted for only 10° and 20° off-axis angles. E,D, and Hplane cut results at 97 GHz are presented.

The on-axis and off-axis measurements of the horn-medium lens system were performed at different times. In the off-axis measurements, the far-field measurement setup presented 4 to 6 dB higher noise level than the on-axis measurements. I do not know exactly what causes this difference. Possible reasons for the noise level difference could be explained as follows. This might be the rectangular to circular waveguide transition (TRC) used for coupling between the WR10 rectangular waveguide of the VNA converter head and the feed antenna. This TRC was found to be loose. The signal level, in particular the XP signal, varied by 5 dB when the TRC was rotated around its self central axis. The other reason might be the power drifts in the VNA that we have lately realized. The variations in the phase and intensity were presented in Figure 6.8. The off-axis measurement system defines the beam pattern up to a signal of -40 dB, which is still an enough level to determine XP signal level.

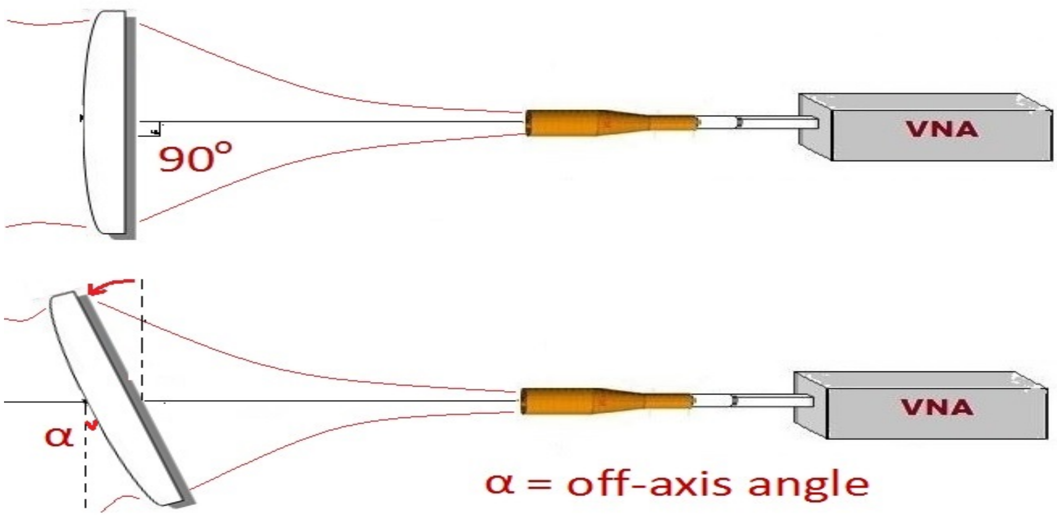

Figure 7.7: Off-axis measurement arrangement of the horn-medium lens system. Upper figure shows the on-axis measurement orientation while lower figure shows how the lens is rotated around its central axis to perform off-axis measurements.

7.3.2 Phase measurements

Phase measurements are known to be very difficult so slight misalignment in the system gives rise to phase distortion. Figure 7.8 shows the measured phase patterns at

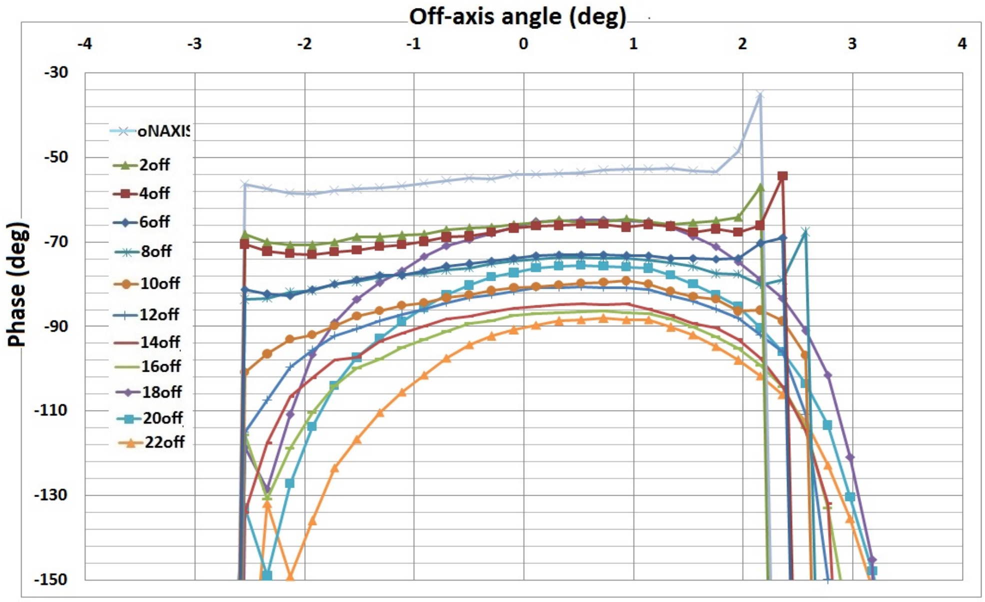

Figure 7.8: Phase pattern measurement results for E plane cut. Figure shows the phase patterns measured for the different off-axis horn-lens configurations for 97 GHz. On-axis phase pattern is also included for comparison.

the H plane cut. The measured patterns present similar phase shifts to the predicted patterns shown in Figure 7.5 even though the values can be different. For example, there is 30° difference between the central peaks of the on-axis and the 22° off-axis phase patterns. This value was predicted to be 15° in the models. The agreement between the measured and predicted phase data is good as shown in Figure 7.9. Model and measurement results are plotted for the on-axis (0°) and most extreme angle (22°). The extent of the main beam, in angle range between $-2.5^\circ \leq \theta \leq 2.5^\circ$, is determined correctly both from the predicted and the measured data.

7.3.3 CP and XP beam measurements

Figures 7.10 and 7.11 compare the measured beam patterns with the simulation patterns calculated at the H plane cut for off-axis angles of 4°, 8°, 12° and 20°. The measured beam patterns are normalized to their maximum. The agreement between the predicted and the measured plots is sustained up to the 8° off-axis patterns with signal level below -35 dB. However the side-lobe levels start to behave differently at angles larger than 8°. Also, Figures 7.12 and 7.13 show the comparison of the measurements and the simulations for the far-field beam patterns. The D and E cut patterns

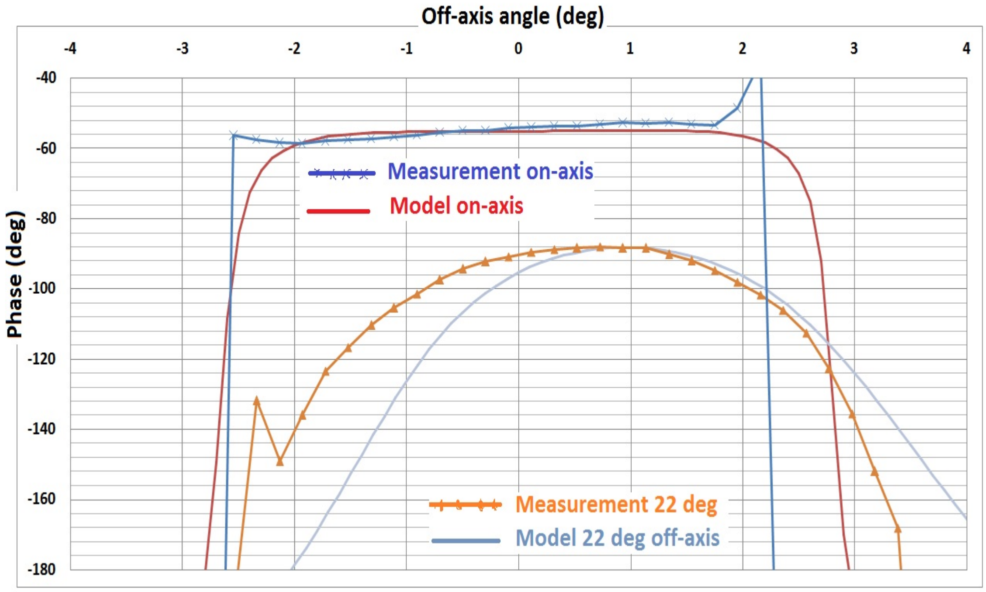

Figure 7.9: Phase pattern comparison between model and measurement for the on-axis and 22° off-axis angles. Model plots were shifted to fit the measured data.

are compared for the 10° and 20°. In the beam patterns of 10° off-axis configuration, simulations and measurements are in agreement below -30 dB signal level. However, a disagreement is observed in the D plane cut patterns of the 20° off-axis configuration. The 20° off-axis comparison results for the E plane cut patterns match well below -35 dB signal level.

Additionally, the maximum XP signal measured at each plane cut with increasing off-axis values. Theoretically, there is no XP at the H plane cut and also the XP value is quickly increasing with increasing off-axis angles at the E plane cut. However, the measured XP increased from ~ -37 dB to ~ -33 dB as the off-axis angle increases. The XP values measured at the D plane cut show up only around the main beam, as predicted from the models. Overall XP beam shape is quite consistent with the predictions. However, the maximum XP levels are different. There is a minimum XP signal dip of -39 dB and two signal peaks at ~ -34 dB. For the 10° off-axis measurements of the E plane cut, the XP signals show up between -39 dB and -40 dB levels. The XP pattern at this signal level could not be well characterized by the measurement setup which sets the noise level around -40 dB.

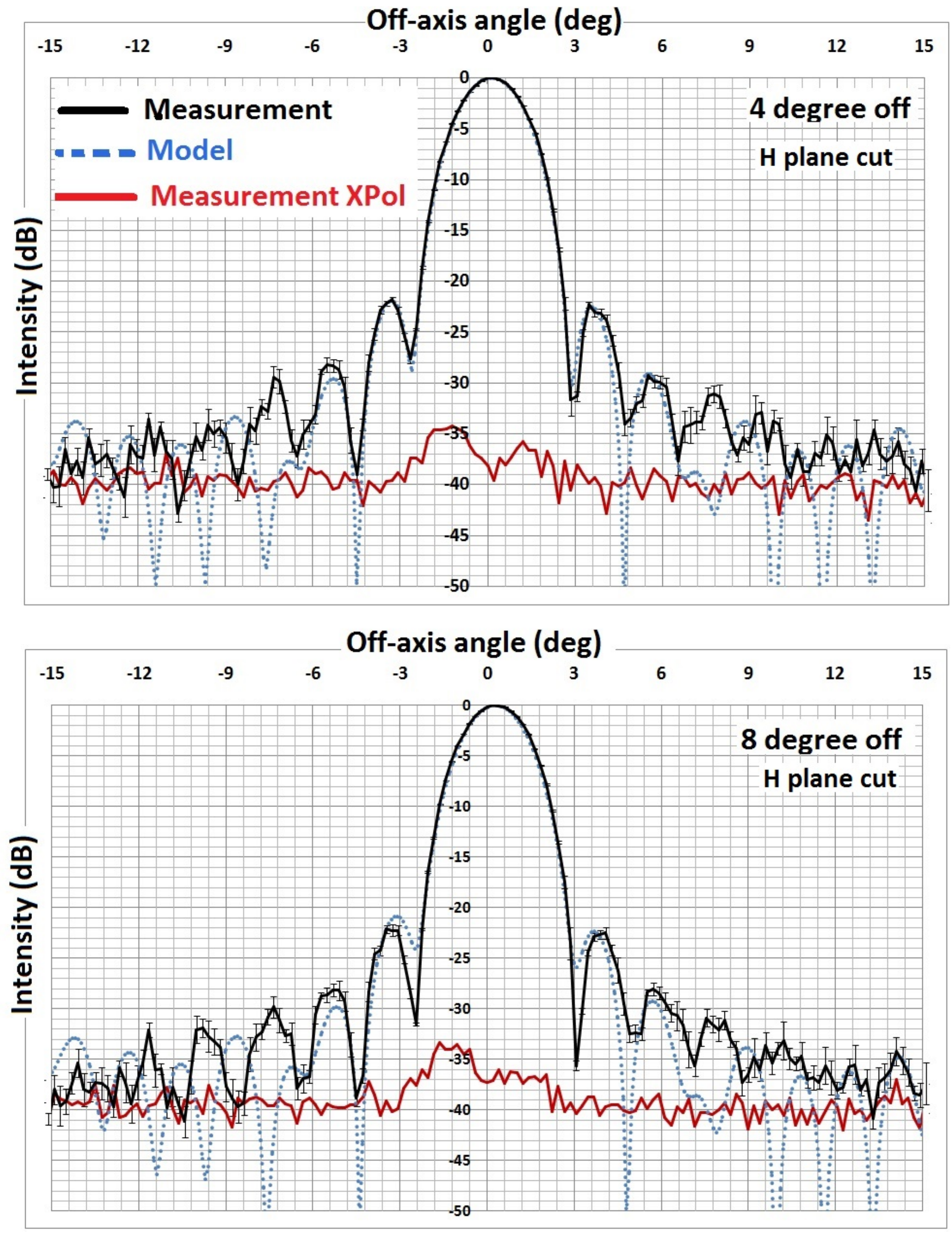

Figure 7.10: The comparison of off-axis beam predictions and measurements performed for the horn-medium lens system. Figure shows both co-polarization and cross-polarization data for the H plane cut measurements. Upper figure shows results for an off-axis of 4° while lower figure shows results for an off-axis of 8°. The measured error bars are also calculated.

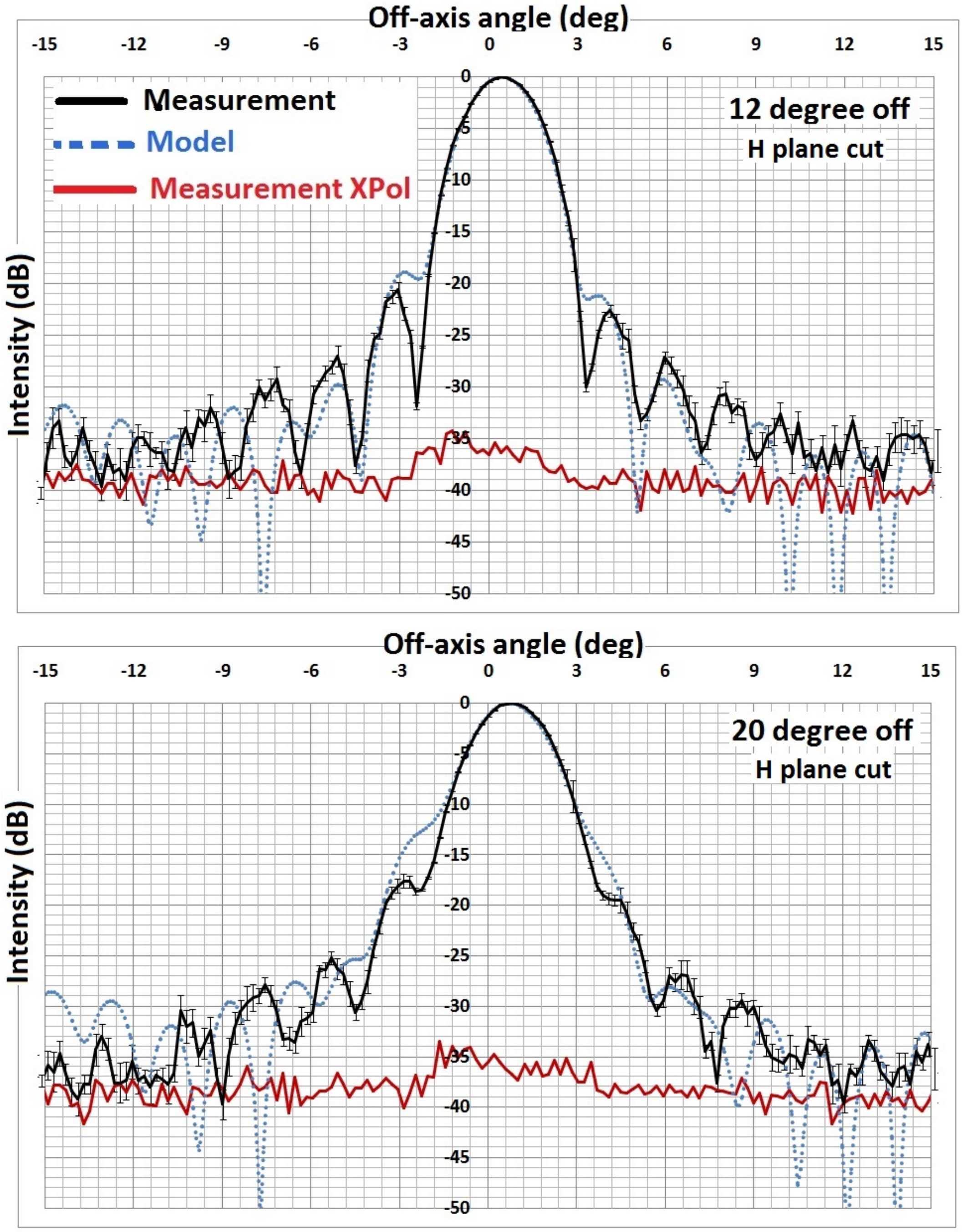

Figure 7.11: The comparison of off-axis beam predictions and measurements performed for the horn-medium lens system. Figure shows both co-polarization and cross-polarization data for the H plane cut measurements. Upper figure shows results for an off-axis of 12° while lower figure shows results for an off-axis of 20°. The measured error bars are also calculated.

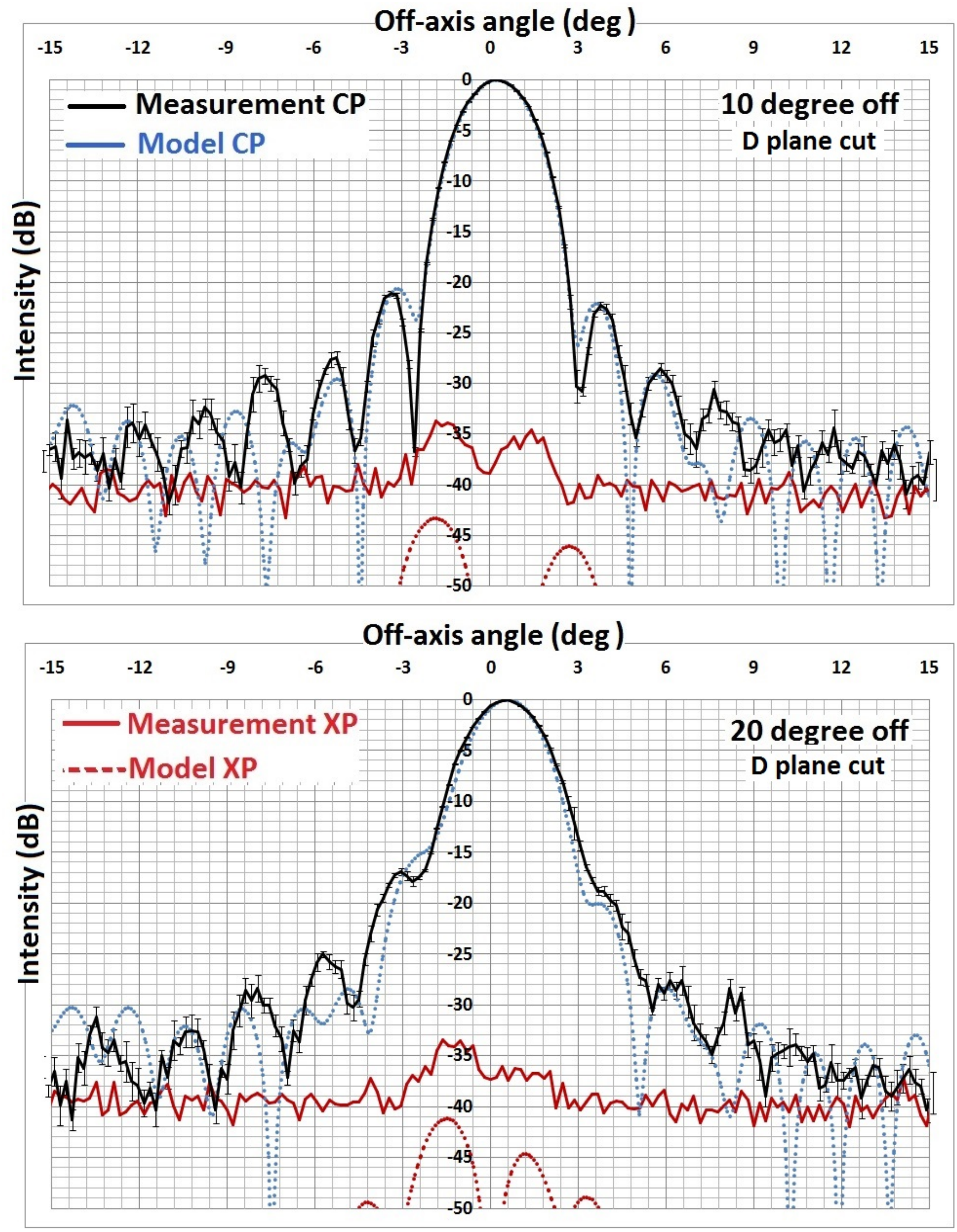

Figure 7.12: The comparison of off-axis beam predictions and measurements performed for the horn-medium lens system. Figure shows both co-polarization and cross-polarization data for the D plane cut measurements. Upper figure shows results for an off-axis of 10° while lower figure shows results for an off-axis of 20°. The measured error bars are also calculated.

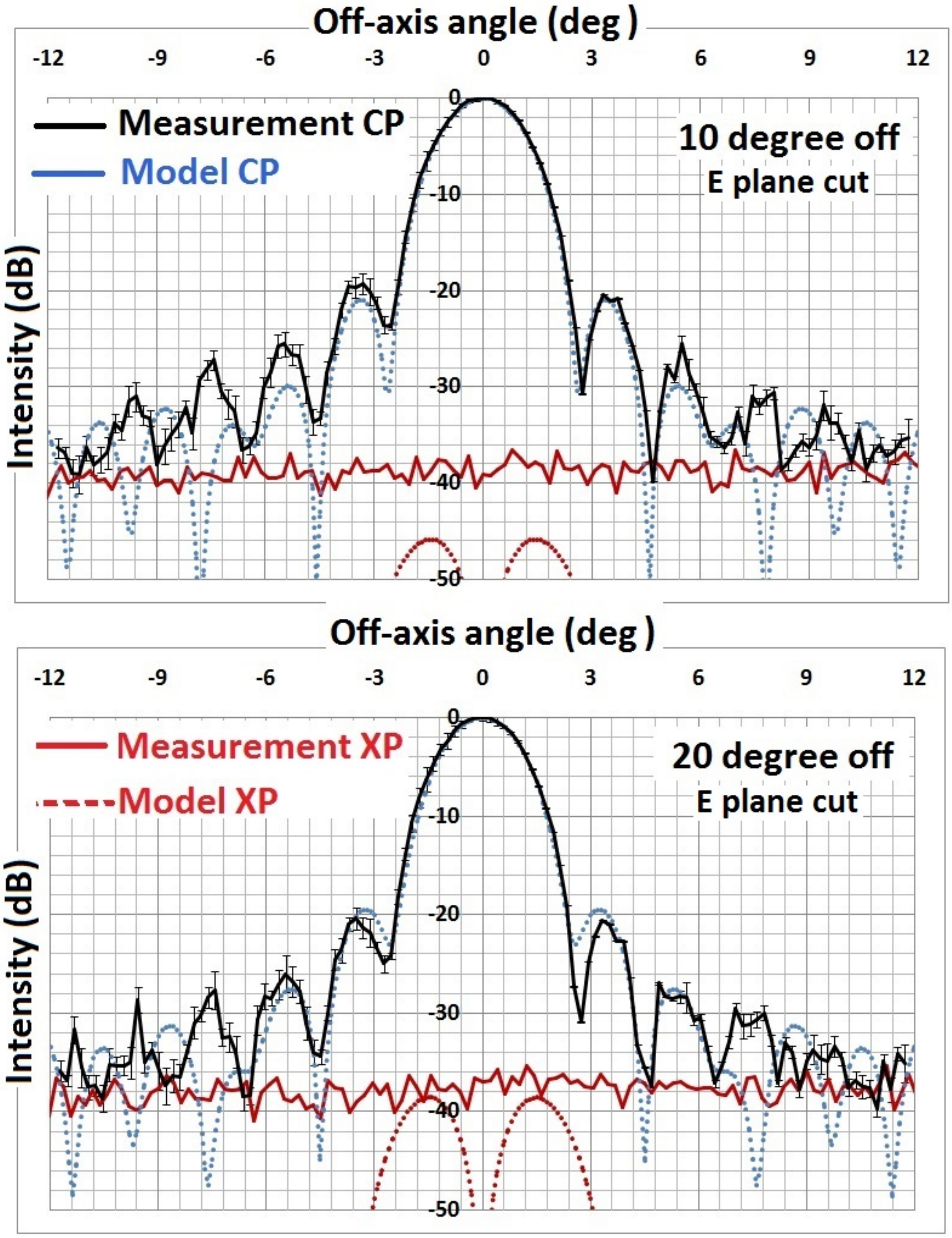

Figure 7.13: The comparison of off-axis beam predictions and measurements performed for the horn-medium lens system. Figure shows both co-polarization and cross-polarization data for the E plane cut measurements. Upper figure shows results for an off-axis of 10° while lower figure shows results for an off-axis of 20°. The measured error bars are also calculated.

7.4 Overall results

Tables 7.1 and 7.2 list the predicted and measured values of FWHM and XP obtained for different off-axis angles. Beam ellipticity (BE) values were calculated by using Equation 7.2. The beam-width values were obtained from maximum and minimum of two orthogonal planes of the E and H plane cuts.

$$BE = \left(\frac{BW_{max} - BW_{min}}{BW_{max}} \right) \tag{7.2}$$

The integrated cross-polarization (IXP) is calculated by using the following equation set.

$$CP(\theta) = \int_f \int_\theta S_{12}(\theta, \phi(\|), f)^2 d\theta df \tag{7.3}$$

$$XP(\theta) = \left(\frac{1}{CP(\theta)} \right) \int_f \int_\theta S_{12}(\theta, \phi(\perp), f)^2 d\theta df \tag{7.4}$$

Polarization state for $\phi(\|)$ is orthogonal to the polarization state for $\phi(\perp)$ for a frequency of *f*, when integrated XP (IXP) level were calculated. The extent of the main beam lobe was considered to be $-2.5^\circ \leq \theta \leq 2.5^\circ$. The noise level puts a limit on the upper signal level. Noise signals are observed outside the main beam extent ($\theta \leq -2.5^\circ, 2.5^\circ \leq \theta$), which normally either does not exist or are very low in the XP signal. Due to existence of noise signals, IXP values become higher when being calculated over the full beam extent ($-15^\circ \leq \theta \leq 15^\circ$).

Also, Figure 7.14 shows the change in FWHM values predicted and measured at tthe three plane cuts. There is a generally good agreement between the results of predictions and measurements for the E plane cut. The H plane data shows a FWHM difference of 10% at maximum. The FWHM values of the H and D plane cuts are increasing, while those of the E plane cut are decreasing, with increasing off-axis angles. Similarly, the measured data track the predicted data.

7.5 Conclusion

This chapter presented characterization studies of off-axis horn-lens systems. First, the best suited focal plane geometry for the horn-medium lens system was determined

Parameter	FWHM(H)	**FWHM (H)**	FWHM(D)	**FWHM (D)**	FWHM(E)	**FWHM (E)**	Beam ellipticity	**Beam ellipticity**
$on-axis$	2.189	**2.251**±0.003	2.189	**2.213**±0.004	2.179	**2.251**±0.005	0.45%	**1.68%**
2° **off**	2.188	**2.214**±0.005	2.179	**-**	2.167	**-**	0.96%	**-%**
4° **off**	2.19	**2.251**±0.005	2.178	**-**	2.166	**-**	1.09%	**-%**
6° **off**	2.192	**2.262**±0.01	2.178	**-**	2.163	**-**	1.32%	**-%**
8° **off**	2.196	**2.288**±0.01	2.178	**-**	2.159	**-**	1.68%	**-%**
10° **off**	2.205	**2.268**±0.03	2.178	**2.276**±0.05	2.153	**2.163**±0.009	2.35%	**6.43%**
12° **off**	2.218	**2.262**±0.03	2.181	**-**	2.145	**-**	3.29%	**-%**
14° **off**	2.237	**2.339**±0.04	2.184	**-**	2.136	**-**	4.51%	**-%**
16° **off**	2.267	**2.35**±0.04	2.191	**-**	2.124	**-**	6.3%	**-%**
18° **off**	2.301	**2.364**±0.05	2.201	**-**	2.109	**-**	8.34%	**-%**
20° **off**	2.367	**2.434**±0.05	2.218	**2.41**±0.011	2.092	**2.189**±0.012	11.61%	**9.17%**
22° **off**	2.454	**2.471**±0.05	2.454	**-**	2.074	**-**	14.75%	**-%**

Table 7.1: FWHM and beam ellipticity values are extracted for the different off-axis angle configurations. The results are given for the E,D and H plane cuts for a frequency of 97 GHz. The bold characters denote the measured values while the others are for the predicted values. The measured data is given with error bars obtained from the standard deviation calculations of many repeated measurements.

Parameter	**Maximum XP(H)**	Maximum XP(D)	**Maximum XP(D)**	Maximum XP(E)	**Maximum XP(E)**	**Integrated XP(H)**	**Integrated) XP(D)**	**Integrated XP(E)**
on − axis	**-36.6** $\pm$0.6**dB**	-44.9 dB	**-38.1** $\pm$0.7**dB**	<-100 dB	**-37**$\pm$0.61 **dB**	**-35.7 dB**	**-34.3 dB**	**-35.5 dB**
2° **off**	**-34** $\pm$0.6**dB**	-45.2 dB	**-**	-60 dB	**-**	**-34.3 dB**	**-**	**-**
4° **off**	**-34.2** $\pm$0.6**dB**	-45.1 dB	**-**	-56 dB	**-**	**-35.5 dB**	**-**	**-**
6° **off**	**-33.5** $\pm$0.6**dB**	-44.7 dB	**-**	-53 dB	**-**	**-35.3 dB**	**-**	**-**
8° **off**	**-33.5** $\pm$0.6**dB**	-43.9 dB	**-**	-50 dB	**-**	**-35 dB**	**-**	**-**
10° **off**	**-33.1** $\pm$0.6**dB**	-43.3 dB	**-34** $\pm$0.55**dB**	-48.3 dB	**-36.5** $\pm$0.6**dB**	**-35 dB**	**-34.4 dB**	**-35.7 dB**
12° **off**	**-34** $\pm$0.6**dB**	-43.1 dB	**-**	-41.2 dB	**-**	**-35.4 dB**	**-**	**-**
14° **off**	**-34** $\pm$0.6**dB**	-42.8 dB	**-**	-40.3 dB	**-**	**-35.4 dB**	**-**	**-**
16° **off**	**-34** $\pm$0.53**dB**	-42.2 dB	**-**	-39.2 dB	**-**	**-35.2 dB**	**-**	**-**
18° **off**	**-34.2** $\pm$0.53**dB**	-41.5 dB	**-**	-38.7 dB	**-**	**-35.7 dB**	**-**	**-**
20° **off**	**-33.3** $\pm$0.53**dB**	-41.2 dB	**-33.5**$\pm$0.51 **dB**	-38.4 dB	**-35.5**$\pm$0.55 **dB**	**-35.8 dB**	**-35 dB**	**-35.5 dB**
22° **off**	**-33.1** $\pm$0.53**dB**	-40.1 dB	**-**	-38.1 dB	**-**	**-35.7 dB**	**-**	**-**

Table 7.2: Maximum and integrated XP values are extracted for off-axis angles. The maximum XP results are given for the E,D and H plane cuts for a frequency of 97 GHz while the integrated XP values were calculated over the frequencies (82-110 GHz) of the W-band. The bold characters denote the measured values while the others are for the predicted values. The maximum cross-polarization for the H plane cut predictions is very low so that it can be negligible. The measured data is given with error bars obtained from the standard deviation calculations of many repeated measurements.

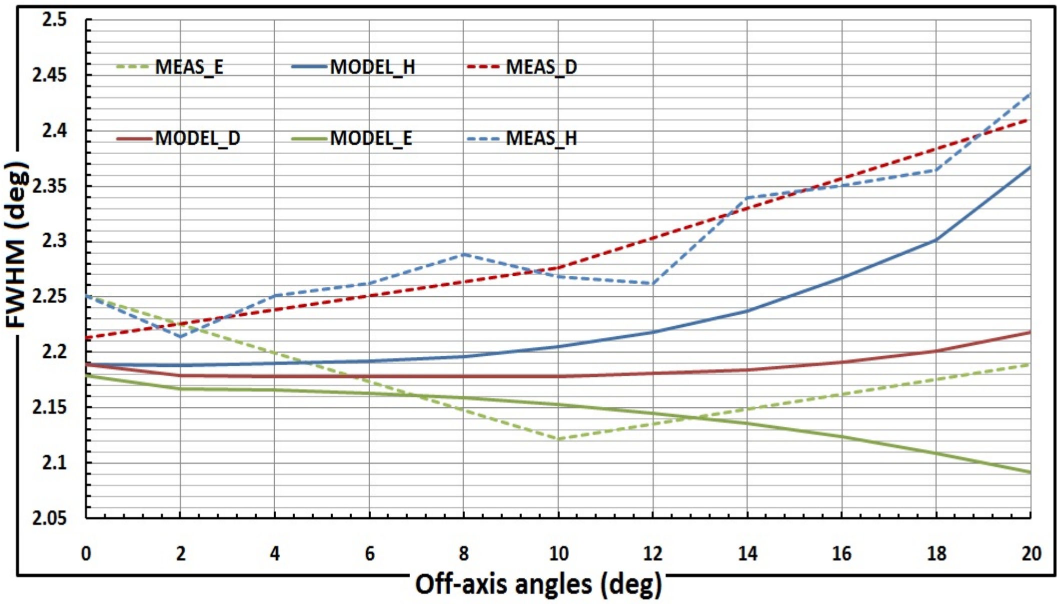

Figure 7.14: The results for full width at half maximum at 3B as a function of off-axis angles. The model prediction values are compared with the measured values for the E, D and H plane cuts for a frequency of 97 GHz.

using ray-based approach of ZEMAX. According to optimization results and manufacture feasibility, the realistic focal plane (RFP) option was chosen. The model analysis of the horn-medium lens system was completed with FEKO. Off-axis configurations were modelled in angular range starting from 2° to 22° in 2° intervals.

The comparison of the measurement and simulation results concluded that the general shape of beam patterns were in agreement up to the off-axis angle of 10°. This agreement broke down at angles larger than 10°. The reason might be the lens size (∼30λ) because the beam shape is increasingly distorted by the lens mount (edge diffractions) with increasing off-axis angle. There is also slight difference in measured and simulated sidelobe levels. This might be due to the use of MM-wave absorbers because a smaller region was covered by these absorbers compared to the test environment, which was prepared for the on-axis measurements. Additionally, maximum and minimum FWHM values, selected between three planes (E, D and H plane cuts), were used to calculate the simulated and measured BE values (see Table 7.1). There is a FWHM difference of 10% at maximum between the measured and predicted data. This difference may be attributed to the FWHM calculation using only three plane cuts instead of selecting maximum and minimum FWHM values obtained from the selective cuts. Also, a better match in the comparison of the FWHM values can be achieved by using the measurements of the 3D scanner system in future. In addition, maximum XP values were calculated in the main beam extent. Due to noise level observed outside the main beam extent (see Table 7.2), the comparison does not seem to be highly consistent for all off-axis angles. Integrated XP level around -35 dB was achieved by the use of a single horn-lens system, which was not optimized for low aberrations. This can be checked with a system comprising several lenses.

Chapter 8

CONCLUSIONS AND ROADMAP FOR FUTURE WORK

8.1 Conclusion

This thesis has questioned how accurately the measurements of horn-lens systems compare with full wave models at mm waves. Not only on-axis pixel characterization but also off-axis pixel characterization of mm-wave lens systems were investigated in this research. This study will contribute to the instrumentation of CMB telescopes dedicated to B-mode polarization measurements and more generally to any mm-wave refractive system.

According to the scientific requirements given in **Chapter 2**, the instrumental requirements are presented for a B-mode mission. These instruments need high sensitivity due to their weak signals and exquisite control of polarization systematic effects such as cross-polarization and beam shape. To this end, the sky beam should be coupled to the detectors by taking into consideration all the effects of diffraction and polarization. This is only possible with a full-wave modeler, such as Method of Moments (MOM). Selection of an ideal optical configuration for future B-mode instruments is still under discussion by different scientific consortiums. The technology readiness level of reflector based systems is already high thanks to CTR configurations. Alternatively, refractor based designs are very promising and preferred by optical designers. However, both lens materials and lens optical systems should be investigated in terms of polarization systematics.

Chapter 3 presented the main theoretical tools that I employed to model the optical components used for my research. PO, which was used with GRASP, was the main optical approach to simulate scattering due to reflective components such as telescope mirrors. My main motivation was to model the refractive components by using a full-wave modeller. The MOM formulation, which solves the Maxwell equations in Integral form, was chosen as the reference model to handle refractive components. The MOM is based on the Surface Equivalence Principle (SEP) when solving the EM problems of the refractive components. Additionally, alternative approaches such as Multi Fast Method of Moments (MLFMM) and Ray Launching Geometrical Optics (RLGO), which were introduced by the FEKO software package, were used to reduce the necessary computational requirements. In this chapter, the W-band corrugated feed horn antenna (Standard feed), which was used as the feed source in all measurements performed during my research, was modelled using three different models: a Mode-matching model with CORRUG, Finite Element Analysis with HFSS, and MOM with FEKO. This analysis has concluded that all simulation tools predicted the far-field radiation pattern of the feed horn accurately, compared to the measured data. In particular, XP beam predictions were in well agreement with the measurements to a high level of precision. Measured XP at maximum was -40.2±0.6 dB, all model data remained within the measurement error. The calculated beam difference of different models to the measured data was found to be below -20 dB. The most promising finding of this analysis was that the mode matching model, which took much less time to complete the simulation, showed almost identical performance to the other two full wave models that required much more time. However, mode matching of the CORRUG was limited to simulation of corrugated horn feeds that have circularly symmetric geometry. There are other software tools running Mode-matching model that can simulate feeds without circular symmetry. Additionally, the mode-matching model does not take into account ohmic losses due to material conductivity.

Refractive components are made of dielectric materials such as HDPE, UHMWPE and silicon. In order to obtain high accuracy both in models and measurements of refractive systems, having correct material information is crucial. In particular, the parameters of refractive index and loss tangent need to be known to four decimal places. When the systematic effects that refractive components introduce were characterized, a collimated beam was used thanks to a free-space S parameters measurement test bench. A quiet zone, which has a dimension of 10x10x20 cm, was generated by using a CATR system in order to locate the materials and components to be tested. The main properties of this system were that maximum XP should be lower than -40 dB and maximum intensity/phase variations should remain within a few dB / 20°. In **Chapter 4**, the full characterization of the test bench was successfully achieved. The PO modelling of the CATR system predicted maximum XP at -39 dB and the intensity/phase variations were predicted to be 4 dB and 4.5° at maximum. Then, the beam characteristics of the system were measured using a 3D scanner system. It measured the phase variations to be a maximum of 7°. Also, the measured variations of the beam intensity differed by 1 dB compared to the predicted data. The maximum XP of the CATR was measured to be -19 dB at maximum, which is much higher than the model predictions. This high value was attributed to the beam probe used in the 3D beam scanner because the maximum XP was first measured to be at -37±1 dB using a standard feed horn. In addition to the beam measurements, the CATR system was calibrated by employing two calibration methods (TRL and TRM) and calibration standards were calculated more accurately with TRL. One difficulty in TRL calibration was a phase singularity problem when the line and through standards are equal. To overcome this, we used a very accurate micrometer during the translation of the stage. Some preliminary tests were accomplished with the test bench by measuring the UHMWPE slab. The experimental data was in well agreement with the model predictions. The refractive index of the UHMWPE was measured to be 1.517±0.001 by using the S_{11} parameter. The other algorithm to extract the refractive index and loss tangent parameters were attempted by measuring two S parameters with phase information. However, we failed to obtain correct values for the dielectric properties of the slab. The problem might be with the measurement accuracy of the transmission parameter (S_{21}). The ability to measure the S_{21} parameter accurately can be improved by understanding the specific features of the CATR system. Also, the CATR system was used to measure the reflection and transmission properties of the lenses that I designed for my research. Again, return loss was measured accurately. However, measurement of transmission loss was not achieved due to the focusing properties of the lens.

Chapter 5 discussed the simulation feasibility of the maximum lens sizes by using different source and lens model approaches. Due to the space requirements for far-field measurements, the first lens prototype (small size lens) had an aperture diameter of 16λ (for a wavelength of 3.09 mm at 97 GHz), whose far-field measurements required maximum 1.5 m distance. This lens choice was first modelled by MOM. In the following investigation, MLFMM was found to be equivalent to the MOM for dielectric simulations. Another useful result of this first lens analysis was using equivalent source inputs such as AP, RAD and SWE, instead of using a real horn antenna in the lens simulations. The maximum beam difference between the full MOM model and the other equivalent approaches was calculated to be below -23 dB. Thanks to using MLFMM lens modelling with illumination of these equivalent source inputs, the computational requirements were reduced by a factor 24 in runtime and a factor 44 in memory requirement. All these findings were very promising to continue with larger diameter lenses. In the second lens analysis (a diameter of 30λ), a medium size lens was modelled by MLFMM. In this model analysis, the approach of the RLGO was compared to the MLFMM model. Except for differences in the maximum XP value (6 dB at maximum), the maximum beam difference between the models for the CP beam predictions was below -25 dB. High XP difference between different model predictions was attributed to the selection of different source inputs. The same lens design was also modelled for near-field calculations. Thanks to this analysis, near-field beam evolution of the lens system could be visualized and different beam locations, which correspond to the maximum and minimum beam size locations, were spotted. In order to see the limits of the agreement between the MLFMM and RLGO models, another plano-convex lens with a diameter of 75λ was modelled. Model agreement was good, with two small exceptions: beam differences of 0.5 dB and 1 dB in first sidelobe and maximum XP levels. Depending on the different feed inputs and the mesh size, modelling of a lens with a maximum diameter of 90λ was found possible by using MLFMM with the allowable computational resources. This investigation was extended to simulations of even larger lenses. Mesh analysis performed for the RLGO modelled lenses showed that the triangular mesh patches can be larger as long as they fit with the problem geometry. Relying on this information, modelling of lenses with diameters larger than 150λ was achieved by using only a mesh size of λ. The other useful tool was to use symmetric electric and magnetic planes in all the lens models mentioned above, if the problem geometry was symmetric.

The two modelled lenses with different sizes were then measured in on-axis configuration in **Chapter 6**. The purpose of this lens characterization study was to compare the present lens simulations with experimental data. Measurements were performed in both far-field and near field. In order to create far field spaces ($\sim$1.5 m for the small lens and $>$5.4 m for the medium lens), the far field measurement setup was developed using the existing beam scanning system at the JBCA. Near field measurements were realized by using a 3D scanner system. This system measured the near field of the medium lens lens system with a mechanical positioning accuracy better than 0.1 mm. Many error analysis tests were performed to understand the limitations of the measurement systems. Alignment of the far-field setup was carried out by using a metal reflector. Uniform phase patterns and symmetric beams showed that this method was adequate. The small lens measurements indicated that the maximum beam difference between the models and measurements was calculated to be -12 dB. The maximum levels of the predicted and measured XP differed by $\sim$5 dB although overall, XP shapes agreed well. We realized that the lens beam suffered diffraction effects due to its relatively small size compared to the beam size of the feed source (3λ). In order to accurately model and measure the lens edge effects, the use of a lens stop for the dielectric lens was found necessary in both simulations and measurements. The far-field measurements of the medium lens presented better agreement with the model predictions. The maximum beam difference was calculated to be -17 dB. Integrated XP spectrum as a function of W band frequencies were calculated from the measured data. Except for individual signal peaks, measured values fluctuated around -35 dB across the band. These signal fluctuations were inherited from the XP pattern of the SF horn. We know this from the Standard feed horn characterization. Maximum XP values were measured to be no more than maximum 4 dB difference from the predictions at the D plane cut. XP values at the H and E plane cuts were measured higher than predicted. This might be due to the instrumental polarization which is visible in the centre of the beam where the lens thickness is larger. In this chapter, ARC studies of the medium lens were also carried out. The UHMWPE medium lens was coated with a suitable ARC material by using a single layer ARC process. Before we characterized the lens, a slab of UHMWPE dielectric was studied for a simple case. Model predictions of the slab were in agreement with the transmission and reflection measurements performed by using the CATR system. The band average of the return loss was measured to be -12.2 and predicted to be -11.6 by using the Transmission-Line model. Similarly, the band average value of the transmission loss was measured to be -0.358 dB and predicted to be -0.32 dB. By using the S_{11} parameter, the refractive index of the UHMWPE dielectric was found to be 1.517 ± 0.001. In order to extract the loss tangent parameter, we needed the S_{21} parameter as well. However, the measurements of the S_{21} did not give rise to accurate loss tangent calculation. After we understood the limitations of the measurements, the analysis was continued with the ARC lens again. The far-field and near field simulations of the lens were conducted with MLFMM models in FEKO. The near-field patterns of the medium lens system taken at the XY plane cut showed -7.9 dB difference between the model and the measurements. The probe beam, which was used for beam scanning in the 3D scanner system, needed data correction for future studies. Finally, return and transmission loss measurements of the medium lens and the ARC-medium lens were performed in the CATR system. Thanks to ARC process, the amount of returned power over the band was reduced to one fifth. The relative transmission measurements of both lenses could be performed due to focusing of the lens beam. An absolute transmission measurement can be achieved by separating the mirrors at a focal length distance. This is also left for future work.

In **Chapter 7**, off-axis characterization of medium lens system was studied. The measured data was found to be in agreement with the model predictions up to the off-axis angle of $10°$. Additionally, beam ellipticities were calculated by using minimum and maximum FWHM values selected between three cut beams (E, D and H planes). The model and measured data of the BE values did not compare well. It is probably due to the use of FWHM values corresponding to the selected planes between only three plane cuts, instead of using the maximum and minimum FWHM values. Due to the high noise level, the XP was limited to $\sim$-40 dB scale so the lower signals could not be observed during the XP measurements at the E and H plane cuts. We think that better measurements can be performed by using the 3D scanner system in future. Even though a medium size lens (30λ) was used in the off-axis beam characterization, the beam shapes were highly distorted with increasing off-axis angle. Larger diameter lens systems or fast lenses with low f# will produce less distortions on the beam pattern due to off-axis pixels. Additionally, integrated XP of a single lens system for all off-axis angle measurements remained around -35 dB. This can be checked for a system of several lenses which is planned to be used for next generation CMB telescopes.

Overall, the results have shown that we can now have a reliable modelling tool for lenses which could be used to model large systems and a system of several lenses. The comparisons of model and data were very promising for contamination of the lens study with the MLFMM and RLGO models. As a final remark, this study becomes very rewarding in increasing the understanding and developing of wide FOV optics for the telescope concepts devoted to polarization measurement of the CMB B-mode.

8.2 Future plans

I would like to extend the lens study to a concept study of a CMB polarization telescope. This study will include designing, modelling and measuring the optimum lens system together with the other components in the telescope system. Use of equivalent sources in FEKO models enables a cascaded model of many components to be modelled with full wave analysis. The beam characteristics of the entire telescope system can be predicted accurately in this way. The experience gained from this study also makes possible examination of the refractive based optics of the B-Pol mission.

Bibliography

[1] Planck‘s web site: http://planck.cf.ac.uk/science/mm-wave-astronomy

[2] Bernard F. Burke and F. Graham-Smith, ”An introduction to radio Astronomy”, Cambridge University Press, Third edition, 2010.

[3] John Kraus, ”The First 50 Years of Radio Astronomy”, Cosmic Search, Vol.4-1, 1982.

[4] J. A. Tauber, et al., ”Planck pre-launch status: The optical system”, A&A, 520, A2, 2010.

[5] Penzias AA and Wilson RW, Astrophysics Journal, Vol.142, 419-421, 1965.

[6] Alpher, R. and R. Herman, Evolution of the Universe, Nature, Vol.162, p.774, 1948.

[7] Steven Weinberg, ”The first Three Minutes”, Second Edition, Basic Books Press, 1993.

[8] Manzoor A. Malik, ”Cosmology with the CMB”, Int. J. of Ast., 2(2):17-22, 2013.

[9] ESA‘s web site: http://www.esa.int

[10] Anthony Challinor, ”CMB anisotropy science:a review”, Proceedings IAU Symposium, No. 288, 2012.

[11] Alan H. Guth, ”Inflationary universe: A possible solution to the horizon and flatness problems”, Physical review D, Vol.23, No.2, 1981.

[12] Cobe‘s web site: http://lambda.gsfc.nasa.gov/product/cobe/

[13] Martin White, et.al., ”Anistropies in the CMB”, annu. rev. Astrophys., Vol.32: 319-70, 1994.

[14] Wayne Hu and Martin White, ”A CMB polarization polarimer”, preprint arXiv:9706147v1, 1997.

[15] J. Bock, et.al.,”Task Force on Cosmic Microwave Background Research”, Final report, 2005.

[16] NASA‘s web site: http://lambda.gsfc.nasa.gov/product/relikt/

[17] D.J. Fixsen, et al., ”The Cosmic Microwave Background Spectrum From The Full COBE Firas Data Set”, The Astrophysical Journal, Vol.473, p. 576-578, 1996.

[18] P. de Bernardis, et. al., ”Mapping the CMB sky: The BOOMERANG experiment”, preprint arXiv:9911461, 1999.

[19] T. Montroy, et. al., ”Measuring CMB polarisation with BOOMERanG”, preprint arXiv:0305593v2, 2003.

[20] J. F. Macas-Prez et al., ”Archeops in-flight performance, data processing, and map making”, A&A, Vol.467, p.1313-1344, 2007.

[21] J.M. Kovac., et. al., ”Detection of polarisation in the Cosmic Microwave Background using DASI”, Nature, Vol.420, 2002.

[22] C.OSullivan, et. al., ”The Quasi-optical design of the QUAD telescope, Infrared Physics and Technology”, Vol.51, p.277-286, 2008.

[23] Leitch, et. al., ”Degree Angular Scale Interferometer 3 Year Cosmic Microwave Background Polarization Results”, The Astrophysical Journal, Vol.624, p.1020, 2005.

[24] Barkats, D., et. al., ”First Measurements of the Polarization of the Cosmic Microwave Background Radiation at Small Angular Scales from CAPMAP”, The Astrophysical Journal Letters, Vol. 619, L127L130, 2005.

[25] A. Kogut , et. al., ”First-Year Wilkinson Microwave Anisotropy Probe (WMAP) Observations: Temperature-Polarization Correlation”, The Astrophysical Journal Supplements, Vol.148, p.161173, 2003.

[26] L. Page, et. al., ”Three-Year Wilkinson Microwave Anisotropy Probe (WMAP) Observations: Polarization Analysis”, The Astrophysical Journal Supplements, Vol.170, p.335376, 2007.

[26] P. Ade, et. al., ”First Season QUaD CMB Temperature and Polarization Power Spectra”, The Astrophysical Journal, Vol.674, p.2228, 2008.

[27] H. Chiang, et. al., ”Measurement of Cosmic Microwave Background Polarization Power Spectra from Two Years of BICEP Data”, The Astrophysical Journal, Vol. 711, p.11231140, 2010.

[28] C. Bischoff, et. al., First Season QUIET Observations:Measurements of Cosmic Microwave Background Polarization Power Spectra at 43 GHz in the Multipole Range $25 < l < 475$” , The Astrophysical Journal 741, 111 (Nov. 2011).

[29] C.L. Bennett, et. al., ”First-yearWilkinson microwave Anisotropy Probe Observations: Preliminary Maps and Basic Results”, The Astrophysical Journal Supplement Series, Vol.148, p.1-27, 2003.

[30] D. Hanson, et. al., ”Detection of B-mode Polarization in the Cosmic Microwave Background with Data from the South Pole Telescope”, preprint arXiv:1307.5830v1, 2013.

[31] P.A.R. Ade, et. al., ”Planck 2013 results.I. Overview of products and scientific results”, preprint arXiv:1303.5062v1, 2013.

[32] George Efstathiou, ”Unravelling the Big Bang with the Planck satellite”, [1]

[33] Planck Collaboration, ”The Scientific Programme of Planck (Bluebook)”, 2005.

[34] N. Mandolessi, et.al., ”Planck pre-launch status: The Planck-LFI programme”, A&A Vol.520, A3, 2010.

[35] B.Maffei, ”Planck pre-launch status: HFI beam expectations from the optical optimisation of the focal plane”, A&A, Vol.520, A12, 2010.

[36] J. A. Murphy, et.al., ”Multi-mode horn design and beam characteristics for the Planck satellite”, Journal of Instrumentation, 5, T0401, 2010.

[37] Planck Collaboration, ”Planck 2013 results. XVI. Cosmological parameters”, submitted to A&, 2013.

[38] P. K. Grimes, et. al., ”Clover-Measuring the cosmic microwave background B-mode polarization”, 20th Int. Symposium on Space Terahertz Tech., 2009.

[39] James Bock, et.al., ”CMB Technology Roadmap for the NASA Inflation Probe”, 2011.

[40] H. C. Chiang, et.al., ”Measurement of Cosmic Microwave Background Polarization Power Spectra from Two Years of BICEP Data”, The Astrophysical Journal, Vol.711, p.1123-1140, 2010.

[41] M. L. Brown, et.al.,”Improved measurements of the temperature and polarization of the CMB from QUaD”, The Astrophysical Journal, Vol.705, p.978-999, 2009.

[42] A. G. Vieregg., et al., ”Optical Characterization of the Keck Array Polarimeter at the South Pole”, Proc. of SPIE, Vol.8452, 845226-1, 2012.

[43] K. Arnold, et.al., ”The bolometric focal plane array of the Polarbear CMB experiment”, Proc. of SPIE, Vol.8452, 84521D-1, 2012.

[44] , W. C. Jones, et. al., ”Instrumental and analytic methods for bolometric polarimetry”, A&A, Vol.470, p.771-785, 2007.

[45] Josquin Errard, PhD Thesis, ”A hunt for CMB B-modes in the systematic contaminants jungle”, Universite Paris, September 2012.

[46] ”A B-Mode Polarization Satellite Mission (B-Pol”), A Proposal in response to the European Space Agency Cosmic Vision 2015-2025 Call D.SCI/DJS/db/21851, 2007.

[47] EPIC (The Experimental Probe of Inflationary Cosmology) mission study team, ”A mission concept study for NASA‘s Einstein Inflation Probe”, 2008.

[48] P. A. R. Ade, et.al., ”Polarization modulators for CMBPol”, Journal of Physics, Conference series 155, 012006, 2009.

[49] Wayne Hu, et.al., ”Benchmark parameters for CMB polarization experiments”, Physical review D, Vol.67, 043004, 2003.

[50] Meir Shimon, et.al., ”CMB polarization systematics due to beam asymmetry:Impact on inflationary science”, Physical review D, Vol.77, 083003, 2008.

[51] Daniel O‘dea, et.al., ”Systematic errors in CMB polarization measurements”, Mon. Not. R. Astron. Soc., Vol.376, p.1767-783, 2007.

[52] Shaul Hanany, et.al., ”CMB telescopes and optical systems to appear in: Planets, Stars, and Stellar Systems (PSSS), Vol.1:Telescopes and Instrumentation”, 2012.

[53] QMAP‘S web site: http://cosmology.princeton.edu/cosmology/qmap/

[54] B. Rabii, et.al., ”MAXIMA: A balloon-borne CMB anisotropy experiment”, Review of Scientific Instruments, Vol.77, 2006.

[55] H. Tran and I. Page, ”Optical elements for a CMBPol mission”, Journal of Physics Conference Series, Vol.155, No.1, 012007, 2009.

[56] Y. Mizuguchi, et. al., ”Offset dual reflector antenna”, Antennas and Propagation, Society International Symposium, Vol.14, p.2-5, 1976.

[57] S. Hanany and D. P. Marrone, ”Comparison of designs of off-axis gregorian telescopes for mm-wave large FOV arrays”, Applied Optics, Vol.41, No.22, 2002.

[58] C. Dragone, ”A first-order treatment of aberrations in Cassegrainian and Gregorian antennas”, IEEE Transactions on Antennas and Propagation, Vol.AP-30, No.3, 1982.

[59] C. Dragone, ”First-order correction of aberrations in Cassegrainian and Gregorian antennas”, IEEE Transactions on Antennas and Propagation, Vol.AP-31, No.5, 1983.

[60] G. Yassin, et.al., ”Compact optical assemblies for large-format imaging arrays”, 16th Int. Symp. on Space Terahertz Technology, 2003.

[61] M. D. Audley, et.al., ”Performance of a microstrip-coupled TES imaging module for CMB polarimetry”, 21st Int. Symp. on Space Terahertz Technology, 2010.

[62] Members of the EPIC-IM study team, ”Study of the Experimental Probe of Inflationary Cosmology - Intermediate Mission for NASAs Einstein Inflation Probe”, 2009.

[63] W. A. Imbriale, ”The 1.4-m telescope for the Q/U imaging experiment”, IEEE Transactions on Antennas and Propagation, Vol.59, No.6, 2011.

[64] A. C. Taylor, et.al., ”CLOVER- A new instrument for measuring the B-mode polarization of the CMB”, preprint arXiv:0407148v1, 2004.

[65] A. Gomez, ”QUIJOTE Telescope design and fabrication”, Proc. of SPIE, Vol.77330Z-1, 2010.

[66] H. Tran, et.al., ”Comparison of the crossed and the Gregorian MizuguchiDragone for wide-field millimeter-wave astronomy”, Applied Optics, Vol.47, No.2, 2008.

[67] H. Tran, et.al., ”Optical design of the EPIC-IM crossed Dragone telescope”, Proc. of SPIE, Vol.77311R, 2010.

[68] K. W. Yoon, et.al., ”The Robinson Gravitational Wave Background Telescope (BICEP): A bolometric large angular scale CMB polarimeter”, Proc. of SPIE, Vol.6275, 2006.

[69] P. Oxley, et.al., ”The EBEX experiment”, Proc. of SPIE, Vol.5543, 2004.

[70] Z. D. Kermish, et.al., ”The Polarbear experiment”, Proc. of SPIE, Vol. 8452, 2012.

[71] M. D. Niemack, et.al., ”ACTPol: A polarisation-sensitive receiver for the Atacama Cosmology Telescope”, Proc. of SPIE, Vol. 7741, 2010.

[72] J. J. McMahon, et.al., ”SPTpol: an instrument for CMB Polarisation”, AIP Conf. Proc., Vol. 1185, 511, 2009.

[73] Y. D. Takahashi, et.al., ”Characterization of the BICEP telescope for high-precision CMB polarimetry”, The Astrophysical Journal, Vol.71, p.1141-1156, 2010.

[74] R. W. Aikin, et.al., ”Optical performance of the BICEP2 telescope at the South Pole”, Proc. of SPIE, Vol. 77410V, 2010.

[75] C. Armitage-Caplan, et.al., ”Cosmic Origins Explorer (COrE)”, A white paper, preprint arXiv:1102.2181, 2011.

[76] P. Andre, et.al., ”Polarized Radiation Imaging and Spectroscopy Mission (PRISM)”, A white paper, preprint arXiv:1306.2259, 2013.

[77] S. Hanany, et.al., ”A cosmic microwave background radiation polarimeter using superconducting bearings”, IEEE, Vol.13, No.2, p.2128-2133, 2003.

[78] LSPE collaboration, S. Aiola, et.al., ”The large-scale polarization explorer (LSPE)”, astro-ph/1208.0281, 2012.

[79] P. de Bernardis, ”The large-scale polarization explorer (LSPE)”, SCAR AAA Meeting, Italy, 2013.

[80] P. de Bernardis and S. Masi, ”The CMB: observing directly the early universe”, Proc. of SPIE, Vol. 844203-1, 2012.

[81] W. C. Gibson, ”The Method of Moments in Electromagnetics”, Chapman&Hall/CRC Press: http://www.crcpress.com

[82] D. B. Davidson, ”Computational Electromagnetic for RF and Microwave Engineering”, Second edition, Cambridge University Press, 2011.

[83] GRASP‘s web site: http://www.ticra.com/products/software/grasp

[84] Knud Pontoppidan, ”Technical Description of GRASP”, TICRA, 2005.

[85] A. C. Ludwig, ”The definitions of Cross Polarization”, IEEE Transactions on Antennas and Propagation, Vol.21-1, p.116-119, 1973.

[86] CST‘s web site: http://www.cst.com/

[87] HFSS‘s web site: http://www.ansys.com/

[88] FEKO‘s web site: http://www.feko.info/

[89] J. Tuovinen, et.al., ”Near-Field Analysis of a Thick Lens and Horn Combination: Theory and Measurements”, IEEE Transactions on Antennas and Propagation, Vol.40-6, p.613-619, 1992.

[90] R. F. Harrington, ”Field Computation by Moment Methods”, Wiley-IEEE Press, 1993.

[91] U. Jakobus, ”Comparison of different techniques for the treatment of lossy/magnetic bodies within the MOM formulation AEU Int. J. Electron. Commun., Vol.54, No.1, 2000.

[92] S. B. Sorensen and K. Pontoppidan, ”Lens analysis methods for quasioptical systems”, EuCAP 2007, p.1-5, 2007.

[93] S. Liao, ”An efficient iterative algorithm for computation of scattering from dielectric objects”, Optics Express, Vol.19, No.4, 2011.

[94] J. Song, et.al., "Multilevel Fast Multipole Algorithm for Electromagnetic Scattering by Large Complex Objects", IEEE Transactions on Antennas and Propagation, Vol.45, N.10, 1997.

[95] L. Greencard and V. Rokhlin, "A fast algorithm for particle simulations", Journal of Computational Physics, Vol.75, p.315-348, 1987.

[96] U. Jakobus, et.al., "Tailoring FEKO for Microwave problems", IEEE Microwave Magazine, p.76-85, 2008.

[97] Personnel communications with FEKO support service.

[98] Z. Wang, et.al., "Equivalent Optical Design of The Bifocal Lens Antenna in Passive Millimeter Imaging System", IEEE, ICMMT Proceedings, 2010.

[99] FEKO User‘s Manual, 2010.

[100] B. Maffei, in preparation, 2013.

[101] A.D. Olver, et.al., "Microwave Horns and Feeds", IEEE Press, Electromagnetic Waves Series 39, 1994.

[102] Emily Gleeson, PhD Thesis, "Single and Multi-moded Corrugated Horn Design for Cosmic Microwave Background Experiments", NUI Maynooth, January 2004.

[103] CORRUG‘s web site: http://www.smtconsultancies.co.uk/products/corrug/corrug.php

[104] F. Ozturk, et.al., "A quasi-optical free-space S-parameters measurement system for material characterization in W and Ka bands", 33rd ESA Antenna Workshop on Challenges for Space Antenna Systems, 2011.

[105] B. Maffei, et.al., "Effects of quasi-optical components on feed-horn co- and cross-polarisation radiation patterns", Proc. of SPIE, Vol.70202H-1,2008.

[106] J. Brossard, et.al., "Dual-reflector compact range modelling: geometrical theory of diffraction analysis and sub-millimetre quiet-zone computation", J. Opt. A.: Pure Appl. Opt., p.108-116, 2003.

[107] Rohde&Schwarz, Application Note, "Measurement of dielectric material properties".

[108] M.N.Afsar, et.al., Proceedings of the IEEE, Vol. 74-1, 1986.

[109] C. Macculi, et.al., ”Optical properties of dielectrics in the mm range: the case of spurious polarization induced by a vacuum window”, Proc.of SPIE, Vol.5498, 2004.

[110] D. Bourreau, et. Al., IEEE Transactions on Instrumentation and Measurement, Vol. 55-6, 2006.

[111] N.Gagnon, et. al., ”Low cost free-space measurement of dielectric constants at Ka band”, IEEE, Microwave Antennas and Propagation, Vol. 151-3, 2004.

[112] A. Elhawil, et.al., IET Sci. Meas. Techn., Vol.3-1, p.39-50, 2009.

[113] M. Le Goff, ”Ka band quasi optical test bench using focusing horns”, 29th European Microwave Conference, 1999.

[114] E.W.M Dudok and D. Fasold, ”Analysis of Compact Antenna Test Range Configurations”, Int. Symp. on Antennas, 1986.

[115] A. D. Olver, ”Compact Antenna Test Ranges”, IEEE, ICAP, Vol.1, p.99-108, 1991.

[116] X. Liu, et. al., ”Design of Tri-reflector Compact Antenna Test Range for Millimetre/Sub-millimetre Wave and THz Antenna Measurement”, IEEE, Int. Workshop on Antenna Technology, p.144-147, 2011.

[117] A.G. Repjar and D. P. Kremer, ”Accurate Evaluation of a Millimeter Wave Compact Range Using Planar Near-Field Scanning”, IEEE Transactions on Antennas and Propagation, Vol.30-3, p.419-425, 1982.

[118] A. V. Raisanen, et.al., ”Feasibility of different antenna measurement techniques”, ICMMT, p.367-371, 1998.

[119] J. Hartmann and D. Fasold, ”Advanced serration design for compact ranges with UTD”, 22th AMTA, 2000.

[120] P. A. Beeckman, ”Prediction of the Fresnel region field of a compact antenna test range with serrated edges”, IEEE, Vol.133, No.2, 1986.

[121] M. Boumans and B. Kalender, ”Measurement comparison serrated edge versus rolled edge compact range”, from http://www.microwavevision.com/sites

[122] A. Munoz-Acevedo, et.al., ”Antenna Measurement System at 300 GHz for the Terasense Project, EuCAP”, p.1-5, 2010.

[123] Mark Whale, PhD Thesis, ”Optical Characterisation of Astronomical Submillimetre Receivers including ALMA Bands 5 and 9”, NUI Maynooth, January 2010.

[124] J. A. Murphy, et.al., ”Gaussian beam mode analysis of partial reflections in simple quasi-optical systems fed by horn antennas”, Infrared Physics & Technology, Vol.44, p.289-297, 2003.

[125] N. Trappe., et al., ”Gaussian Beam Mode Analysis of Standing Waves Between Two Coupled Corrugated Horns”, IEEE, Vol.53, No.5, 2005.

[126] B. Maffei, et.al., ”Implementation of a quasi-optical free-space S-parameters measurement system”, 35th ESA Antenna Workshop on Antenna and Free Space RF Measurements, 2013.

[127] Samuel Silver, ”Microwave Antenna Theory and Design”, 1st edition, McGraw-Hill Press, 1949.

[128] Paul F. Goldsmith, ”Quasioptical Systems (Gaussin beam quasioptical propagation and applications)”, IEEE Press, 1997.

[129] Notes on Lens Theory, from http://www.lasercomponents.com/uk/

[130] J.R.Risser, ”Microwave Antenna theory and design (Chapter 11)”, McGraw-Hill, New York, 1949.

[131] Personnel communications with M. Candotti, 2013.

[131] Web site: http://www.rohde-schwarz.com

[132] P. Schemmel, ”A near field 3D scanner for millimetre wavelengths”, 35th ESA Antenna Workshop on Antenna and Free Space RF Measurements, 2013.

[133] ”Time domain measurements using vector network analyzer ZVR”, Rohde&Schwarz, Application Note 1EZ44-0E

[134] F. Ozturk, et.al., ”Systematic effects introduced by lenses at MM-wavelengths in CMB applications”, Proc. of SPIE, Vol.84520I-1, 2012.

[135] RS company‘s web site: http://uk.rs-online.com/web/

[136] J. W. Lamb, ”Miscellaneous data on materials for millimetre and submillimetre optics”, Int. Journal of Infrared and Millimeter Waves, Vol.17, No.12, 1996.

[137] J. Lau, ”Millimeter-wave antireflection coating for cyrogenic silicon lenses”, Applied Optics, Vol.45, No.16, 2006.

[138] Hyperphysics‘s web site: http://hyperphysics.phy-astr.gsu.edu/hbase/

[139] S. J. Orfanidis, ”Electromagnetic Waves and Antennas”, from www.ece.rutgers.edu/ orfanisi/ewa

[140] E. Hecht, Optics, 4th edition, Addison Wesley Press, 2002.

[141] ZEMAX Optical Design Programme, User‘s guide manual, 2004.

[142] P. C. Hargrave, et.al., ”Coated dielectric lens design, modelling and measurements for future CMB polarimetry missions”, 7th EuCAP, 2013.

[143] B. G. Keating, et.al., ”An instrument for investigating the large angular scale polarization of the CMB”, astro-ph/0111276v2, 2002.

Appendix A

Electromagnetic theory

A.1 Electromagnetic Theory (EMT)

The polarization, diffraction and interference properties of light require more sophisticated concepts/descriptions than simple approaches such as ray optics. The wave optics completes the general frame of light with a concept of EM wave. The basic principles underlying EM wave propagation is fundamentally derived from Maxwell's equations. The following four equations are famously known as Maxwell equations for a given homogenous medium in the most general case.

$$\nabla \times E = -\frac{\partial B}{\partial t} \tag{A.1}$$

$$\nabla \times H = -\frac{\partial D}{\partial t} + J \tag{A.2}$$

$$\nabla \cdot B = 0 \tag{A.3}$$

$$\nabla \cdot E = -\rho_e \tag{A.4}$$

Their corresponding quantities in the electrical source are given as follows;

- ρ is the electric charge density in the units of $\frac{Coloumb}{m^2}$.
- J is the electric current density in the units of $\frac{Ampere}{m^2}$.

Two quantities describe the EM field;

- E is the electric field vector in the unit of $\frac{Volt}{m}$.
- H is the magnetic field vector $\frac{Ampere}{m}$.

Two other quantities also describe the effect of the fields on matter;

- D is the electric displacement vector in the unit of $\frac{Coloumb}{m^2}$.
- B is the magnetic induction vector in the units of $\frac{Weber}{m^2}$.

D and B are also called as electric and magnetic flux densities respectively. They are related to the field vectors with the equations as

$$D = \varepsilon E$$
$$B = \mu H$$

where ε and μ are the permittivity and permeability of the medium. They can be modified by the electric and magnetic susceptibilities of the material of interest mentioned in the next sub-section. These equations show the transmission ability of materials. For the vacuum conditions, they become ε_0 and μ_0 with the values;

$$\varepsilon_0 = 8.854x10^{-12}\frac{Farad}{m}$$
$$\mu_0 = 4\pi x10^{-7}\frac{Henry}{m}$$

These two parameters are used to determine the characteristic impedance of the medium.

$$Z = \sqrt{\frac{\mu}{\varepsilon}} \tag{A.5}$$

For a special case, the vacuum impedance is given as

$$Z_0 = \sqrt{\frac{\mu_0}{\varepsilon_0}} = 377ohm. \tag{A.6}$$

The other quantity remained undefined is the electric current density given by the equation.

$$J = \sigma E \tag{A.7}$$

σ is the material conductivity. It is also called as Ohm‘s law in the EMT. It is mostly accepted as ≈ 0 for dielectric materials however it should be known to high precision.

- **Medium parameters**

From the EM perspective, the materials can be categorised under two groups; conductors and dielectrics. In conductors, there are a number of electrons moving free to help connectivity inside the material. In dielectric medium, however, all charges are connected to their atom strongly and can only be moved slightly due to the effects of EM force. The dielectric characteristics different than free-space are determined by these slight displacements. The electric displacement vector appears in the Maxwell equations written for the most general case. Let us have a look at where it comes from.

The electric and magnetic polarization properties of the dielectric material are given as follows;

$$\varepsilon = \varepsilon_0(1 + X_e)$$
$$\mu = \mu_0(1 + X_m)$$

X_e and X_m are the electric and magnetic susceptibilities of the material respectively and determined by the microscopic structures of material. By using the relationship between the E and D, they become;

$$D = \varepsilon E = \varepsilon_0(1 + X_e)E = \varepsilon_0 E + \varepsilon_0 X_e E = \varepsilon_0 E + P \tag{A.8}$$

P defines the dielectric polarization induced by an external EM field.

$$P = \varepsilon_0 X_e E \tag{A.9}$$

From this equation, dielectric constant (relative dielectric permittivity) is determined as;

$$\varepsilon_r = \frac{\varepsilon}{\varepsilon_0} = 1 + X_e \tag{A.10}$$

By using the relationship for ε_r and $n = \sqrt{\frac{\varepsilon}{\varepsilon_0}}$, the refractive index can be defined as;

$$\varepsilon_r = n^2 \tag{A.11}$$

- **Derivation of the Electric and Magnetic Field Equations**

Maxwell equations derived in differential form should be converted into the integral form, as the radiation problems can be handled easier by using the integral forms of the Maxwell equations for the MOM formulation. Time dependency of the field quantities in the Maxwell equations are suppressed in the new formulation.

Let's say $B(t) = Be^{jwt}$ and take its time derivative;

$$\frac{\partial B(t)}{\partial t} = jwBe^{jwt} = jwB(t). \tag{A.12}$$

We know $B = \mu H$ and go back to the first Maxwell equation A.1,

$$\nabla \times E = -\frac{\partial B}{\partial t} = -jw\mu H \tag{A.13}$$

Similarly, the second Maxwell's equation A.2 becomes

$$\nabla \times H = -\frac{\partial D}{\partial t} + J = J - jw\varepsilon E \tag{A.14}$$

The third and fourth Maxwell's equations A.3 and A.4 remain the same as they were.

$$\nabla \cdot B = 0$$
$$\nabla \cdot E = \rho_e$$

After we obtain the time independent forms of the Maxwell equations, the electric and magnetic fields are derived by taking the curl of the first Maxwell equation A.13.

$$\nabla \times \nabla \times E = -jw\mu\nabla \times H \tag{A.15}$$

Using the vector identity, the left hand side of the equation becomes;

$$\nabla(\nabla \cdot E) - \nabla^2 E = \nabla \times \nabla \times E \tag{A.16}$$

and using the second Maxwell‘s equation A.14, the right hand side of the equation becomes;

$$-jw\mu\nabla\times H=-jw\mu(J+jw\varepsilon E)=w^2\mu\varepsilon E-jw\mu J. \tag{A.17}$$

Substituting the equation of continuity $\nabla\cdot J=-jwq_e$ and wave-number $k=w\sqrt{\varepsilon\mu}$ into Equation A.17, the last form of the equation becomes

$$\nabla^2E+k^2E=jw\mu J-\frac{1}{jw\varepsilon}\nabla(\nabla\cdot J) \tag{A.18}$$

Equation A.18 is an in-homogenous differential equation. At this point, the Green‘s function is introduced. It is a special function to solve in-homogenous differential equations.

$$\nabla^2G(r,r^{'})+k^2G(r,r^{'})=-\delta(r,r^{'}) \tag{A.19}$$

The scattering electric field due to the electric current is obtained in terms of the electric current density and the Green‘s function.

$$E(r)=-jw\mu\int\int\int G(r,r^{'})[J(r^{'})+\frac{1}{k^2}\nabla^{'}\nabla^{'}\cdot J(r^{'})]dr^{'} \tag{A.20}$$

Similarly, the scattering magnetic field due to the magnetic current is obtained in terms of the magnetic current density and the Green‘s function.

$$H(r)=-jw\varepsilon\int\int\int G(r,r^{'})[M(r^{'})+\frac{1}{k^2}\nabla^{'}\nabla^{'}\cdot M(r^{'})]dr^{'} \tag{A.21}$$

This is where r and $r^{'}$ are the source and observation points as shown in figure A.1 respectively.

After this point, the Green‘s function must be solved to obtain G$(r,r^{'})$. This is an in-homogenous differential equation. Assuming that the Green‘s function is the solution for a point source, the solution can be obtained in two steps in spherical coordinate system due to its spherical symmetry:

- Find the solution for homogenous equation
- Substitute the solution into the in-homogenous equation to obtain the ultimate solution to the electro-dynamic Green‘s function

The radial term of the Laplacian Green‘s function is written in spherical coordinate system.

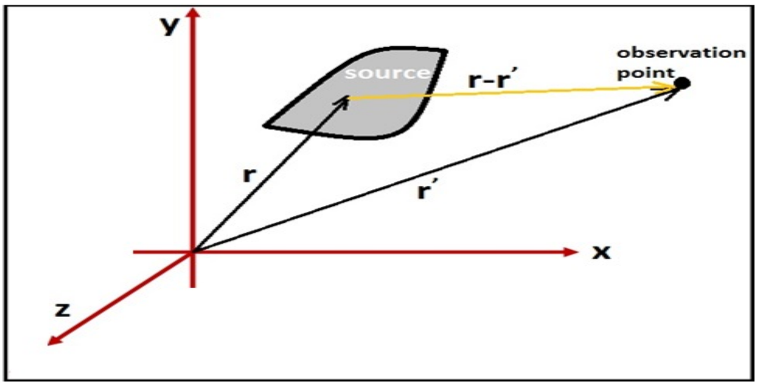

Figure A.1: The figure shows the source and the observation points for the coordinate system of the EM problem.

$$\nabla^2 G = \frac{1}{r^2}\frac{d}{dr}\left(r^2\frac{dG}{dr}\right) = \frac{d^2G}{dr^2} + \frac{2}{r}\frac{dG}{dr} \tag{A.22}$$

This expression is also equal to the following equation;

$$\nabla^2 G = \frac{d^2G}{dr^2} + \frac{2}{r}\frac{dG}{dr} = \frac{d^2(rG)}{dr^2}. \tag{A.23}$$

After the related substitutions are done, the homogenous equation yields,

$$\frac{d^2(rG)}{dr^2} + k^2(rG) = 0. \tag{A.24}$$

The solution of this equation is known as;

$$G = A\frac{e^{-jkr}}{r} + B\frac{e^{jkr}}{r}. \tag{A.25}$$

The equation is a superposition of incoming and outgoing waves. If the outgoing part is only picked, then the solution remains with

$$G = A\frac{e^{-jkr}}{r}. \tag{A.26}$$

Now, this solution must satisfy the in-homogenous Green function. In order to determine the wave amplitude A, the boundary conditions for an electromagnetic point source as assumed in the beginning are used.

1. $G(r,r') \rightarrow 0$ as $r \rightarrow \infty$

   This requirement is satisfied by the radiation decay with increasing r.

2. This condition will be applied to the integral to calculate the amplitude A for $r = 0$.

The integration of the Green‘s function is realised over a spherical volume with a radius of a around the point source. The solution to the homogenous Green function obtained is substituted in to Equation A.19 by taking the volume integral of both sides.

$$A\int\int\int\left[\nabla\cdot\nabla\left(A\frac{e^{-jkr}}{r}\right)+k^2A\frac{e^{-jkr}}{r}\right]dV=-\int\delta(r-r^{'})dV \tag{A.27}$$

The volume integral of the dirac delta function at the right hand side of the equation gives 1 only at $r = r^{'}$.

$$\int\delta^3(r-r^{'})dV=1 \tag{A.28}$$

The first term of the equation at the left hand side is converted to a surface integral by using the divergence theorem.

$$\int\int\int\nabla\cdot\nabla(A\frac{e^{-jkr}}{r})dV=\int\int\hat{n}\cdot\nabla(\frac{e^{-jkr}}{r})dS \tag{A.29}$$

At the surface of the sphere, $\hat{n}$ becomes $\hat{r}$. When the surface integral part is evaluated, it yields;

$$4\pi a^2\left[\frac{\partial}{\partial r}\left(\frac{e^{-jkr}}{r}\right)\right]_{r=a}\rightarrow\lim_{a\rightarrow 0}4\pi a^2\left[\frac{\partial}{\partial r}\left(\frac{e^{-jkr}}{r}\right)\right]_{r=a}=-4\pi. \tag{A.30}$$

The second term gives 0 as a goes to 0. Hence,

$$k^2\int_0^a\frac{e^{-jkr}}{r}4\pi r^2dr=4\pi k^2\int_0^a re^{-jkr}dr=0 \tag{A.31}$$

When we evaluate all calculated equations, the amplitude A becomes $1/4\pi$ and finally the Green‘s function is obtained as

$$G(r,r^{'})=\frac{e^{-jk|r-r^{'}|}}{4\pi\mid r-r^{'}\mid}. \tag{A.32}$$

The Green‘s function is calculated for an electromagnetic point source. It may also be left undefined to be calculated for any other type of external field source. As a result, the last format of the field quantities are given as

$$E(r) = -jw\mu \int\int\int [J(r') + \frac{1}{k^2}\nabla'\nabla' \cdot J(r')] \frac{e^{-jk|r-r'|}}{4\pi \mid r-r' \mid} dr' \quad (A.33)$$

$$H(r) = -jw\varepsilon \int\int\int [M(r') + \frac{1}{k^2}\nabla'\nabla' \cdot M(r')] \frac{e^{-jk|r-r'|}}{4\pi \mid r-r' \mid} dr' \quad (A.34)$$

A.2 Stoke‘s parameters

Stokes parameters are used to describe the polarization states of the CMB signal [143]. Suppose that we have an electric field with a frequency of f propagating along the z-axis to be

$$E = E_x cos(2\pi f t + \phi_x)\hat{x} + E_y cos(2\pi f t + \phi_y)\hat{y}. \quad (A.35)$$

The time-averaging Stokes parameters given as

$$\begin{aligned} I &= < E_x^2 + E_y^2 > & (A.36) \\ Q &= < E_x^2 - E_y^2 > & (A.37) \\ U &= 2 < E_x E_y Cos\phi > & (A.38) \\ V &= 2 < E_x E_y Sin\phi > & (A.39) \end{aligned}$$

where I is the total intensity, V is for the circular polarization and Q and U specify the linear polarization in cartesian coordinates (x,y,z). The Q is the intensity difference between the x and y components while the U is the intensity difference between the diagonal directions. Finally, ϕ is the phase difference between electric vectors.

Appendix B

Parabolic and Hyperbolic Mirrors

B.1 Parabolic mirror

This appendix presents the procedure that was followed to design the parabolic mirror for the CATR system. According to ray-based approach, all ray paths emanating from the focus, reflecting from the parabolic mirror and propagating through the plane aperture should take the same distance to create a plane wave medium. This is important because the rays should be coherent in phase. In dual reflector structures like CATR, a sub-reflector is then added to reshape the beam and shorten the geometric structure. The feed-horn is placed at the focus point which is the first focal point of the hyperbolic subreflector. After the beam is reflected from the sub-reflector, the beam appears to come from the second focus of the sub-reflector, which is also coincident with the focal point of the parabolic main reflector. The two parameters that define a parabola are the focal length f and the diameter of the reflector aperture, D. The parabola equation is given as;

$$z = \frac{x^2 + y^2}{4 \cdot f} \tag{B.1}$$

where x,y and z are defined in the cartesian coordinates. An off-axis parabolic reflector is a small part of a full parabola. Due to its off axis geometry, the parabola relations should be re-derived. In order to generate an off-axis geometry, the parabolic mirror is first translated and then rotated as shown in Figure B.1. The off-axis parameters are calculated using Equation B.2.

$$\theta_c = arctan\left(\frac{2 \cdot f}{D' + D/2}\right) \tag{B.2}$$

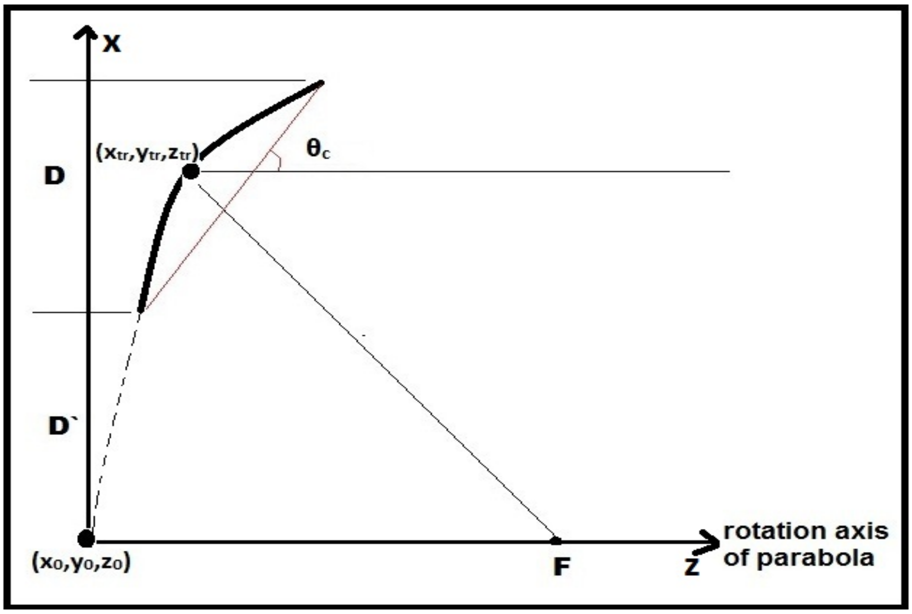

Figure B.1: The off-axis orientation of the parabola is generated by translating the origin and rotating the curve. D' and θ_c are off-axis parameters for translation and rotation respectively. F gives the focal point of the parabolic system.

The vertex of the coordinate frame is shifted to the center of the paraboloid curve so that a rotationally symmetric paraboloid is defined. The center of the new coordinate system is at (x_{tr}, y_{tr}, z_{tr}). In order to achieve these transformations, the transformation matrices of the translational and rotational operations are described in terms of $(x_\circ, y_\circ, z_\circ)$. The origin of the coordinate system is first moved in the axes of x and z and then rotated around y-axis.

$$\begin{pmatrix} x_t \\ y_t \\ z_t \end{pmatrix} = \begin{pmatrix} 1 & 0 & 0 \\ 0 & 1 & 0 \\ 0 & 0 & 1 \end{pmatrix} \begin{pmatrix} x \\ y \\ z \end{pmatrix} + \begin{pmatrix} -x_{0t} \\ -y_{0t} \\ -z_{0t} \end{pmatrix} \tag{B.3}$$

$$\begin{pmatrix} x_{tr} \\ y_{tr} \\ z_{tr} \end{pmatrix} = \begin{pmatrix} \cos\theta & 0 & \sin\theta \\ 0 & 1 & 0 \\ -\sin\theta & 0 & \cos\theta \end{pmatrix} \begin{pmatrix} x - x_{0t} \\ y - y_{0t} \\ z - z_{0r} \end{pmatrix} \tag{B.4}$$

Parameters B.5 are substituted as following.

$$(x_0, y_0, z_0, \theta) = (D', 0, \frac{d^2}{4f}, \theta_c) = (76.7, 0, 18.384, 61.54^\circ) \tag{B.5}$$

c	550 mm
a	-275 mm
e	-2
foci	1100 mm

Table B.1: The geometrical parameters define the hyperbolic shape mirror to be constructed.

$$z = 0.54 \cdot x + 185.81\sqrt{364.5 \cdot x + 26707 - y^2} \tag{B.6}$$

Final equation (B.6) for the parabola is used to draw and fabricate the parabolic mirrors.

B.2 Hyperbolic mirror

In case of our CATR, eccentricity of the hyperboloid curve becomes negative. The hyperbolic geometry has two focal points and the distance between them is defined by 2c. The curves are located between the two foci. In this configuration, the convex side is used to reflect the beam. The focus behind the sub-reflector is called a virtual focus because it does not take any beam. The distance between the vertices is 2a. These parameters and the off-axis geometry of the hyperbolidal curve are indicated in Figure B.2. The hyperboloids satisfy the following relations and parameters given in Table B.1.

Parameters that define a hyperbola are given as follows;

$$z = c - (a/b)(b^2 + x^2 + y^2)^{0.5} \tag{B.7}$$

$$b = (c^2 - a^2)^{0.5} \tag{B.8}$$

$$e = c/a \tag{B.9}$$

x and y denotes the half-axes of hyperboloid sub-reflector. Two conditions determine the eccentricity of a hyperbolic sub-reflector.

- e < -1 corresponds to the concave hyperboloid.

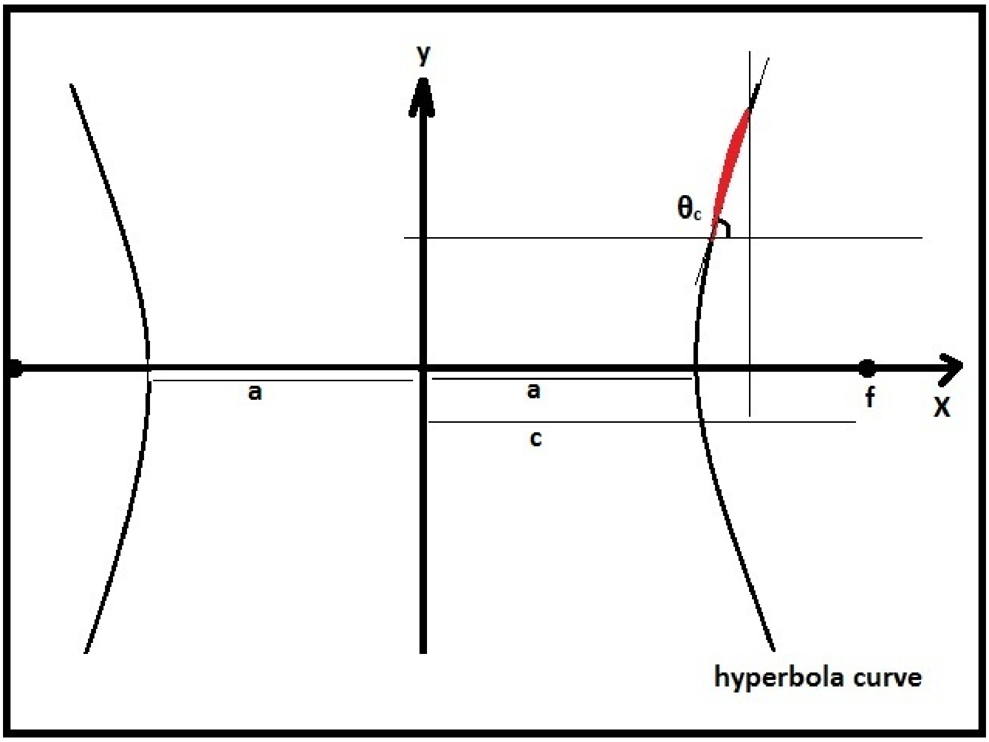

Figure B.2: The red curve shows the part of the full hyperbola curve used for the hyperbolic mirror. The off-axis orientation of the hyperbola is generated by translating the origin and rotating the curve. F donates the focal point of the hyperbolic system.

- e $>$ 1 corresponds to the convex hyperboloid.

The same matrix elements as those of the off-axis parabolic curve are used to translate the hyperbolical curve to its new position. Again, the center of the new coordinate system is at (x_{tr}, y_{tr}, z_{tr}). The transformation matrices of the translational and rotational operations are described in the previous section. After some algebra and the parameters are substituted, the new definition of the off-axis hyperbolical reflector is obtained as given;

$$z = 1.15x + 9.5 \pm \sqrt{0.71x^2 + 22.35x + 1420 + y^2/3}. \tag{B.10}$$

Appendix C

Simulations with FEKO

This appendix discusses the modelling issues regarding to the full-wave simulations of the horn-lens system with the Method of Moment (MOM) supplemented with the Surface Equivalence Principle (SEP) within the commercial software package FEKO suite 6.2.

C.1 Hardware requirements

The software installation requests for 2.1 GB free hard disk space. Our technology group at JBCA has three computers dedicated to the EM simulations only. The computers have a RAM usage of 64 GB, 128 GB and 196 GB. The computation models of the FEKO can be parallelized to maximum six processors. The FEKO license is valid for the 64-bit windows version. This license allows simulation tasks to be distributed into the processors so that the large size problems could be handled.

When the memory requirements are not met by available resources of the computer, the computation tasks can also be divided in sub-simulation domains by storing the data, which were calculated from the matrix elements to solve the linear set of equations. For example, the first model of the small size lens used a RAM of 508 GB in total, however the FEKO divided the calculation set into the four sub-simulation domains with a maximum memory usage of 127.26 GB, which was allocated for each part of the simulation run. However, there is an upper limit with 1 TB for the maximum memory requirement that the computer can allocate space to write the temporary solution files.

C.2 Solution steps with the FEKO

The solution process consists of three main steps: generating the model with a feed selection, setting the solution tools, requesting/obtaining the calculations of the electromagnetic field parameters. Figure C.1 describes how the solutions are obtained with the problem developed with FEKO. There are two main interfaces at which EM problem can be developed and analyzed within FEKO. The development of the problem is realized in the CADFEKO layout while solutions are analyzed in the POSTFEKO.

1. **Generating the model**

   This part is divided into three sections: constructing the problem geometry, assigning the excitations and meshing the model. The model geometry is constructed by using the CADFEKO interface. Many geometric tools that help create the problem model are provided in the CADFEKO layout as shown in Figure C.2. Initially, the user should define the parameter variables to be used when constructing the model.

   When constructing the feed model, the geometry of the corrugated feed horn antenna generated in the AUTOCAD was used. Firstly, the model is extracted by using the *.dxf file of the model which is a 2D line with the corrugations. This line is sweeped by 360° to generate the 3D model of the feed horn antenna. In order to model the corrugated structure with the MOM correctly, an external surface is also needed. This is because the exterior of the real feed-horn is a smooth wall, not a corrugated geometry. The corrugated part was surrounded with two cylinders and one conic geometries fitted with the inside geometry as shown in Figure C.3. In order to make sure that the model is united, the geometry is simplified by removing disconnections.

   Then, among the many different types of ports that can be utilised within the FEKO, a waveguide port was used to define the excitation plane. This port was added to the entrance face of the circular waveguide to create a waveguide excitation with a fundamental mode. The number of the modes can be specified when needed more.

   The second part of the model comprises of the dielectric lens antenna to be illuminated by the corrugated feed horn. A new medium with its electrical properties should be inserted into the library to be used to define the dielectric material of the lens. For example, I used the UHMWPE dielectric material to make the

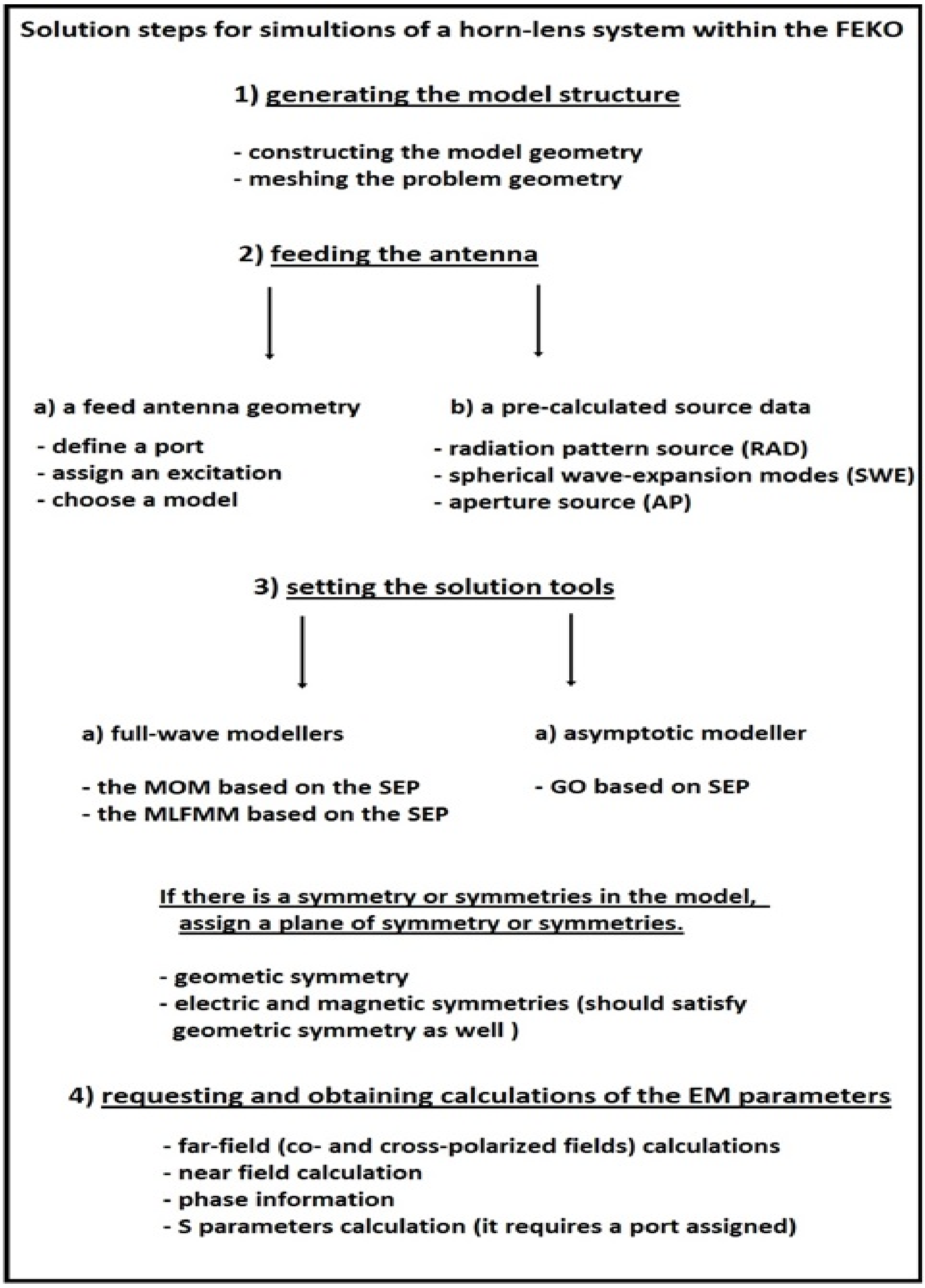

Figure C.1: The solution steps for the simulations of a horn-lens system designed in the FEKO are detailed in this chart.

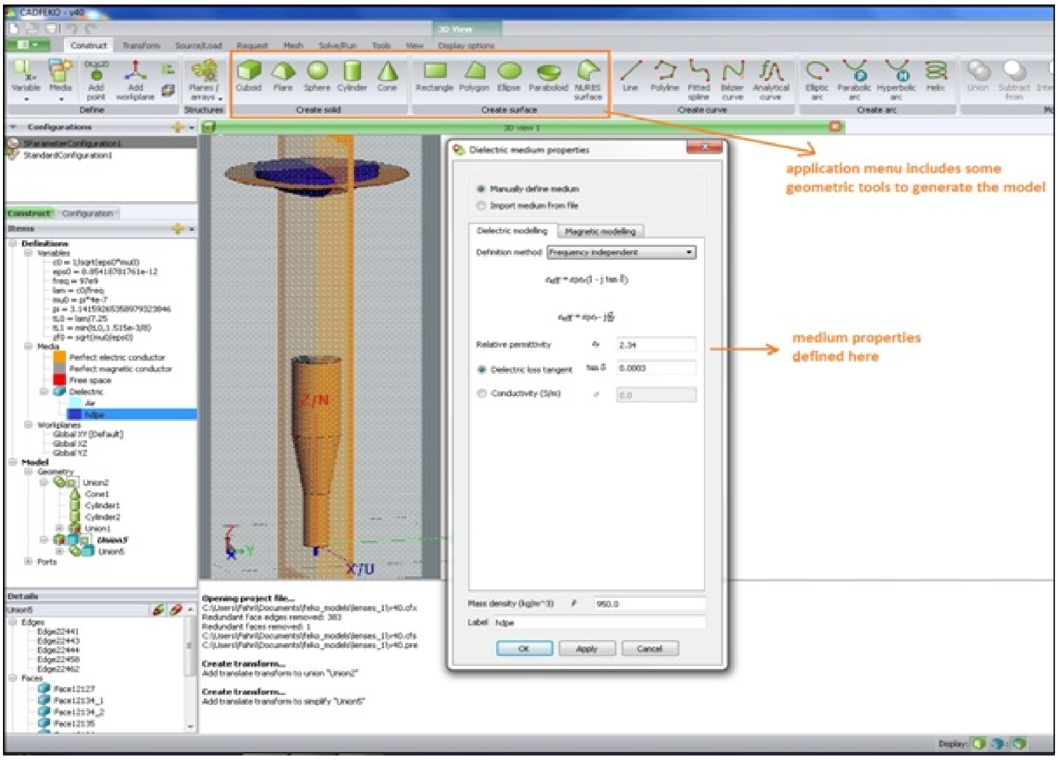

Figure C.2: The figure shows the CADFEKO layout which helps to generate the solid FEKO models. Material properties of a new medium can be inserted into the media settings.

lens so I introduced the material properties of the UHMWPE such as values of dielectric permittivity and loss tangent into the software as shown in Figure C.2.

The last step of the model preparation is the mesh operation. The model geometry comprising the feed and the dielectric lens is discretized into triangular mesh elements to obtain a solution for the problem. The triangular mesh elements generated are shown in Figure C.4. Area of each triangular mesh element should be less than at least $\lambda/70$ corresponding to the side length of the triangle of $\frac{\lambda}{5}$ to $\frac{\lambda}{6}$ but preferably minimum $\frac{\lambda}{8}$. The optimum value is decided according to the problem structure meshed, the accuracy required and the computer memory constraints allowed. It is known the finer mesh elements to be assigned lead to high accurate results. The operating wavelength corresponding to the central simulation frequency determines the length of the edges of the triangle mesh element (Ref-User manual). When the volume is meshed by using tetrahedral

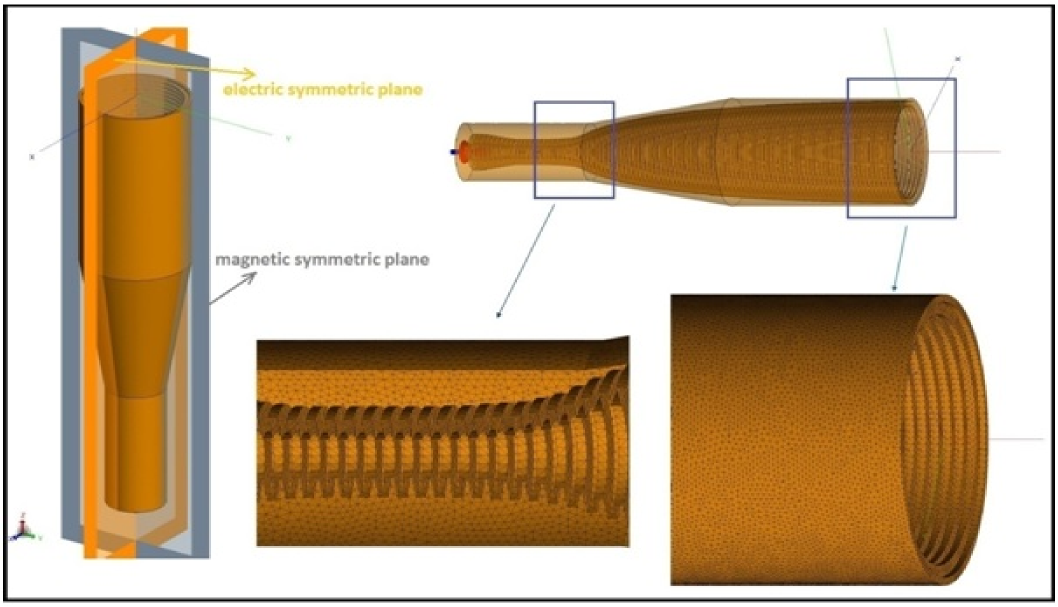

Figure C.3: The details of the feed-horn‘s solid model is shown in figure. The outside structure of the horn has a transparent view in the top figure.

volume mesh elements for the VEP and the FEM models, the problem boundaries require more care. Thus, the edge length of the mesh elements at medium interfaces should be chosen around $\frac{\lambda}{10}$. This value can be relaxed up to $\frac{\lambda}{8}$ inside the region.

After this point, the lens model construction in the FEKO is explained.

The optical design of the horn-lens system is generated by following the solution steps explained in the introduction of this section. The following gives some details of the MOM model created in the FEKO starting from the design variables. The CADFEKO model of the lens antenna system consists of two elements: the feed and the lens. In some models, the equivalence source data is preferred to be used so there is no need to construct a feed model in these cases. As the feed model is introduced in Section 3.7.1, I will skip this step and proceed to the dielectric lens model. The small size lens (SL) was detailed below and the same steps were followed for the medium size lens (ML) model.

The UHMWPE dielectric is defined by specifying dielectric permittivity and loss tangent.

- Add the UHMWPE dielectric material to the medium catalogue specifying

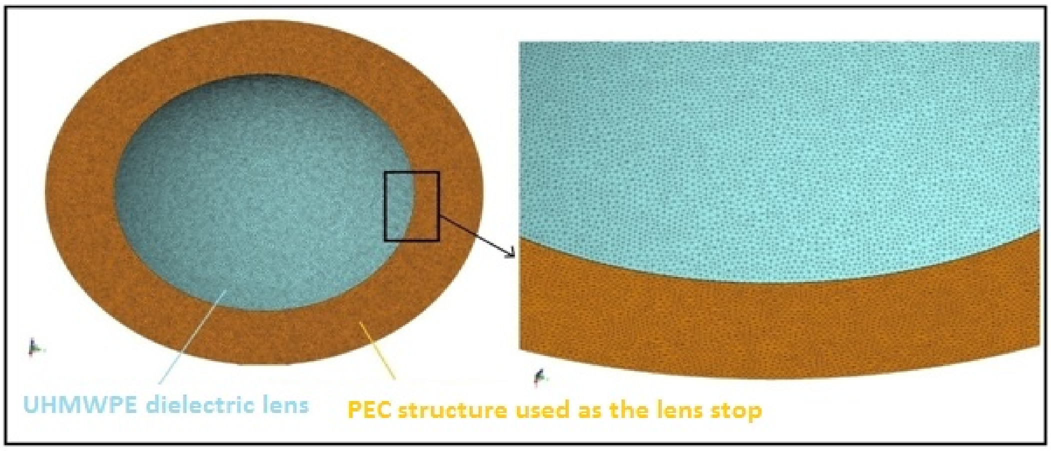

Figure C.4: The dielectric lens with a PEC ring around it. The continuity of the triangular mesh elements are important for an accurate model solution.

the dielectric permittivity as 2.3 and the tangent loss as 3×10^{-4}.

The SL is a plano-convex spherical lens which one face has a planar surface while the other has a spherical surface.

- Create a sphere with a radius of 36.112 mm along the z-axis at the center of the main coordinate system.
- Split the radius to arrange the edge thickness of the lens from the x-axis plane.
- Create a cylinder with a radius fitted with the half diameter of the splitted sphere. The cylinder must have a height of 2.42 mm to specify the central thickness of the lens.
- Add the cylinder to the splitted sphere and union these two parts.
- Simplify the geometry to make sure that all physically and electrically connected parts are combined together and any disconnections are removed.
- Translate the united lens body a distance of 68.75 mm from the origin.

This is the focal length of the lens calculated by the thick lens formula considering the phase center of the antenna. The lens axis was aligned to be illuminated along the z-axis. The created body is a perfect electric conductor by default so the pre-defined material is assigned as the lens material. For the SL, the mesh length is specified as $\lambda/8$ and the number of the mesh elements is 101336 including the PEC ring around the lens.

- A global mesh definition is set as $\lambda/8$.

If there are available symmetries in the geometry of the problem and the field distribution of the feed, geometric, electric and magnetic planes of symmetry can be assigned to reduce the computational requirements of the simulation.

- Set an electric plane symmetry at $y = 0$ and a magnetic plane symmetry at $x = 0$.

In this lens system study, the main calculation method is Method of Moments (MOM) together with Surface Equivalence Principle (SEP) to model the dielectric structure. The SEP model is explained in details in Section 3.3.3.

- Set the solution tool as the MOM (or MLFMM) with the SEP using the face properties of the dielectric lens body.

The specifications of the calculation requests may vary depending on the requested parameters. If the output parameters will be used as an equivalence source, the angular increments should be highly fine.

- Sample the calculation points for the far field request between $0°$ and $180°$ for the θ and $0°$ to $360°$ for the ϕ. Set the angular increments $0.1°$ for θ and $45°$ for θ.

2. **Setting the solution tool and requesting the calculations**

   Depending on the electrical size of the problem and available computational resources, an appropriate method in solving the problem is chosen. The best suited method for the specific problem should be decided by the user considering the points indicated above. As far as the high frequency models such as the GO and the PO are concerned, the following discussion can be made. For example, the SL is a 16λ diameter lens which is insufficient to employ the geometrical optics approximation. Moreover, the PO with the FEKO is not a valid option, because the model does not account for the currents in the shadowing regions, the back surface of the lens. To this end, the properties of the lens face and region are set to use the MOM with the surface equivalence principle (SEP) as the main code. There are the other special solution options that suit for the face and the region of the problem body that will be discussed in the subsequent sections.

In order to accelerate the solution process and reduce the required computational resources, symmetrical planes can be specified. The geometry, electric and magnetic symmetric planes are available to define at the planes of $x = 0$, $y = 0$ and $z = 0$.

- The problem geometry must be symmetric along the chosen plane when a geometric symmetry is assigned. There is no memory reduction but runtime due to the operation of the geometric symmetry plane.

- In order for the electricity symmetry plane to be defined, the geometrical symmetry condition should be met as well. Further requirements should be satisfied by the sources. Figure C.5a describes these requirements on sources for an electric symmetry plane. We understand that the electric symmetry plane can be replaced by a perfect electric conductor (PEC) platform without modifying the field distribution

- Similarly, the geometrical symmetry condition should be met as well. As shown in Figure C.5b, the requirements should be satisfied. Under these conditions, we understand that the magnetic symmetry plane can be replaced by a perfect magnetic conductor (PMC) platform without modifying the field distribution.

Since the matrix equation to be solved is reduced to half by introducing othe symmetry conditions, the memory requirement halves. However, the electric and magnetic symmetries do not work with the MLFMM model. Using symmetry in connection with the MLFMM will not reduce the computational requirements with respect to both memory and time, as only the geometry is mirrored. According to the model chosen above, a 3D far field data is calculated at 97 GHz which is the central frequency of the feed-horn antenna. The operating frequency selected can be either a single frequency or a range of frequencies. The latter does not speed up the simulation, because the simulation runs to calculate field quantities for each frequency value in the frequency domain. The full cut of the far field request is created for a range of polar angle θ and azimuthal angle ϕ. For θ, the angle ranges from 0° to 180° in 0.1° intervals. For ϕ, the angle

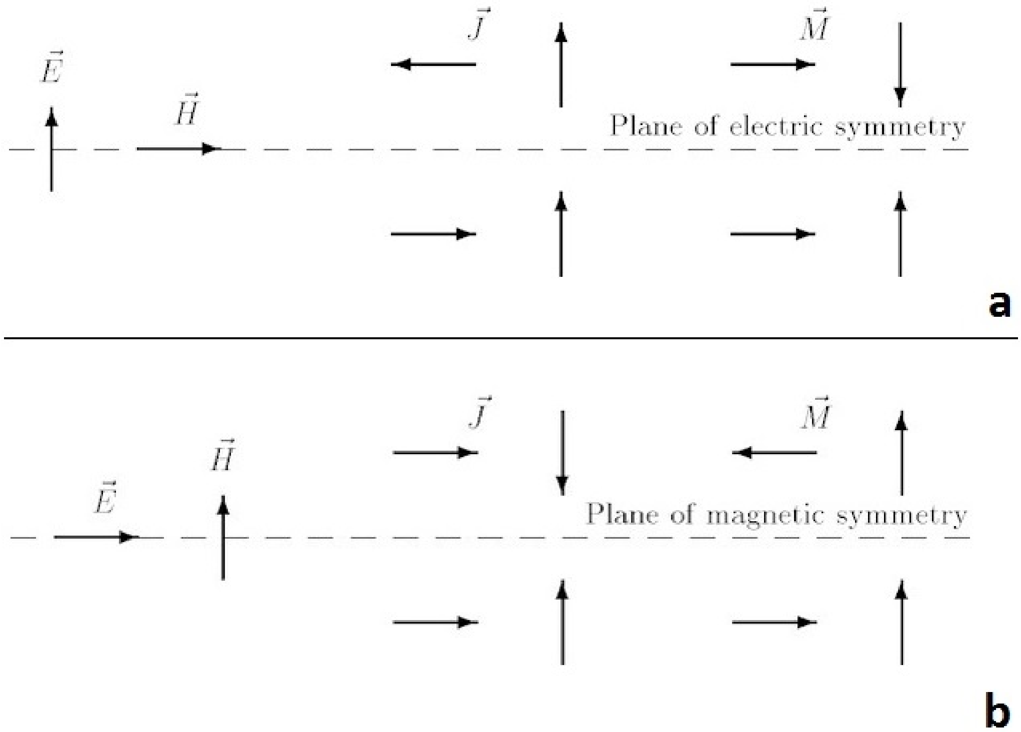

Figure C.5: Upper: A plane of electric symmetry should satisfy the current density requirements set on sources. The electric current density becomes anti-symmetric while the magnetic current density becomes symmetric according to the plane chosen as electrically symmetric Lower: A plane of magnetic symmetry should satisfy the current density requirements set on sources. The magnetic current density becomes anti-symmetric while the electric current density becomes symmetric according to the plane chosen as magnetically symmetric [88].

ranges from 0° to 180° in 1° intervals. This gives a very fine angular sampling of the far field data, as the equivalence sources of the feed-horn (e.g. spherical wave expansions and radiation pattern discussed in Section 3.6) are required to be sampled as many calculation points as possible.

3. **Getting the EM parameters**

   After the model construction and the solution settings with the request of field quantities to be calculated, the solver is ready to start to launch the simulation. After the simulation is completed, the other layout called POSTFEKO is used to plot the computed results versus off-axis angle θ at any cut plane of ϕ. The co- and cross-polarization components of the radiation beam pattern are obtained in both forms of gain and electric fields. The phase information and S11 parameter is also calculated by default if otherwise specified.